UNIVERSITY OF OKLAHOMA

GRADUATE COLLEGE

TRIAXIAL AND INJECTION EXPERIMENTS ON ROCKS AND THEIR IMPACT ON PERMEABILITY AND ACOUSTIC EMISSIONS

A THESIS

SUBMITTED TO THE GRADUATE FACULTY

in partial fulfillment of the requirements for the

Degree of

MASTER OF SCIENCE

By

ROHIT BAKSHI
Norman, Oklahoma
2017

TRIAXIAL AND INJECTION EXPERIMENTS ON ROCKS AND THEIR IMPACT ON PERMEABILITY AND ACOUSTIC EMISSIONS

A THESIS APPROVED FOR THE
MEWBOURNE SCHOOL OF PETROLEUM AND GEOLOGICAL ENGINEERING

BY

____
Dr. Ahmad Ghassemi, Chair

____
Dr. Xingru Wu

____
Dr. Catalin Teodoriu

DEDICATION

To my family – especially my aunt, uncle, grandfather and grandmother who are no longer with us but have guided my life in many ways -wish you were here at this milestone in life. Without all of you, this would not have been possible.

ACKNOWLEDGEMENTS

First and foremost, I would like to extend my sincere gratitude to supervisor Dr. Ahmad Ghassemi. His valuable guidance and support have helped me to complete my thesis. I look forward to working under his guidance in the future also.

Secondly, I am grateful to Dr. Xingru Wu and Dr. Catalin Teodoriu for being the co-chairs and providing valuable suggestions for further improving the quality of thesis.

Thirdly, I would like to thank all my colleagues at the geomechanics lab especially Yawei Li, Dr. Xue Jun Zhou, Mostafa Halvaei Eskandari, Elahe Khosravi and Lianbo Hu who have provided valuable help and provided useful discussions that have helped me complete my work. Thanks also to Stephen, Alex and Zhi for being supportive throughout my work. Special thanks to Jyotaditya, Shantanu, Maulin and Ankita for their help in conducting some tests without which this work would have not have been complete.

My deepest and sincere gratitude to my entire family, none more important than my parents, Satish and Veena and my wife Krupa – without their support and sacrifices, this work would have been impossible. I only wish I was not bound by a few sentences to express how grateful and appreciative I am for their love and support throughout my entire life.

Also thanks to the rest of my family – siblings, in-laws, aunts and uncles.

My time in Norman would have been very difficult without my friends Jyotaditya, Shantanu, Maulin, Himanshu, Nur, Sama, Sarvesh, Subbu, Ankita, Dhanya, Vineet, Aparajita, Abhishek, Sami and Janny. I hope we remain friends forever and our paths cross again in future.

TABLE OF CONTENTS

LIST OF TABLES

List of Figures

ABSTRACT

Understanding the various micromechanical processes that occur in a rock under in-situ stress conditions has been a major imperative of rock mechanics. Some of the applications of rock mechanics include the science of earthquakes, improved recovery of energy from hydrocarbon and enhanced geothermal systems (EGS), civil and mining engineering to name a few. To obtain a comprehensive understanding of these micromechanical processes, triaxial experiments (heated and non –heated) have been performed while monitoring stress, strain, permeability alteration, wave velocity, and acoustic emissions. A variation of triaxial testing in which failure is caused by increasing the pore pressure of the sample during triaxial loading has also been carried out and studied. A range of rocks with a wide distribution of properties has been tested for this purpose – this includes sandstone, shale, rhyolite, rhyolitic tuff, basalt, limestones and granite. The reservoir rocks were also characterized using mineralogical and pore structure (SEM and thin sections) analysis.

Permeability of is an important rock property, and in this work, rock permeability variation has been studied during triaxial compression tests for a number of tuffs and basalts from potential EGS sites. Correlations have been found which link the change in permeability after failure to the rock's initial porosity. It has been shown that axial permeability reduces for high porosity samples while it increases for low porosity samples after triaxial loading. Using the data for a range of rocks a porosity cut-off value for transition from decrease to increase of permeability has been proposed. Porosity of all samples was also measured and has been provided – in most cases the influence of confining pressure has also been provided.

In addition, Acoustic emission (AE) generation has monitored during the failure process and at various stages of triaxial deformation. Depending upon rock type, high or low AE activity has been observed. It has been observed that sandstones, granites and basalts generate high AE while limestone while certain types of tuffs rich in clay minerals do not generate much AE activity. Rocks that display ductile failure do not generate high acoustic emissions while brittle failure almost always does. In this study, ductile tuff samples generated less than 10 events up to failure whereas brittle samples from the same well generated greater than 1000 events.

The AE events were located to better depict areas of high AE activity within the samples. Higher AE activity was always observed in the fractured area and zones closer to the fracture. In addition to the above temporal and spatial analysis, Moment tensor analysis has also been performed using two techniques –one simplistic based on first wave arrival and the second with full tensor inversion with the primary aim of understanding emission source type – shear, tensile or mixed. Results show that both techniques only slightly differ from each other. Energy released during fracturing, amplitude of events and their frequency has also been studied for the rocks tested. The results show that maximum energy release happens during fracturing and a range of frequencies are generated during fracturing with no specific frequency tied to fracturing process.

Using the strain, stress, permeability, wave velocity and AE data sets, the micromechanical processes which usually culminate into the shear fracture has been illustrated for the rocks tested. In relation to permeability change, pore collapse and micro-cracking compete with each other during loading and depending upon the rock porosity, the final permeability may be higher or lower. It has been argued in this thesis that the above kind of analysis – combining several methods of data monitoring including stress, strain, wave velocities, permeability, mineralogical, pore structure and acoustic emission analysis with moment tensor inversion is a powerful tool for elucidating the micromechanical or macromechanical evolution of damage, during the deformation of rock.

Overall it has been shown here that in a triaxial test, permeability alteration within a rock is strongly linked to rock porosity and the event of largest change in permeability always coincides with a major release of AE. It has also been shown that volumetric strain determines the changes in permeability more strongly than any other parameter. The triaxial-injection tests were completed successfully for a range of rocks. The results show that there are differences in results obtained while using this test instead of the standard triaxial test. Several high temperature tests were also performed and associated parameters calculated -it has been concluded that temperatures higher than 100 ^{O}C are needed for observing changes in elastic properties as compared to room temperature testing.

OBJECTIVES AND THESIS STRUCTURE

The focus of this thesis is on three linked parameters – triaxial compression and injection-induced failure in rock, and the effects on permeability and the associated acoustic emissions. Both room temperature and elevated-temperature tests are used depending on the project need and rock/system availability. Rocks studied for this work include a diverse set of rocks which includes sandstone, rhyolite, rhyolitic tuff, basalt, rhyodacites, shale and granite.

In this study, a variety of samples from oil and geothermal wells as well as quarries have been tested. It has been an aim of this study to have a diverse set of rocks with different mineralogical composition and textures and fabrics to identify trends if possible. Results for a total of 21 samples are reported here. The results include strength and elastic parameters, permeability changes, effects of heating and cold water injection during (some samples) and detailed acoustic emission analysis. In the end a correlation of all the above mentioned parameters has been provided. The thesis consists of six chapters:

1. Chapter 1- Literature Survey: This chapter provides an overview of some relevant published literature related directly or indirectly to this thesis.
2. Chapter 2 - Sample description: This chapter describes the textural and mineralogical properties of the various samples that have been tested (pore structure analysis done using thin sections and SEM imagery have been provided in the Appendix 1).
3. Chapter 3 - Triaxial testing: This chapter describes the triaxial testing procedures and results including strength and elastic parameters obtained from

all the samples. Also included are results of the heating related parameters (strain caused, coefficient of expansion etc.) for the case of tests at elevated temperatures.

4. Chapter 4 –Permeability and Porosity analysis: This chapter details the porosity and before and after failure (axial) permeability of all the samples described in the previous section. This is helpful in understanding the influence of triaxial fracturing in altering sample axial permeability
5. Chapter 5 – Acoustic Emissions analysis: This chapter provides information about the results of the acoustic emissions analysis conducted on all the samples. Information provided here includes number of hits (cumulative and rate), energy released, source analysis (identifying shear, compressive and tensile failure mode) using first arrival waveform polarity method as well as Moment tensor analysis for a few samples.
6. Chapter 6 – Conclusions and recommendations.

CHAPTER 1: INTRODUCTION AND LITERATURE REVIEW

PERMEABILITY

One of the most critical parameters for characterizing the productivity of a hydrocarbon or EGS reservoir is its permeability. Unconventional petroleum and geothermal resources occur in low permeability rocks. Economic production requires enhancing permeability. This is done mainly by hydraulic stimulation in order to create new fractures or cause natural fractures and weakness planes to slip thereby improving permeability. Permeability development is dependent on rock type, and deformation characteristics (i.e., ductile vs brittle). Therefore, understanding how permeability is created and evolves during stimulation is useful for stimulation design. As a result experiments need to be conducted in the lab to better understand this process.

Rock permeability is usually measured using the Darcy's law (Darcy, 1856) where a number of assumptions must be made around fluid properties (incompressible), fluid velocity (laminar flow), rock properties (homogeneous) etc. Although Darcy derived this equation using experiments on sediments, it can also be derived simply from the basic fluid flow equation - the Navier Stokes equation.

Laboratory measurement of permeability is done by using one of the three methods – steady state, unsteady state (or transient technique) (Brace et al., 1968; Jones, 1988) and pore pressure oscillation technique (Kranz et al., 1990; Fischer, 1992; Fischer and Paterson, 1992; Bernabe´ et al., 2006). Steady state measurement technique is the most reliable technique for measuring permeability as it involves the most fewer assumptions of all the three techniques mentioned earlier. However, its biggest limitation is the time taken for calculating permeability values (Metwally and Sondergeld, 2011). This method takes even longer if fluids with lower mobility like liquids are used. Pulse decay on the other hand usually takes half the time but has a more uncertainty in the measurements. In this thesis, all of the permeability measurements done during the triaxial testing have been done using steady state method to reduce uncertainty.

In this thesis, most of the measurements have been done using Nitrogen gas for reducing time required for measurements (use of water takes six to 10 times more time as compared to gas due to lower mobility). Viscosity and other corrections have been applied whenever necessary. Presence or absence of fractures has been studied by various authors as well (Sinha et al., 2012) and results show that the permeability's can be higher by several magnitudes if fractures are present.

Laboratory methods for finding permeability using gas as the pore fluid has been found to however always lead to higher apparent permeability for any porous sample (Klinkenberg, 1941). Klinkenberg referred to this as being due to a phenomenon called as slip and came out with a method to account for this effect. Akkutulu et al. in 2011 demonstrated that simple Klinkenberg corrections weren't sufficient for measuring permeability in shales and other ultra-low permeability rocks. The authors derived a new more complex equation and referred to it as the 'modified Klinkenberg correction' for such rocks. In this regard, an important aspect of findings by Mathur et al.,2016 that have been used as part of this thesis is the fact that if pore pressures are maintained at high levels (>2000 psi), these complex slip corrections are no longer required as the error becomes insignificant at those pore pressures.

Jones presented a slight modification of the technique of unsteady state technique in his paper in 1996 which has also been used for measuring variation of permeability with different confining pressures (before triaxial testing) of most of the samples tested as part of this thesis work. This was done using a commercial machine set up referred to as the AP-608 porosity-permeability measurement system by core test systems.

Most of the rocks used for this thesis work had extremely low permeability – in the order of nano Darcy scale (1 nano Darcy equals 10^{-22} m^2). Measuring permeability in such tight rocks can be challenging. Although Brace, 1968 successfully measured permeability as low as micro darcy scale for westerly granite in the 1960's using argon and water, it is only in the last decade that several authors have studied this phenomenon in detail, mainly for shales due to the advent of hydraulic fracturing in tight oil and gas reservoirs. These authors (Cui et al. 2013; Sinha et al. 2012; Bustin et al. 2008; Mathur et al. 2016) have shown that permeability as a parameter in low permeability rocks (<1 mD) is highly sensitive to numerous factors which include sampling scale, pore shapes, their sizes, distribution, pore pressures, fluid type, temperature, stresses involved (horizontal or vertical), time used for measurements, machine and human error etc.

Stress dependent permeability has been a focus of study since the 1960's. In nature, a wide range of temperature, pressure and stress states are observed. Hence understanding the influence of these parameters especially stress with permeability can help provide insights into coupling of sample deformation and its capability to transport fluid (Zhu and Wong, 1997). For the low porosity rocks, it has been shown by several authors that once dilatancy sets in a triaxial experiment, the permeability increases by 2-3 orders (Moore et al., 1986, 1994; Zhang et al., 1994; Peach and Spiers, 1996; Siddiqi et al., 1997; Mitchell and Faulkner, 2008). Investigation into this phenomenon by the authors revealed that this is due to microcracking within the sample. A more recent study by Paola et al, 208 has provided more insights in to this phenomenon by using anhydrites as the low porosity rocks.

The testing on low porosity rocks was studied more with primary focus on marble (Zhang et al., 1994), halites (Peach and Spiers, 1996; Stormont and Daeman, 1992) and granite (Zoback and Byerlee, 1975; Brace et al. 1968, 1978). However, it has long been known that most igneous rocks like granites, basalts, rhyolites, certain types of Tuff fall in the range of ultra-low permeability rocks, though hardly any experiments have been done on measuring permeability for these rocks with the earliest attempt at measuring those for nuclear radiation study purposes done by contractors for the US government in their report ONWI-458, 1983. Even in these experiments, only fractured igneous rocks were taken whose permeability values were in milli Darcy (mD) range or higher. The development of Enhanced geothermal systems (EGS) however has made it imperative to understand the permeability of these rocks and to understand the stress-permeability correlation for these rocks which is otherwise very well known for clastics (Wilhelmi, B, 1967; Byerlee, 1975). The first detailed study on impact of stress on permeability for higher porosity sandstones was done by Zhu and Wong (1997) where they tested five different sandstones (Adamswiller, Berea, Boise, Darley Dale and Rothbach) in the porosity range of 15% to 35% over a wide range of confining pressures. Their key finding was that for all sandstone except Darley dale the permeability decreased as the sample dilated. A direct correlation was observed between porosity of the sample (Darley Dale had porosity of 12-14%, rest had 17% or higher) and its final value of permeability. It was observed that except for Darley Dale sandstone with the lower porosity, all other samples had their permeability reduced even with dilatancy. A key finding of this thesis work will show that’s this behaviour isn’t restricted to sandstones but is also seen in Newberry Tuff specimens. This finding is possibly the first time that this behaviour is being reported for igneous rocks. Another key finding was bringing forward the concept of critical stress state- C*. The author demonstrated that in cataclastic flow regime, with increasing deviatoric stress there would be significant reduction in porosity (and hence permeability) if the mean stress level crossed a threshold called as the critical stress – C*. Wang and Park in 2002 demonstrated the same phenomena when they tested sandstone triaxially and did real time measurements of permeability (this work has also been done in this thesis).

Very few experiments have been conducted to study the effect of measuring permeability in a transverse direction on a core sample than the usual axial direction – in fact only four such publications were found (Greenkorn and Johnson, 1964; Stavrogin and Tarasov, 2001; Dautriat et. al., 2009; Korsnes et. al. ,2006). There are many more that deal with this topic from the point of view of theory though – Bai et. al., 2002, Davies et. al., 2001; Fatt and Davis, 1952; Dobrynin, 1962. Of the four mentioned earlier, only two authors (Stavrogin et. al, 2001 and Dautriat et. al., 2009) measured the effect of before and after fracturing at the same stress level; the other two dealt only with measuring permeability before failure and comparing results. On a non-fractured rock, the differences between the two methods of measurement are not expected to be large unless rock is anisotropic or has layers of varying properties. In such an experiment on Chalk cores (~40% porosity) by Korsnes et. al., 2006, four out of eight samples showed 20-40% higher permeability using transverse measurements rather than axial while the other four didn't show any differences at all. On sandstones (~31% porosity), a larger difference (40% to 100%) was observed with the horizontal values being always higher (Korsnes et al., 2006). These tests were conducted at low effective confining pressures of 3 and 6 MPa (~500 psi and ~1000 psi). In another experiment performed by Dautriat et. al., 2009, differences of 40-60% were seen between axial and transverse measurements of permeability with transverse again being higher. Overall, a reduction of permeability (both horizontal and axial) was always seen at the end of the experiment – just as can be expected for high porosity samples – this sample's porosity was ~22%. The three samples tested here were also highly anisotropic with differences of 100% between the initial values of axial permeability and radial values at the start of the triaxial experiment. Hence it isn't possible to understand if the use of a different permeability measurement direction(in this case – transverse versus axial) made a difference. The one example which is most relevant for this work though due to the testing of low as well as high porosity samples is work by Stavrogin and Tarasov (2001) in their famous book on experimental testing. The authors measured the differences in pre-and post fracture permeability for marble (low porosity), sandstones (medium to high porosity) and lignite (high porosity) using both axial and transverse measurement methods. Their work showed that there are huge differences when comparing axial and transverse permeability values – for confining pressures of 5 and 10 MPa, the difference between permeability variations between transverse and axial measurements after fracture was four orders of magnitude (10000 times). At higher confining pressure of 25 MPa, the differences reduced to 1-1.5 orders only. According to the authors, these differences arise due to two effects: those caused due to test procedure and the micro-fracturing caused in sample during the deformation process. The test procedure difference alludes to the ‘end effect’ of platens – the stress distribution in the sample is distorted due to friction between ends of specimen and the loading platens. This causes concentration of stress in the middle of the sample (and consequently maximum deformation) whereas the ends which are close to platens are affected the least and hence permeability changes least in that area. Hence transverse flow would be expected to be higher (fractured or unfractured sample). This effect was shown to play a huge role in rocks that fail in ductile mode (Stavrogin and Tarasov (2001)– while the axial permeability after failure was seen to have decreased (as will be seen in Sample GEO-N2-3858.5-H1’s failure in chapter 4), the transverse permeability values had increased by 10-10000 times with a ratio of 800-1600 between transverse and axially measured values. The same ratio for more brittle samples was 3-13 due to this factor being negligible (refer section 4.3.1 in the book).

The second factor – changes caused by micro-fracturing, is more complex and refers to the fact that shear fractures created in sample after triaxial fracturing favor transverse measurements due to a high permeability zone created by micro and macro-fractures always intersects the transverse placed pore pressure ports as compared to axial ports which may or may not have the fracture intersecting them.

Measurements of permeability during testing – whether done axially or horizontally can therefore create a big difference especially if the fracture doesn’t intersect the ends. As explained earlier, for low porosity samples (<5%), the difference in axial and horizontal permeability is 3 to 6 orders of magnitude depending upon confining pressure used. For higher porosity samples, permeability reduces and the same authors showed that for both axial and horizontal measurements, differences seem to be far less when comparing axial and horizontal permeability. Many of the samples tested (majority) had fractures that did not intersect the ends. Therefore, the real permeability could be up to 3-6 orders higher. It should be noted that on a production scale or commercial viability, a reservoir (hydrocarbon or EGS) has limited to no potential if its permeability is in nanodarcy as compared to if its permeability is in milli Darcy (mD) hence making correct measurements and interpretation of reported permeability values very important. This thesis will cover several examples of how permeability changes as we tested low porosity and high porosity rocks.

HIGH TEMPERATURE TRIAXIAL TESTING

First studied extensively by Bartlett, Adie and Wheeler (1910), the field of influence of heat on rock properties has many applications in civil engineering, petroleum, nuclear and EGS industry. Wheeler reported that rocks when taken to 1000 ^{o}C and back had different lengths in the end due to permanent deformation of the intrinsic structure and different responses of the underlying compounds within the rock. Hockman and Kessler (1950) tested a large number of granite samples over a smaller temperature range of 60 ^{o}C and found that when heating rates were extremely low at 0.4 ^{o}C/min, no permanent deformation in rocks were observed i.e process was reversible in terms of rock properties. Warren and Latham, 1970 used AE to understand microcracking in rocks while being subjected to large thermal gradients. They concluded 10 ^{o}C /min was a safe heating rate to avoid large scale micro fracturing. Todd et al. (1973) further refined this to 5 ºC/min in but couldn't test below this due to equipment limitations.

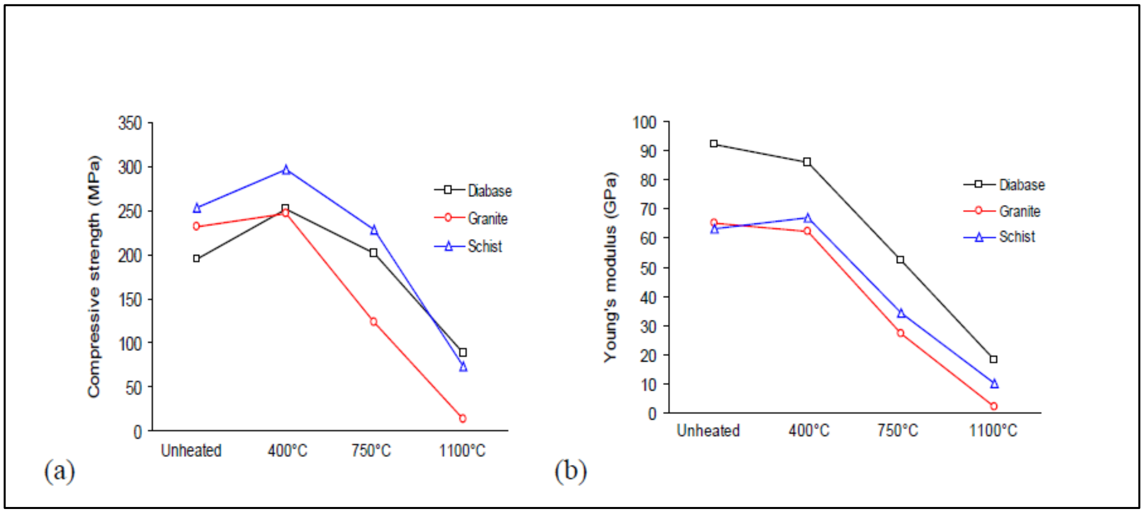

Figure 1: Trend of (a) compressive strength of the studied rock types subjected to heat treatment at different temperature levels and (b) Young's modulus of the studied rock types subjected to heat treatment at different temperature levels (*taken from Saiganag, 2012*)

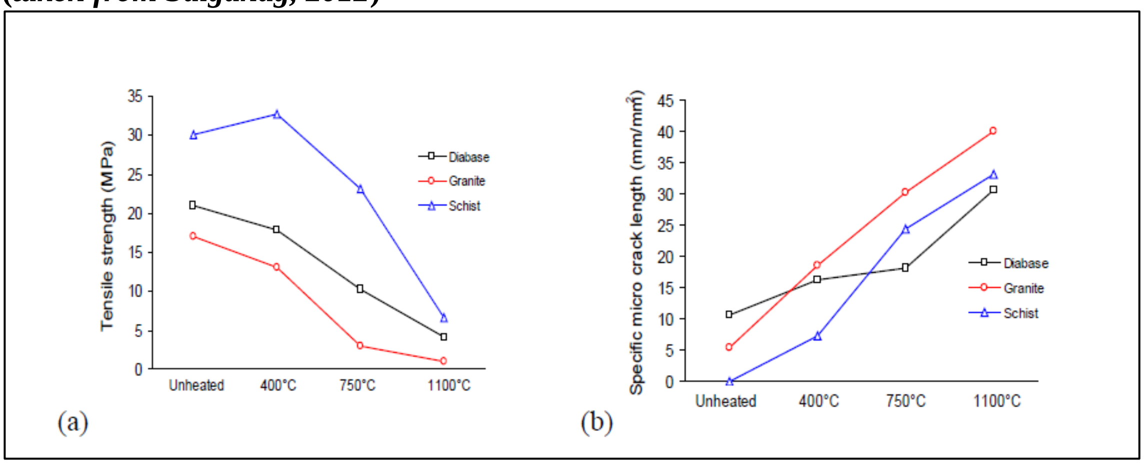

Figure 2: Trend of the a) tensile strength of the studied rock types subjected to heat treatment at different temperature levels and (b) the micro-crack distribution of the studied rock types subjected to heat treatment at different temperature levels (*taken from Saiganag, 2012*)

Richter and Simmons in 1974, tested several lunar igneous rocks under thermal conditions to understand their coefficients of thermal expansion and resulting cracking within the sample. They reported that for heating rates that were higher than 2 ºC, or temperatures of 350 ^{o}C, permanent strains are developed within the sample which are inelastic. Yong and Wang in 1980 showed that Acoustic emissions (AE) were generated even if rocks were heated at rates as low as 0.4 ^{o}C/min. The work done as part of this thesis matched the results from Yong and Wang -temperature increase rates of even 0.3 ^{o}C/min were found to generate some AE.

Saiganag (2012) tested several types of rocks to heated conditions up to 1500 ^{o}C and then studied the impact on elastic modulus, Poisson's ratio and strength (compressive and tensile) once they had cooled down. It was reported that a heating or cooling rate of above 2 ^{o}C causes micro cracks into the sample during heating and cooling. Plots shown above show that up to about 400 ^{o}C the properties didn't change much but after that, there was a clear impact on properties as temperature was changed. In the plots, we can see that strength, young's modulus and Poisson's ratio don't change much but micro crack length does increase even if rocks are subjected to temperatures of 100 ^{o}C. For the purpose of this thesis, rocks were heated to temperatures of 95 ^{o}C maximum and their properties have been studied. AE generated during heating of rocks gives an idea about whether micro cracking occurs in the sample. Experiments performed by some authors (cite examples here) have concluded rates of less than 2 ^{o}C for no micro cracking. It has been shown in this work that this might dependent on rock type and in case of basalts, AE was generated during heating even at rates as low as 1 ^{o}C (Simmons and Cooper, 1977; Ritcher and Simmons, 1974).

As for thermal heat coefficient, Bauer and Handin calculated the value as $5.3x10^{-6}$. As will be shown in later chapters, these values were very well replicated in heated experiments performed on basalts. They also calculated the strain seen in Basalts with temperature up to 800 ^{o}C. As will be shown later, results obtained while testing basalts as part of this thesis matched very well with the above results.

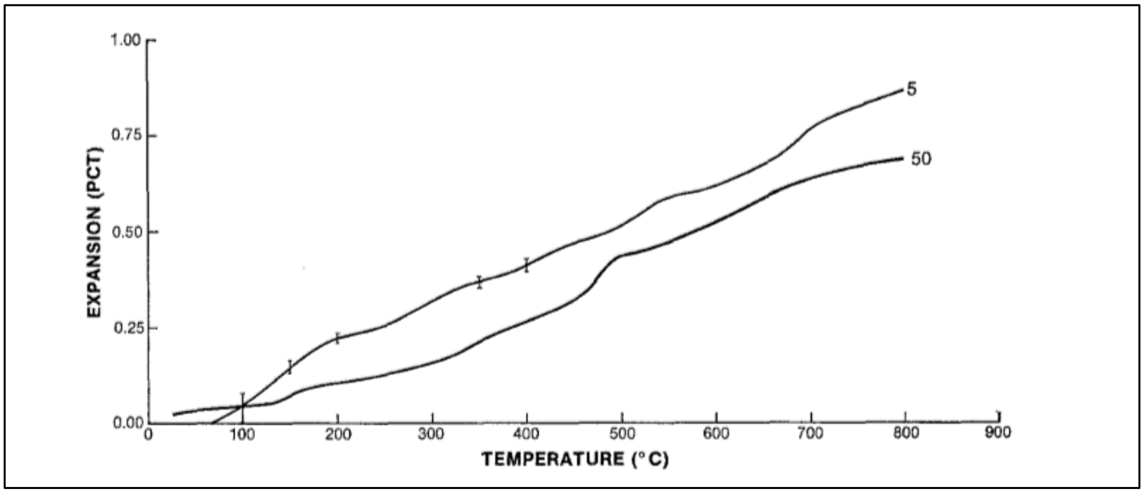

Figure 3: Linear thermal expansion of Cuerbio Basalt under different confining pressures (5 and 50 MPa) showing its variation with temperature. ***(After Bauer and Handin)***

ACOUSTIC EMISSIONS

Applying stress on a rock, whether elastically or inelastically, can cause a change in its dimensions. This strain energy is stored in part as elastic strain and a part is converted to several other forms of energy including thermal, magnetic electrical, chemical and acoustical energy. The acoustic energy is of immense interest for understanding stress related effects on rocks or metals and has been a subject of great interest since 1920's when it was first used for finding cracks in metals. AE can provide comprehensive information on the origination of a discontinuity (flaw) in a stressed component. These discontinuities release energy as they grow. This energy can travel through the medium in the form of high frequency waves which in turn can be received through sensors or acoustic crystals which convert it into a voltage. These signals are called acoustic emissions. In 1928, A.F. Ioffe published a paper on the mechanical properties of crystals, which can be considered as the beginning of research into the acoustic emissions of rocks. Its first commercial use as a non-destructive method on metals was by J.Kaiser in the 1950's. AE frequencies for rocks or metals are usually in the range of 100-1000 kHz which is above frequency of audible sound. However, they exist in the entire frequency spectrum with earthquakes having a frequency of only a few Hz. The amount of acoustic emissions released and associated energy is a function of size of the source event and its velocity. This is the reason why a sudden brittle fracture gives a much higher response than a creep experiment where damage is much lower. As noted by Lavrov and Shkuratnik in 2004, the total count and number of AE pulses are time integrals of the count rate and the AE activity and are the most widely used acoustic emission monitoring parameters which positively correlate with the inelastic strain rate. If the velocity of the waves produced by the source and the difference in arrival time between the different crystals is known, then the location of the event can be done in 3-D. For 3-D location, a minimum of four crystals is therefore required. In this regard, the correlation integral is useful which is defined as:

$$C(R) = \frac{2N_R(r < R)}{N(N-1)}$$

Where, $N_R(r<R)$ is the number of source pairs separated by a distance r (shorter than the given R) and N is the total number of events analyzed. This can be further used for fractal analysis and hypocenter determination.

The most famous initial paper on this subject for rocks is certainly Scholz's 1968 paper in which he linked micro-cracking, brittle and ductile failures to the Acoustic emissions (AE) recorded during several compression tests done on rock samples. He also tried to link axial and volumetric strain to AE generated at various stages of the triaxial experiments.

Figure 4 below shows the various parameters of an AE signal.

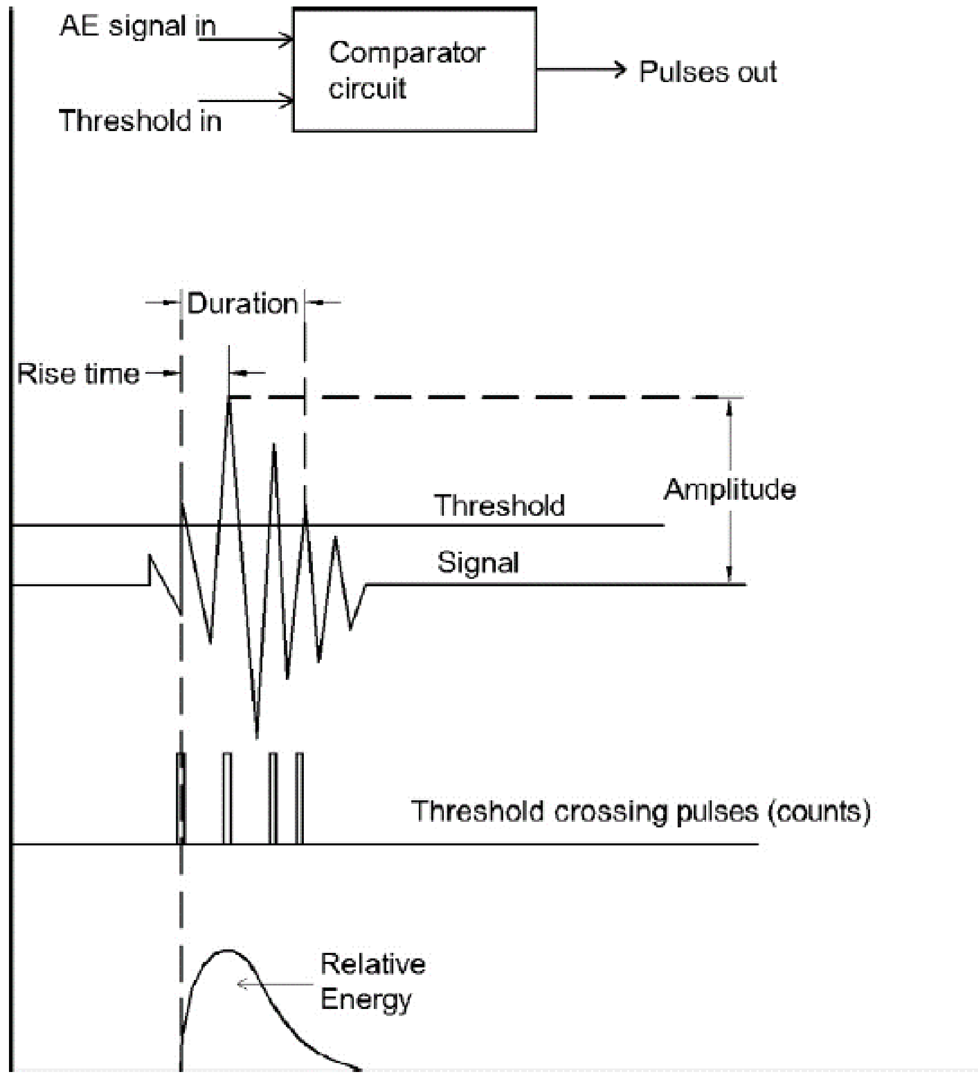

Figure 4: Definition of different parameters of an AE signal (*after Roberts and Talebzadeh, 2003*)

The Kaiser effect is one of the most famous and interesting effects observed in the AE of metals and rocks. This effect, first found by Kaiser in 1930's first for metals, says that if metals or rocks are repeatedly loaded again and again, little or no AE would be generated until the previously attained highest stress is exceeded. It was subsequently demonstrated by Goodman (1963), Chen (1976,1977) and Dunegan and Taro (1971) that this exists also for rocks. In a way, it can be said that the rock remembers the maximum stress applied on it.

CHAPTER 2: ROCK SAMPLE DESCRIPTION, MINERAL CONTENTS AND PETROPHYSICAL PROPERTIES

The seven types of rocks tested as part of this thesis are Berea sandstone, Sierra white granite, Rhyolitic tuff, Rhyodacite, hydrothermally altered Tuff, Basalt and Shale. Their textural and mineralogical description is provided in this chapter along with results of their dynamic tests. A more detailed explanation of textural properties and pore structure can be found in the Appendix 1.

TEXTURAL AND MINERALOGICAL PROPERTIES

Berea sandstone

Berea sandstone is a clastic rock with large grains (>1 mm) and composed primarily of quartz (>90%). A very homogeneous grayish color rock, Berea sandstone is characterized by high porosity (18-20%) and permeability (100mD-200mD). A detailed analysis on the geology and properties of the Berea sandstone has been provided by Pepper et. al., 1953. The Berea Sandstone tested for analysis as part of this thesis was provided by in the form of 1’x1’x1’ blocks by Cleveland quarries. These were cored with water as a coring fluid to obtain core samples of the 2”x1”, 4”x2” and 4”x2.5” sizes. One such picture of the 1” sample which was tested subsequently is shown below:

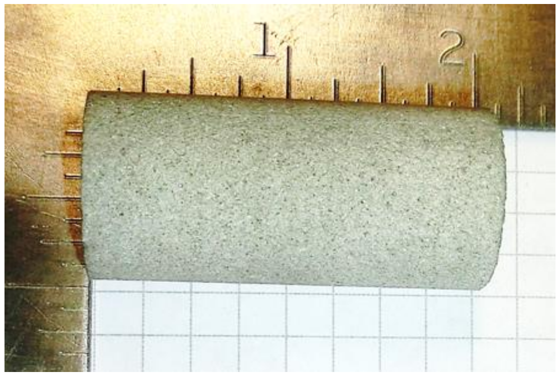

Figure 5: Picture of a 1" diameter Berea Sandstone used for testing.

The mineralogical composition of the rock as provided by the company is shown in Table 1 below. As can be seen, it is comprised mostly of silica (>93%) with other minerals forming the remaining 7%.

Table 1: Compound composition percentage for Berea Sandstone

Compound	Composition (Percentage weight)
SiO_2	93.13%
Al_2O_3	3.86%
Fe_2O_3	0.11%
FeO	0.54%
MgO	0.25%
CaO	0.10%

The permeability of the rock block was provided by the supplier to be in the 100-200 mD range. This was tested individually on all samples after coring and found to be in the 75-150 mD range. The porosity was also measured on all samples before testing and found to be 18-20%. Procedure for measuring permeability and porosity has been explained in the chapter four. Thin section and SEM images were also taken to understand the texture and pore structure – these have also been provided (Figure 181, Figure 182 and Figure 183) in the Appendix 1. These images show that pores are well connected and are round in shape with some presence of clays.

Sierra White Granite

One four-inch length, two-inch diameter Sierra white granite sample (Figure 6)was tested.

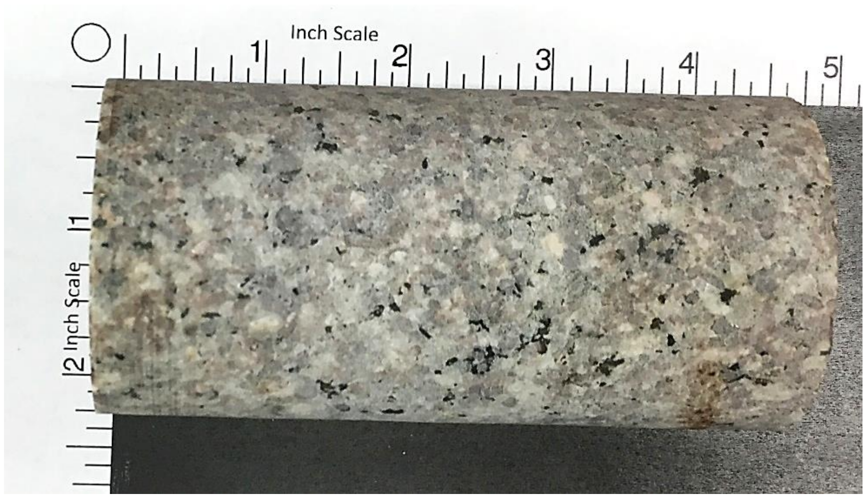

Figure 6: Picture of the Sierra white granite used for testing

The mineralogical analysis was also conducted and is shown in Table 2 and Table 3 below. As can be seen, Feldspars constitute 52% while silica comprises over 30% with the rest being micas and other minerals. The thin section and SEM images taken for this sample and shown in Appendix 1 (Figure 184, Figure 185) shows that the structure is very low porosity (<1% porosity) with large grains (>2 mm) very well interlocked into each other. Very few clay particles can be seen.

Table 2: Compound percentage in Sierra White granite using XRD

Compound	**XRD (Weight %)**
SiO_2	63.9%
Al_2O_3	20.7%
CaO	2.8%
Fe_2O_3	3.2%
Na_2O	4.3%
MgO	1.1%
TiO_2	0.1%
Others	3.9%

Table 3: Mineral percentage in Sierra White granite using XRD

Mineral	**XRD (Weight %)**
Quartz	30.1
Albite	47.4
Clinochlore	4.7
Biotite	1.7
Magnetite	0.9
Cummingtonite	0.3
Chlorapatite	0.8
Muscovite	8.2
Microcline	5.6

Samples from the INEL-1 well

Two core sections each of length 0.5 ft – one from 1558 m depth and another from 3160 m depth of the INEL-1 well were provided by the Idaho National laboratories (INL) for geomechanical characterization. The samples are rhyolite tuffs and rhyodacites based on work by Moss and Barton, 1990. The INEL-1 well is a well drilled into the Snake river valley as part of the Snake river geothermal consortium (SRGC)'s efforts to understand EGS potential in the area. Details of this well and the associated EGS resource are provided in Anders et al., 2014; Rodgers et al, 1998; Kuntz et al, 2002; Welhan et al, 2002; Miller et al, 1978; Bakshi et. al., 2016 and Moos and Barton, 1990. Four two-inch length and one-inch diameter plugs were extracted from these core sections (Figure 7). According to geological studies, rock types in this well are mainly rhyolite tuffs, rhyodacites, basalts and lava deposits (Miller et. al.). The section of core tested here is rhyolitic tuff at 1558 m (4874 ft) and rhyodacite at 3160 m (10365 ft). Pore scale characterization was also performed using thin section and Scanning electron microscope (SEM) imaging – this has been provided in the Appendix 1(Figure 189, Figure 190). These show a very tight rock structure with very little porosity, especially in the deeper section. Also, it can be seen that the rock porosity is not connected at a lot of places.

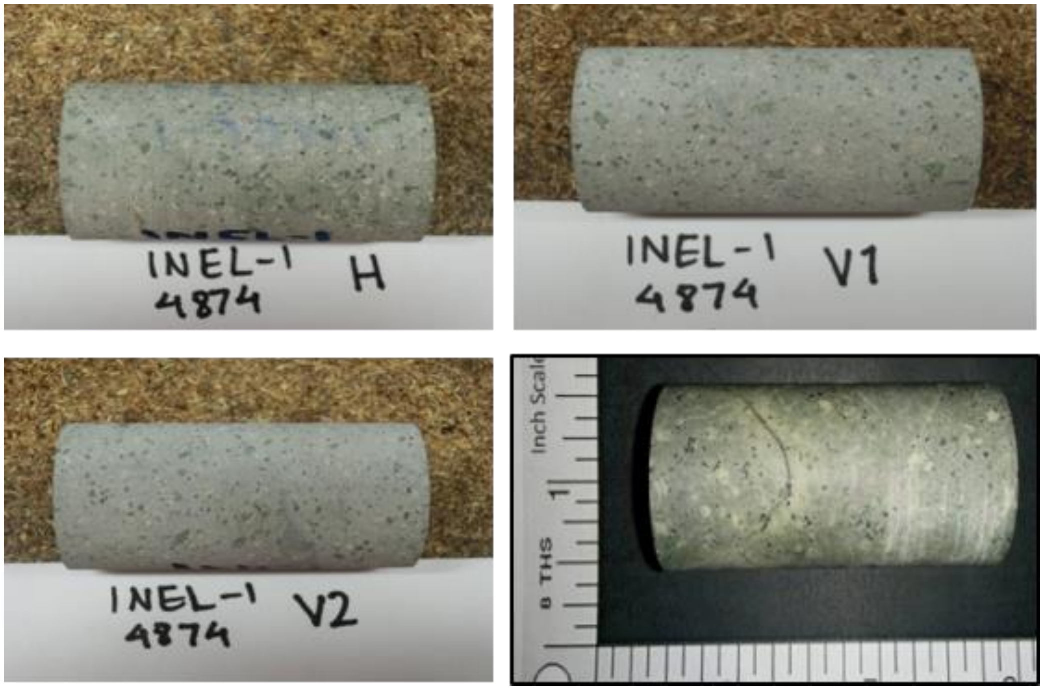

Figure 7: Four samples from the INEL-1 well. These are primarily rhyolites (H, V1 and V2) or rhyodacites. The depths of H, V1 and V2 are 4874 ft while the fourth sample (bottom right) comes from a depth of 10365 ft.

The mineral composition of these core sections was analysed using Fourier transform infrared spectroscopy (FTIR). Table 4 shows the mineral composition of the two core sections.

Table 4: Mineral composition in the INEL-1 core plugs using FTIR

Mineral	**INEL-4874 ft (% composition)**	**INEL-10,365 ft (% composition)**
Quartz	25.55	23.13
Orthoclase Feldspar	25.48	10.87
Oglioclase Feldspar	16.25	10.06
Illite	16.78	2.85
Albite	6.07	21.30
Calcite	0.00	6.83
Dolomite	1.33	4.60
Smectite	4.21	3.04
Kaolinite	1.04	0.09
Mixed Clays	0.88	13.50
Siderite	2.38	2.98

We can see from the above that Feldspars constitute 27-42% of the composition here followed by silica (quartz) at 24-27%.

Samples from the GEO-N2 and OXY 72-3 wells

The GEO-N2 and OXY 72-3 wells are located close to the Newberry volcano (Oregon, USA) and form a part of the EGS resource there (Figure 191). Details regarding the caldera and the several wells drilled (including the GEO-N2 and OXY 72-3) have been provided by Williams (1935), Bargar et al. (1999) and Fitterman et al. 1988.

The GEO-N2 well lies about 2.8 km outside the west flank of the Newberry caldera (Bargar et al. 1999). Cladouhos et al. (2011) suggested that GEO N2 cores have basaltic to rhyolitic silicic lava flows with intervening flow breccia, lithic tuff and volcanic sandstone. This well, drilled to a total depth of 4400 ft., has an average temperature gradient of 124^{o} C/km. The OXY 72-3 well on the other end, is located relatively much closer to the caldera rim on the west side of the Newberry volcano (Figure 191 in Appendix 1). It has an average thermal gradient of 137^{o} C/km (Bargar et al., 1999). For more details regarding these two wells and the associated EGS resource, refer to Bargar et al., 1999.

Eleven 2.5” diameter full core sections Figure 192, Figure 9) of varying length from depths of 3858-4361.5 ft. from the GEO N2 well (Figure 192)and one core section of 1.88” diameter from the OXY 72-3 well (3861-3862 ft.) were provided by the University of Utah Core Library for geomechanical characterization (also see Wang et al., 2016). The full core sections have been shown in Figure 192 in Appendix 1 and Figure 9. The core sections have been classified into two groups for the ease of reporting – the first group consists of the five core sections shown in Figure 192 – labelled as sections A, B, C, D and E from depths of 3681-3682 ft. (OXY 72-3 well), 3858-3859 ft. (GEO-N2 well), 4360.5-4361.5 ft. (GEO-N2 well), 4163.5-4164.5 ft. (GEO-N2 well) and 4179.5-4180.5 ft. (GEO-N2 well) respectively. These shall be henceforth referred to as the 'Cored plugs from the GEO-N2 and OXY 72-03 well'. The second group consists of six core sections with sections 1-4 believed to be from 4200-4400ft depth while section 5 was from 4378.5-4385 ft and section 6 from 4239.5 – 4245.5 ft. (all six of them from the GEO-N2 well). These will be referred hence forth as the "Full core GEO N2 samples". In the first group, out of the many plugs extracted from these five core sections, six plugs -five of them from the GEO-N2 well and one from the OXY 72-3 well were tested. Two were tested under heated conditions (GEO-N2-4361-V2 and GEO-N2-4361-V3).

Figure 8: Six core plug samples from the GEO-N2 well (Group 1) and OXY-72-03 well; with the exception of GEO-N2-4180-H1 and GEO-N2-4163-H1, all others were 1” in diameter and 2” long. GEO-N2-4163-H1 had a length of 1.6”.

The pictures of these six plugs are shown in Figure 8. A detailed textural description is provided in Table 5.

Table 5: Textural properties of the cored GEO-N2 and OXY 72-03 well samples

	OXY-72-3-3861.5-V2	GEO-N2-3858.5-H1	GEO-N2-4361-V2	GEO-N2-4361-V3	GEO-N2-4163-H1	GEO-N2-4180-H1
Depth	3861.5 ft (Oxy 72-03 well)	3858.5 ft	4361 ft	4361 ft	4164 ft	4180 ft
Length (mm)	51.98	46.07	51.98	52.17	39.30	51.12
Length to Diameter ratio	2.05:1	1.83:1	2.05:1	2.02:1	1.56:1	2.01:1
Density	2.74 g/cc	2.20 g/cc	2.53 g/cc	2.51 g/cc	2.21 g/cc	2.42 g/cc
Sample texture	Sample is dark gray to black in color. Sample has an aphanitic structure with few small red grains (<1 mm) (refer fig 68). No fractures or cracks can be seen within the sample with naked eye.	Sample is purplish green in color. Sample has an aphanitic texture with few white depositions (>3mm) spread throughout sample. The sample (with the exception of the inclusions) looks fine grained with grain diameters <1 mm.	Sample is greenish gray in color and has a porphyritic structure with large white grains (>3mm) interspersed within an otherwise fine grained sample. No fractures or cracks can be seen within the sample with naked eye.	Sample is greenish gray in color and has a porphyritic structure with large white grains (>3mm) interspersed within an otherwise fine grained sample. No fractures or cracks can be seen within the sample with naked eye.	Sample is purplish in color and has an aphanitic structure with large white grains (>3mm) interspersed within an otherwise fine grained sample. No fractures or cracks can be seen within the sample with naked eye.	Sample is maroonish gray in color and has an aphanitic very structure with large white grains (>3mm) interspersed within an otherwise fine grained sample. No fractures or cracks can be seen within the sample with naked eye.

More detailed information about these samples including thin section images.is provided in Appendix 1 (Figure 193 to Figure 212). These show a very low porosity matrix with the few pores also being mostly unconnected for samples from depths of 4163 ft and Oxy 72-03 well's samples.

From the Group 2, six full core sections were available which were tested without further coring although their ends were grinded to achieve smooth ends (+/- 0.1mm parallelism between the two flat ends). These six core sections are shown in Figure 9.These samples were labelled based on their depth with a suffix representing the serial number of sample. The samples from 4200-4400 ft depth were provided in a finished condition (smooth ends with a parallelism of +/-0.1 mm between the two ends; Samples GEO-N2-4382-I1 and GEO-N2-4243-I1 had non-smooth ends and they were grinded to get smooth ends with a parallelism of +/- 0.1mm. All the cores had a diameter of 2.5 inches and their length to diameter ratios varied from 1.5:1 to 2:1. Three of these were tested at high temperatures (~90^{o} C). Details of samples including their length, diameter, textural properties and presence of veins/fractures are provided in Table 6.


8 THS
Inch Scale


8 THS
Inch Scale
Inch Scale
N2

Figure 9: Pictures of finished core samples (Group 2) before testing from top to bottom – Sample GEO-N2-4300-I1 (top left), GEO-N2-4300-I2 (top right), GEO-N2-4243-I1, GEO-N2-4300-I3 (left), GEO-N2-4300-I4 (right) and GEO-N2-4382-I1. Descriptions are provided in Table 6 and Appendix 1.

Table 6: Textural properties of the GEO-N2 full core samples

	GEO-N2-4300-I1	GEO-N2-4300-I2	GEO-N2-4300-I3	GEO-N2-4300-I4	GEO-N2-4382-I1	GEO-N2-4243-I1
Depth	~4000 ft	~4000 ft	~4000 ft	~4000 ft	4378.4 -4385 ft	4239.5-4245.5ft
Diameter (mm)	63.53	63.97	63.53	63.55	63.39	63.50
Length (mm)	112.13	94.97	125.63	101.22	127.51	122.40
Length to Diameter ratio	1.76:1	1.5:1	2:1	1.6:1	2:1	2:1
Density	2.71 g/cc	2.70 g/cc	2.70 g/cc	2.69 g/cc	2.64 g/cc	2.74 g/cc
Sample texture	Dark gray in color. Aphanitic with few siderite and hematite minerals spread throughout sample	Dark gray in color. Aphanitic with few siderite minerals spread throughout sample	Dark gray in color. Aphanitic with few calcite minerals spread throughout sample. Large carbonate and chalcedony crystals present	Dark gray in color. Aphanitic with few calcite minerals spread throughout sample	Light gray in color. Aphanitic with few siderite and hematite minerals spread throughout sample.	Dark gray to purplish in color. Aphanitic in texture, few calcite and hematite crystals present.
Presence of observable fractures	Single large observable healed fracture from one end of sample to just before other end of sample	None	Two major observable healed fractures present in sample	Single large observable healed fracture from one end of sample to just before other end of sample	Two observable horizontal healed fractures present	Large number of horizontal and vertical healed fracture veins throughout the sample.

The thin section images of Samples GEO-N2-4243-I1, GEO-N2-4382-I1 and GEO-N2-4300-I1 are provided in the Appendix 1 as well. These show the fine-grained structure of these samples with very few pore spaces. A full textural description of these samples has also been provided in Table 6.

The mineralogy was tested using XRD analysis. Four samples were tested – one from GEO-N2-4300-I2, one each from GEO-N2-4382-I1 and GEO-N2-4243-I1 (locations shown in Fig 1 and 2 for all) and one sample was taken from the white colored healed fractures (veins) present in GEO-N2-4243-I1. There are two ways of representing the composition of a rock – in terms of mineral content or in terms of the chemical compounds – XRD provides both. This data can help determine the type of rock being tested. A summary of the XRD compositions are shown below graphically in Figure 10and Figure 11 in terms of the minerals as well as the respective compound content. The XRD clearly shows that these rocks are primarily basalts with some calcite present in the healed fractures. As will be seen in chapters on triaxial testing, they have high strength and high Young's modulus, consistent with rocks of basaltic nature. Actual numbers are provided in Table 7 and in Appendix 1. Also, refer Bakshi et al, 2016 for more details.

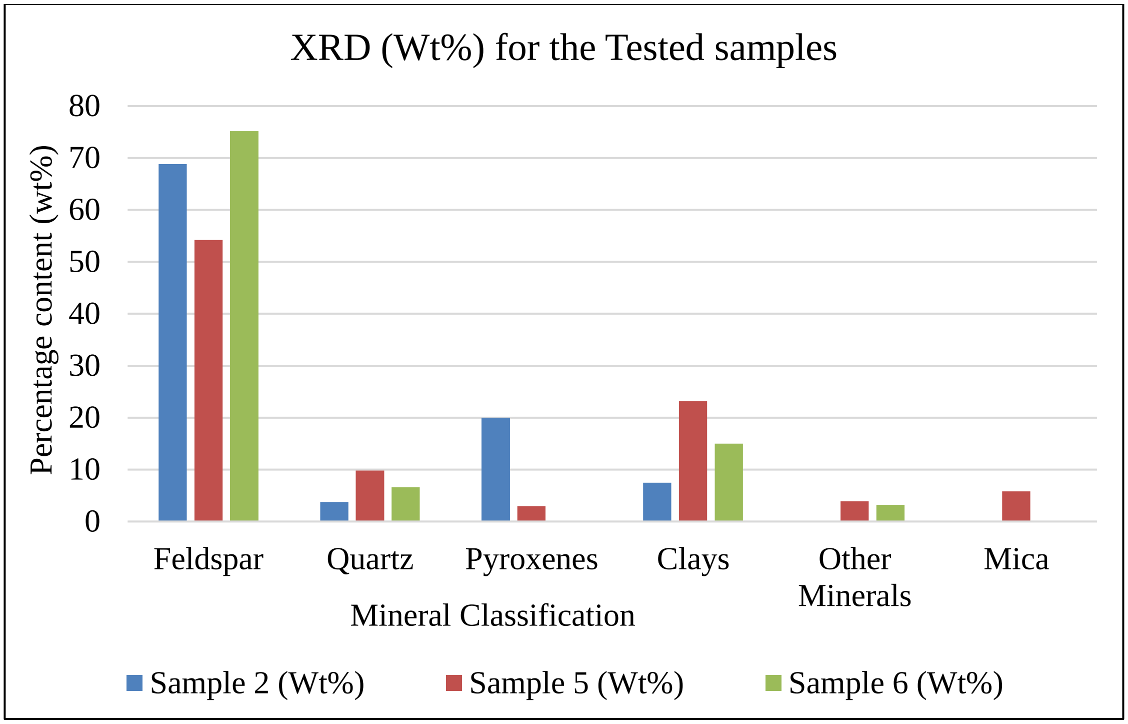

Figure 10: Mineral composition comparison in samples 2, 5 and 6 based on XRD analysis. High Feldspar content can be seen in all samples while the rest vary.

Table 7: Mineral content in samples GEO-N2-4300-I2, GEO-N2-4383-I1 and GEO-N2-4243-I1.

Mineral	**GEO-N2-4300-I2 (Wt%)**	**GEO-N2-4382-I1 (Wt%)**	**GEO-N2-4243-I1 (Wt%)**
Feldspar	68.8	54.2	75.2
Quartz	3.8	9.8	6.6
Pyroxenes	20	3	<1
Clays	7.5	23.2	15
Other Minerals	<1	3.9	3.2
Mica	<1	5.8	<1

From the Table 7, we can see that all samples have a high feldspar content – 68% in GEO-N2-4300-I2, 54% in GEO-N2-4382-I1 and 75% in GEO-N2-4243-I1. Pyroxenes form 20% of the GEO-N2-4300-I2 while clay composition varies from 7- 23% in these samples. Looking at overall compound content, these samples are comprised of 48-53% silica with high Aluminium oxide and Calcium content. It can be seen from Table 37 that the healed fractures (veins) have 50% quartz and 50% carbonates (Ankerite and Dolomite).

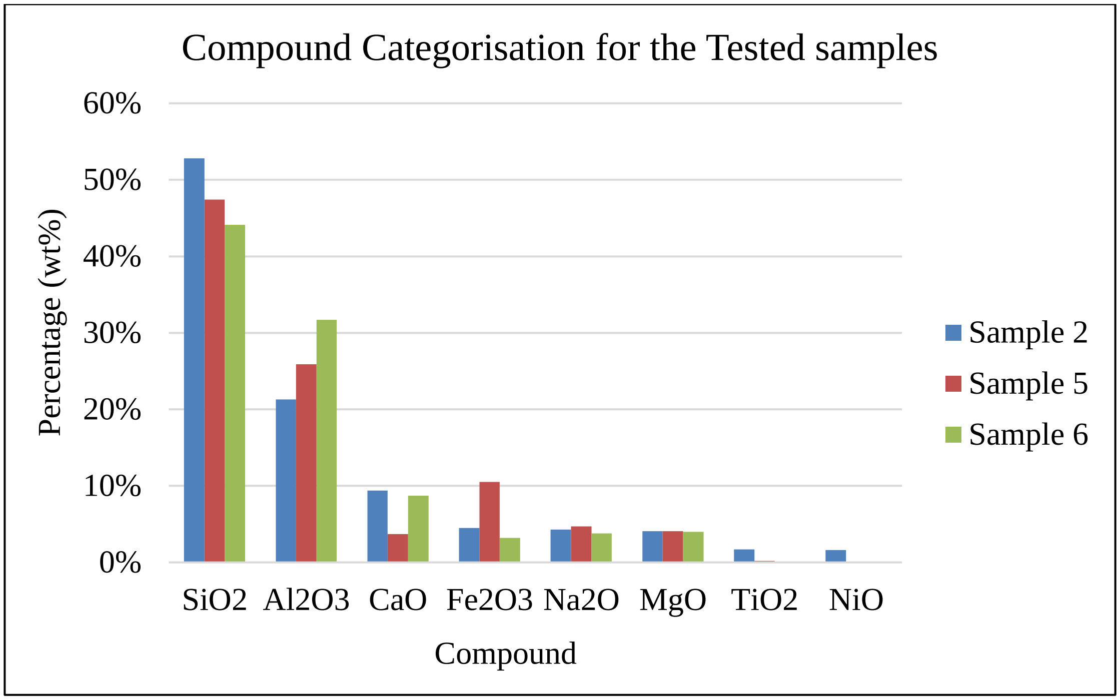

Figure 11: Compound composition comparison in samples 2,5 and 6 based on XRD analysis. Silica varies from 44-53% while Aluminium oxide and calcium comprise the next two compounds in terms of weight.

DYNAMIC VELOCITY MEASUREMENTS

Dynamic velocity tests were carried within the triaxial cell just before the test and in some cases after the test for all the samples that came from the EGS wells (INEL-1, GEO-N2 and OXY-72-3). Velocities should be ideally measured at the in-situ conditions although measuring them at unconfined pressures and then comparing those to higher pressures gives a qualitative idea of the compressibility of the material. Large differences (>20%) are caused in high compressibility materials and vice-versa.

Tests were carried out with axially placed compressional and shear crystals, both of frequency 500 Hz, placed within the top and bottom platens (Figure 13 is an example for the platens made for the 2.5” samples for GEO- N2).

Before conducting dynamic tests, each sample’s dimensions and weight were recorded; the bulk density of each sample was then calculated.

By measuring the travel time through the sample and subtracting the travel time from platen to platen (without a sample in between), the wave velocities of compression and shear waves through the rock were measured. The Young’s modulus and Poisson’s ratio based on these measurements were then recorded and reported. A picture of this test set-up has been shown below.

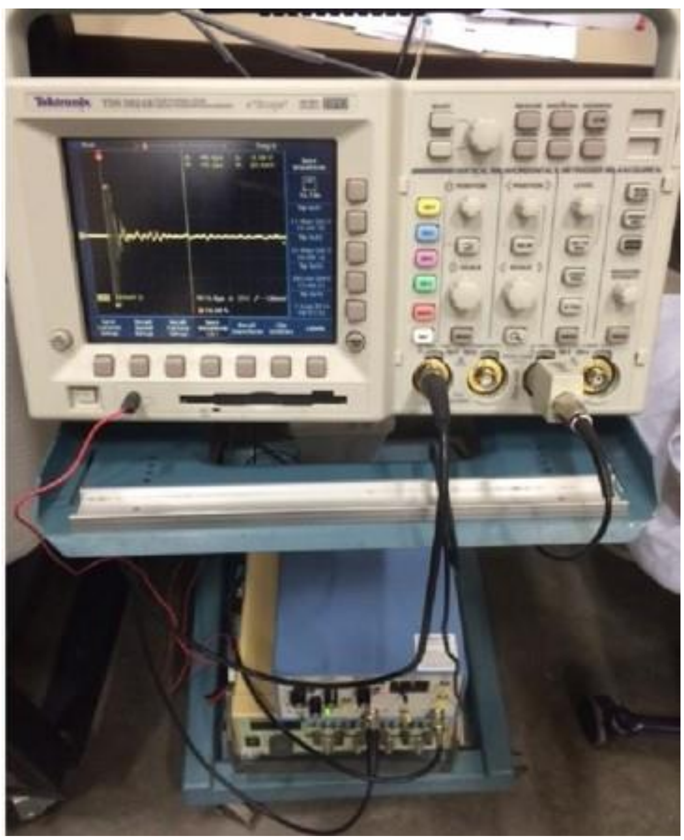

Figure 12: Figure shows oscilloscope used for measuring the compressional and shear velocities.

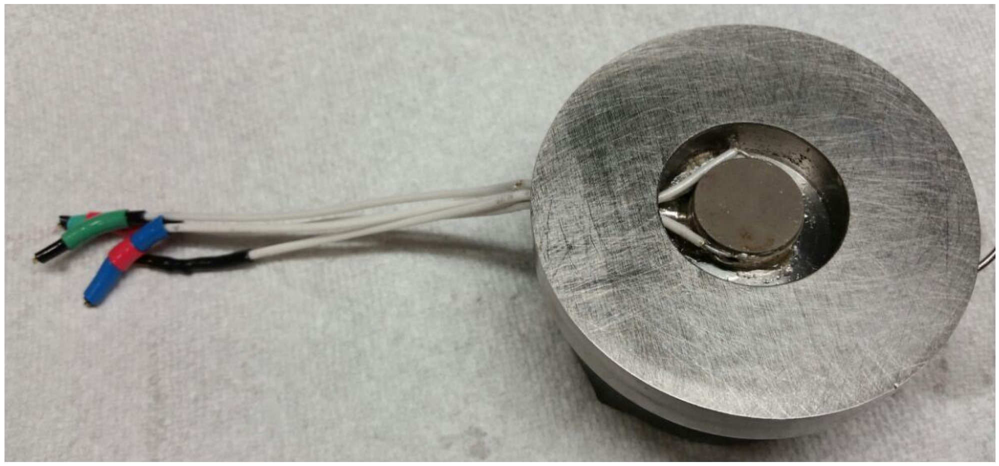

Figure 13: Figure shows the Vp, Vs crystals housed within the loading platens for the 2.5" diameter samples firmly attached to the surface of the platen with epoxy.

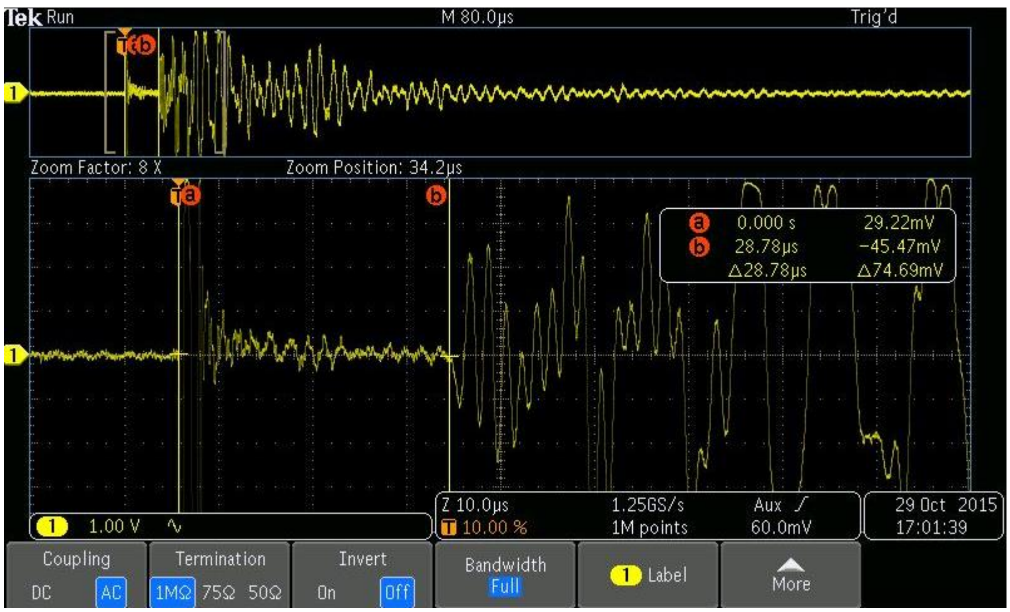

Figure 14: Oscilloscope signal for one of the samples as an example. The time required for wave to travel from one end to the other end of the sample is recorded and together with the length of the sample, the velocity is calculated. A good signal is one where the transition from the initial noise to a high amplitude can be clearly seen without ambiguity (as shown above). Corrections must be applied for the platen material.

The values of dynamic Young's modulus and dynamic Poisson's ratio were calculated using the following standard equations:

$$E = \rho_{bulk} V_p^2 \frac{(1-2\upsilon)(1+\upsilon)}{(1-\upsilon)}$$

$$\upsilon = \frac{V_p^2 - 2V_s^2}{2(V_p^2 - V_s^2)}$$

Where E is the dynamic Young's modulus, υ is the dynamic Poisson's ratio, ρ_{bulk} is the bulk density of the material, Vp and Vs are the compressional and shear velocities respectively. It must be pointed out here that values of dynamic Young's modulus and dynamic Poisson's ratio are usually different from the so called static Young's modulus and static Poisson's ratio which are direct measurements (and not based on an indirect formula like dynamic Young's modulus) of these parameters.

Ultrasonic measurements have obvious advantages over the static measurements in that the tested sample need not be prepared for measurements (or sometimes destroyed) and measurements can be carried out within the field by using available log instruments. However, these measurements are an indirect way of measuring a mechanical parameter on which full confidence can be obtained only by actual compressional or extensional test like UCS or a triaxial test. Therefore, the dynamic moduli can be different from static measurements (Christaras, Auger and Mosse 1994; Ciccoti and Mulargia 2004; Guégen and Palciauskas 1994; Rodríguez Sastre and Calleja 2004; Saenger, Krüger and Shapiro 2006; Song et al. 2004). In almost all studies, dynamic modulus is usually higher. The authors cited above have pointed out that these differences exist due to presence of fractures, planes of weakness, discontinuities etc. Also, how static measurements are carried out (slope up to half of peak strength, linear portion or secant values – all are accepted ISRM guidelines) can have an effect on static values and may therefore offer varying differences between the static and dynamic young's modulus.

As an example, Cicotti and Mulargia (2004) found out differences between the static and dynamic values of 30% although Al-Shayea (2004) found out differences of upto 85%. It is usually seen that when static Young's modulus is higher than 50 GPa, the differences between the two start to reduce (Martinez et al., 2012).

In the case of all the six core samples of 2.5" diameter, no significant differences were observed (< 5%) for the compressional and shear velocities measured at 500 psi and 3500 psi. The detailed data is provided in Appendix one for reference for all the six samples. This shows the well consolidated nature of these rocks. The compressional velocities (at 3500 psi confining pressure) ranged between 4894 m/s to 5457 m/s while the shear velocities range between 2758 m/s to 3286 m/s. Vp/Vs ratios ranged from 1.60-1.89. Based on these velocities, dynamic elastic modulus and dynamic Poisson's ratio have been calculated and are shown in Table 8.

Table 8: Dynamic measurements on the GEO-N2-full core samples group 2 (all values are at 3500 psi confining pressure).

Sample	Density (g/cc)	P-wave velocity (m/s)	S-wave velocity (m/s)	Dynamic Elastic Modulus (GPa)	Dynamic Poisson's ratio	Vp/Vs
GEO-N2-4300-I1	2.71	5309	3086	64.4	0.24	1.72
GEO-N2-4300-I2	2.71	5262	3027	62.2	0.25	1.74
GEO-N2-4300-I3	2.70	5312	2967	60.5	0.27	1.79
GEO-N2-4300-I4	2.69	5226	2758	53.6	0.31	1.89
GEO-N2-4382-I1	2.64	4894	3061	58.2	0.18	1.60
GEO-N2-4243-I1	2.74	5457	3286	71.8	0.22	1.66

For the one inch N2-GEO samples, compressional velocities at 3500 psi confining pressure ranged between 3011 m/s to 5675 m/s while the shear velocities range between 2073 m/s to 3224 m/s. The Vp/Vs ratios range from 1.45-1.79 (average 1.63). Based on these velocities, dynamic elastic modulus and dynamic Poisson's ratio have been calculated and are shown in Table 9. More detailed data showing influence of confining pressure on velocities is shown in the Appendix 1.

Table 9: Dynamic measurements on the GEO-N2 and Oxy 72-03 well core plugs at 3500 psi confining pressure.

Sample	P-wave velocity (m/s)	S-wave velocity (m/s)	Dynamic Elastic Modulus (GPa)	Dynamic Poisson's ratio	Vp/Vs
OXY-72-3-3861.5-V2	5675	3173	70.11	0.27	1.79
GEO-N2-4361-V2	5100	3224	61.49	0.17	1.58
GEO-N2-4361-V3	4787	2788	48.56	0.24	1.72
GEO-N2-4180-H1	3011	2073	19.94	-	1.45

As for the INEL-1 well, samples, compressional velocities at 3500 psi confining pressure ranged between 3872 m/s to 5293 m/s while the shear velocities range between 2516 m/s to 3425 m/s. Vp/Vs ratios range from 1.41-1.55 (average 1.51). Based on these velocities, dynamic elastic modulus and dynamic Poisson’s ratio have been calculated and are shown in Table 10 below.

Table 10: Dynamic measurements on the INEL-1 well core plugs at 3500 psi confining pressure.

Sample	P-wave velocity (m/s)	S-wave velocity (m/s)	Dynamic Elastic Modulus (GPa)	Dynamic Poisson's ratio	Vp/Vs
V1	4089.46	2633.74	36.36	0.15	1.55
V2	3872.02	2516.81	32.64	0.13	1.54
H	5292.86	3425.12	59.40	0.14	1.55
Sample 4 - 10,365 ft	4648.65	3286.62	55.14	-	1.41

As can be seen, both compressional and shear velocities increase with depth. There is significant difference between velocities measured between vertical and horizontal plugs from the 4874 ft depth. This indicates anisotropy between vertical and horizontal properties. As can be seen in the static measurements section later, this translates into a higher strength for the horizontal core plug as compared to a vertical plug as expected.

For the Barnett shale sample, Table 11 provides the values.

Table 11: Dynamic measurements on the Barnett Shale (BS) core plug at 1500 psi confining pressure.

Sample	P-wave velocity (m/s)	S-wave velocity (m/s)	Dynamic Modulus (GPa)	Dynamic Poisson's ratio	Vp/Vs
BS-01-45	4161	2578	41	0.19	1.61

CHAPTER 3. TRIAXIAL COMPRESSION TESTING RESULTS

For the tests described in this chapter, either a standard triaxial or multistage triaxial test as described in chapter 1 on literature survey is conducted or instead a triaxial-injection test is conducted. In a triaxial-injection test or better described as a triaxial test combined with injection (to replicate in-situ stimulation practice), the sample is failed by increasing pore pressure (reducing effective confining pressure) at pre-determined conditions of stress. The test provides useful data for stimulation treatment design. Two variants of this test were performed. In the first case, the sample was stressed axially to a pre-determined level (close to failure based on analysis of reservoir stress data) with a certain confining pressure, then the pore pressure was increased and the sample deformation was observed. If the sample did not fail, a higher pore pressure and/or differential stress was applied to induce failure. In the second case, the sample was loaded until the deflection in the volumetric strain was observed. Then, the pore pressure was increased to bring the sample to failure. In each case, the principal stresses at failure were measured.

For each sample, whichever test was used, has been mentioned explicitly below.

Following measurements were carried out during triaxial testing:

1. Stress measurements were carried out using an internal load cell (range of 1500 kN and 0 to 150^{o}C). These were checked for calibration before testing both using an external device and by using Aluminum as a standard.
2. Strain measurements (axial and radial) were carried out with LVDT’s or strain gauges and sometimes both. In every stress strain plot shown in this report, the

method of strain measurement is mentioned clearly. A comparison between strain measurements using LVDT's (Linear variable differential transducer) and strain gauges is also shown whenever available. In most cases, they were found to agree well with each other.

3. Dynamic velocity measurements (to measure Vp, Vs) -described in chapter two already.
4. Permeability measurements- Described in chapter four (set up, results etc).
5. Acoustic Emissions: Described in chapter five in detail including set up and results.

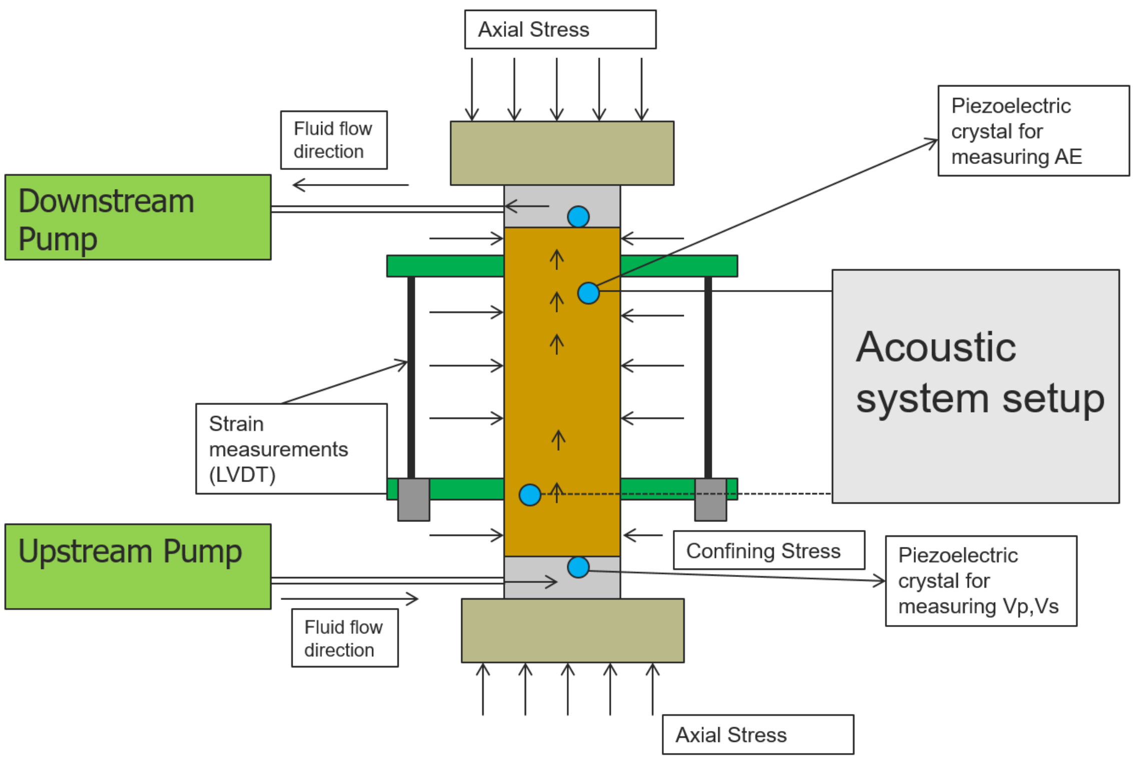

Figure 15: Figure showing a schematic of the sample testing.

A figure showing the schematic of a sample while being tested is shown in Figure 15. An actual picture of sample being tested in provided in Figure 16.

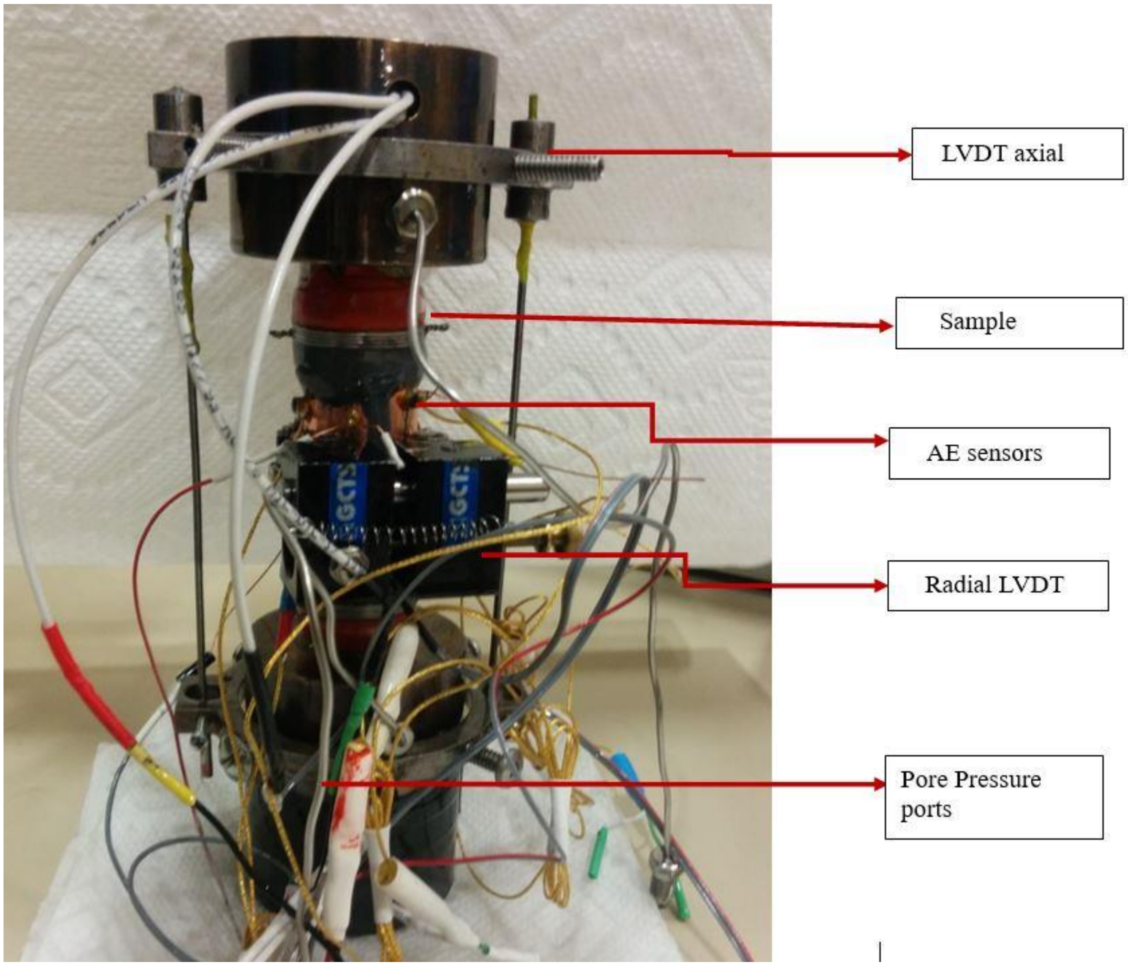

Figure 16: Picture of a sample ready for testing.

BEREA SANDSTONE

Standard triaxial compression tests were performed at four different confining pressures on three different samples labelled as samples A, B, C and D (refer to Appendix 1 for SEM images of Berea sandstone). While samples A, B and C were 1inch in diameter and approximately 2 inch in length, sample D was 2.5 inch in diameter and 4 inch in length. A strain loading rate of $5x10^{-5}$ was used for all samples. Figure 17 shows the differential pressure versus strain curves (axial, radial, and volumetric). All three samples failed in brittle failure mode with a large drop in load bearing capacity at the time of failure and relatively low total strain.

Figure 18 shows a picture of the rock specimens after the test.

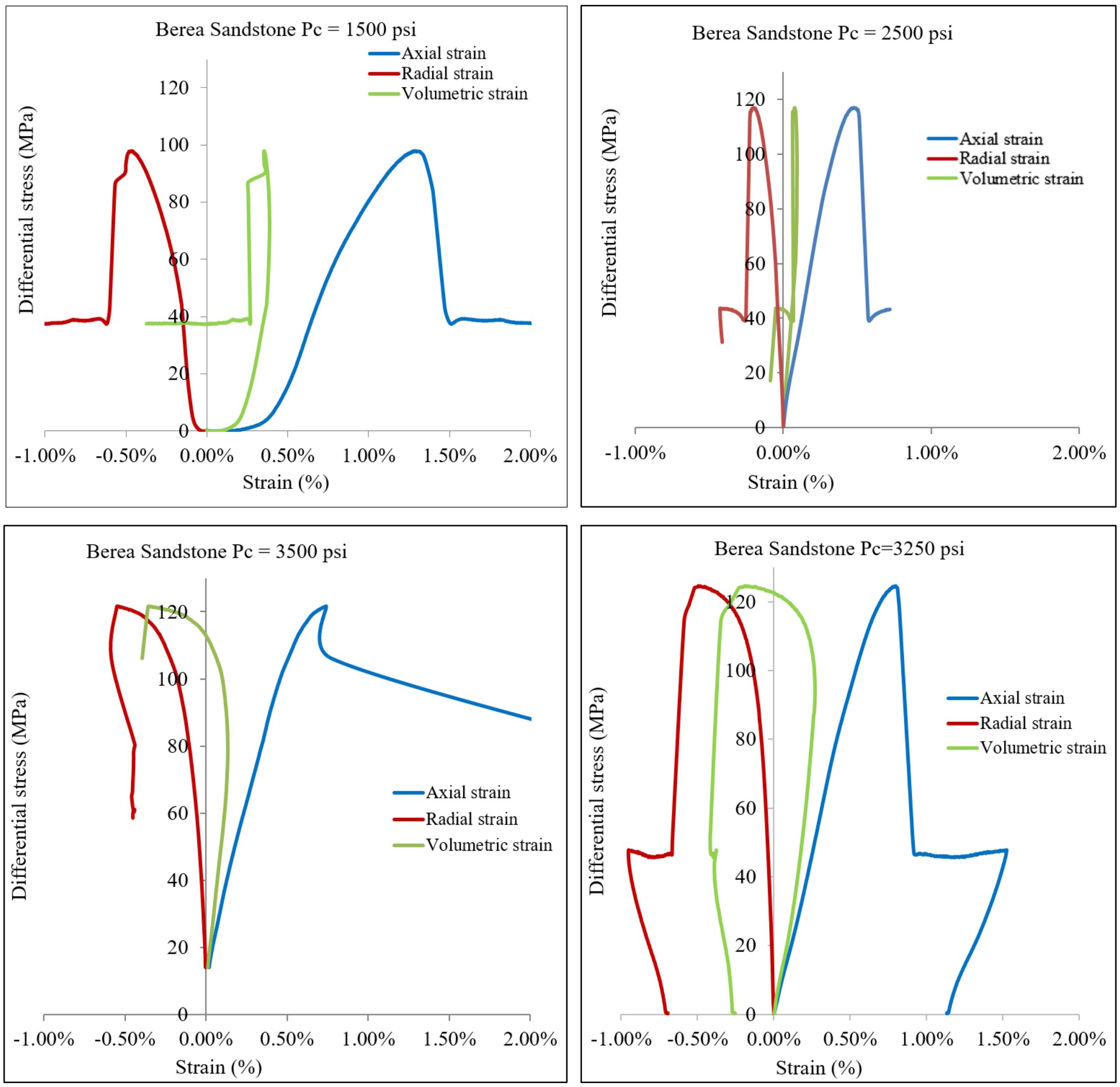

Figure 17: Stress strain plots for Berea Sandstone.

Figure 18: Plugs of Berea sandstone after triaxial compression testing - confining pressure increases from right to left (top). As can be seen, for the lowest confining pressure, axial fractures are created. As confining pressure increases, the sample fails with just one inclined fracture.

SIERRA WHITE GRANITE

A single 2-inch diameter Sierra white granite sample was tested at an effective confining pressure of 1000 psi with AE measurements (see Chapter 5 for details). Sample failed with two fractures initiated from one end of the sample but not extending till the other end (Figure 20).

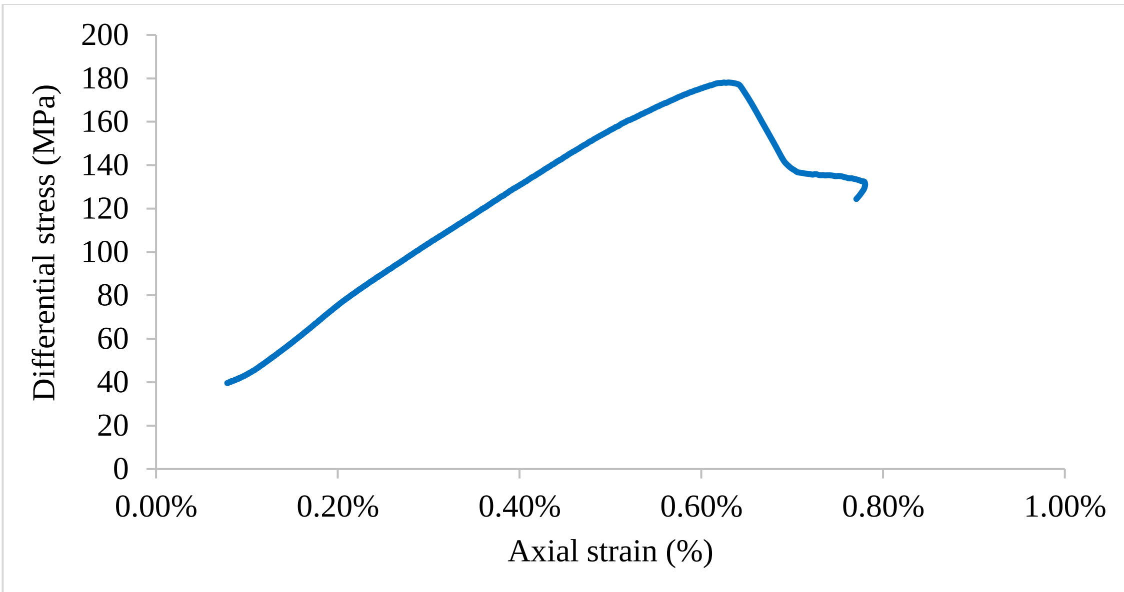

Figure 19: Stress strain plot for the 2-inch diameter Sierra white granite. Only axial strain measurements were available.

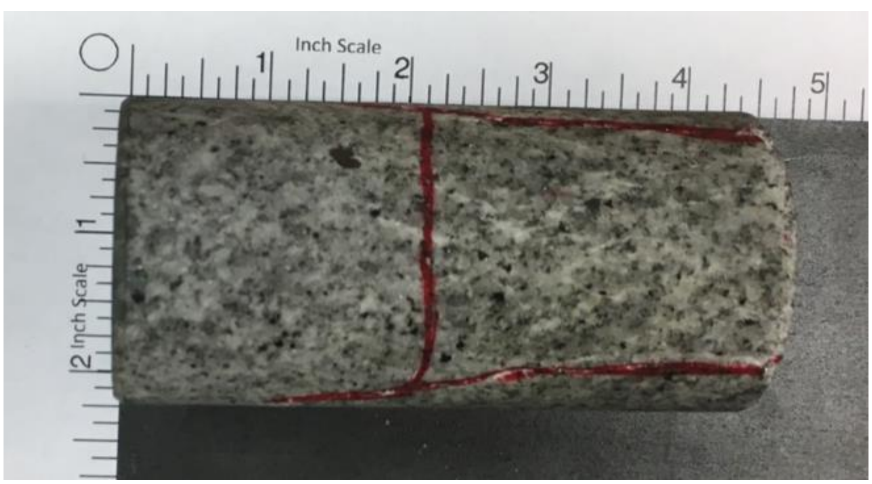

Figure 20: After triaxial test picture of the Sierra white granite showing fracture locations (marked in red). The fractures do not extend to the other end. Since

effective confining pressure was low, fractures can be seen to be semi-vertical and not highly inclined

RHYOLITIC TUFF AND RHYODACITES FROM THE INEL-1 WELL

As discussed in Chapter 1, four samples from the INEL-1 well were tested. Three of them (V1, V2 and H-all rhyolitic tuff) were from a depth of 4874 ft. while one plug (INEL-sample 4-rhyodacite) was from a depth of 10365 ft. For two samples, V2 and H, triaxial-injection method was used. For the other two, (sample V1 and INEL-sample 4), multistage triaxial tests were conducted; four to five different confining pressure stages were used for these tests. In the multistage triaxial experiments, the volumetric strain deflection in conjunction with AE information has been used to define the stopping point of loading (Tran et al (2010), Kovari and Tisa (1975), Kovari et al. (1983), Kim and Ko (1979), Crawford and Wylie (1987)). This test has been successfully applied to similar rock type by Wang et al., 2016.

The following procedure was followed:

1. Sample is jacketed using thin copper of 0.003" thickness and 8-12 acoustic crystals are added on the jacket at fixed locations.

2. Sample is then hydrostatically loaded to the required confining pressure slowly while monitoring strain.

3. The axially load is then increased until volumetric strain deflection is observed, at this point sample is unloaded. Confining pressure is changed for the next stage. This is repeated until the last stage.

4. In the last stage, failure is initiated using injection (unless otherwise stated) while the sample is under a confining pressure of 3500 psi and an axial load which causes a negative change in volumetric strain. This has been described earlier.

Figure 16 shows an actual sample for testing along with all measurement instruments added, ready for testing.

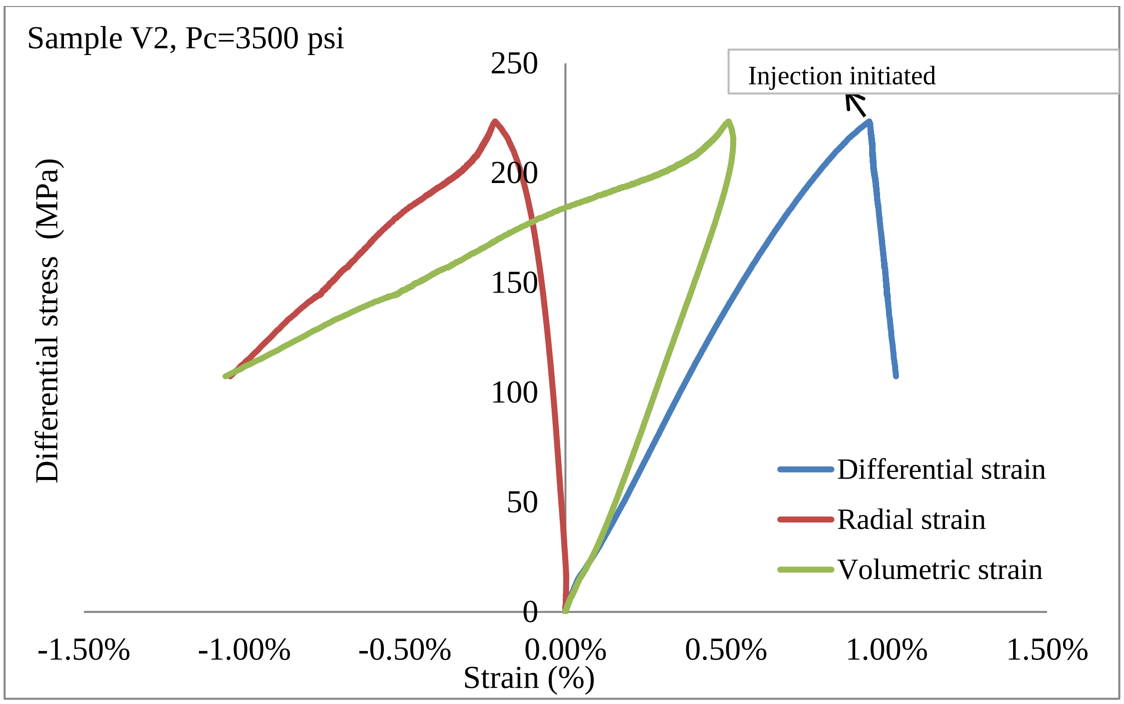

Figure 21: Stress strain plot for Sample INEL-V2. The point at which injection was initiated is shown as well. Also, refer Figure 17.

As can be seen from Figure 22, sample INEL-V2 was failed using triaxial injection. After reaching a certain displacement, the actuator was held constant for making stress constant. An assumption here is that holding displacement constant would also keep stress constant until pore pressure is introduced into the sample. The risk here is that if deviatoric stress doesn't remain constant due to actuator displacement being constant before pore pressure is introduced, then sample may not fail even with the reduced effective confining pressure as deviatoric stress would have fallen. In actual practice, it was observed that stress remained constant at least to +/-1 MPa for the period that stable returns were observed (indicative – see Figure 60 for example where displacement was held constant and stress can be seen to be constant with variations of less than 0.5 MPa over 15 minutes). After holding displacement constant, gas was passed through sample to increase pore pressure. The onset of failure does have a time component- as gas passes through the sample, it creates a higher pore pressure than what was initially. This however takes some time depending upon sample permeability leading progressively to failure. The rate of load handling capacity decreases slowly initially but accelerates later as the pore pressure become uniformly higher, reducing effective confining pressure pushing the Mohr circle to the left. Sample ultimately fails after some time.

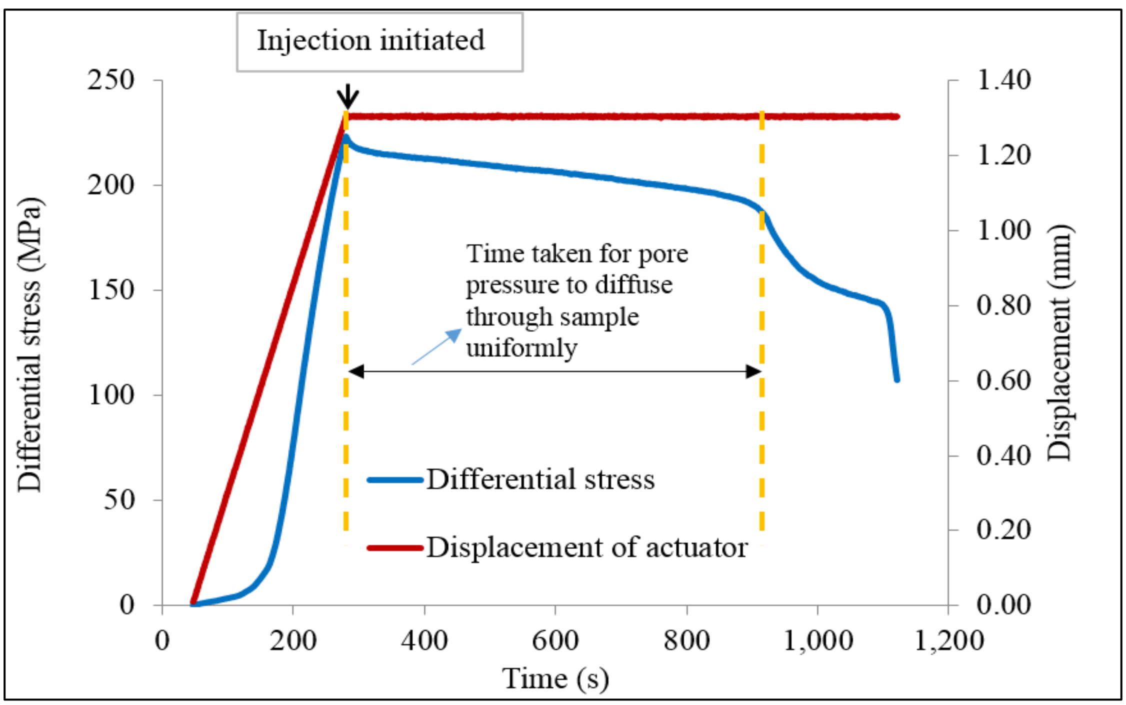

Figure 22: Triaxial injection plot for sample INEL-V2. As can be seen displacement of actuator was held constant at one point and after that injection was initiated which led to sample failure.

Figure 23 below shows the multistage testing results for sample V1. Four different confining pressures have been used. The corresponding Mohr circle is shown below in Figure 24. The final failure equation is:

$$\tau = 0.9261\sigma + 29.5$$

Where τ is shear stress (MPa) and σ is normal stress (MPa).

Figure 25 below shows the stress-strain plot for sample H. This sample was also tested at a confining pressure of 3500 psi and failed by injection when the volumetric strain showed a deflection. Figure 26 shows this more clearly- as injection was initiated, displacement of actuator was stopped to hold stress constant. After some time, sample failed.

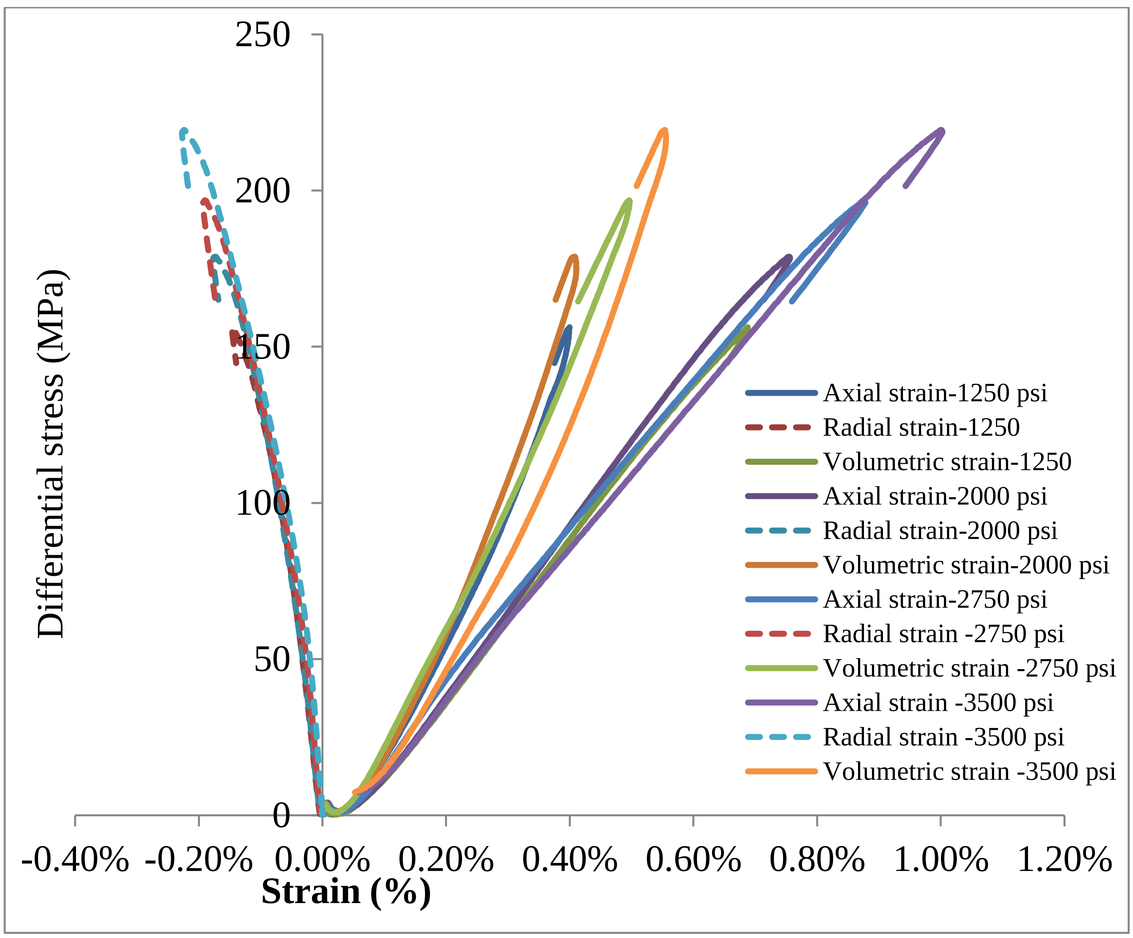

Figure 23: Multistage stress strain plot for Sample INEL-V1.

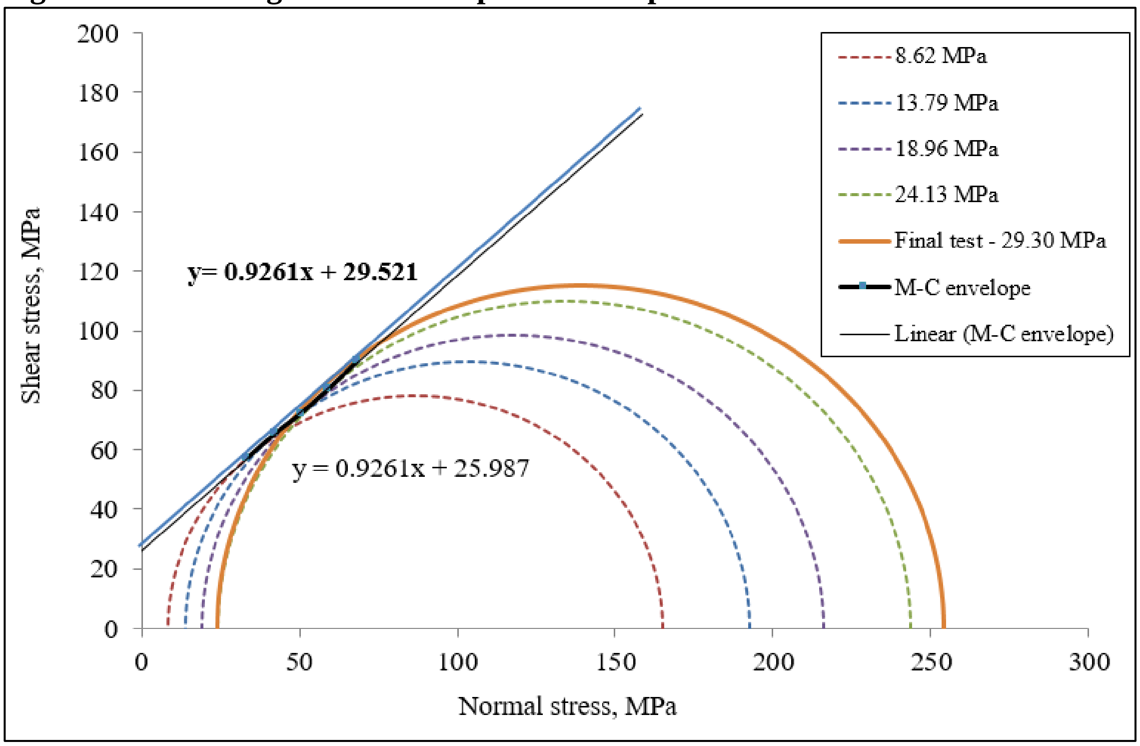

Figure 24: Mohr-Coloumb plot for Sample INEL-V1.

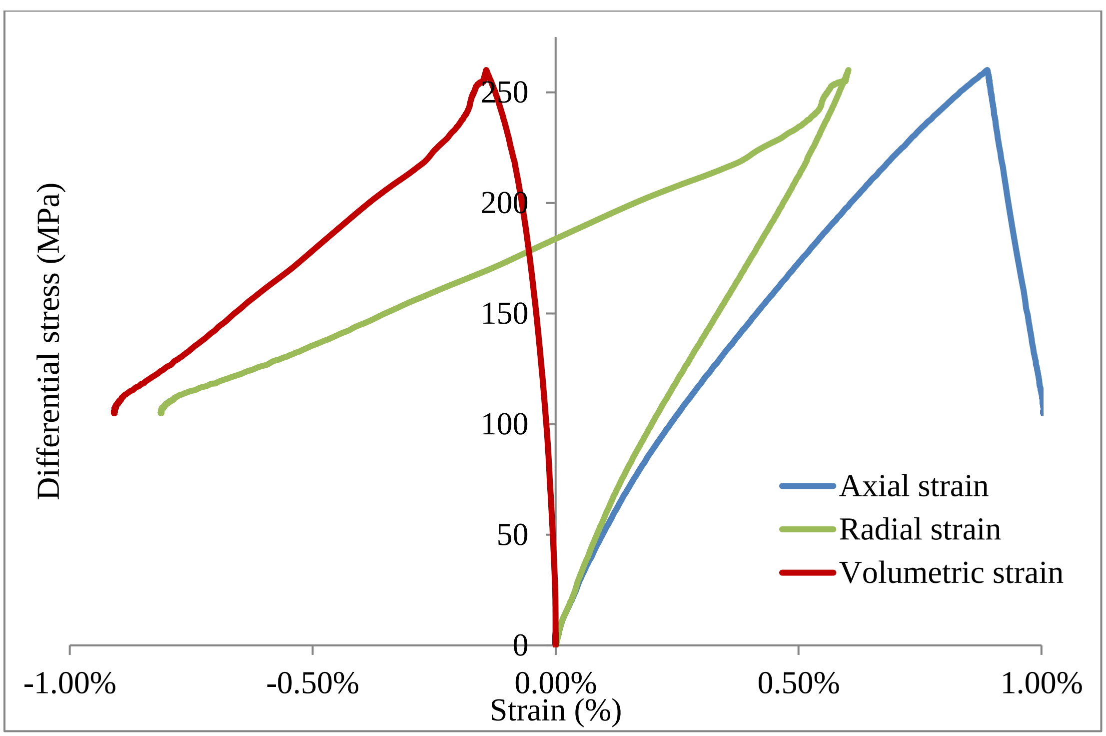

Figure 25: Stress strain plot for sample INEL-H.

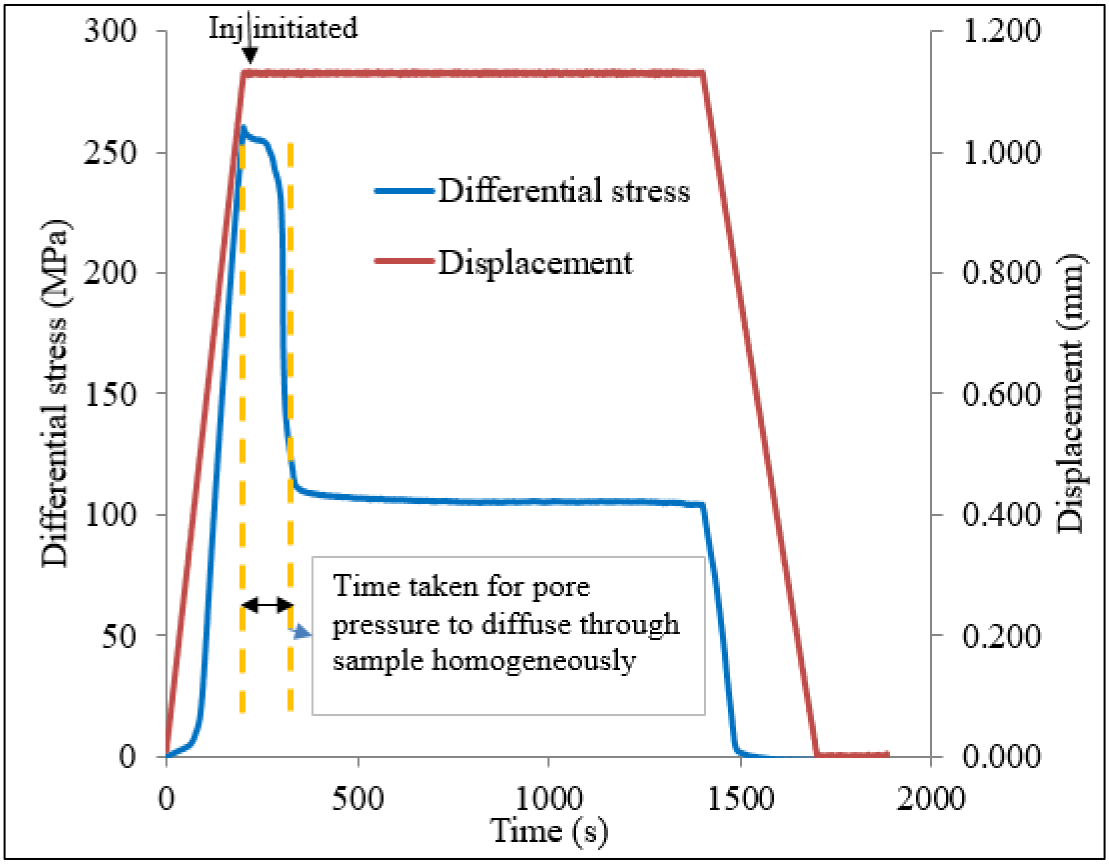

Figure 26: Triaxial injection plot for sample INEL-H. As can be seen displacement of actuator was held constant at one point and after that injection was initiated which led to sample failure.

Figure 27 and Figure 28 show the multistage triaxial test plots and the Mohr-Coulomb plot for sample number 4.

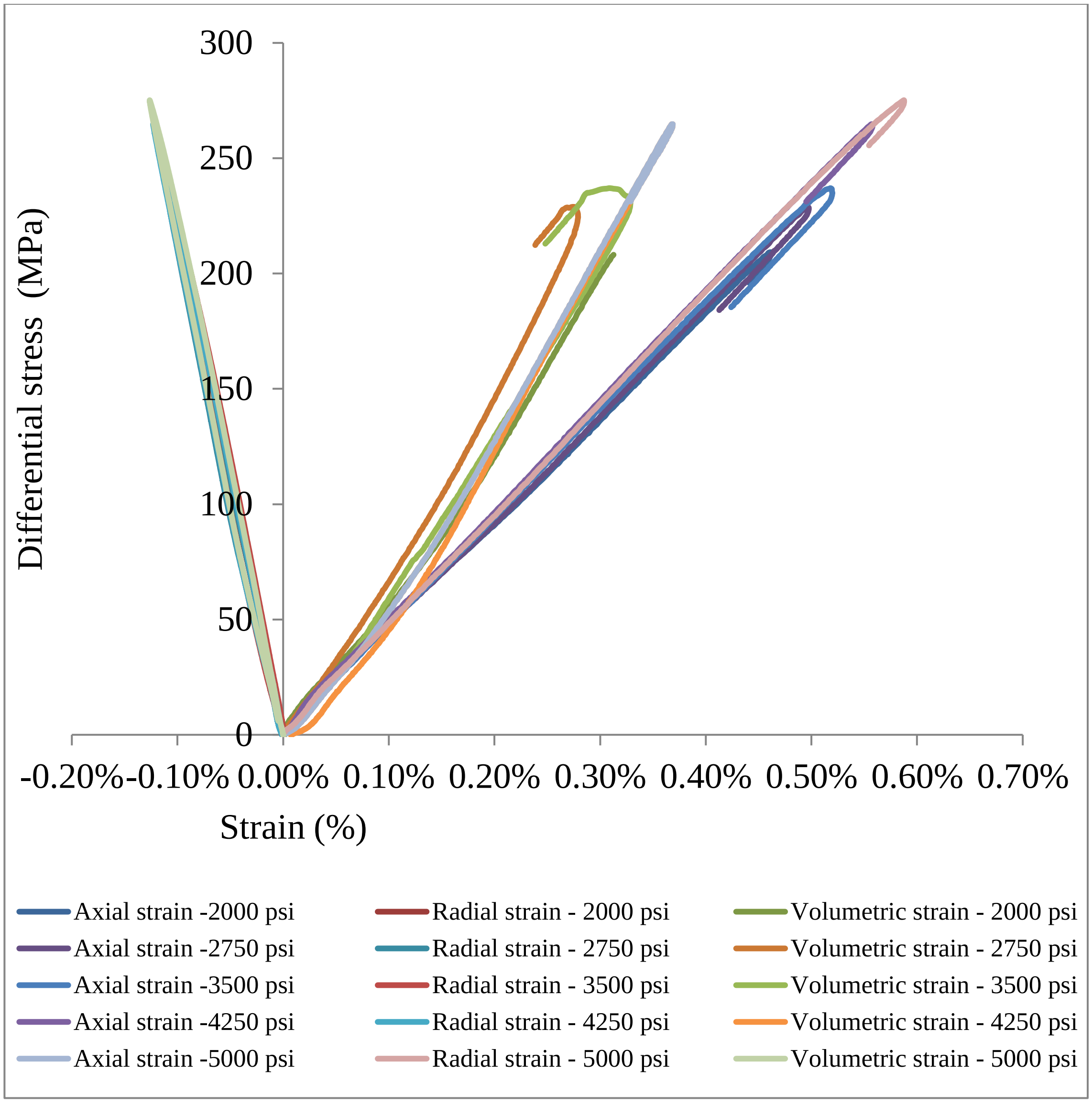

Figure 27: Multistage triaxial test results for INEL -sample 4.

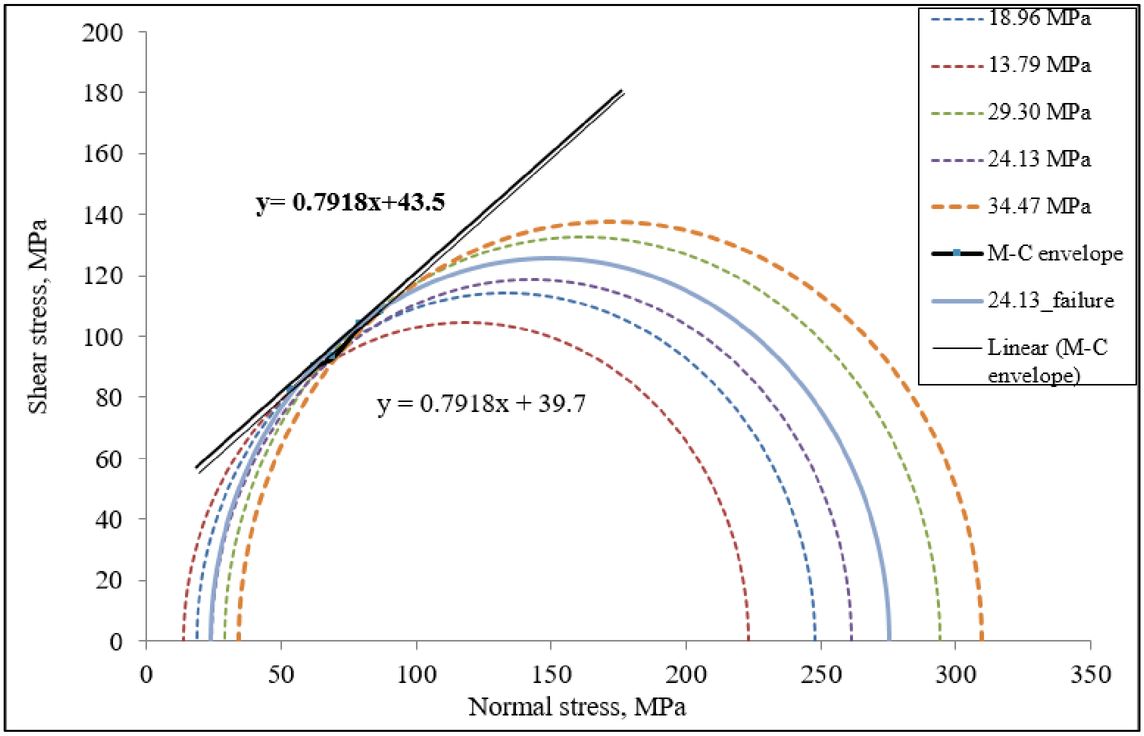

Figure 28: Mohr-Coloumb plot for INEL-Sample 4 from the INEL-1 Well.

Figure 29: Pictures of samples after testing; copper jacket hasn't been removed to prevent sample disintegration. Red lines show clear fractures seen on surface. Location of these fractures in 3-D space within the sample has been studied in chapter five using acoustic emissions.

Table 12 shows a summary of the results for the INEL-1 well samples.

Table 12: Summary of triaxial testing results for the INEL-1 well samples.

	Sample			
	V1, 4874ft	V2, 4874ft	H, 4874ft	Sample-4, 10365ft
Static Young's modulus (GPa)**	27.5	27.0	34.8	46.8
Static Poisson's Ratio**	0.17	0.15	0.16	0.16
Unconfined Compressive Strength (MPa)*	132.2	-	-	179.2
Cohesion (MPa)*	29.5	-	-	43.5
Friction angle*	42.8^{o}	-	-	38.2^{o}
Peak strength (MPa)**	229.8	223.5	260.1	251.4
Dynamic Young's modulus	36.4	32.6	59.4	55.1
Dynamic Poisson ratio	0.15	0.13	0.14	-

*-Values calculated using Mohr-Coloumb envelope
** - Values at 3500 psi confining pressure

Following inferences can be made from the above measurements on the INEL-1 well samples:

1. There is some anisotropy between horizontal and vertical plugs from the 4874ft core. Horizontal plug shows higher strength and higher young's modulus in both static and dynamic measurements.

2. Dynamic and static Poisson's ratios are almost same (within 10%). However static and dynamic young's moduli are different (14-41% difference, average 25%) but show similar trend in all four plugs with higher values in dynamic

measurements. The theory of why differences exist between the two have already been discussed in detail in section on Dynamic velocity measurements (Chapter 2).

3. Deeper core samples are stronger than the shallower core and have higher elastic modulus. This correlates very well with their porosities (lower porosity in deeper core) and velocities (higher velocity in deeper core).

4. Young's modulus increases very slightly as confining pressures are increased in the multistage triaxial tests– this indicates that these rocks are well compacted already.

GEO-N2 Core Samples

These samples have been described earlier in detail in Chapter two. The primary objective was to conduct a Triaxial-Injection test by injection of fluid into the sample at pre-determined conditions of pressure (differential and confining) and also collect all possible geomechanical parameters for the sample. For the injection tests, fluid must be injected until stable returns are observed at the downstream end of the sample to ensure pore pressure was uniform. If sample failure doesn't occur, increase differential stress to the point of volumetric strain transitioning from contraction to dilatancy and then induce sample failure by injection of pore fluid (to reduce effective confining pressure). Also, determine the deformation properties and the strength envelope whenever possible, analyze AE and permeability variations.

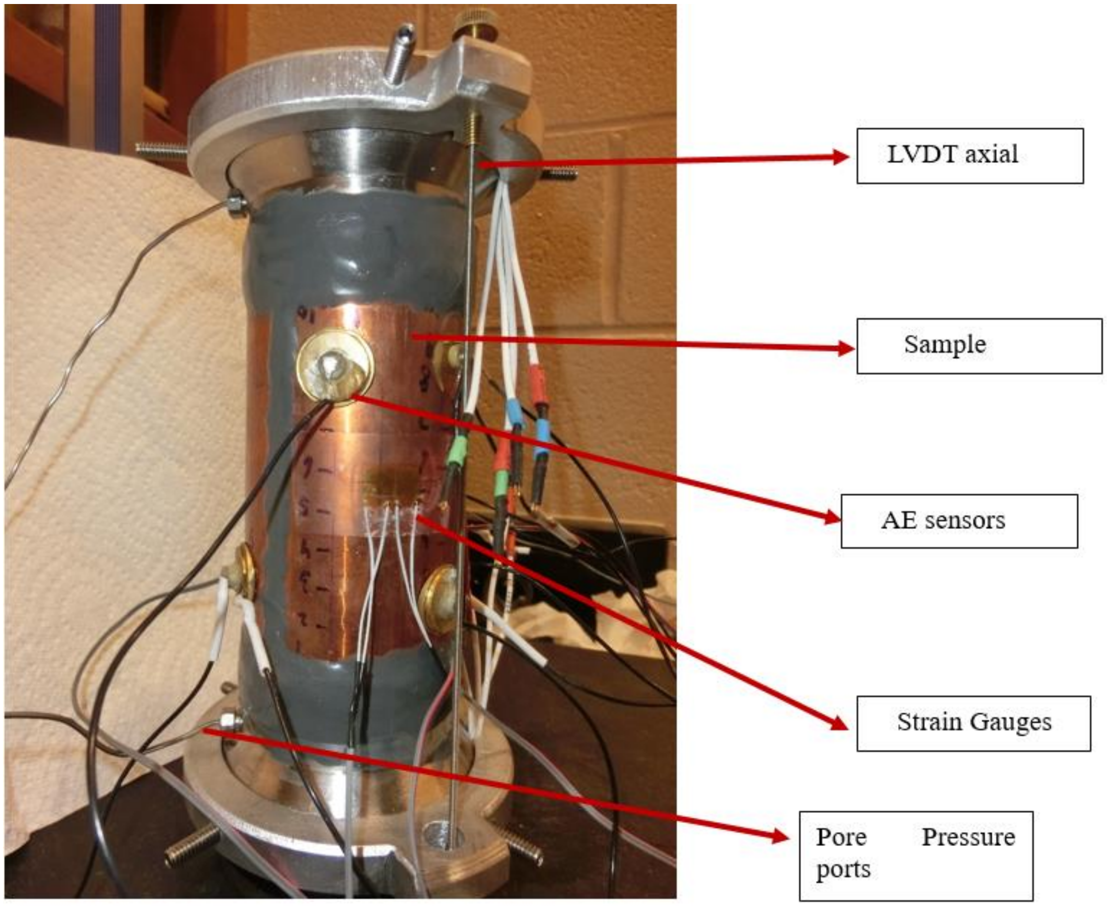

Figure 30: Figure showing GEO-N2-4300-I1 instrumented and ready for testing. The copper jacketing and epoxy protection can be seen clearly.

To meet these objectives, multistage triaxial tests, conventional triaxial or triaxial-injection tests have been used. A total of six triaxial-injection tests - one for each core sample were carried out.

A schematic of the test set for all the samples is shown in Figure 30 and Figure 31. The latter shows an actual set up of the sample inside the MTS 315 frame.

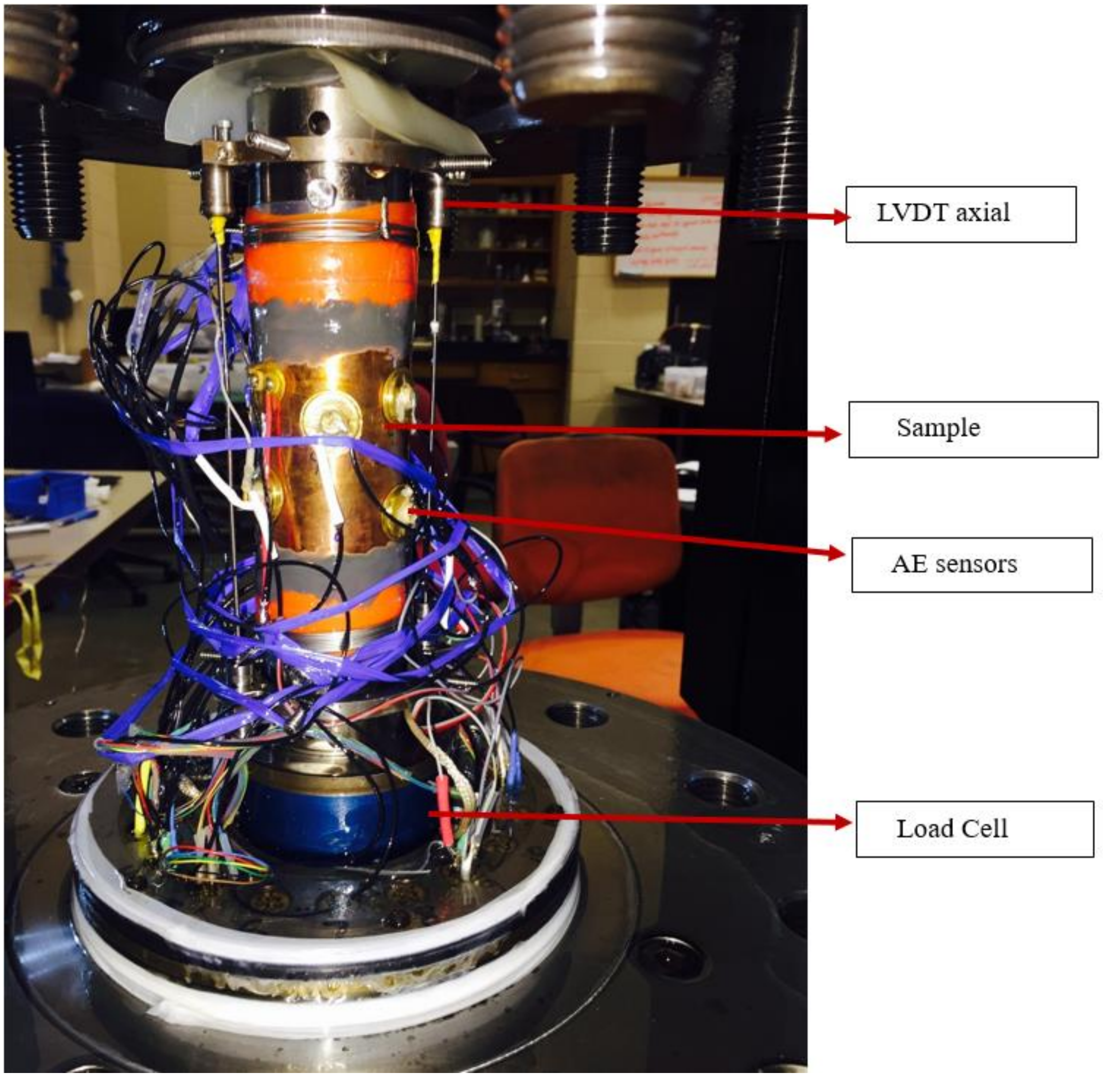

Figure 31: Figure showing a picture of sample inside the 315-frame ready for testing.

Sample GEO-N2-4300-I1

Picture of GEO-N2-4300-I1 and its textural, mineralogical description has already been provided in previous chapter. Some more such information is provided in appendix one. For GEO-N2-4300-I1, following steps explain sequentially the triaxial-injection testing carried out:

1. The sample was placed within the MTS 315 frame with the LVDT, strain gauge, Vp, Vs, Pore pressure and acoustic emissions (AE) connections set up. Confining pressure was applied slowly reaching a final value of 5500 psi. Vp, Vs measurements were carried out at 500 psi, 3500 psi and 5500 psi.
2. Pore pressure was applied via the two syringe pumps with the upstream pump at 2000 psi and downstream pump at 1800 psi. Flow was measured and sample was left undisturbed till steady state was achieved. Effective confining pressure was thus at 3500 psi.
3. The sample was then loaded using a strain loading rate of $1x10^{-5}$ strains/sec while recording the stress, strain (radial and axial), permeability, velocity (Vp and Vs) and acoustics related information. Once a differential stress of 11000 psi was reached, pore pressure was increased by injection of gas creating a net differential confining pressure of 1000 psi (from the initial 3500 psi). Injection was maintained till uniform flow on both ends was observed. However, the sample didn't show failure. This completed the first part of the experiment as per the mentioned objectives.
4. In the second phase, the effective confining pressure was once again increased to 3500 psi (by lowering pore pressure back to 2000 psi) and sample loaded again till the volumetric strain showed dilatancy and then sample's effective confining pressure was then reduced again to 1000 psi by increasing pore pressure to mimic a stimulation treatment. Sample failed with a peak load of 96 MPa dropping to 78 MPa. At this point differential stress was maintained constant by holding displacement constant and then permeability was measured. The permeability showed an increase to 170.1 nD from the initial 26.7 nD. It should be noted that triaxial loading causes a

decrease in permeability before onset of dilatancy when the volumetric strain is positive; however, this sample had a net positive volumetric strain yet showed a large increase. This behavior can only be attributed to either creation of new fracture(s) within the sample or deformation sliding of pre-existing cracks (sample compression closes existing pores reducing permeability while fracture formation increases it – the two processes compete as the sample keeps getting loaded). This was confirmed on actual observation of the sample – the existing axial fracture *'grew'* to intersect both the ends of the sample (it initially was intersecting just one end -see Figure 33.

5. It is important to also point out here that upon actual observation of the sample (Figure 33 and Figure 34) after the test, the sample was still intact albeit with the fracture growth as described above. It is estimated that a complete failure of the sample would have *generated* a higher permeability increase (complete failure being defined here as sample's load bearing capacity reducing by more than 50% as compared with the current 20%).

Permeability changes for this sample has been described in chapter 3 in more detail.

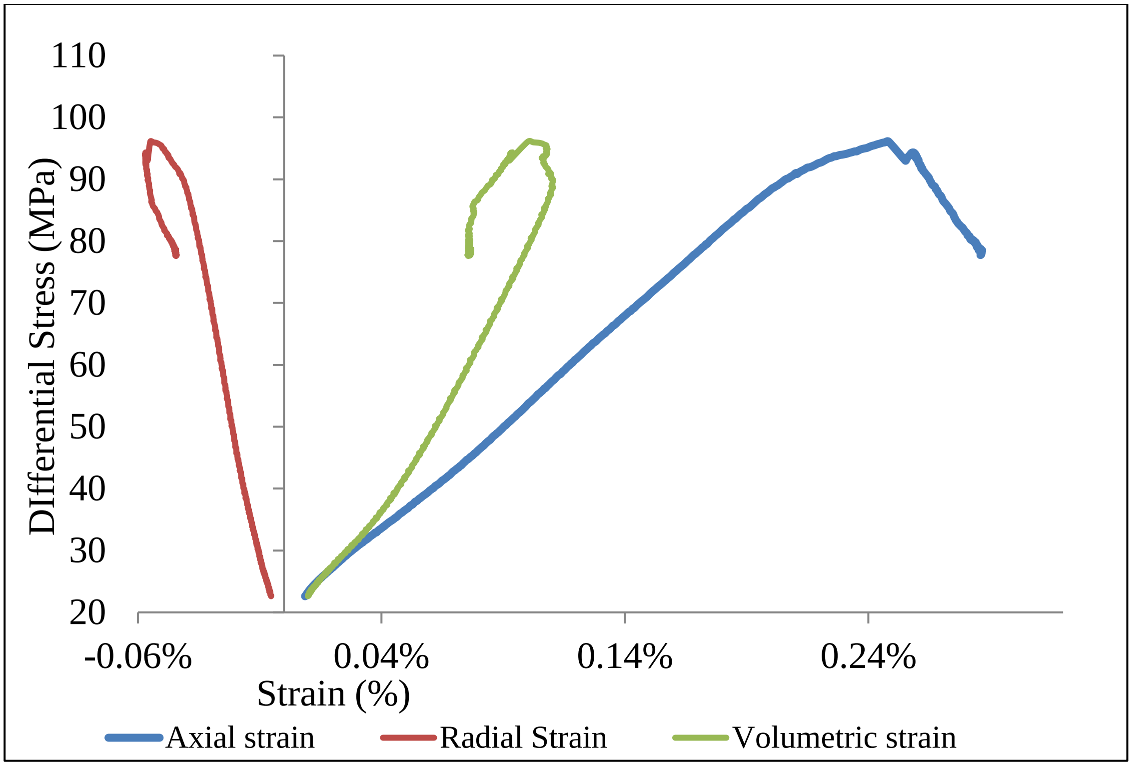

Figure 32: Plot showing stress strain plot for GEO-N2-4300-I1. Axial strain was measured using LVDT while radial strain was measured using strain gauges.

All the calculated parameters-Young's modulus, Poisson's ratio, peak strength etc have been summarized in a single table for all the six samples in Table 13.

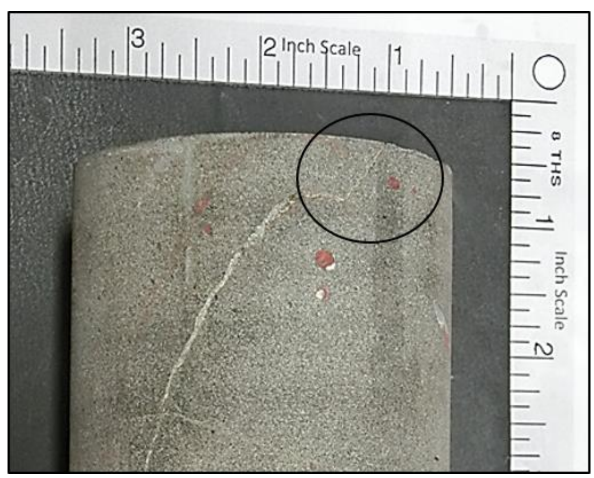

(Before failure)

After failure

Figure 33: After failure picture for sample number 1 (right) as compared to pre-failure picture (left). As compared to initial sample picture (left), we can see that the fracture has grown towards the end (encircled) and also appears more prominent after failure.

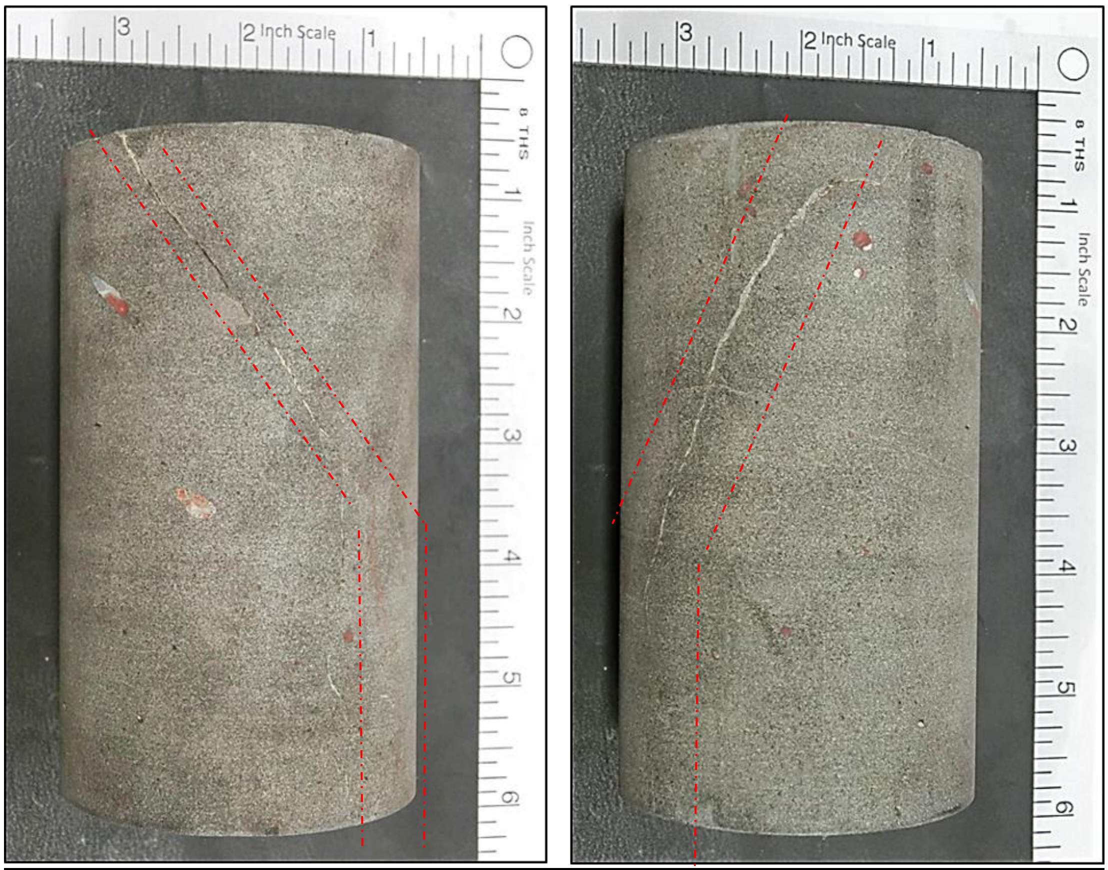

Figure 34: After failure picture for GEO-N2-4300-I1 showing fractures (within red dotted lines). Most of the existing healed fractures became more prominent after failure although sample didn't disintegrate after failure.

Sample GEO-N2-4300-I2

Preliminary information about sample two has also been provided in chapter two. An important point to note was that this sample had no healed fractures unlike all other five samples.

For GEO-N2-4300-I2, following steps explain sequentially the triaxial-injection testing carried out:

1. The sample was placed within the MTS 315 frame with the LVDT, strain gauge, Vp,Vs, Pore pressure and acoustic emissions (AE) connections set up. Confining pressure was applied slowly reaching a final value of 5500 psi. Vp, Vs measurements were carried out at 500 psi 3500 psi and 5500 psi.
2. Pore pressure was applied via the two syringe pumps with the upstream pump at 2000 psi and downstream pump at 1800 psi. Flow was measured and sample was left undisturbed till steady state was achieved. Effective confining pressure was thus at 3500 psi.
3. The sample was then loaded using a strain loading rate of $1x10^{-5}$ strains/sec while recording the stress, strain (radial and axial), permeability, velocity (Vp and Vs) and acoustics related information. Once a differential stress of 11000 psi was reached, pore pressure was increased by injection of gas creating a net differential confining pressure of 1000 psi (from the initial 3500 psi). Injection was maintained for 30 mins. However, the sample didn't show failure. This completed the first part of the experiment as per the mentioned objectives.
4. In the second stage, the effective confining pressure was again brought back to 3500 psi, and then the sample was loaded again till the differential stress was 160 MPa.

Gas was re-injected creating an effective confining pressure of 550 psi, however sample still didn't show any failure. This stage was added to evaluate if a higher deviatoric stress would cause failure.

5. In the third stage of loading, sample differential stress was increased till the volumetric strain showed a change in slope indicating that it was approaching inelastic failure region. Then, gas was again injected in to the sample creating an effective confining pressure of 550 psi. Failure was observed – sample load bearing capacity reduced to 197 MPa from 271 MPa as gas was injected and held constant there even with gas injection maintained for several minutes. Permeability was calculated at this stage after restoring the confining pressure of 3500 psi. It was observed to be higher by about seven times. This can happen only if there is fracture formation in the sample. The observed peak load was 271.6 MPa.
6. In the fourth and final stage of loading shown in Figure 37, the confining pressure was raised again to 3500 psi and sample was differentially loaded. It was observed that sample could be loaded to a higher load and it failed exactly at the same stress of 271 MPa. This was done at a confining pressure of 3500 psi. This seems to indicate that the fracture got closed as soon as the effective confining pressure reached 3500 psi.
7. It should be noted that the stress strain plots in Figure 36 show small 'kinks' at 75 MPa and 160 MPa, these have no physical significance – the sample loading was merely paused for some time for acoustic and permeability measurements and hence the strain shows some 'creeping' behavior at those points.

Observations: As compared to GEO-N2-4300-I1, this sample had much higher strength (three times). This sample had a low L/D ratio of 1.48 (which typically results in an increase in observed strength versus a higher L/D ratio). However, it is proposed that the principal factor that causes the large increase in strength of this sample is the fact that it had no observable fractures before testing. This is in contrast to the other samples tested which showed large clearly observable fractures running across the length of the respective samples.

8. The sample upon observation showed a large fracture across the length of the sample intersecting its ends and at an angle of 40^{o} from the vertical axis.

Figure 35: Picture of GEO-N2-4300-I2 picture after failure. The induced fracture had an angle of 40^{o} with the axis.

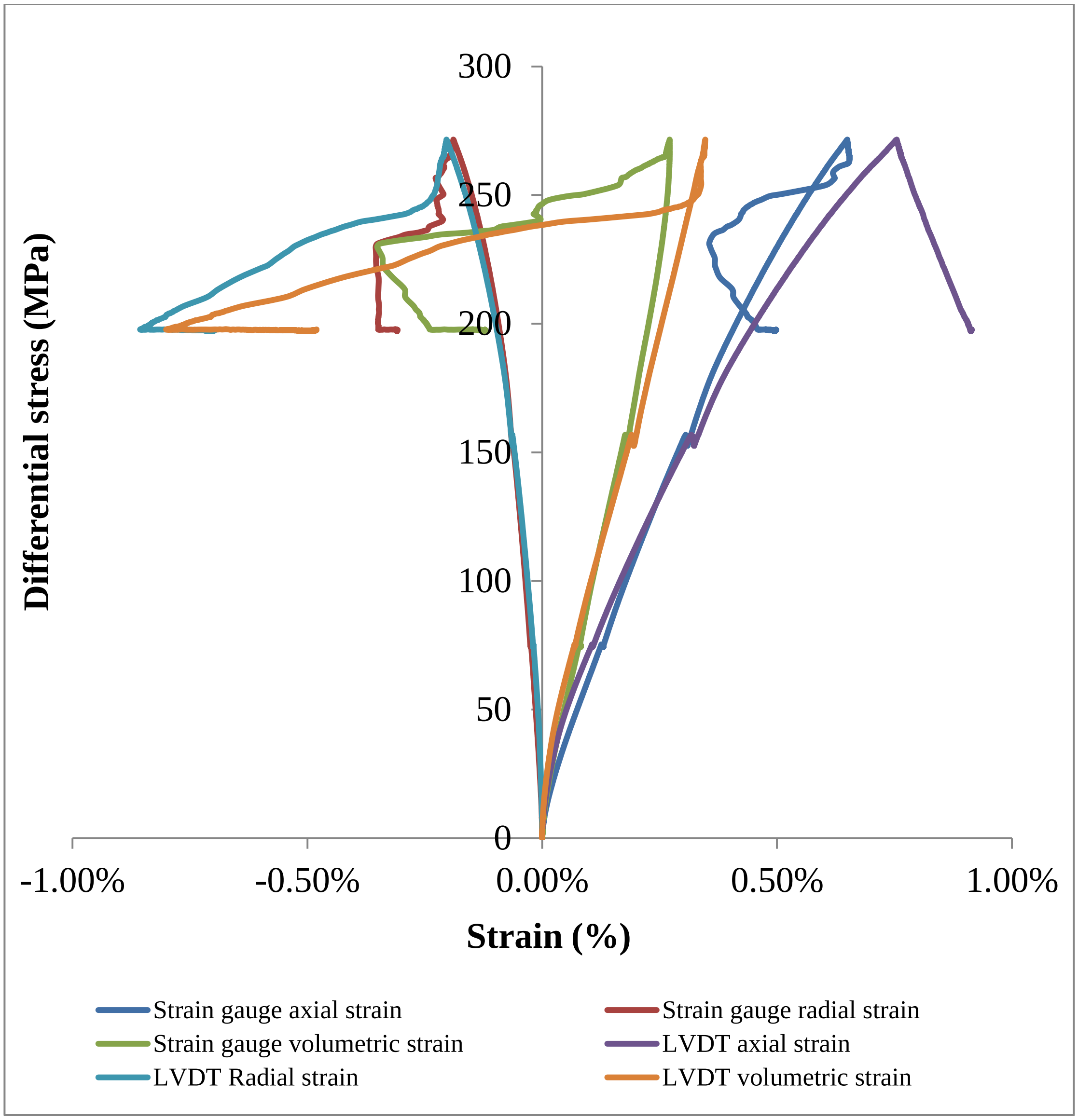

Figure 36: Stress strain plot for GEO-N2-4300-I2, both LVDT and strain gauge based measurements are shown here, note that strain up to stage three (injection stage) is only shown. For strain up to stage four, see Figure 37 below.

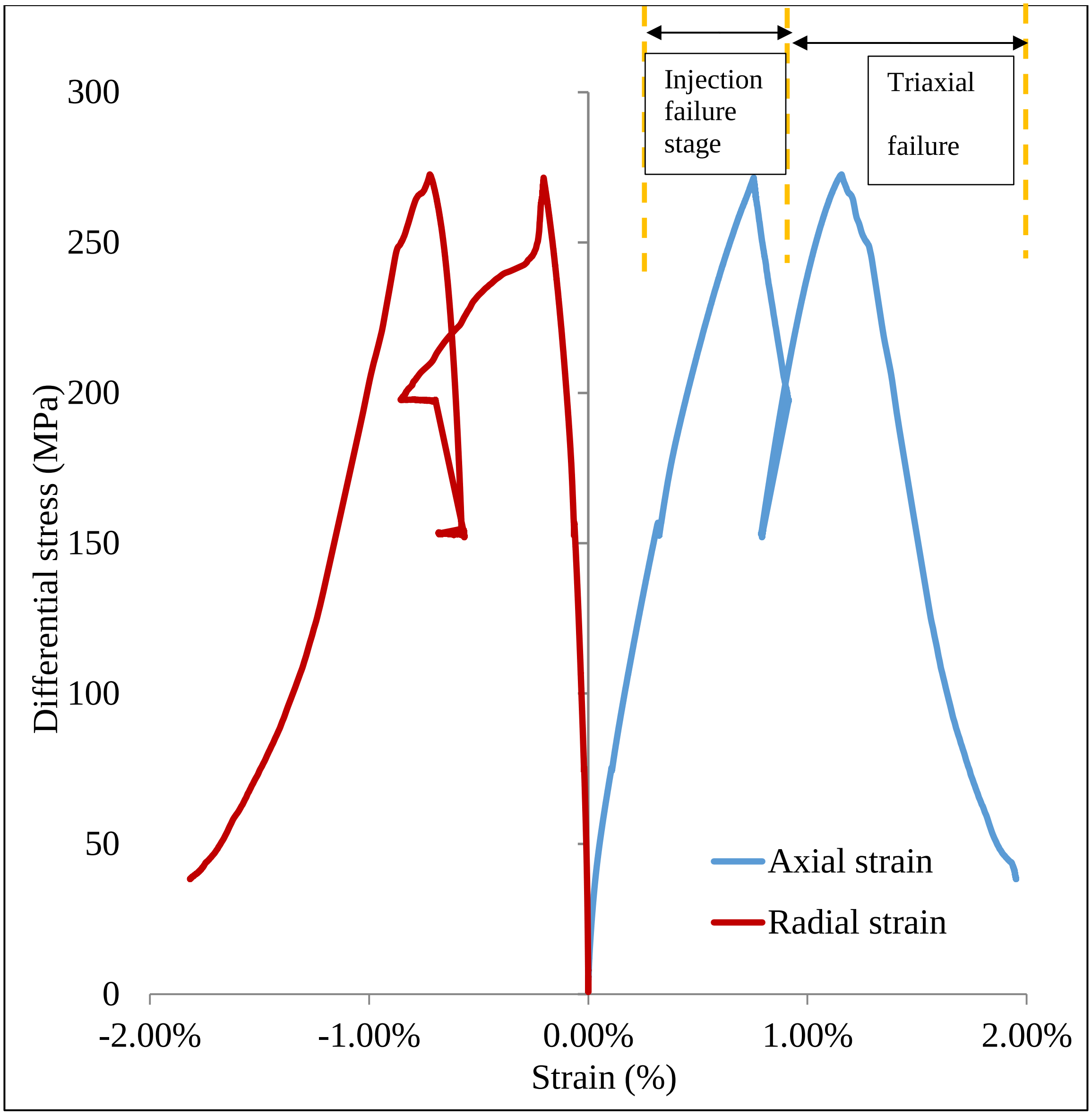

Figure 37: Stress strain plot for sample no 2, showing both the injection stage and triaxial stage. In the first stage, sample failed by injection when effective confining pressure was reduced to 1000 psi. However, once the confining pressure was restored back to 3500 psi, sample behaved like an intact rock allowing loading up to the same level as earlier (when it failed by injection). This seems to indicate that fracture closure happened once the confining pressure was restored back to 3500 psi.

Sample GEO-N2-4300-I3

For GEO-N2-4300-I3, following steps explain sequentially the triaxial-injection testing carried out:

1. Sample was placed within the MTS 315 frame with the LVDT, strain gauge, Vp,Vs, Pore pressure and acoustic emissions (AE) connections set up. Confining pressure was applied slowly reaching a final value of 5500 psi. Vp, Vs measurements were carried out at 500 psi 3500 psi and 5500 psi.

2. Pore pressure was applied via the two syringe pumps with the upstream pump at 2000 psi and downstream pump at 1800 psi. Flow was measured and sample was left undisturbed till steady state was achieved. Effective confining pressure was thus at 3500 psi.

3. The sample was then loaded using a strain loading rate of $1x10^{-5}$ strains/sec while recording the stress, strain (radial and axial), permeability, velocity (Vp and Vs) and acoustics related information. Once a differential stress of 11000 psi was reached, pore pressure was increased by injection of gas creating a net differential confining pressure of 500 psi (from the initial 3500 psi). Injection was maintained for 30 mins. However, the sample didn't show failure. This completed the first part of the experiment as per the mentioned objectives.

4. In the second phase, the effective confining pressure was once again increased to 3500 psi and sample loaded again till the volumetric strain showed dilatancy and then sample's effective confining pressure was reduced to 1000 psi by increasing pore

pressure to mimic a stimulation treatment. Sample failed with a peak load of 90.63 MPa. At this point differential stress was removed and permeability measured. The permeability showed an increase to 228.3 µD from the initial 0.098 µD. The sample failed exactly along the existing fractures (Figure 40).

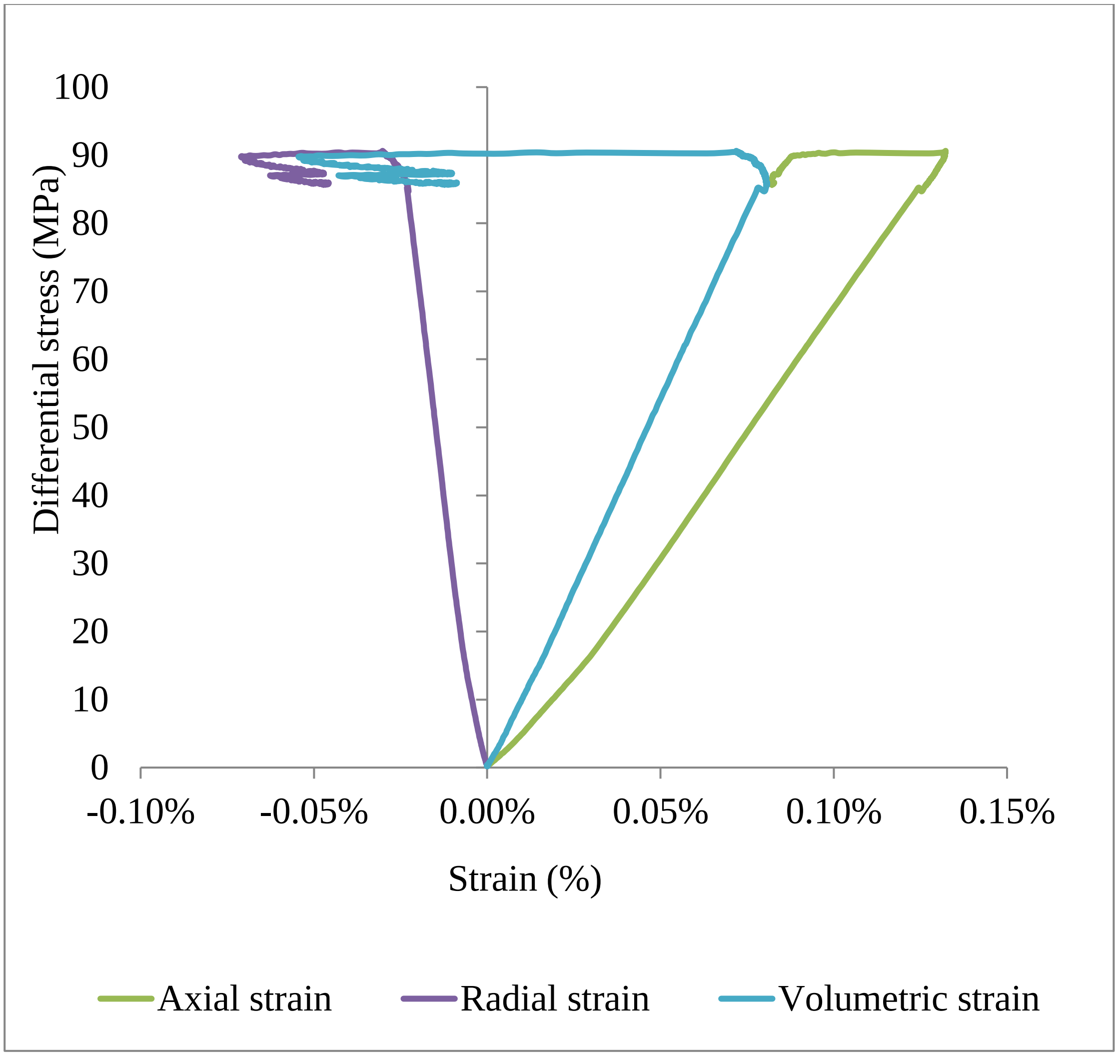

Figure 38: Plot showing stress strain plot for GEO-N2-4300-I3 (All strains shown here have been calculated using strain gauges, for a combined LVDT -strain gauge plot see figure 34 below)

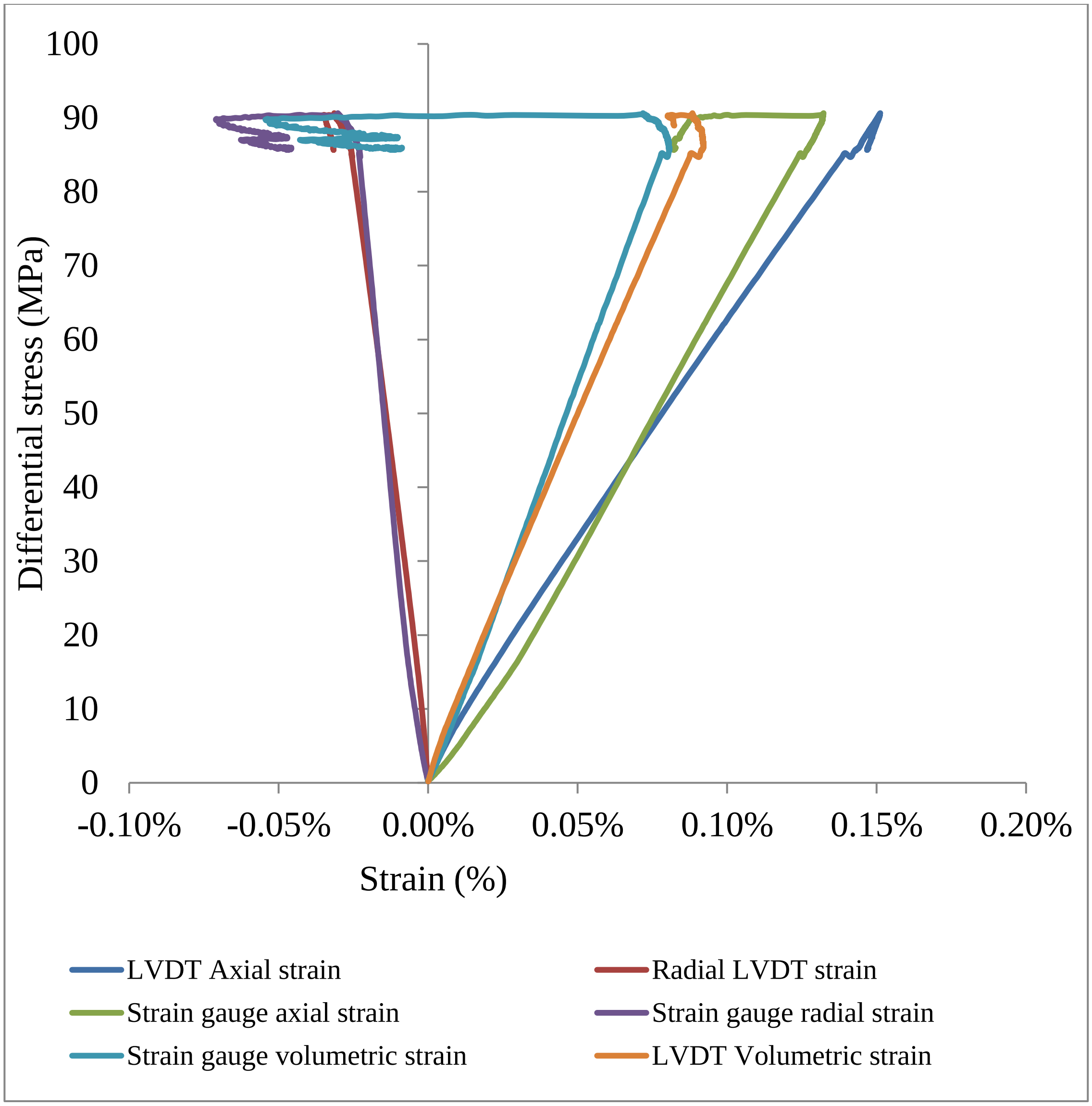

Figure 39: Plot showing stress strain plot for GEO-N2-4300-I3 (Both LVDT and strain gauge measurements are shown). The LVDT and strain gauge readings match well with each other although axial strain using LVDT is slightly higher.

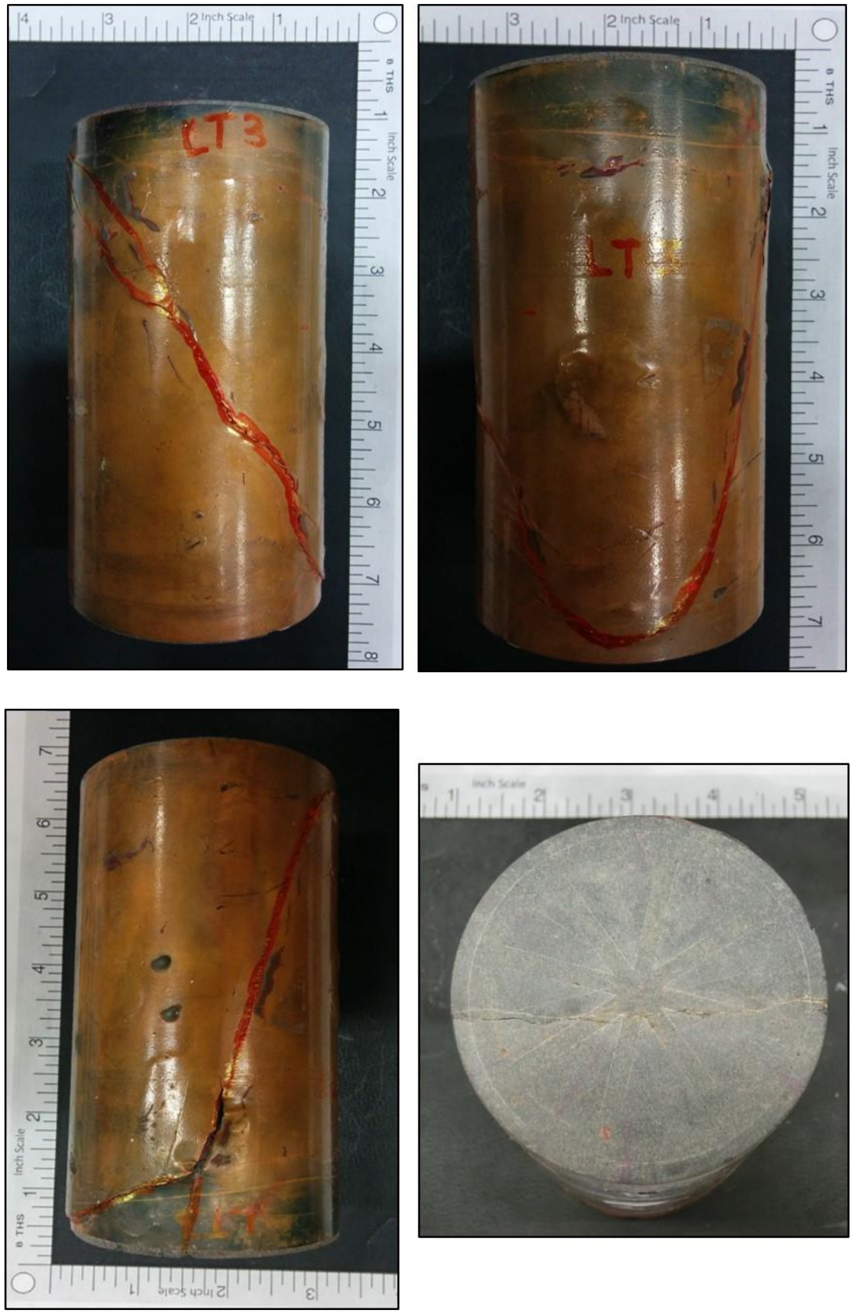

Figure 40: Post injection test pictures show that the sample GEO-N2-4300-I3 failed along existing fractures-the inclined fracture had an angle of 30º with the vertical. Fracture extended to both ends of the sample, enhancing the axial permeability. Copper jacket hasn't been removed to preserve sample integrity.

Sample GEO-N2-4300-I4

The primary objective was to conduct a Triaxial-Injection test by injection of fluid into the sample at pre-determined conditions of pressure (differential and confining). This test was different from the previous three samples in that it was conducted at a higher temperature of 90^{o}C.

Following explains the triaxial testing in detail.

Step 1: Heating the sample and observation of hydrostatic creep:

Motivation: The reason for testing these rocks at elevated temperatures were several fold:

1. These rocks come from a EGS reservoir where temperatures as high as 150 ^{o}C have ben encountered (Bargar et. al., 1999). It makes sense to test them at higher temperatures to gauge their elastic or other properties closer to the actual temperatures that might be expected.
2. To calculate impact of heating on rock properties- including thermal stress, strain and coefficient of expansion. Compare values of parameters obtained from a room temperature test with higher temperature test to understand if it makes a difference.

Sample was therefore heated to a temperature of 90 ^{o}C at a rate of 1.5 ^{o}C/min while being confined at both ends. Figure 41 shows the plot for the same:

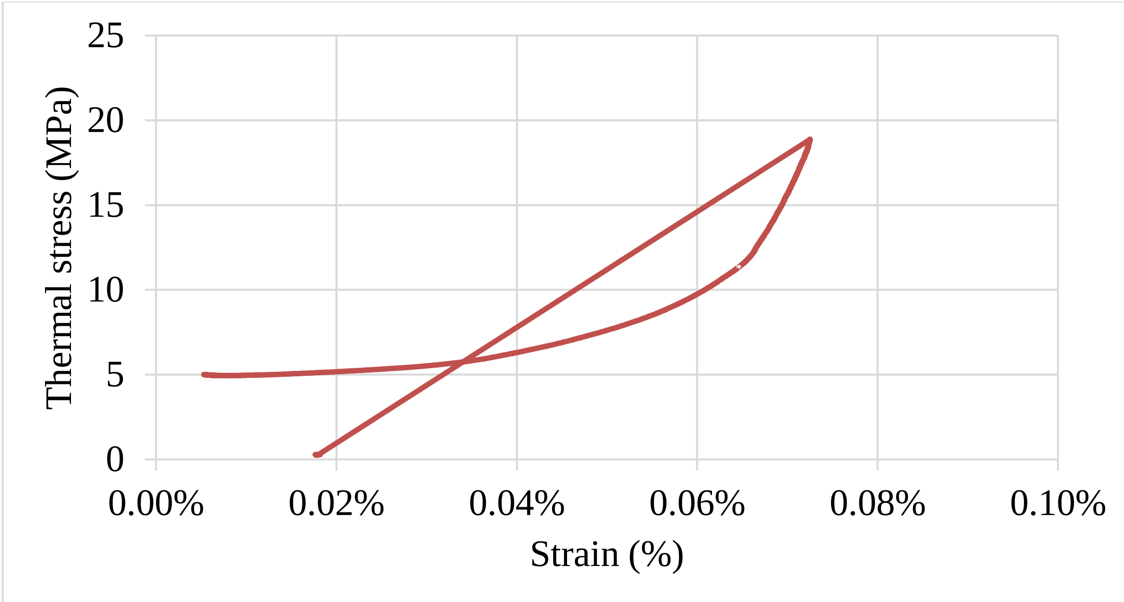

Figure 41: Thermal stress and strain developed in GEO-N2-4300-I4 while being heated.

Once the rock sample temperature began increasing, thermal stresses were generated and the sample's axial stress of increased by 19 MPa by the time temperature increased to 90 ^oC deg C from 23 ^oC deg C indicating the tendency to expand due to heating. When the ends of a sample are confined, the coefficient of expansion can be calculated from the formula:

$$\sigma_{thermal} = -\alpha E(\Delta T) \qquad \text{------ Equation 1}$$

Where,

$\sigma_{thermal}$ = Thermal stress (Pa)

E = Young's modulus (Pa)

α = Coefficient of thermal expansion

ΔT = temperature difference, in ^oC.

Based on the above experiment, the value of α was calculated to be $7.1x10^{-6}$ /^oC.

To prevent sample from getting fractured due to high stress, the sample was unloaded back to unconfined conditions and then allowed to cool down and then the heating process was repeated but this time without any confinement. After the temperature of 90 ^{o}C was reached, it was then maintained at that temperature for 24 hours. During this period, strains were recorded. Axial strain plot is shown below:

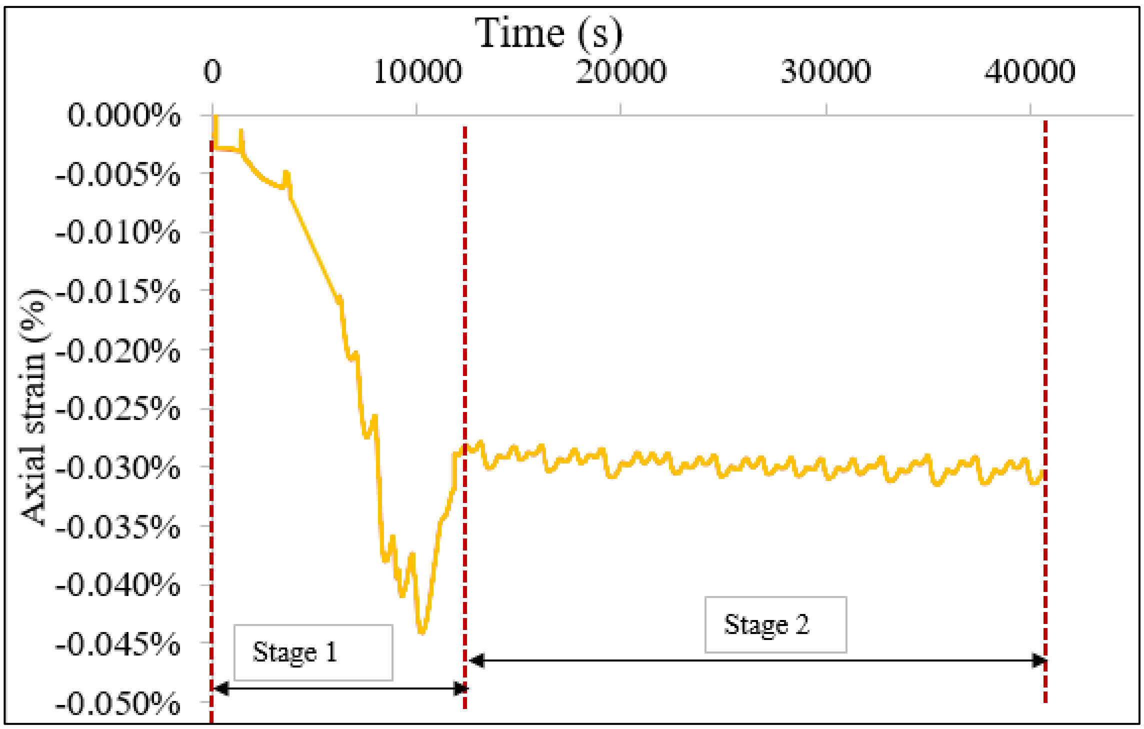

Figure 42: Figure shows effect of heating on GEO-N2-4300-I4. It can be seen that during the initial heating phase (Stage 1), the sample length increases in length rapidly but later on, in stage 2, it stabilizes and we can see an overall increase in length of approximately 0.03%. The final temperature is 90 ^{o}C from an initial 23 ^{o}C.

We can clearly see that there are two phases in heating up a sample – in the first part, as the sample is heated up from room temperature to 90^{o}C over a period of more than 3 hours, it expands in length although non-uniformly at first before stabilizing after a few hours (post heating phase also shown in figure). Some fluctuation still exists in the post heating phase due to inability of machine to hold temperature completely steady.

Overall, we can see that the sample shows about 0.03% axial strain.

For an unconfined sample, using the strain developed solely due to heating of sample can be linked to the coefficient of expansion using the following formula:

$$\frac{\Delta L}{L} = \alpha \Delta T \text{ ------------- Equation 2}$$

Where,

$\Delta L/L$ is the axial strain developed due to heating,

α = Coefficient of thermal expansion

ΔT = temperature difference in ^{o}C

Based on the above, the coefficient of expansion was calculated to be 4.5×10^{-6} $/^{o}C$

Also, once the sample reached a temperature of 90 ^{o}C, sample was left undisturbed to record hydrostatic creep effects at high temperatures (confining pressure of 3500 psi). Figure below shows the axial creep rates measured by using LVDT (green) and strain gauges (black).

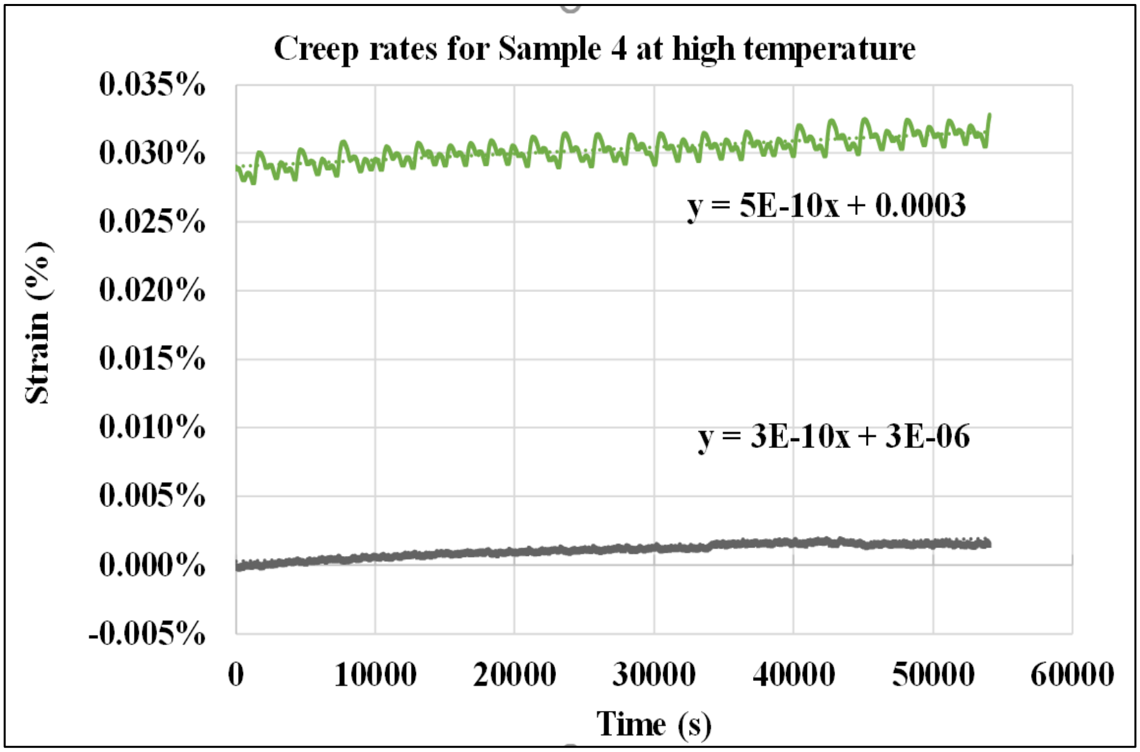

Figure 43: Creep (Hydrostatic) measured at 90º C at a confining pressure of 3500 psi for sample number 4 measured for a period of 13 hours. An average of 4x10^{-10} strains/sec of creep can be seen. Green represents strain calculated by using axial LVDT and black represents strain calculated by using a radial strain gauge.

Cold water Injection into the rock at high temperature conditions:

The aim of this test was to understand if a triaxial-injection test under heated conditions and at conditions of 24.13 MPa (3500 psi) confining pressure and 68.95 MPa (10000 psi) vertical stress in high temperature conditions would be successful. Cold water was used to mimic actual field conditions to simulate a 'thermal shock'. For this test, the sample which had already been at a temperature of 90^{o}C for 24 hours and at a confining pressure of 3500 psi, was loaded up to 75 MPa vertical stress and then cold water at 5^{o}C was passed through the sample from both ends for about 20 mins. Stress was held constant for this part of the test at 68.95 MPa. Sample however, didn't fail. Later gas was also flowed through till returns were observed (which confirmed the uniformity of pore pressure within the sample). Sample still didn't fail. Figure 44 below shows the stress and strain plots vs time for this part of the test. As we can see, while stress remains same, strain just shows creep behaviour (no failure).

When samples were being heated, some AE activity was observed throughout the process – it was observed to be high initially and decreased later. This reflects the fact that heating alters the structure of the rock with some irreversible changes. This aspect is covered in detail in chapter five on Acoustic emissions analysis.

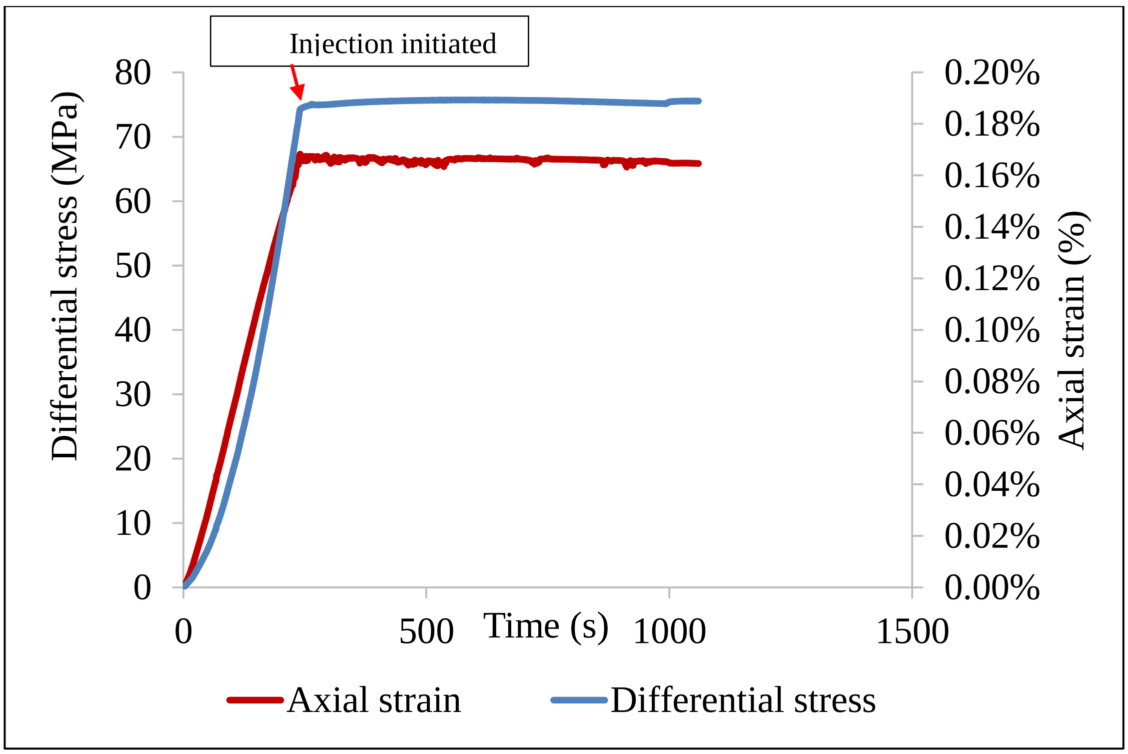

Figure 44: Figure shows the triaxial-injection test conducted on sample GEO-N2-4300-I4 under heated conditions with cold water injection. As can be seen, no change in stress/strain (except creep) occurs due to injection.

Measured value of young's modulus and Poisson's ratio showed no significant difference as compared to the room temperature test.

Triaxial test at high temperature conditions:

For the last part of the test, the sample was triaxially tested at a confining pressure of 1500 psi while maintaining the temperature of 90^{o} C. Figure below shows the stress strain plot for the test.

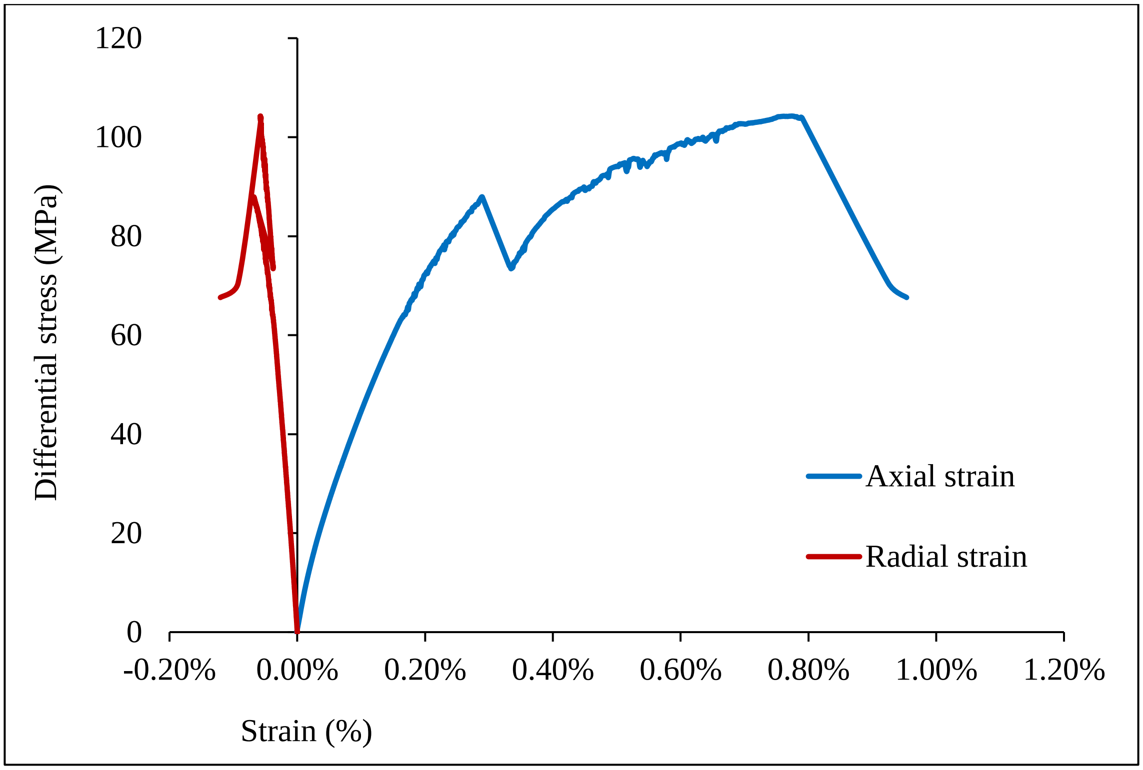

Figure 45: Stress strain plot for GEO-N2-4300-I4, axial strain was measured using LVDT and radial strain using strain gauges.

We can see the plot has two failure points, one at 0.3%, and the other at 0.8%. This is due to formation of two major fracture planes in the sample during the triaxial loading. The natural fracture has an angle of 32^{o} with the vertical. The first one is the reactivation of healed pre-existing fracture and the other is formed due to triaxial testing of the sample (Figure 46).

Figure 46: Figure shows GEO-N2-4300-I4 after failure has two distinct fractures.

Sample GEO-N2-4382-I1

A description of each of the tests conducted on the sample is shown below:

1. Room temperature triaxial test for measurement of elastic parameters - Confining pressure was increased to 3500 psi at room temperature. The sample was then loaded to a differential stress of 45 MPa (6530 psi) at a strain rate of $1x10^{-5}$ strains/sec and then unloaded back to no axial stress. Young's modulus and Poisson's ratio were calculated based on this test results and are shown in Table 13. As already mentioned earlier, the elastic values were measured up to half of peak strength-referred to as the average elastic modulus.
2. Heating up the sample - Now, the sample was heated at a rate of $1.5^{o}C$/min. Strains

(axial and radial) were recorded using LVDT. Below plots show the effect of heating on the strain:

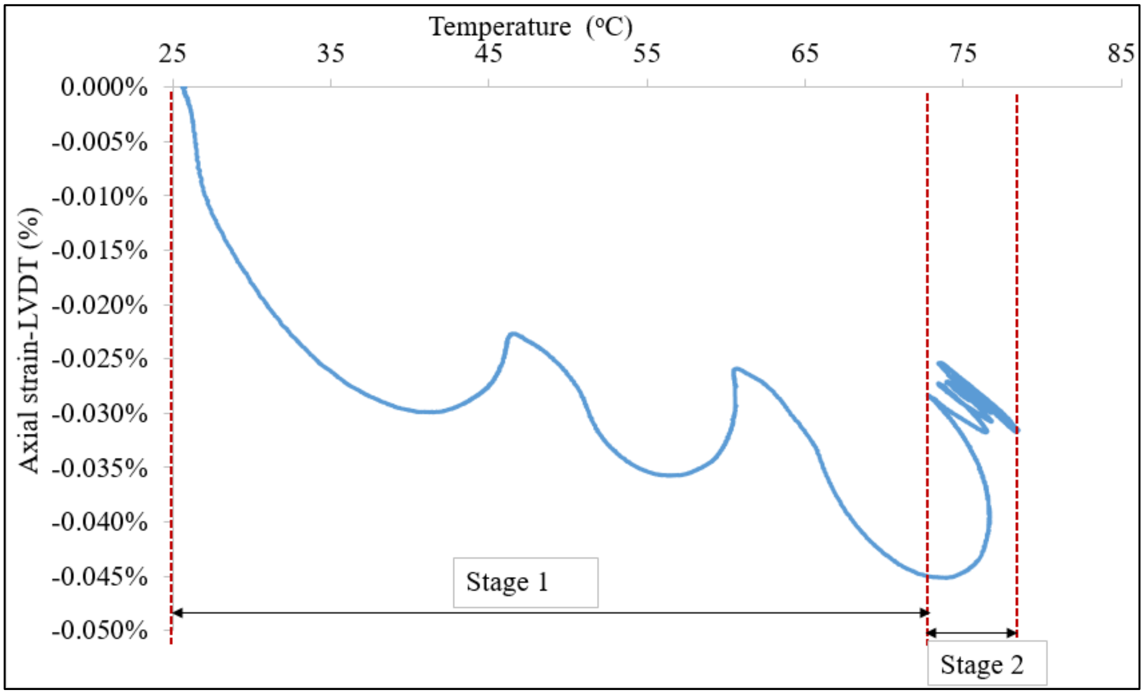

Figure 47: Figure shows effect of heating on sample GEO-N2-4382-I1 axial strain. Two phases can be seen – Stage 1, the heating phase in which heat causes sample to increase in length but non-uniform heating of sample (outer layers get heated up first as compared to inner layers), causes fluctuations in strain till sample becomes heated uniformly and Stage 2, where the sample has heated up uniformly causing the fluctuation to be much lower.

As can be seen, the sample increases in length by almost 0.03% when the temperature is raised to 75 °C from 25 °C. In the end, we can see some fluctuation in strain which is due to the temperature controller error in maintaining sample temperature – it still varies by +/- 2 °C once stable.

Another way to represent this is by using a time and temperature vs strain plot (Figure 48).

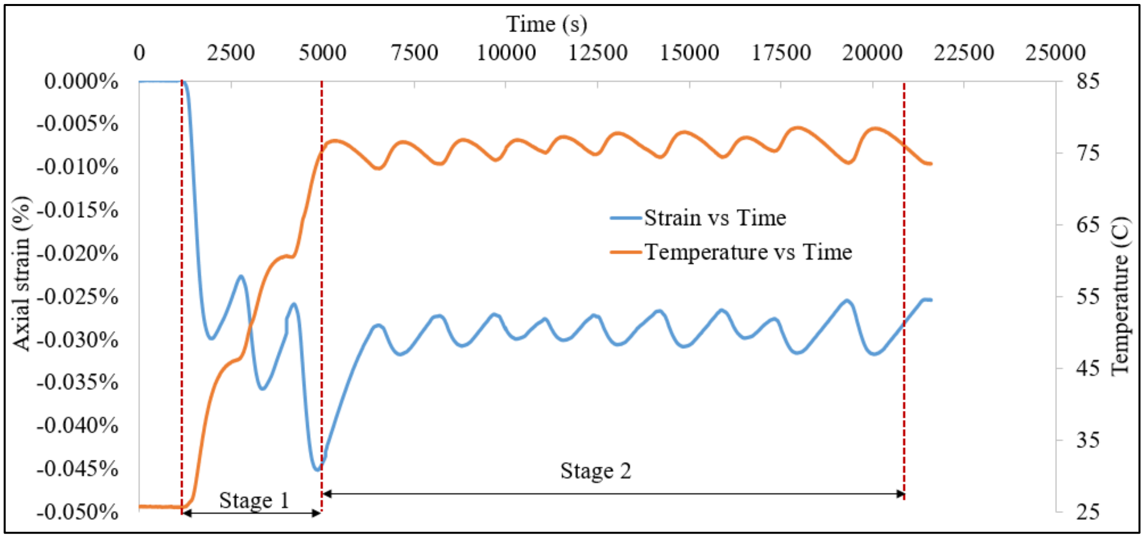

Figure 48: Axial strain and temperature versus time for GEO-N2-4382-I1. Stage 1 shows the initial heating stage where non-uniform heating causes large fluctuations in strain while stage 2 shows reduced fluctuation which is due to inability of machine to hold temperature completely constant (need better insulation). This causes corresponding fluctuation in strain.

This plot shows that temperature varies by +/- 2 ^{o}C which results in changes in strain. Using the equation two described earlier, the coefficient of expansion comes out to be $4x10^{-6}/^{o}C$.

For GEO-N2-4382-I1, following steps explain sequentially the triaxial-injection testing carried out:

1. Verifying if sample will fail due to injection - This test was conducted to understand if a stimulation carried out by injection of gas into the sample resulting into an effective confining pressure of 1000 psi (from the initial 3500 psi) would be successful. Sample was therefore subjected to estimated in-situ conditions – 10000 psi vertical stress and 3500 psi horizontal stress. Sample was axially loaded to a vertical stress of 10000 psi at a strain rate of $1x10^{-5}$ strains/sec while maintaining a confining pressure of 3500 psi and temperature of 90 ^{o}C. Then vertical stress was

maintained constant at 10000 psi while nitrogen gas was injected at a pressure of 2500 psi resulting into an effective confining pressure of 1000 psi. Injection was maintained for 30 mins from both the ends of the sample to reach desired pore pressure faster. The sample did not fail.

2. **Multistage Triaxial testing**

A multistage triaxial testing program was conducted to construct a Mohr circle failure envelope for the sample. Sample was tested at effective confining pressures of 3500 psi, 2000 psi and 1500 psi – it was failed at 1500 psi effective confining pressure. Figure 49 and Figure 50 below show the stress strain plots and the Mohr – Coloumb envelope constructed for the sample. The point at which deflection in volumetric strain (onset of dilatancy) occurred was taken as the failure strength for that particular confining pressure. The rock failed at a peak strength of 181 MPa at confining pressure of 1500 psi. It may be noted that this is much higher than GEO-N2-4300-I1, GEO-N2-4300-I3 and GEO-N2-4300-I4 which had fractures and is comparable to GEO-N2-4300-I2 which also had no fractures. This shows that presence/absence of healed fractures makes a large difference in strength of the core.

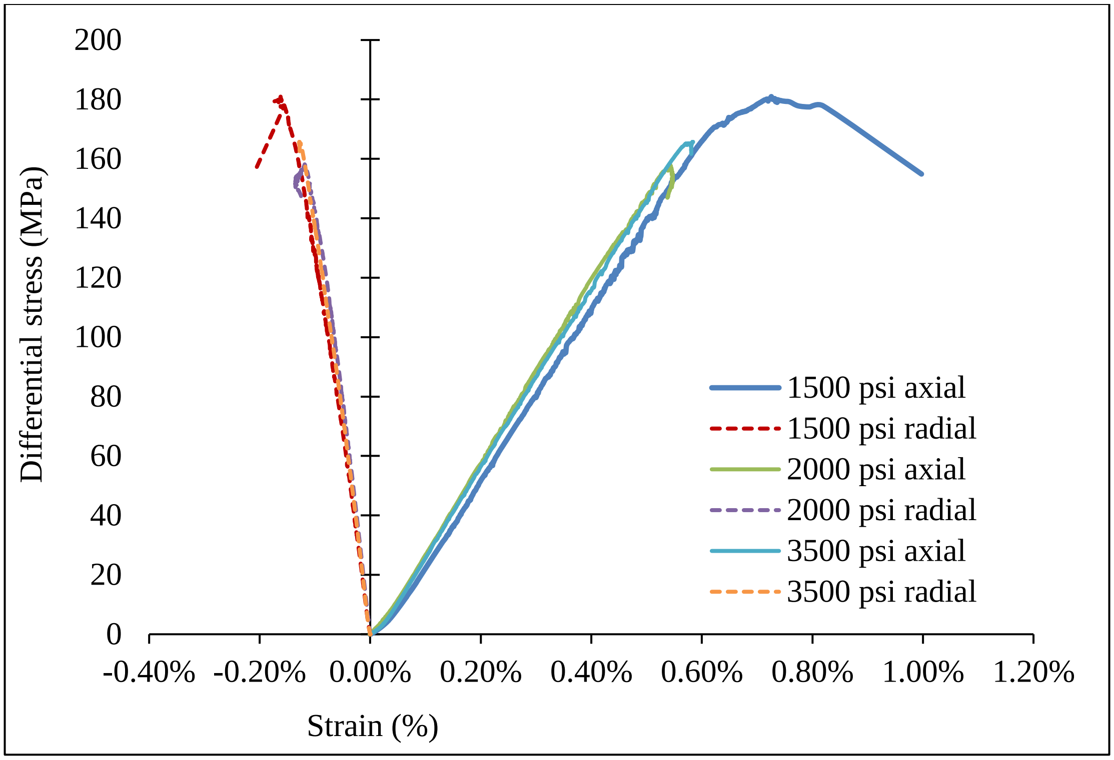

Figure 49: Multistage stress strain plot for GEO-N2-4382-I1 showing the axial and radial strains for the various confining pressures. As can be seen, radial strains don't change much with increase in confining pressures although the slope of the axial strain (Young's modulus) increases slightly as confining pressure is increased. Final failure is brought about at 1500 psi confining pressure.

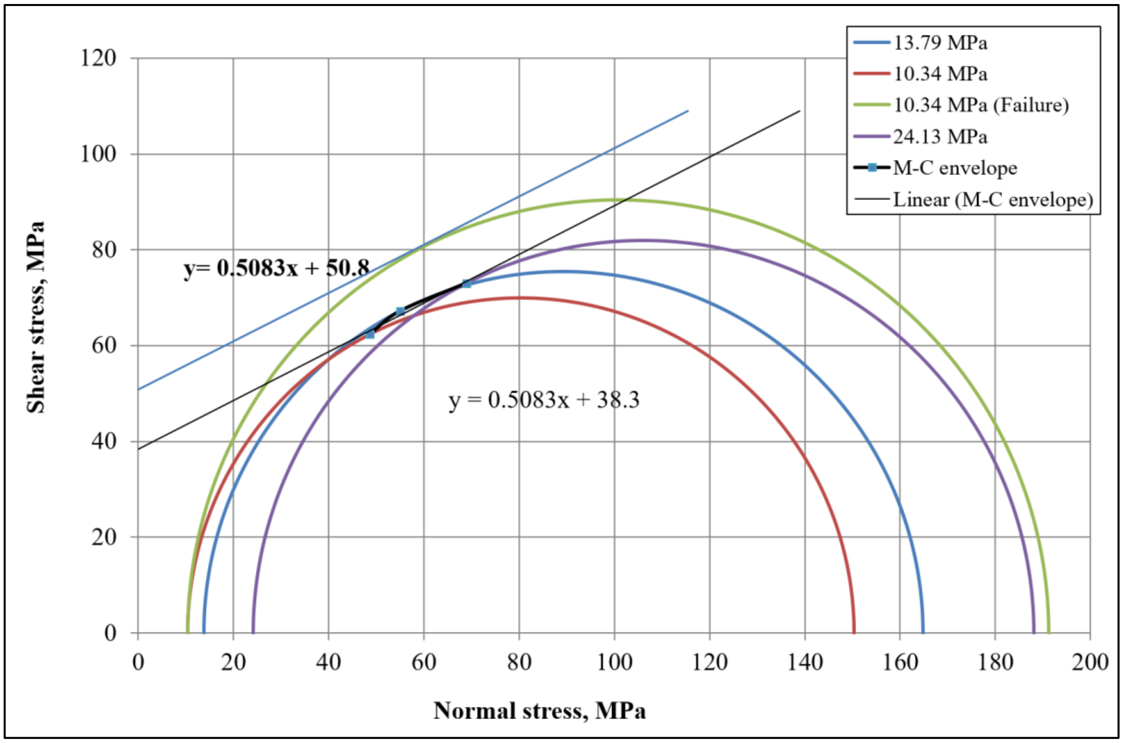

Figure 50: Mohr-Coulomb plot for GEO-N2-4382-I1. Three confining pressures were used – 4500 psi, 2500 psi and 1500 psi. Sample was failed at a confining pressure of 1500 psi. A line parallel to the tangent to the three circles was used to draw a line which intersected the Mohr circle for 1500 psi confining pressure.

Based on the above the friction angle and cohesion were calculated. These are:

1. Friction angle, φ = 26.7°
2. Cohesion, c = 50.8 MPa
3. UCS = 164.7 MPa

The formula used for calculating UCS:

$$UCS = \frac{2 * c * Cos\varphi}{1 - sin\varphi}$$

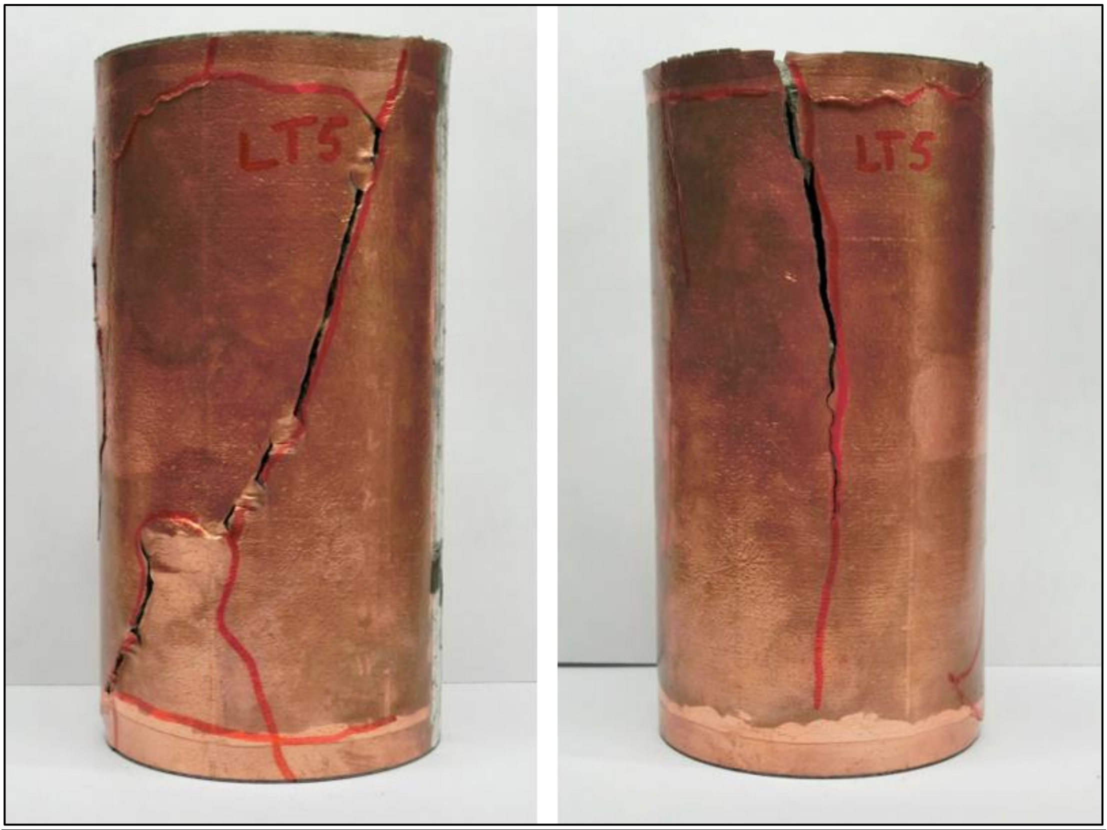

Figure 51: GEO-N2-4300-I4 pictures after failure (two views). We can see multiple fractures although one major inclined fracture intersecting both ends can be seen along both views of the sample.

Sample GEO-N2-4243-I1

Testing Results (Stress Strain diagrams below)

A description of each of the tests conducted on the sample is shown below:

1. **Room temperature test for measurement of elastic parameters** - Confining pressure was increased to 3500 psi at room temperature. Sample was then loaded to a differential stress of 70 MPa (10150 psi) at a strain rate of $1x10^{-5}$ strains/sec. and then unloaded back to no axial load. Average Young's modulus and Poisson's ratio were calculated based on this test results and are shown in Table 13.

2. Heating up the sample - Now, the sample was heated at a rate of 1.5°C/min maintaining the stress conditions as 3500 psi confining with no axial stress. Axial strain was recorded using LVDT to quantify the length change of the sample. Below plots show the effect of heating on the strain:

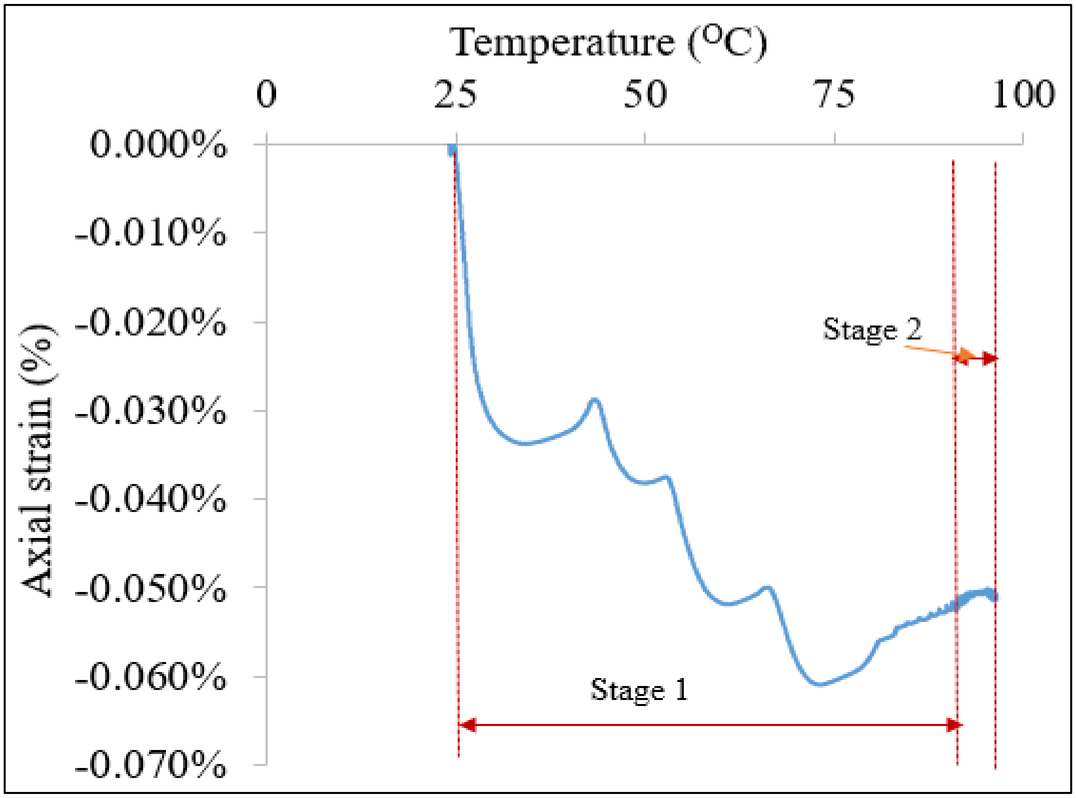

Figure 52: Figure shows effect of heating on sample's axial strain. Two phases can be seen – a heating phase (Stage 1) in which heat causes sample to increase in length but non-uniform heating of sample (outer layers get heated up first as compared to inner layers), causes fluctuations in strain till sample becomes heated uniformly. The strain then stabilizes in stage 2.

As can be seen, the sample increases in length by almost 0.05% when the temperature is raised to 75 °C from 25 °C. In the end, we can see some fluctuation in strain which is due to the temperature controller error in maintaining sample temperature – it still varies by +/- 1 °C once stable.

Another way to represent this is by using a time and temperature vs strain plot (Figure 53).

We can clearly see that the strain stabilizes after a few hours and then just shows normal hydrostatic creep.

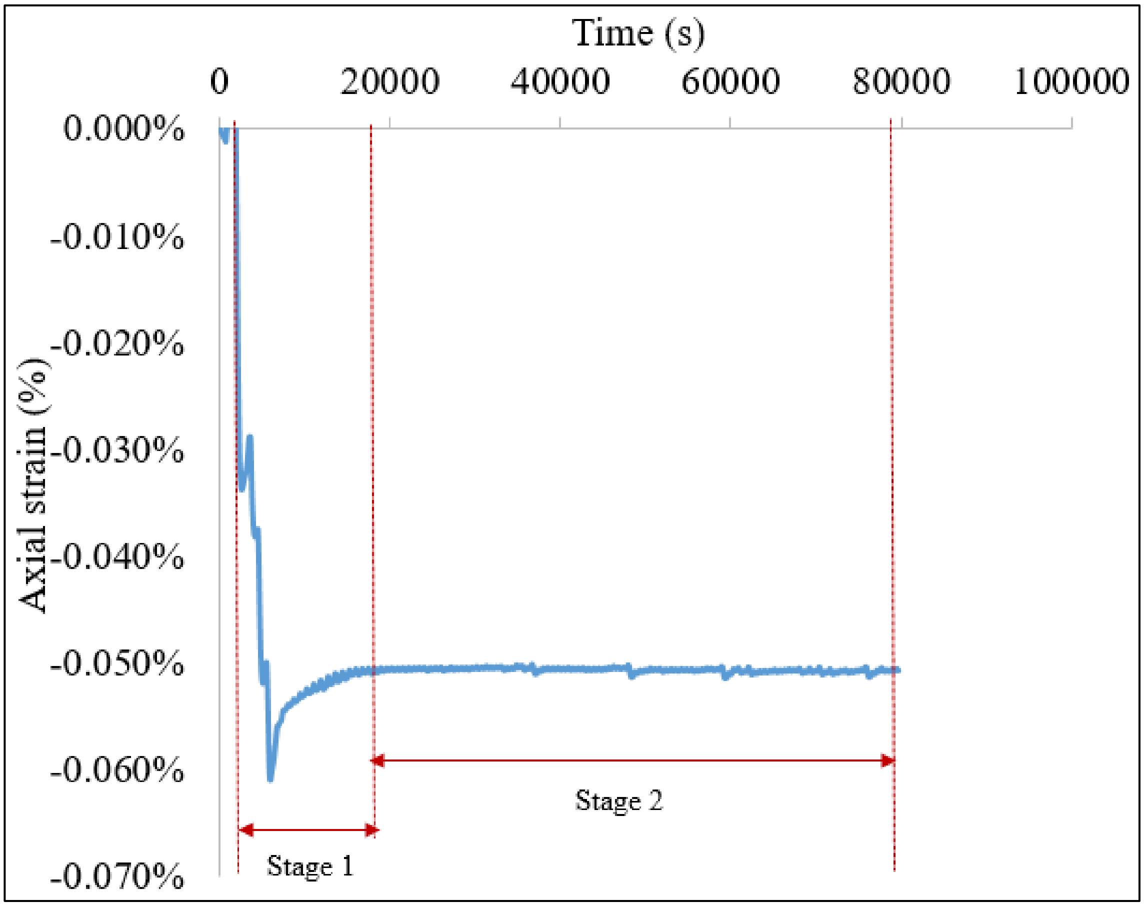

Figure 53: Axial strain versus time for GEO-N2-4382-I1. We can see that in the Stage 1, the sample has non-uniform expansion as heat travels through the sample. In the post heating phase (Stage 2), strain stabilizes. Overall an increase in length of 0.55% can be observed.

3. **<u>Verifying if sample will fail due to injection</u>** - This test was conducted to understand if a stimulation carried out by injection of gas into the sample resulting into an effective confining pressure of 1000 psi (from the initial 3500 psi) would be successful. Sample was therefore subjected to the estimated in-situ conditions of

10000 psi vertical stress and 3500 psi horizontal stress. Sample was axially loaded to a vertical stress of 10000 psi at a strain rate of $1x10^{-5}$ strains/sec while maintaining a confining pressure of 3500 psi and temperature of 90 ^{o}C. Then vertical stress was maintained constant at 10000 psi while nitrogen gas was injected at a pressure of 2500 psi resulting into an effective confining pressure of 1000 psi. Injection was maintained for 30 mins from both the ends of the sample to reach desired pore pressure faster. However, sample didn't fail. This answered one desired question for testing of this sample - that sample won't fail due to a stimulation treatment with an effective confining pressure of 1000 psi (assuming a vertical differential stress of 10000psi).

4. Triaxial test at high temperature conditions

For the last part of the test, the sample was failed by injection at a confining pressure of 2500 psi while maintaining the temperature of 90^{o} C. Figure below shows the stress strain plot for the test.

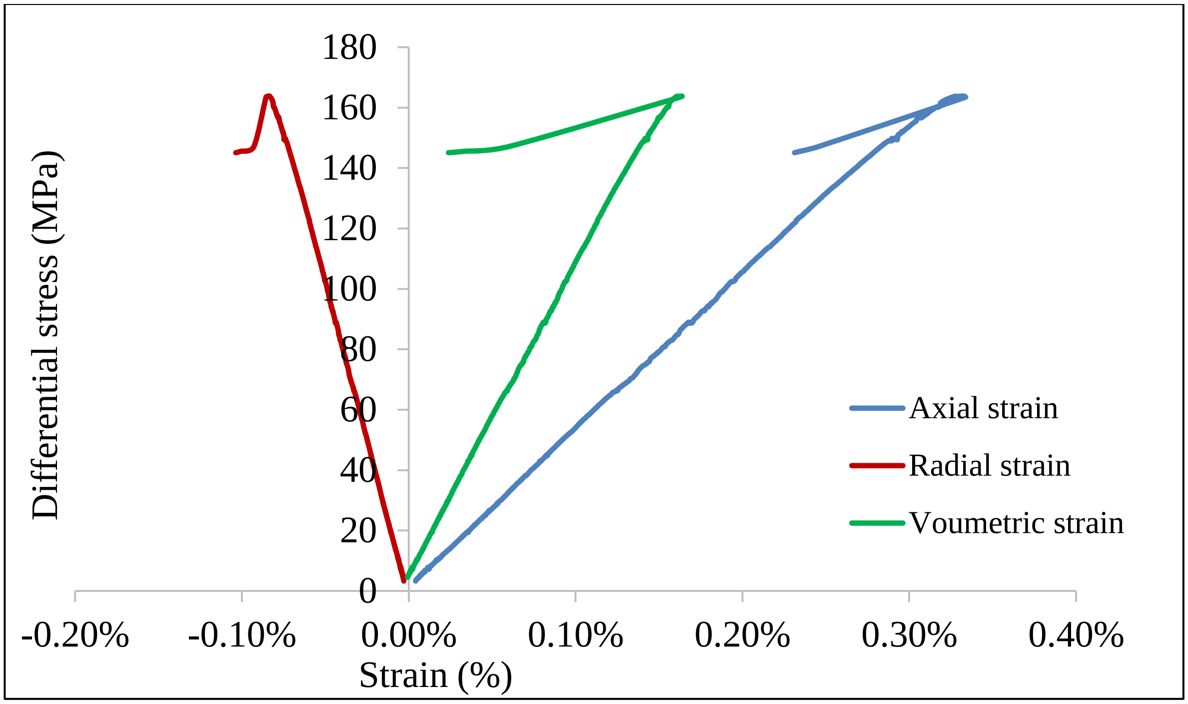

Figure 54: Stress strain plot for GEO-N2-4243-I1 showing axial, radial and volumetric strain. All strains measured here have been measured using strain gauges.

Figure 55: Sample GEO-N2-4243-I1 pictures after failure (two views). We can see a single fracture at an angle of about 45º running across the sample.

A table containing all the six sample's testing results (including coefficient of expansion) is provided below for reference.

Table 13: Summary of static and dynamic measurement results performed on full core samples from the GEO-N2 well. All samples failed in brittle mode.

	GEO-N2-4300-I1	GEO-N2-4300-I2	GEO-N2-4300-I3	GEO-N2-4300-I4	GEO-N2-4382-I1	GEO-N2-4243-I1
Effective Confining Pressure	3500 psi	3800 psi	3800 psi	1500 psi	(Several)	2500 psi
Test conducted	Triaxial-Injection	Triaxial-Injection, Triaxial	Triaxial-Injection	Triaxial-Injection, Triaxial	Multistage Triaxial	Triaxial-Injection
Temperature (°C) of test	23	23	23	90	90	90
Static Young modulus (GPa)	43.4*	52.8*	51.1*	41.9*	41.7*	60.7*
Static Poisson's ratio	0.17*	0.17*	0.19*	0.22*	0.29*	0.26*
Peak Strength (MPa)	96.1	271.6	90.6	112.6	180.9	163.8
Dynamic Young modulus	64.4	62.22	60.53	53.6	58.2	71.83
Dynamic Poisson's ratio	0.24	0.25	0.27	0.22	0.18	0.22
Coefficient of Expansion	NA	NA	NA	5.77×10^{-6}	4×10^{-6}	7.14×10^{-6}

* - 24.13 MPa (3500 psi) confining pressure

Comparison of Static and Dynamic Young’s modulus:

Figure 56 shows a comparison of static and dynamic Young’s modulus for all the samples.

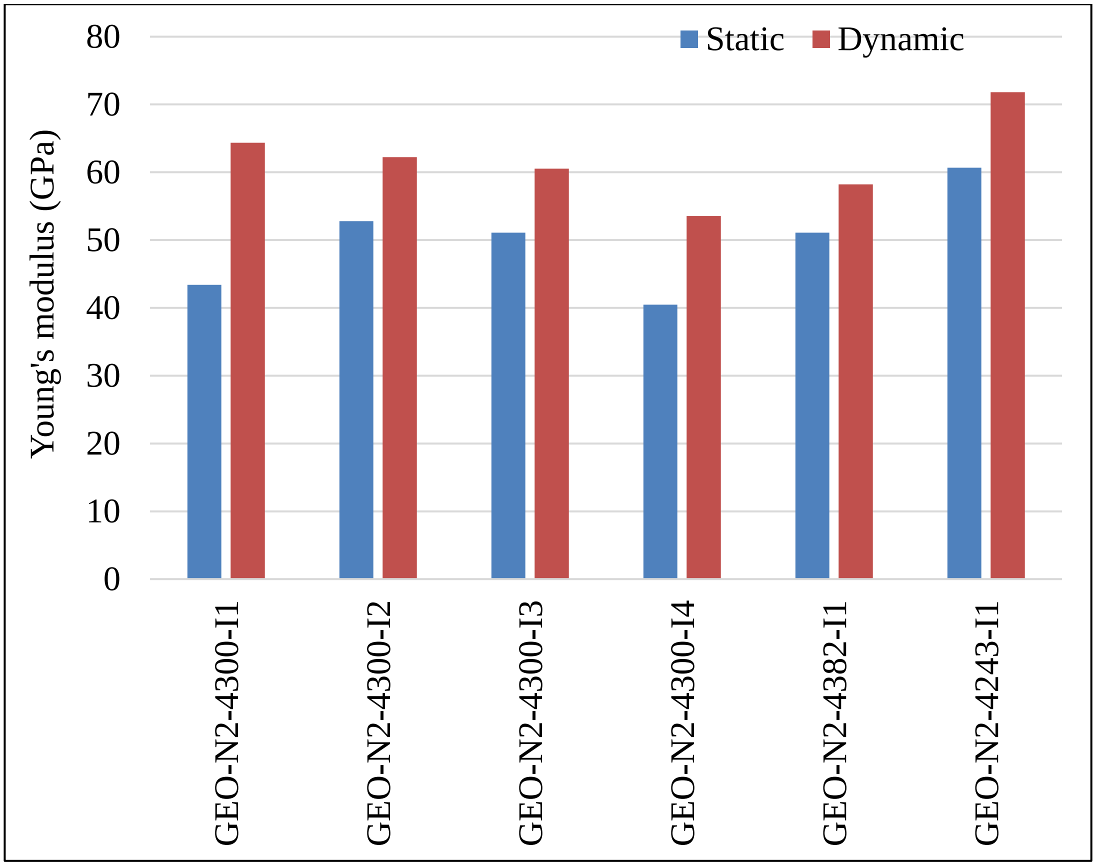

Figure 56: Comparison of static and dynamic Young’s modulus for all the six GEO N2 full core samples.

As can be seen, the average difference between the static and dynamic Young’s modulus is 19% with actual values differing by 12-33%, dynamic values were always higher.

When compared with the Poisson’s ratio, the differences reduce with an average difference of 11%, no fixed trend being there between which one was higher/lower (Figure 57).

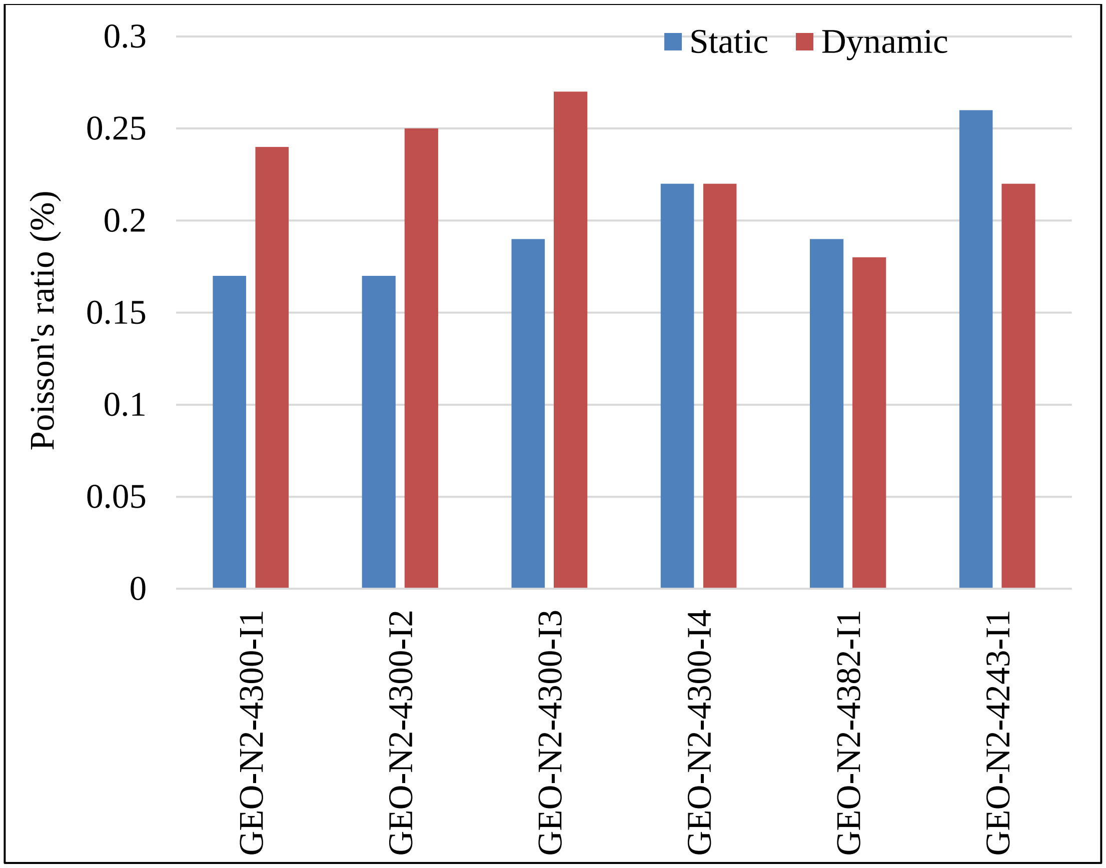

Figure 57: Comparison of static and dynamic Poisson's ratio for all the six samples.

Conclusions from the triaxial testing results of the full core samples from the N2-GEO well:

1. A successful application of triaxial-injection technique has been demonstrated in these experiments. GEO-N2-4300-I1, GEO-N2-4300-I2, GEO-N2-4300-I3 and GEO-N2-4243-I1 were tested successfully using this technique. In none of the cases, did the rocks fail at the ins-situ simulated conditions of 70 MPa vertical pressure and 24 MPa horizontal pressure. The actual failure conditions and strength have been summarized in Table 13 for reference.
2. Sample GEO-N2-4382-I1's Mohr-Coulomb envelope has been generated. . This sample GEO-N2-4300-I2 which had no observable healed fractures showed

much higher strength than the rest-all of which had large healed fractures. Hence presence of healed fractures substantially changes the strength of the core – this can be seen in the strength of the sample GEO-N2-4300-I2 (no observable fractures) which was 3 times more than samples GEO-N2-4300-I1, GEO-N2-4300-I3 and GEO-N2-4300-I (several healed fractures). Similarly, GEO-N2-4243-I1's (no fractures) strength was almost two times that of the samples with fractures. Overall, samples with no fractures showed considerably high strength (UCS >160 MPa) than most other rocks.

3. Average Young's modulus varied between 41-61 GPa and is not influenced by presence/absence of healed fractures. These high numbers reflect the high strength and brittleness of the core.

4. Static Poisson's ratio was on an average less than 0.20. This also shows the brittle nature of the rock.

5. Very high tensile strength, upto 27 MPa (Average 20 MPa) was observed in these samples using Brazilian strength testing (Appendix 3). This shows that any hydraulic fracturing treatment would require considerably high injection pressure.

6. No significant effect of heat was observed on these rocks in terms of strength or elastic parameters. This could be probably due to the temperature being too low for these parameters to be affected (need >350 Celsius). About 0.03% strain was observed in hydrostatic heating of the sample. The average thermal coefficient of expansion for all the three samples that were tested at high temperatures- GEO-N2-4300-I4, GEO-N2-4382-I1 and GEO-N2-4243-I1 was found to be 5.67×10^{-6} /ºC.

Cored samples from the GEO-N2 and OXY 72-03 wells

These six samples have already been described in chapter 2 and the Appendix 1. Below section describes each sample's triaxial testing in detail.

Sample GEO-N2-4361-V3

Test Objective

The primary objective was to conduct a Triaxial-Injection test by injection of fluid into the sample at pre-determined conditions of pressure (differential and confining). Fluid must be injected until stable returns are observed at the downstream end of the sample to ensure pore pressure was uniform. If sample failure doesn't occur, increase differential stress to the point of volumetric strain transitioning sample from contraction to dilatancy and then fail sample by injection of pore fluid to reduce effective confining pressure.

Following explains the triaxial testing in detail:

1. Heating the sample and observation of Creep:

Sample was heated at a rate of 3^o C/min to a final temperature of 80 ^{o}C. Temperatures were monitored using four thermocouples placed around the sample with one thermocouple being attached on to the sample (see Figure 63). Temperature stability was maintained by using an insulating jacket placed around the triaxial sample and temperature variation within the cell at any point during the tests was found to be +/- 1 ^{o}C. Once the final temperature was achieved, sample was left to stabilize for about 5 hours. Axial strain plots are shown below (vs time as well as temperature).

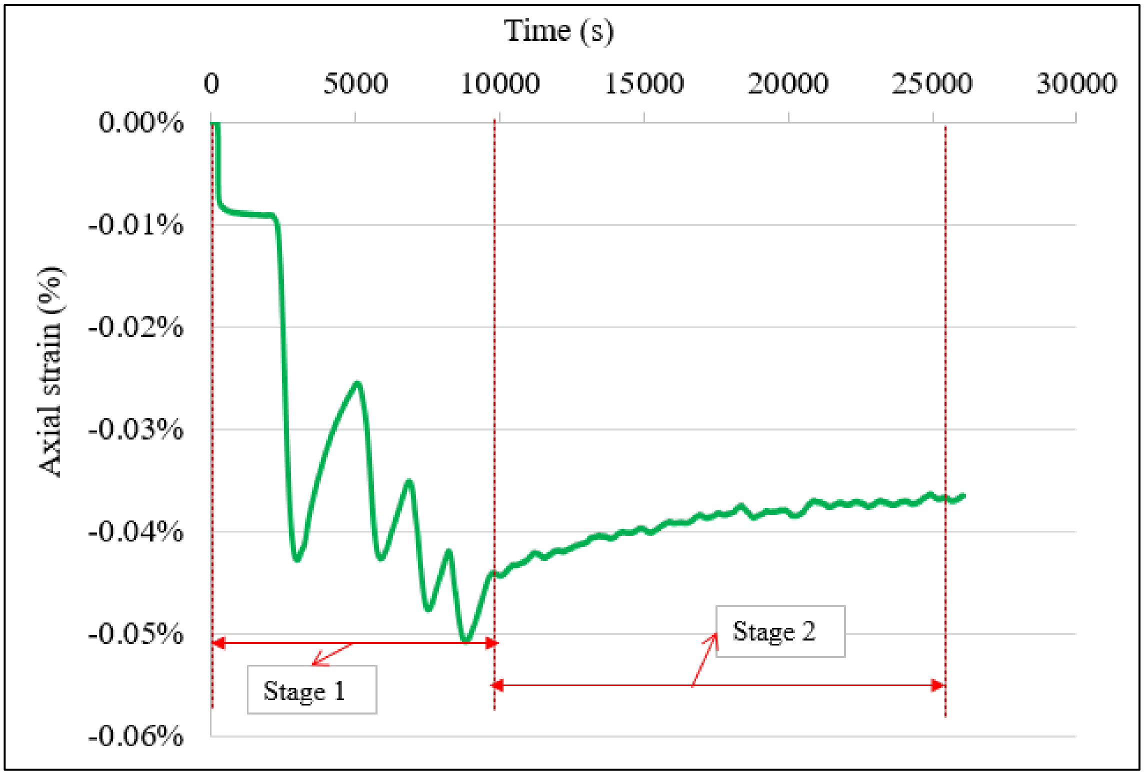

Figure 58: Figure shows effect of heating on sample GEO-N2-4361-V3. We can see that in the initial phase of the sample being heated (stage 1), it increases in length rapidly but later on, in stage 2, it stabilizes and we can see an overall increase in length of approximately 0.037%. The final temperature is 80°C from an initial 25 °C.

We can clearly see that there are two phases in heating up a sample – in the first part, as the sample gets heated up from room temperature to 80°C over a period of more than 3 hours, it expands in length although non-uniformly at first before stabilizing after a few hours (Post heating phase also shown in figure). Very minor fluctuation still exists in the post heating phase due to inability of machine to hold temperature completely steady. Overall, we can see that the sample shows about 0.037% strain.

Using equation 1, the coefficient of thermal expansion comes out to be $6.21x10^{-6}$.

Also, once the temperature of 80 °C was achieved, sample was left undisturbed to record hydrostatic creep effects at high temperatures (confining pressure of 3500 psi). Figure below shows the axial creep rates measured by using LVDT's.

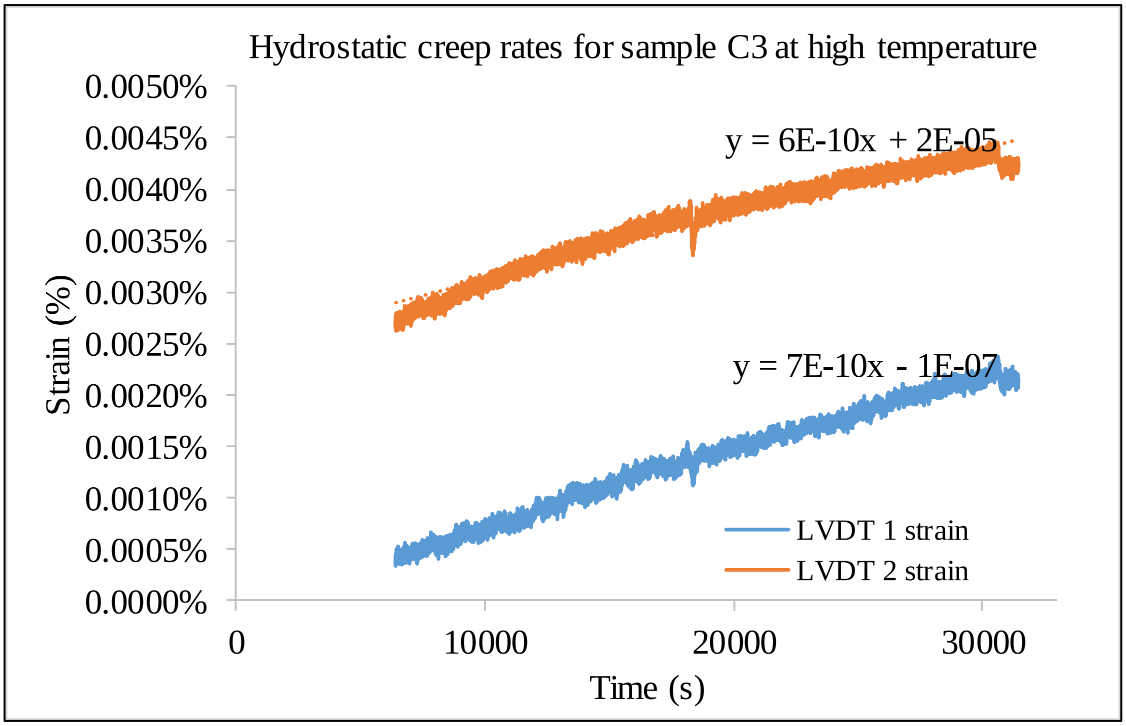

Figure 59: Creep (Hydrostatic) measured at 80º C at a confining pressure of 3500 psi for sample GEO-N2-4361-V3 measured for a period of 10 hours. An average of 6.5×10^{-10} strains/sec of creep can be seen.

2. Injection of cold water into the rock at high temperature conditions

The aim of this test was to understand if a triaxial-injection test under heated conditions and at conditions of 24.13 MPa (3500 psi) confining pressure and 68.95 MPa (10000 psi) vertical stress in high temperature conditions would be successful. For this test, the sample which had already been at a temperature of 80ºC for 10 hours and at a confining pressure of 3500 psi, was loaded up to 68.95 MPa vertical stress and then cold water at 5ºC was passed through the sample from both ends for about 30 minutes at a pore pressure of 2500 psi (effective confining decreased to 1000 psi from 3500 psi). Stress was held constant for this part of the test at 68.95 MPa. Sample however, didn't fail.

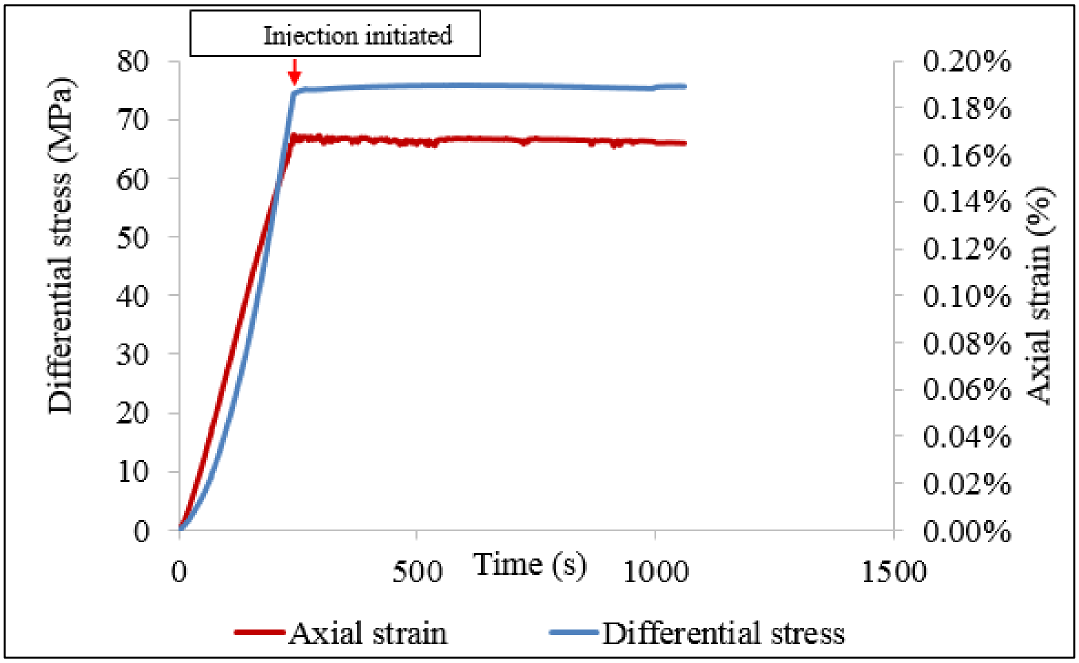

Figure 60: Triaxial injection stage where sample GEO-N2-4361-V3 was loaded upto 75 MPa by holding displacement constant and effective confining pressure was decreased to 6.9 MPa (1000 psi), however sample didn't fail.

Later gas was also flowed through at same pore pressure till returns were observed (which confirmed the uniformity of pore pressure within the sample). Sample still didn't fail.

Following this, the differential stress was increased axially till sample volumetric strain showed deflection from initial direction (shifted from contraction to dilatancy). Then gas was again injected at a pressure of 2500 psi resulting into the effective confining pressure dropping to 1000 psi from the initial 3500 psi. Sample was successfully failed using this technique; stress strain plots are shown below (Figure 61) for reference.

Sample failed with a single fracture running from one end of the sample to approximately the middle of the sample. Angle of friction as measured directly from the sample was found to be 44° (Figure 62).

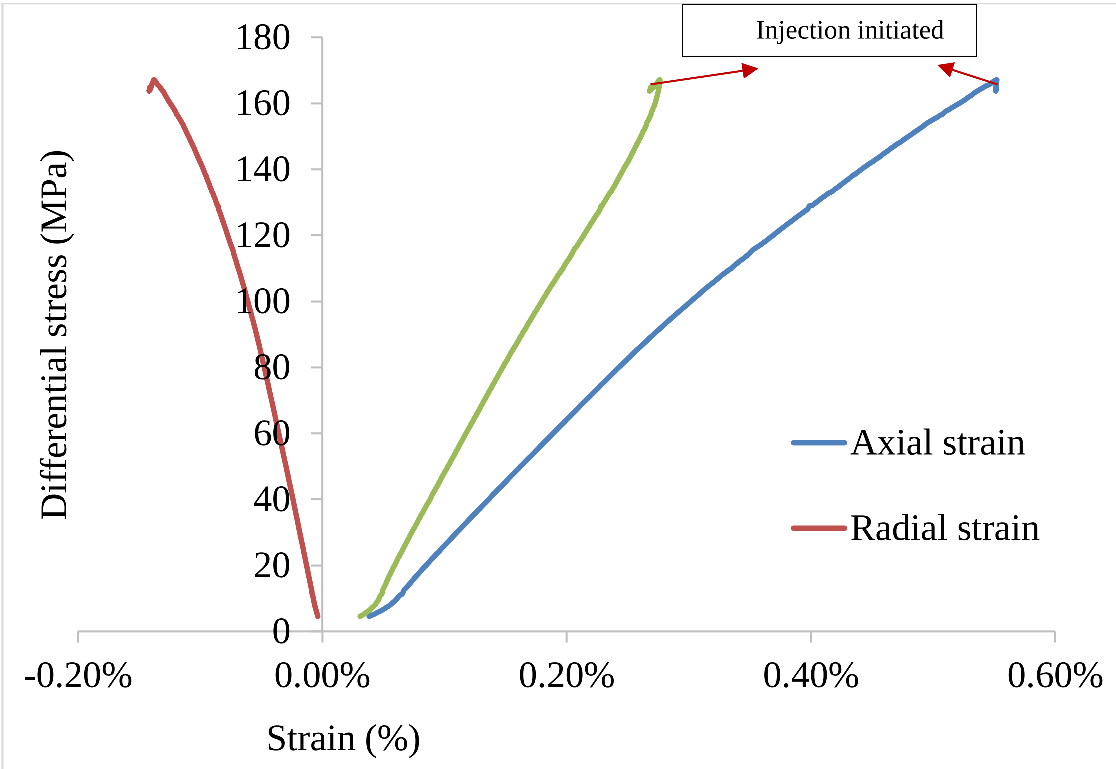

Figure 61: Stress strain plot showing axial, radial and volumetric strain for Sample GEO-N2-4361-V3. The machine had to be stopped in emergency mode after sample failure as it happened very fast, hence no data was recorded beyond the early failure part

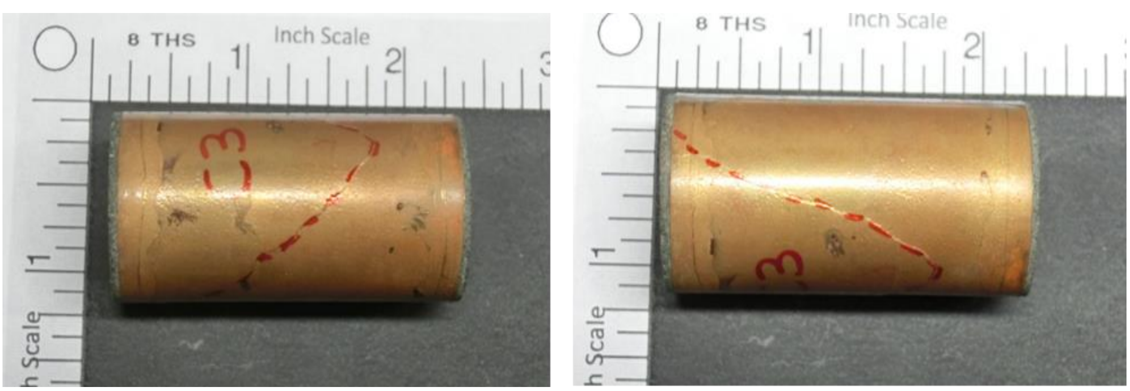

Figure 62: Post-test pictures of sample GEO-N2-4361-V3 showing the fracture formed after failure (red dotted). Sample has been kept in copper jacket to preserve it.

Sample GEO-N2-4361-V2

The test objectives and testing pattern was exactly same as previous sample GEO-N2-4361-V3. Results are presented here.

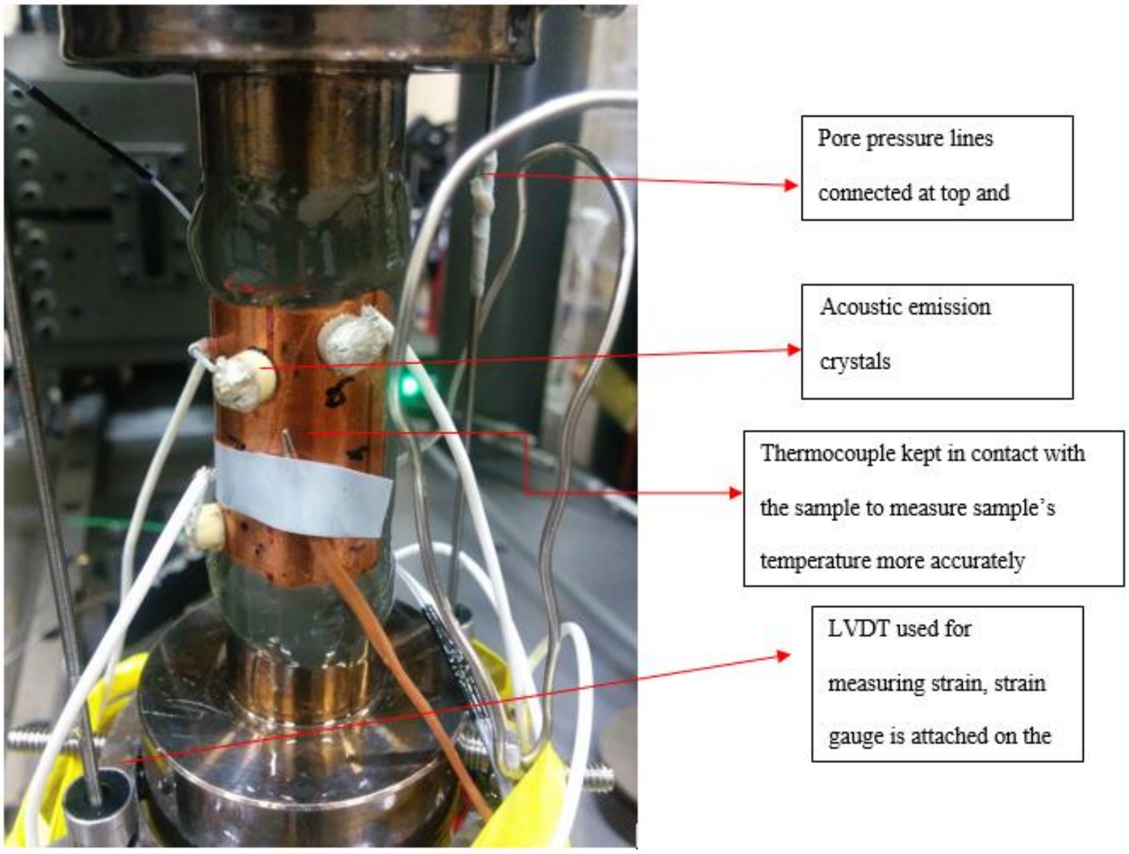

Figure 63: Close up view of sample GEO-N2-4361-V2 within the frame showing the thermocouple and acoustic emission crystals attached to sample.

Heating up the sample - The sample was heated at a rate of 1.5 ^{o}C/min. Axial strain was recorded using LVDT to quantify the length change of the sample. Below plots show the effect of heating on the strain:

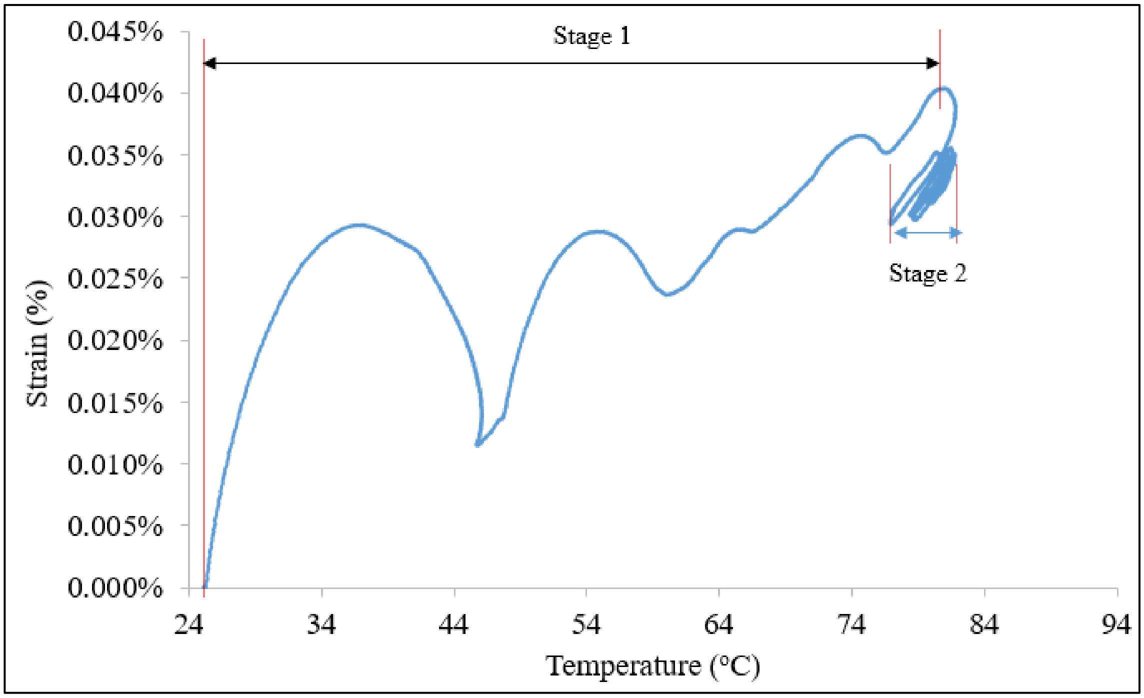

Figure 64: Figure shows effect of heating on sample's axial strain. Two phases can be seen – Stage 1, which is the heating phase in which heat causes sample to increase in length but non-uniform heating of sample (outer layers get heated up first as compared to inner layers), causes fluctuations in strain resulting into alternate contraction and expansion-although overall there's expansion. In stage 2, strain starts to stabilize as the sample's temperature becomes uniform throughout.

As can be seen, the sample increases in length by almost 0.033% when the temperature is raised to 75 ^{o}C from 25 ^{o}C. In the end, we can see some fluctuation in strain which is due to the temperature controller error in maintaining sample temperature – it still varies by +/- 2 ^{o}C once stable.

Another way to represent this is by using a time and temperature vs strain plot (Figure 65). We can clearly see that the strain stabilizes after a few hours and then just shows normal hydrostatic creep.

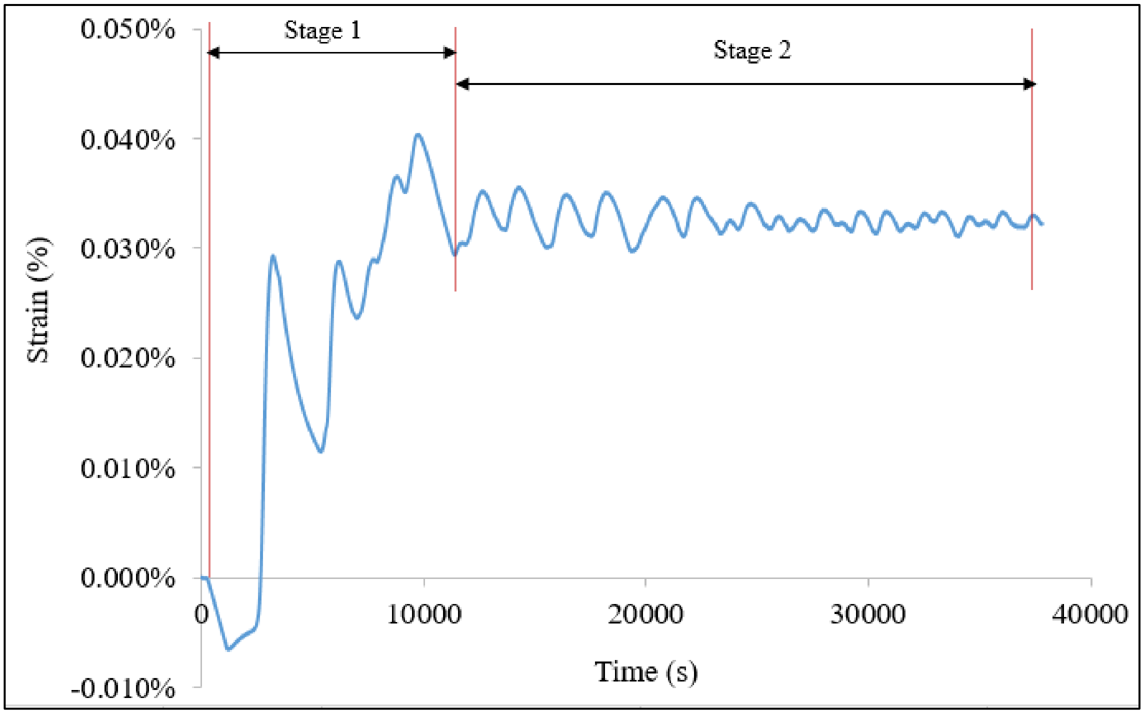

Figure 65: Axial strain versus time for sample GEO-N2-4361-V2. Stage 1 and stage 2 as described previously can be seen in a different format here.

Using Equation 2, the coefficient for thermal expansion comes out to be 5.85×10^{-6}.

Triaxial test at high temperature conditions

For the second and final last part of the test, the sample was failed triaxially at a confining pressure of 3500 psi while maintaining the temperature of 80^{o} C. Figure 66 below shows the stress strain plot for the test.

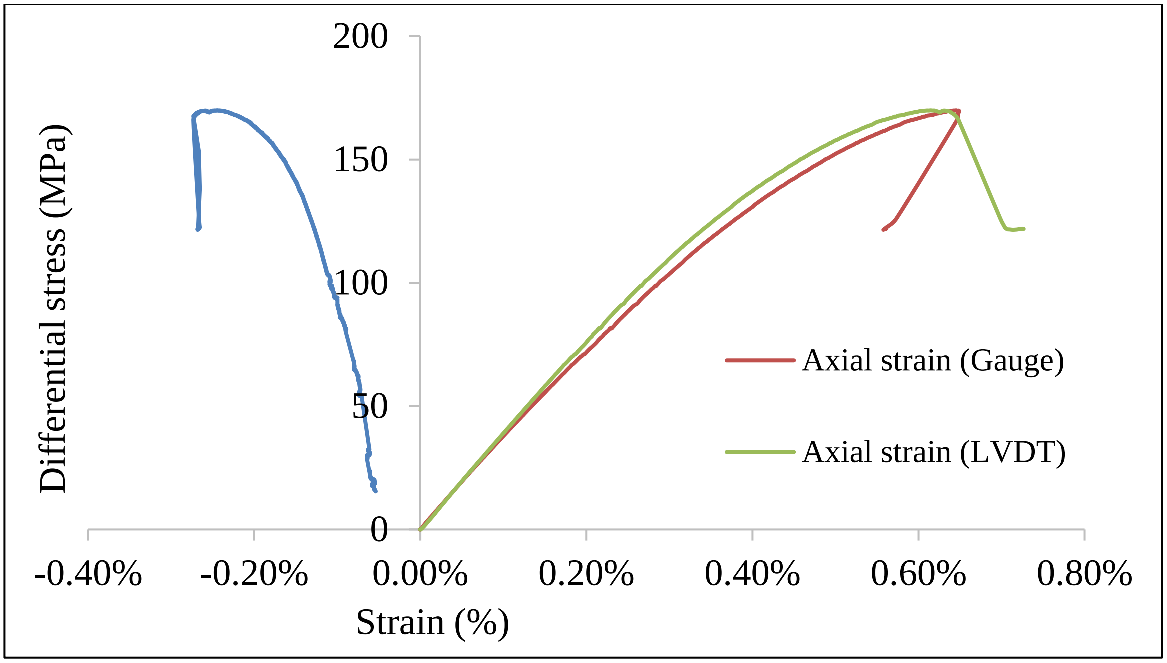

Figure 66: Stress strain plot for GEO-N2-4243-I1 showing axial and radial strain.

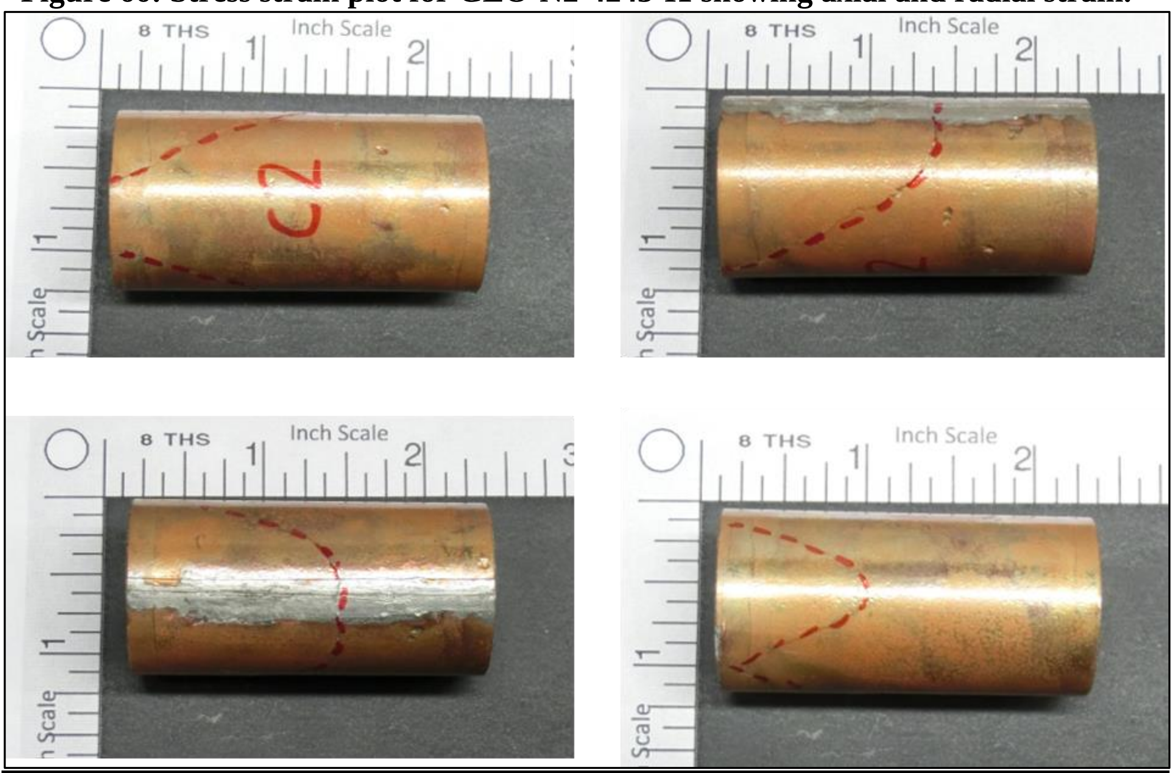

Figure 67: Sample pictures for GEO-N2-4361-V2 after failure (four views). We can see two fractures running mid-way across the sample.

Sample OXY-72-3-3861.5-V2

The aim of this test was to understand if a triaxial-injection test under conditions of 24.13 MPa (3500 psi) confining pressure and 68.95 MPa (10000 psi) vertical stress would be successful. For this test, the sample was subjected to a confining pressure of 24.13 MPa (3500 psi) and then was loaded up to 68.95 MPa (10000 psi) vertical stress and then nitrogen gas was passed through the sample from both ends for 3.5 hours at a pore pressure of 2500 psi (effective confining decreased to 1000 psi from 3500 psi). The higher time for this sample was warranted due to its low permeability, it took this time to achieve stable flow across the sample. Stress was held constant for this part of the test at 68.95 MPa. Sample however, didn't fail.

Following this, the differential stress was increased at an effective confining pressure of 3500 psi and sample was failed triaxially. Sample failed with a single fracture running from one end of the sample to approximately the middle of the sample. Angle of friction as measured directly from the sample was found to be 41^{o} (Figure 69 below).

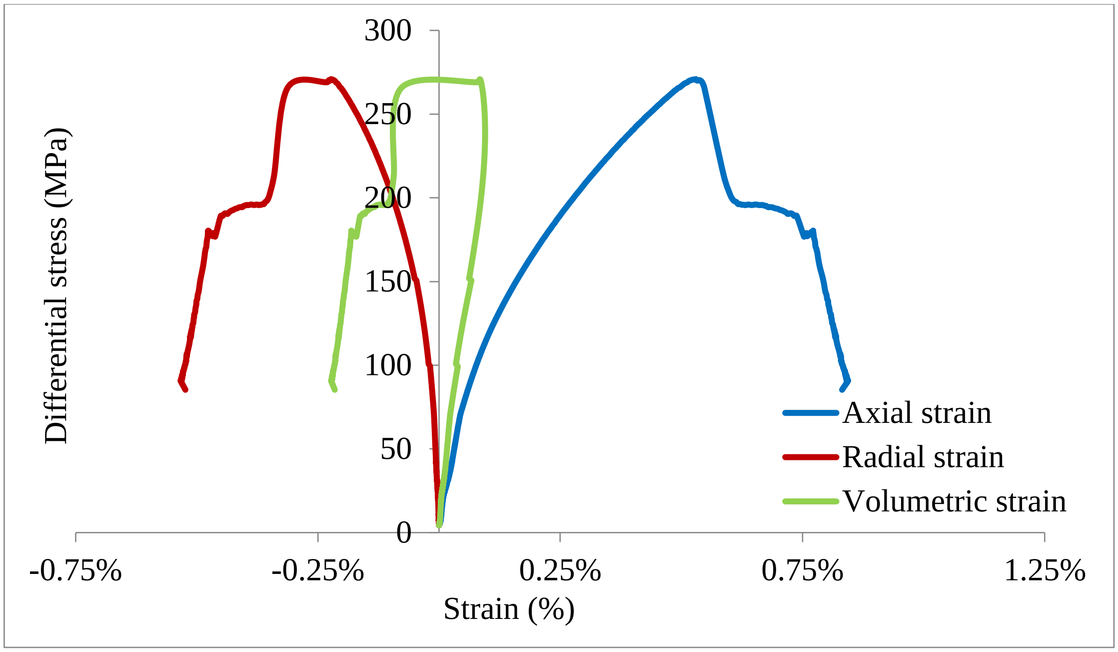

Figure 68: Stress strain plot showing axial, radial and volumetric strain.

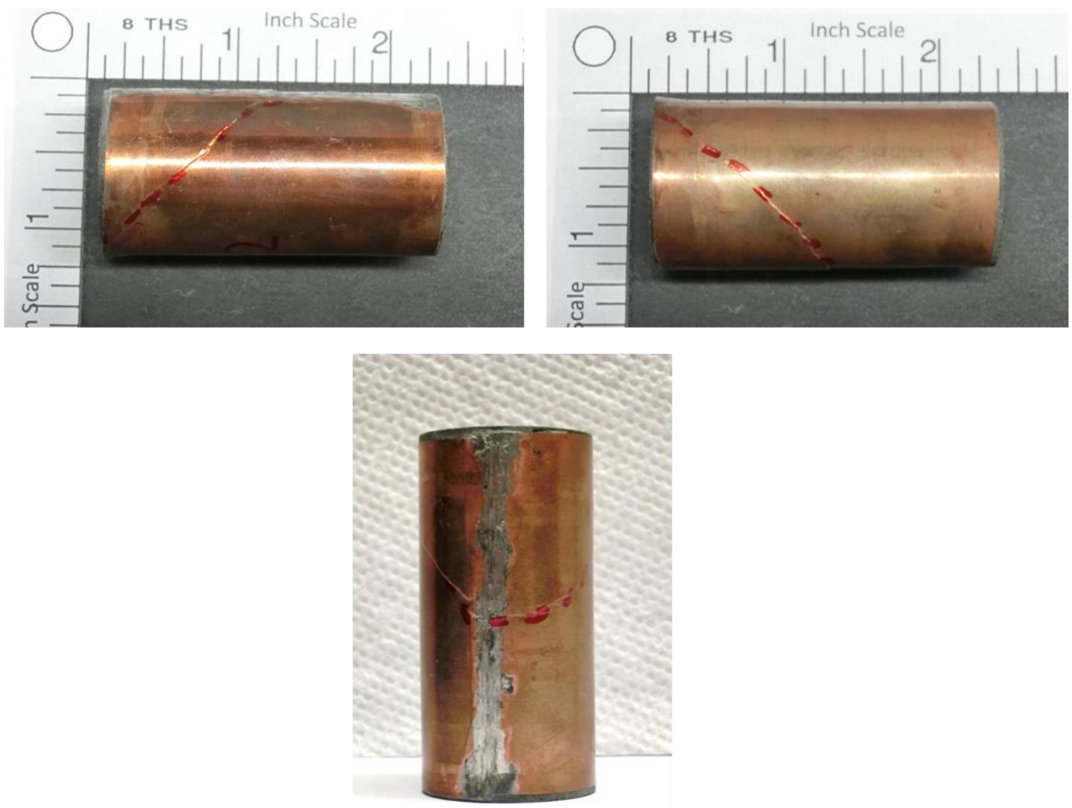

Figure 69: Post-test pictures of sample OXY-72-3-3861.5-V2 showing the fracture formed after failure (red dotted). Sample has been kept in copper jacket to preserve it. Angle of fracture is 32^{O} with respect to the vertical.

Sample GEO-N2-3858.5-H1

This sample was subjected to triaxial –injection test with permeability and AE monitoring. The primary objective was same as previous samples.

Sample was tested with a confining pressure of 4570 psi with a pore pressure of 1535 psi, making the effective confining pressure as 3035 psi. A pressure differential of 70 psi was applied across the sample for gas to be able to flow from top to bottom of sample for permeability measurements. Permeability measurements were carried out continuously (see chapter four for detailed procedure) throughout the test with readings taken at few seconds' intervals.

Stress Strain plot observations:

Sample failed in a ductile mode which is clearly seen in the shape of the stress strain plot as well as the actual picture of the sample after testing (Figure 70). The deviatoric stress versus strain plot (radial or axial) doesn't clearly show the peak strength due to highly ductile nature of the failure. It should be noted that the sample may have failed in ductile mode due to high effective confining pressure applied across the sample. Its original depth is 3858 feet where the horizontal stress may be far less, approximately 1300 psi (Assuming a normal faulting regime in all cases with a vertical stress gradient of 1.1 psi/ft and a horizontal stress 1/3rd of that value).

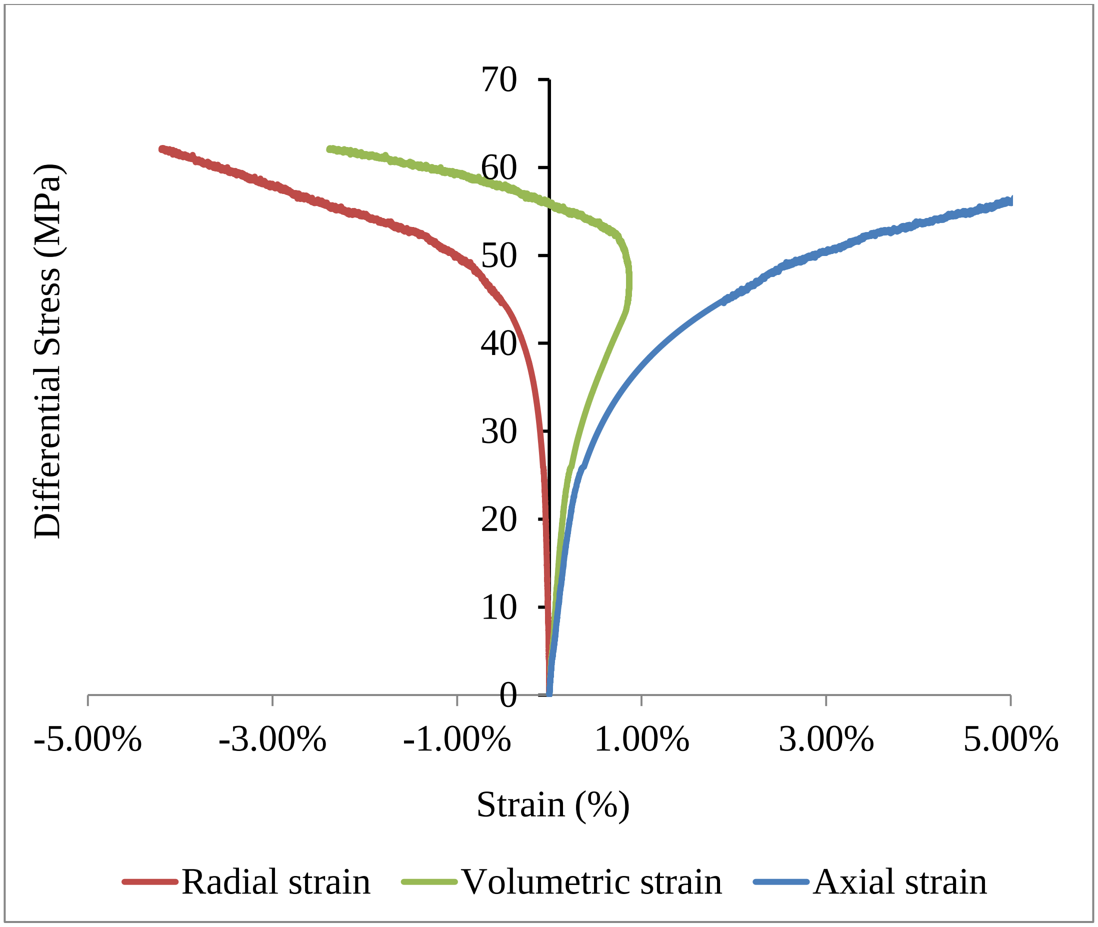

Figure 70: Stress vs. Strain Plot of Loading Stage for the GEO-N2-3858.5-H1 sample. A highly ductile response can be seen.

Figure 71: Pictures of sample GEO-N2-3858.5-H1 after test – picture shows the ductile failure mode (no clear fracture; center bulging out). Final length of sample was 39 mm, reduced significantly from the initial 46mm.

GEO-N2-4163-H1

The objective of this test was similar to previous tests - to establish a relationship between Stress, strain, Permeability and AE. This sample had a low L/D ratio of 1.6. This sample was tested at a lower confining pressure of 1000 psi. Gas was used as the pore fluid.

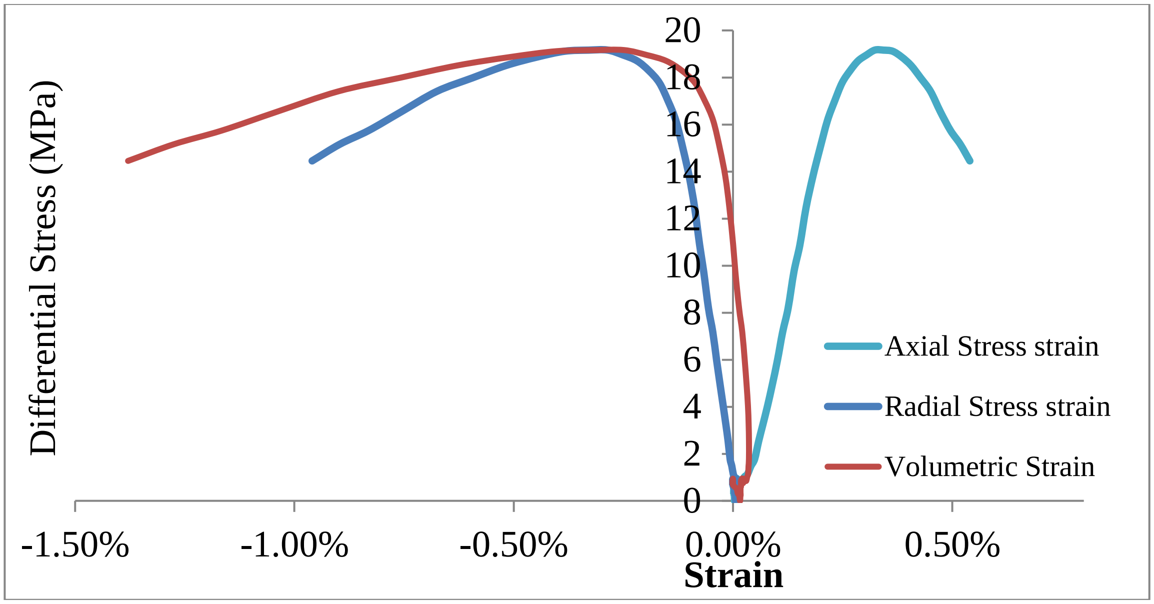

Figure 72: Stress vs. Strain Plot of Loading stage for GEO-N2-4163-H1. A brittle failure was observed.

Figure 73: Pictures of sample after failure showing a single axial fracture running across the sample's length

Results summary and comments – Specimen had no noticeable crack before testing. Sample was tested with a confining pressure of 2500 psi but with a pore pressure (Nitrogen) of 1500 psi with a differential pressure of 100 psi across the sample. It failed with a single noticeable fracture running across the length of the sample at an angle. The fracture intersected the ends at the ends. Plots showing relationship between the three parameters are shown below. The permeability declined while the sample was triaxially compressed. This is in line with other results on Tuff rock specimens. AE wasn't recorded during this test.

GEO-N2-4180-H1

The objective of testing this sample was similar to other samples testing objective - to establish a relationship between Stress, strain, Permeability and AE for sample GEO-N2-4180-H1. An effective confining pressure of 2800 psi was used.

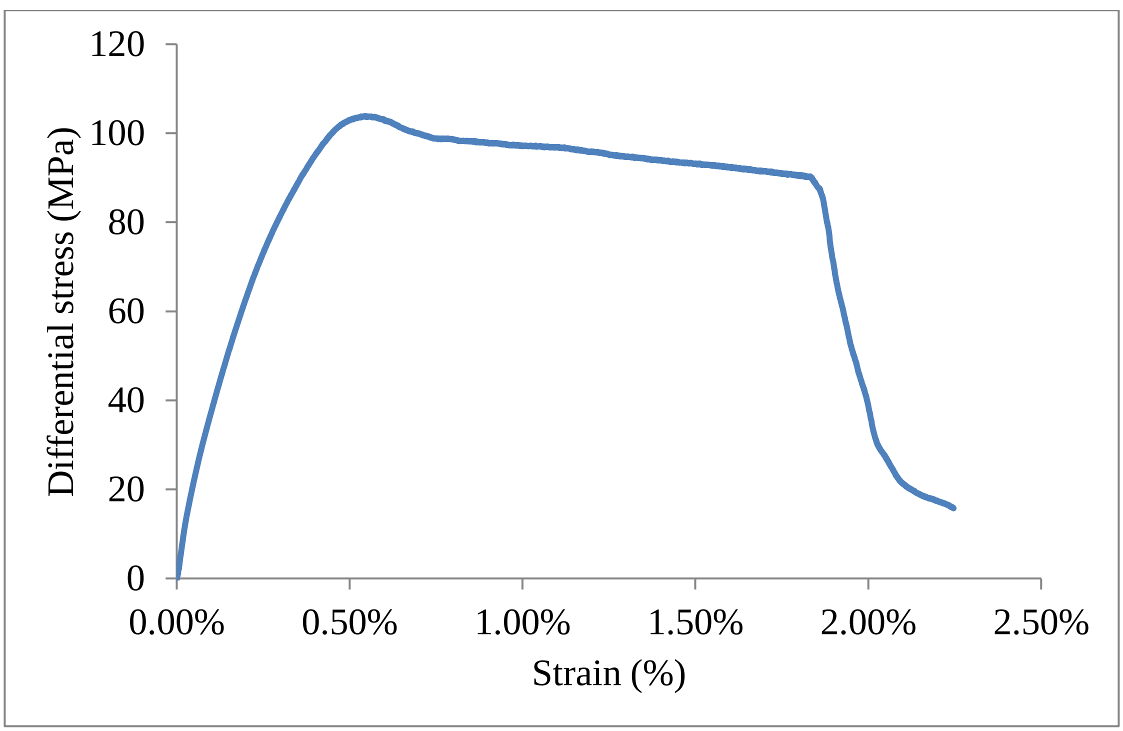

Figure 74: Differential stress vs. strain plot of loading and unloading stage

Results and comments:

Specimen had no noticeable crack before testing. Sample was tested with a confining pressure of 3930 psi but with an average pore pressure of 1100 psi with a differential pressure of 200 psi across the sample. The higher differential pressure was necessitated by the low permeability of the sample. It failed along a single noticeable fracture running from one end of the sample (bottom) to about halfway across the sample, intersecting at the side surface.

Table 14: Summary of triaxial testing on the cored samples from GEO-N2 and the Oxy 72-03 well

	Test Conducted	Temperature of test (°C)	Static Young's modulus	Static Poisson's ratio	Peak strength (MPa)	Dynamic Young's modulus	Dynamic Poisson's ratio	Coefficient of thermal expansion
OXY-72-3-3861.5-V2	Triaxial-injection, Triaxial	23	51.7	0.24	270.9	70.11	0.27	-
GEO-N2-3858.5-H1	Triaxial-injection	23	8.43	0.19	44	-	-	-
GEO-N2-4361-V2	Triaxial-injection	80	37.83	0.29	169.9	61.49	0.17	5.85×10^{-6}
GEO-N2-4361-V3	Triaxial-injection, Triaxial	90	41.23	0.22	167.1	48.56	0.24	6.21×10^{-6}
GEO-N2-4163-H1	Triaxial	23	9.13	0.4	19.16	19.94	-	-
GEO-N2-4180-H1	Triaxial-injection	23	27.86	-	103.85	-	-	-

Table 15: Comparison of static and dynamic Young's modulus for all the samples at 3000 psi confining pressure (both static and dynamic).

Plug	Static Young's modulus	Static Poisson's ratio	Dynamic Young's modulus	Dynamic Poisson's ratio
OXY-72-3-3861.5-V2	51.7	0.24	70.11	0.27
GEO-N2-3858.5-H1	8.43	0.19	11.56*	0.22*
GEO-N2-4361-V2	37.83	0.29	61.49	0.17
GEO-N2-4361-V3	41.23	0.22	48.56	0.24
GEO-N2-4163-H1	9.13	0.40	19.94	-
GEO-N2-4180-H1	27.86	-	-	-

Note: Blank values means these were not recorded during testing

* - GEO-N2-3858.5-V1 sample's value as GEO-N2-3858.5-H1's wasn't measured

As can be seen in Table 15, the difference between the static and dynamic Young's modulus is 18%-100% with dynamic values being always higher. When compared with the Poisson's ratio, the differences reduce with an average difference of 7%, no fixed trend being there between which one was higher/lower.

Correlation of porosity with triaxial test results and velocity results

Porosity was found to be one parameter with which several other calculated or measured parameters correlated very well. Following five figures show this:

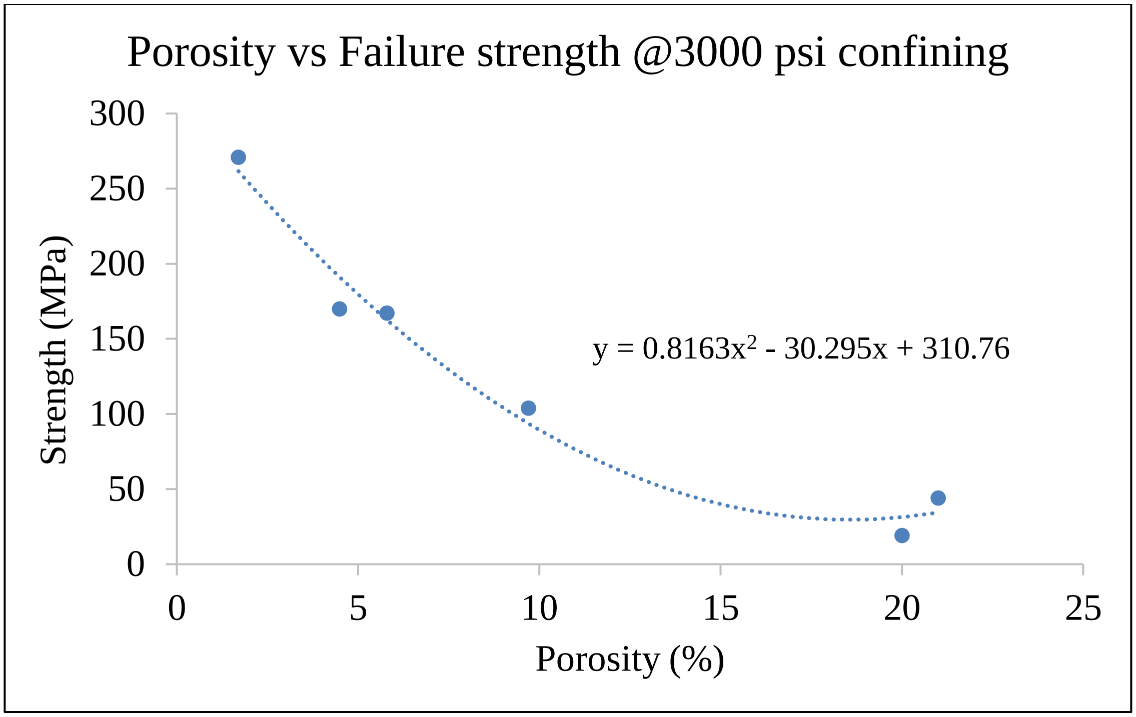

Figure 75: Correlation of triaxial failure strength with porosity for the group 2, cored tuff samples. A good correlation can be observed with strength declining with increasing porosity. The correlation coefficient (r^2) declines from 97% to 87% in case a linear correlation is used.

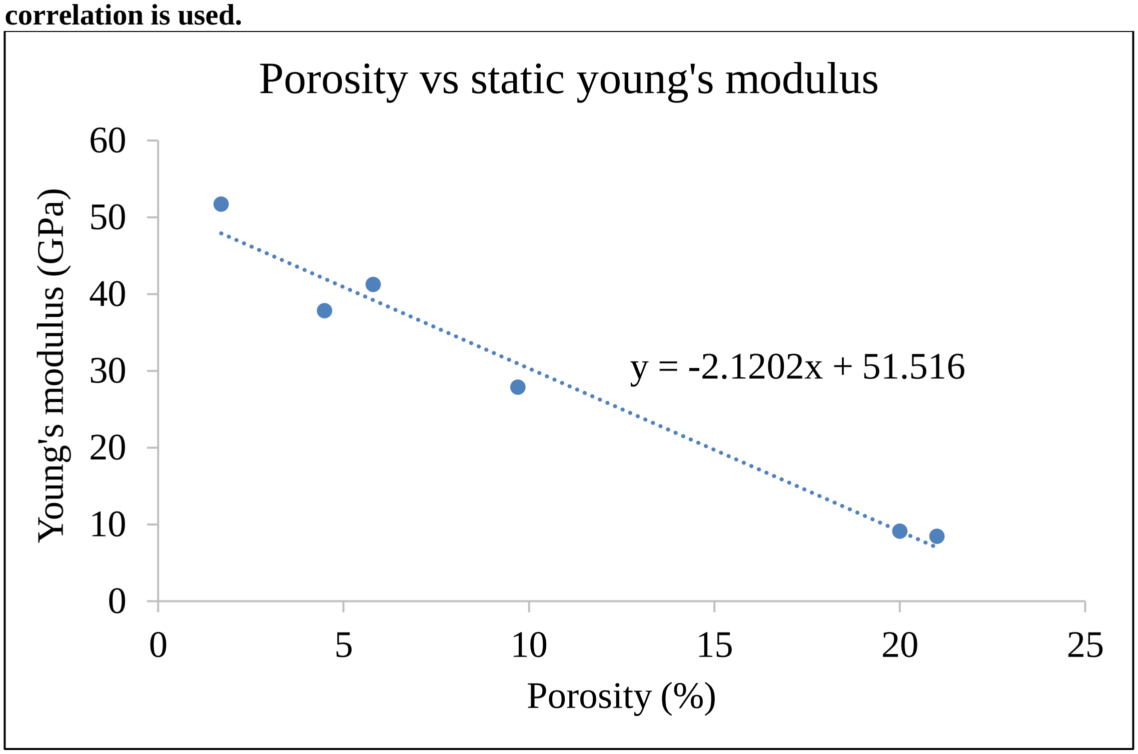

Figure 76: Correlation of static young's modulus strength with porosity for the group 2, cored tuff samples. A good correlation can be observed with the modulus declining with increasing porosity.

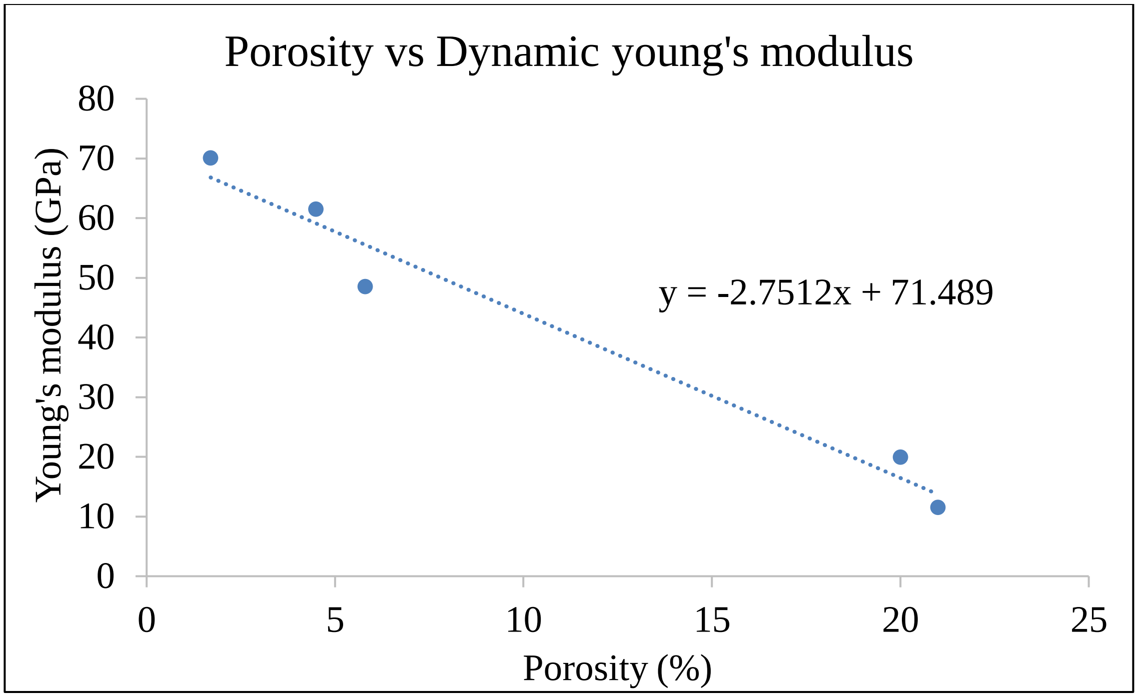

Figure 77: **Correlation of dynamic young's modulus strength with porosity for the group 2, cored tuff samples. A good correlation can be observed with modulus declining with increasing porosity.**

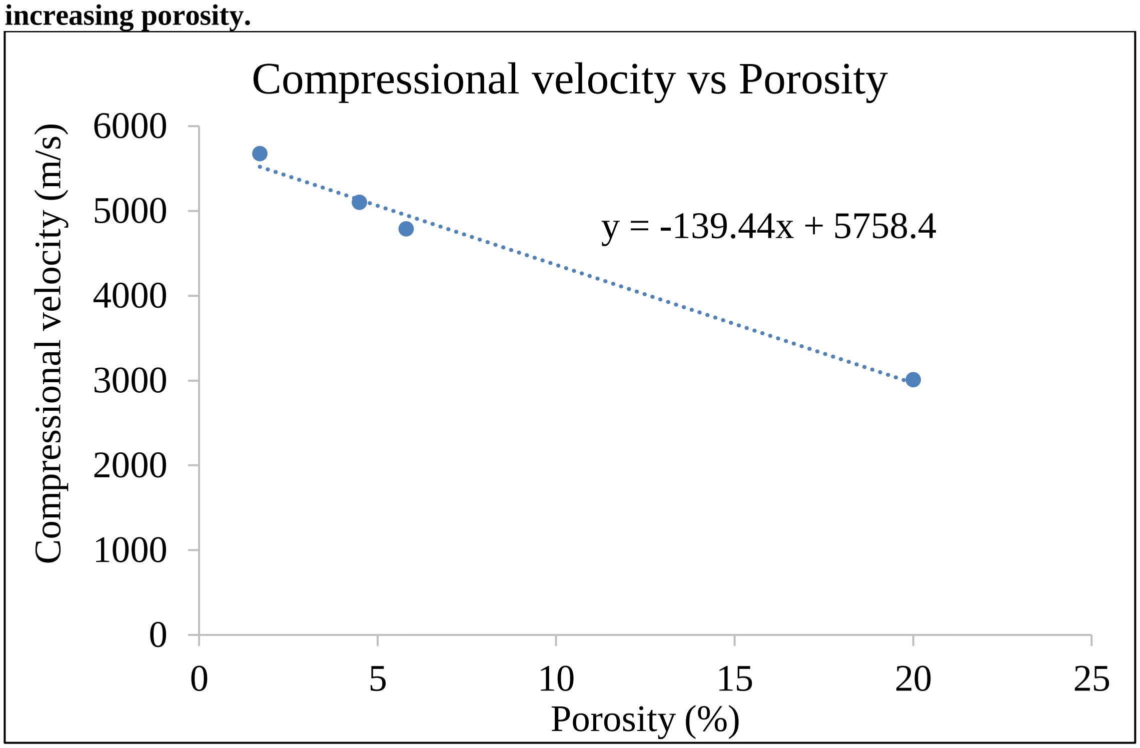

Figure 78: **Correlation of compressional velocity with porosity for the group 2, cored tuff samples. An excellent correlation can be observed with velocity declining with increasing porosity (as expected).**

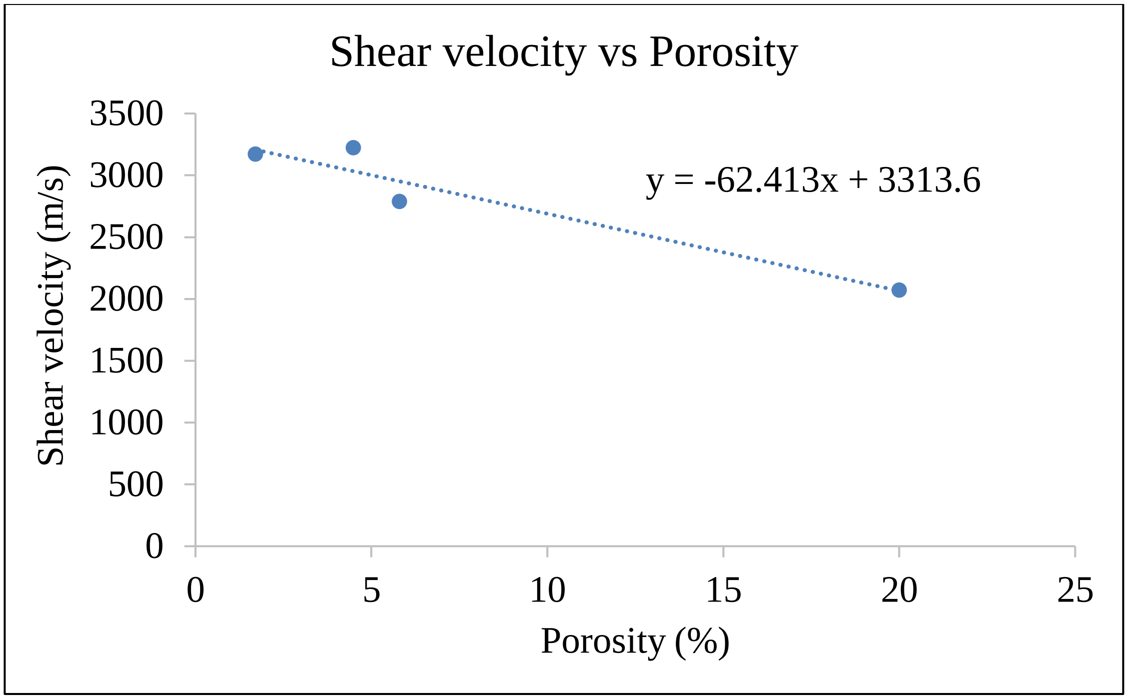

Figure 79: Correlation of shear velocity with porosity for the group 2, cored tuff samples. A good correlation can be observed with velocity declining with increasing porosity (as expected).

CONCLUSIONS

1. A successful application of triaxial-injection technique has been demonstrated in these experiments.

2. All specimens were tested at a confining pressure of ~3000 psi (except sample GEO-N2-4163-H1). Core plugs from 'OXY-72-3-3861.5-V2' and 'GEO-N2-4361-V2' showed a highly brittle response to loading while 'GEO-N2-3858.5-H1' and 'GEO-N2-4180-H1' showed a ductile response.

3. The three parameters – strength, Young's modulus (static and dynamic) and permeability are a function of porosity – figures above demonstrate this clearly.

4. Static Poisson's ratio was on an average less than 0.25. Higher porosity samples (>10%) were always ductile while lower porosity samples were highly brittle.

5. No tensile strength measurements were available on these rocks samples but the test carried out on core from the same well as part of a separate project showed that tensile strengths were on an average about 1/5th to 1/6th of the triaxial strength when strength was measured at 3000 psi confining pressure. If the correlation holds, it would mean that any hydraulic fracturing treatment would require considerably high injection pressure for 'OXY-72-3-3861.5-V2' and 'GEO-N2-4361-V2' core sections (>20 MPa), tensile strengths for 'GEO-N2-4163-H1' and 'GEO-N2-3858.5-H1' would be much lower (<10 MPa) and for 'E' would be average (10-20 MPa).

6. In terms of compressional and shear velocities, compressional velocities showed a very wide range from 3000-5700 m/s while shear velocities also ranged from 2100-3100 m/s with a Vp/Vs ratio average of 1.63. Velocities were a strong function of porosity of the sample.

7. No significant effect of heat was observed on these rocks in terms of strength or elastic parameters. This could be probably due to the temperature being too low for these parameters to be affected (need >350 Celsius). Coefficients of expansion have been recorded and provided in Table 14.

BARNETT SHALE TEST

A single one inch diameter sample Barnett shale sample was tested as part of this work to understand correlation between stress, strain, permeability and Acoustic emissions. Figure 80 shows the stress-strain plot for this sample. The sample was tested at a confining pressure of 1500 psi (Sample's depth was 4000 ft, so assumed horizontal stress as 1/3rd of vertical stress@ 1 psi/ft).

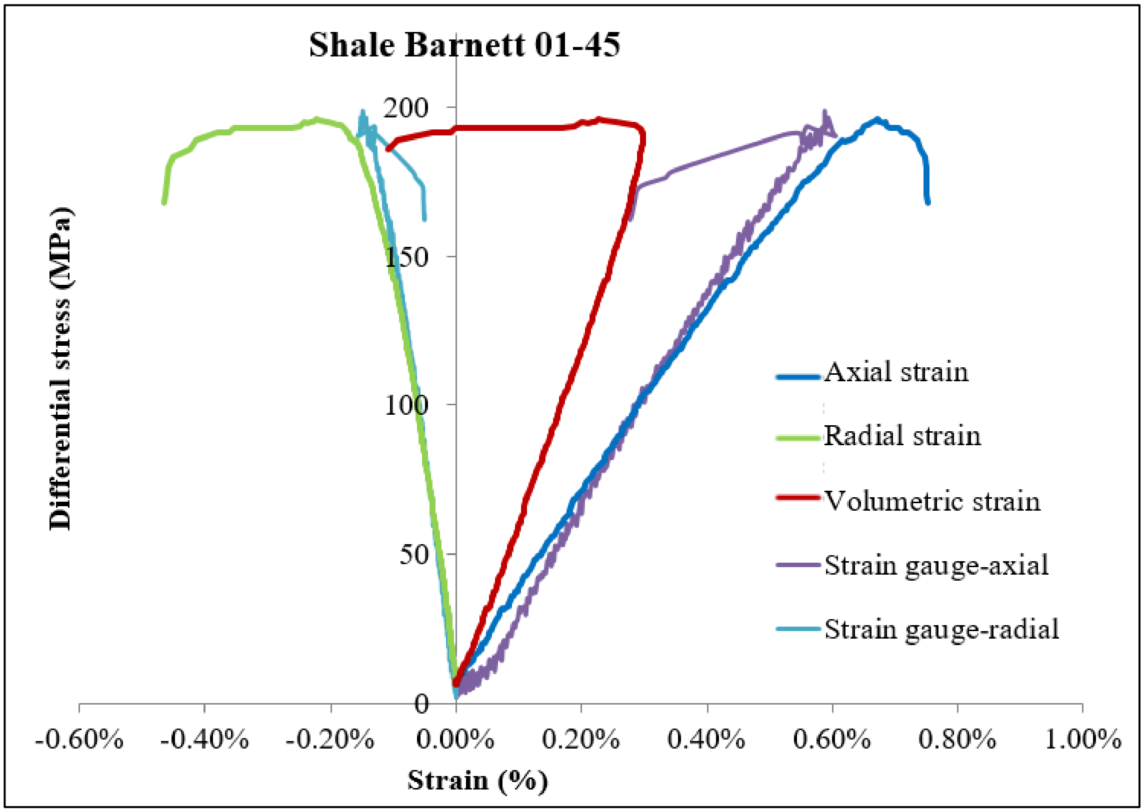

Figure 80:Stress strain plot for the Barnett Shale sample 01-45 showing differential stress and strains (axial, radial and volumetric). Sample was failed by triaxial compression.

Table 16: Results from triaxial testing of Barnett Shale sample 01-45

Parameters	**Value**
Maximum stress at failure	198.9 MPa
Young's modulus	32.48 GPa
Poisson's ratio	0.21
Maximum strain at failure (axial)	0.90 %

Sample failed with a fracture running half-way across the sample. Overall it demonstrated a higher strength than conventional shale samples.

CHAPTER 4: PERMEABILITY ALTERATION DUE TO TRIAXIAL TESTING

Introduction

The AP-608 machine by Core test systems was used for measuring the porosity of the samples before triaxial testing. The Porosity was measured using Boyle's law technique by Helium expansion. Boyle's law states that the pressure (P) of any ideal gas multiplied by its volume (V) will give a constant value (at a constant temperature). Boyle's law as related to core analysis, refers to the ability to determine an unknown volume by expanding a gas of a known pressure and temperature condition into a void space (core) of known volume and using the resulting pressure to calculate the unknown volume. Therefore, by knowing P1, P2 and V2, V1 can be calculated. Helium is injected at both the ends of the core sample to achieve equilibrium faster.

Permeability measurements were made in two steps – first using the standard unsteady state pressure decay technique in the AP-608 system and later using steady state when the sample was transferred to the triaxial cell. Klinkenberg corrections were applied to correct for slippage. After the initial measurement of permeability was done, the sample was then transferred to the triaxial cell and steady state permeability technique was used for measuring permeability (real time or at fixed intervals). The triaxial set up with permeability measurement is shown in a schematic in Figure 15. To achieve steady state, two precision syringe pumps (Figure 81) were used to maintain a small pressure differential ranging from 10 psi to 100 psi across the sample under a given confining pressure.

Nitrogen gas was used as the pore fluid in most of these experiments. One way to avoid the need for slip (Klinkenberg) corrections is to use higher pore pressure (>2000 psi) which results into lower fluid velocities within the sample reducing slippage effects (Mathur et al, 2016). This method was used for all permeability measurements described here. The confining pressure must be adjusted to maintain the required effective confining pressure during the test. Then, sample is left for achieving steady state – this is achieved when the flow rate in both the upstream and downstream pumps becomes approximately the same (example shown in Figure 82). This confirms uniformity of pore pressure within the sample. The time period to achieve steady state varies – for rocks of nano-darcy permeability, 6-12 hours are needed (if using gas only, liquids can take a week or more).

Figure 81: TELEDYNE ISCO Syringe Pump and Controller

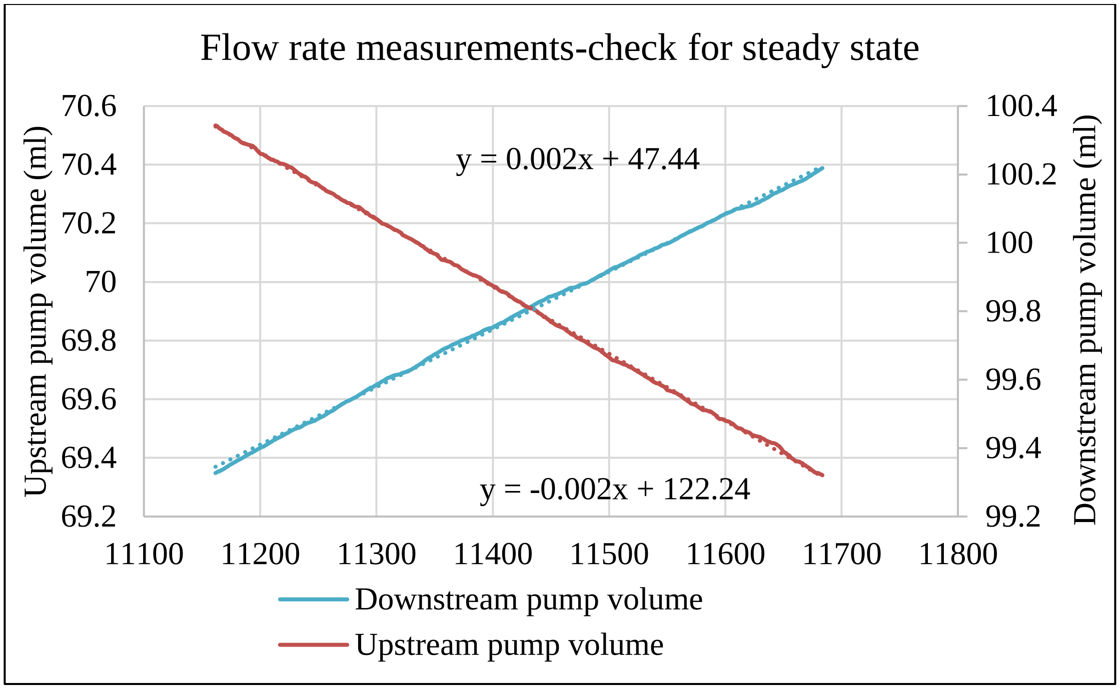

Figure 82: Plot shows example of steady state equilibrium between upstream and downstream pumps.

For all the samples tested for the purpose of this report, Nitrogen gas was used unless otherwise stated.

The permeability of rocks is controlled by a number of factors and can therefore can range from mD to nD range – the various processes that control these for igneous rocks are described by Sruoga et al (2004) and Dobson et. al. (2003).

In this section, results are provided individually for all the samples. In the end, an overall analysis is presented.

BEREA SANDSTONE SAMPLES

The porosity was measured on all samples before testing and found to be 18-20%. The triaxial test results of the Berea Sandstone samples tested as part of this work have already been provided in chapter 3. Three samples – referred to as samples A, B and C were tested at three different confining pressures. Permeability was tested individually on all samples after coring and is reported here for each sample. These measurements were continuously carried out on these samples – meaning real time measurements were made as the triaxial testing was being carried out. A detailed analysis of results is provided with each figure below.

1. Test1: Effective confining Pressure 1000 psi (Sample A).

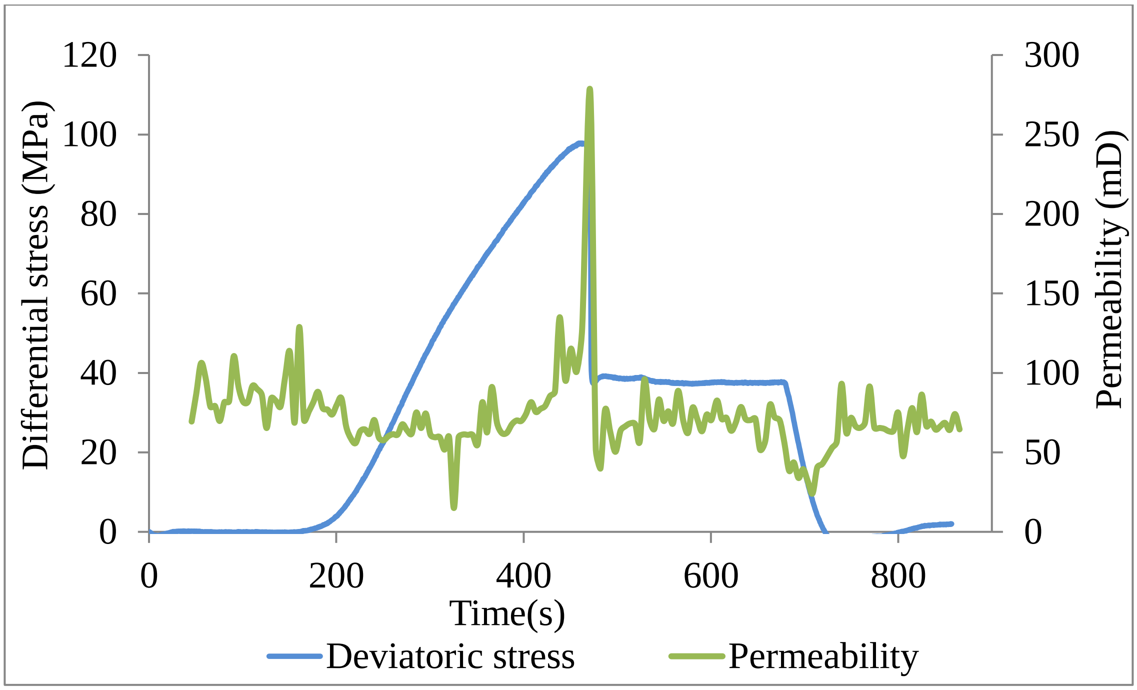

Figure 83: Plot showing relationship between differential stress and permeability for Berea sandstone for an effective confining pressure of 1000 psi. Description is provided below.

Result comments – Specimen had no noticeable crack before testing. Sample was tested with a confining pressure of 1300 psi but with a pore pressure of 275 psi with a differential pressure of 150 psi across the sample with mineral oil as the pore fluid. It failed with a single noticeable fracture running across the length at an angle to the axis of the sample (

Figure 18). Stress strain plots and after failure pictures have already been shown in chapter three. The fracture did not fully intersect the ends.

As can be seen from Figure 83, overall the complete plot shows a strong correlation between loading and permeability. It decreases initially but as the sample reaches close to failure, the permeability shows a slight increase. This could be due to initiation of micro fracturing and breaking of bonds between grains as sample approaches failure. When the fracture is formed, permeability shows a large increase which lasts for a small time as the fracture closes due to the confining pressure.

This behavior can be better analyzed by using the volumetric strain versus permeability plot a shown in Figure 84. This same figure has been divided into three zones to better understand rock behavior.

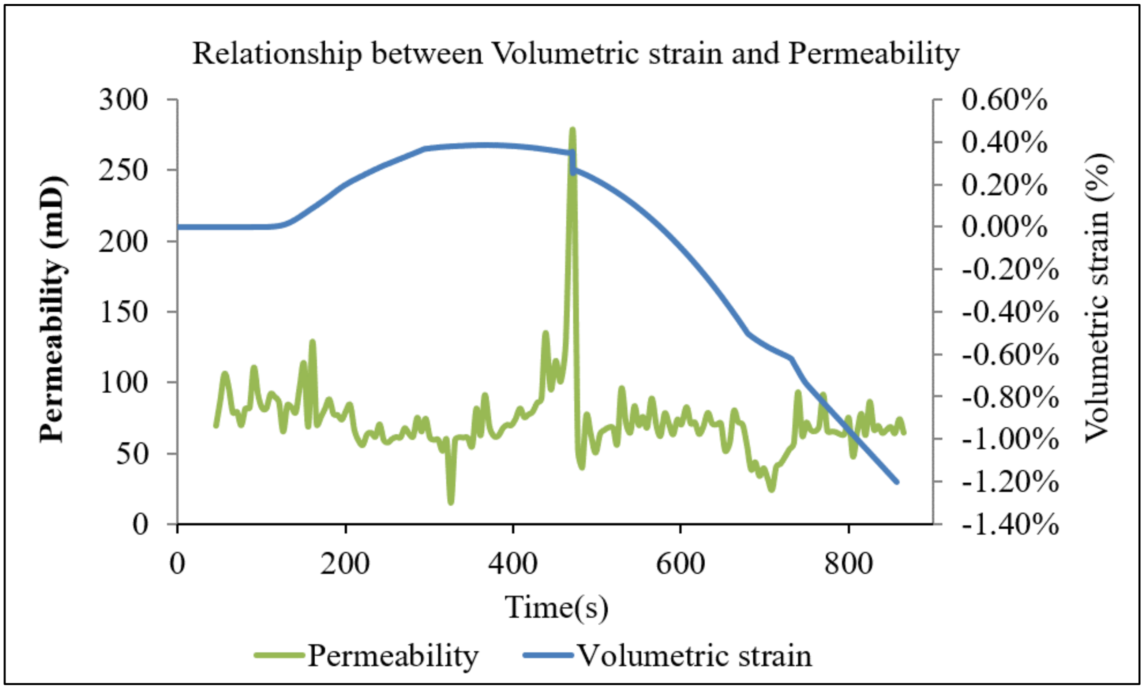

Figure 84: Volumetric strain versus permeability relationship for Berea sandstone - GEO-N2-4300-I1.

in Figure 85.

a) Zone one represents the area where volumetric strain becomes more positive –

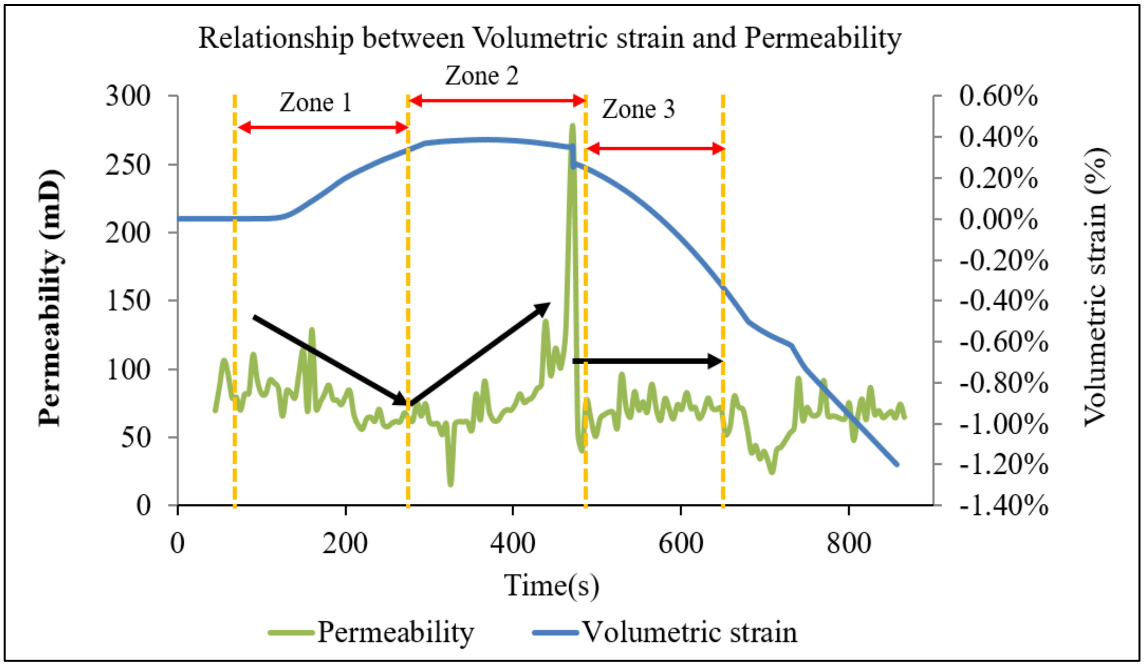

Figure 85: Volumetric strain vs Permeability plot divided into three zones for analyzing behavior of triaxial fracturing on Berea sandstone sample-A.

Overall sample volume decreases in this zone –hence volumetric strain becomes positive. As a result, sample permeability steadily decreases as pore throats close or come closer to each other reducing porosity – permeability reduces as porosity reduces.

b) Zone two represents the area where volumetric strain starts stabilizing and reverses direction indicating sample volume starting to become overall higher than previously. This starts happening close to failure. As can be seen in the next chapter, AE starts picking up in this zone which indicates high micro-cracking starts to occur which can result in micro fractures which enhance sample permeability. As sample fails, a very high value of permeability is reached instantaneously but quickly falls down to initial values seen at the beginning of zone two.

c) In zone three, with continued compression of sample (which actually just causes sliding on the large sample fracture), permeability remains fairly constant. This can be easily explained as the sample volume increases by a large margin after failure as can be seen from the volumetric strain plot.

2. Test Sample B: Effective confining Pressure of 2500 psi.

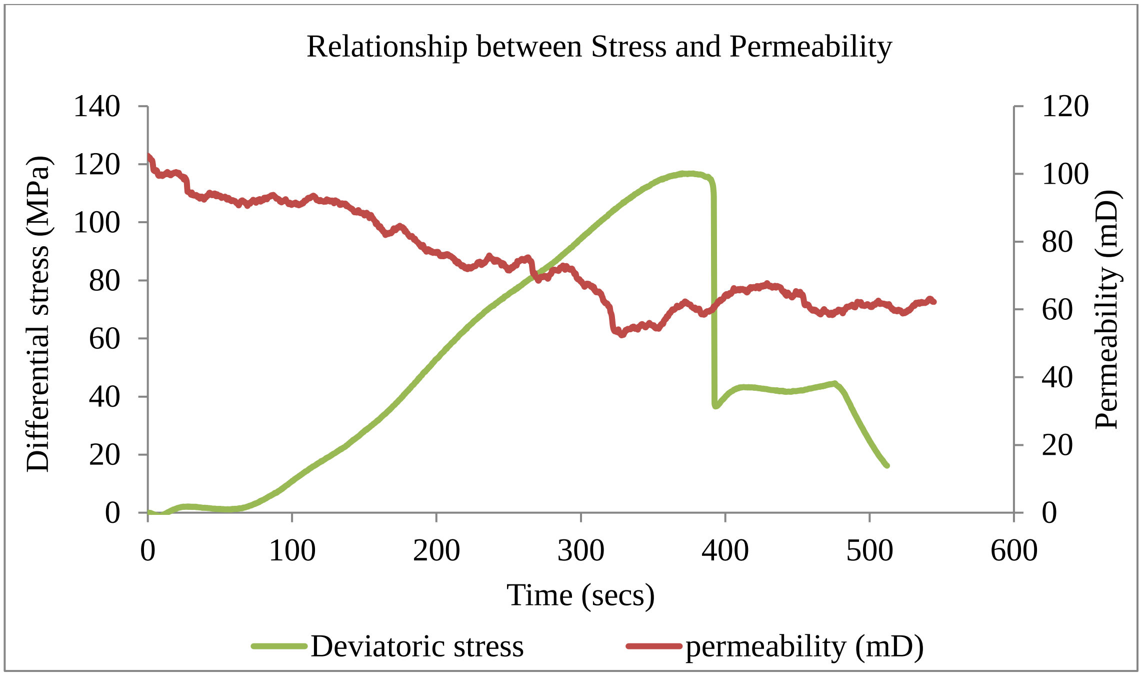

Figure 86: Differential stress versus Permeability for Berea sandstone sample-B.

Specimen had no noticeable crack before testing (Figure 5). Sample was tested with a confining pressure of 3500 psi but with a pore pressure of 1104 psi (Nitrogen) with a small differential pressure of 10 psi across the sample. It failed with a single noticeable fracture running across the length at an angle to the axis of the sample (

Figure 18). The fracture did not intersect the ends fully.

The results show that permeability of the sample reduced with increasing axial load but shows an increasing trend from the point when the sample is near failure (similar to sample-A). The sample's permeability doesn't get affected much after failure; it stays stable in the sliding phase (same as sample A) and shows a slight increase after load is completely removed from the sample-this stage wasn't included in results for sample A.

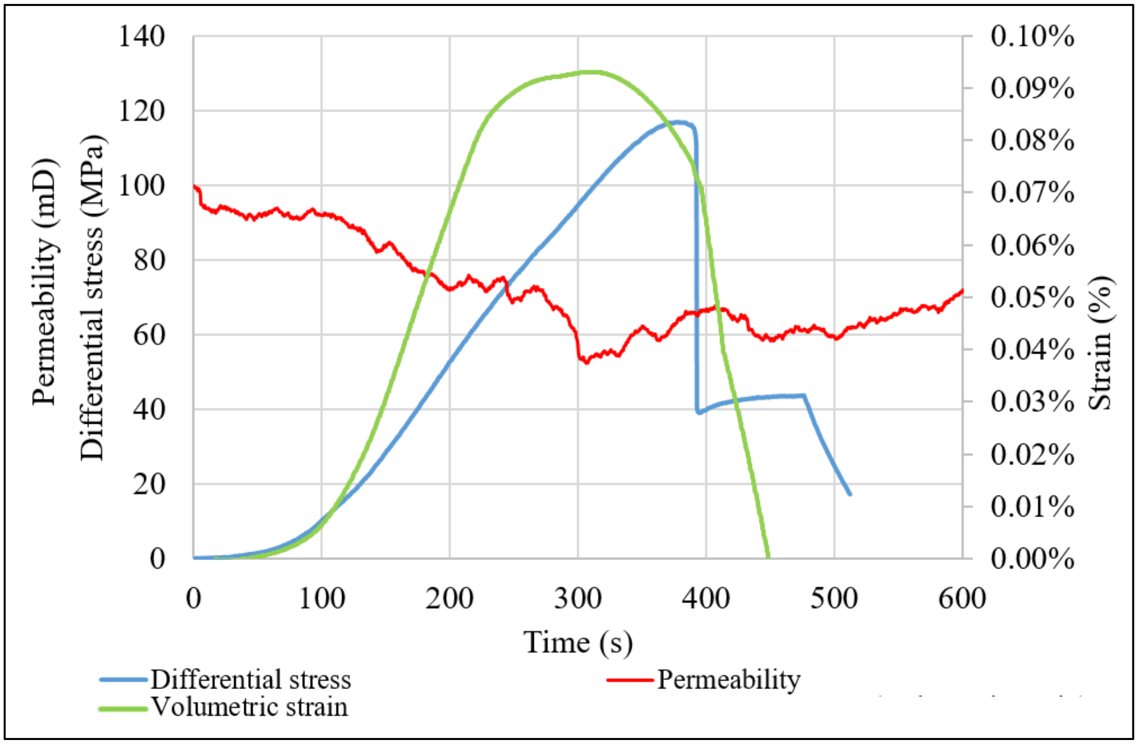

Figure 87: Figure showing correlation of stress, permeability and volumetric strain for Berea Sandstone sample-B.

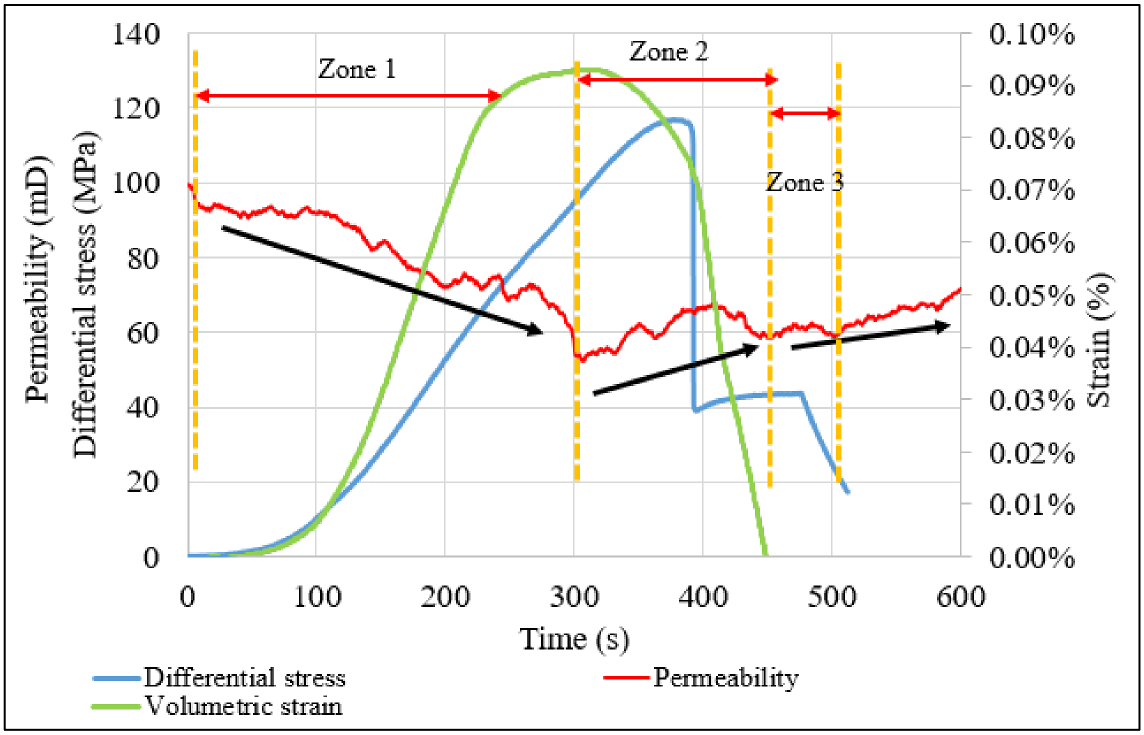

Figure 88: Volumetric strain and stress vs Permeability plot divided into three zones for analyzing behaviour of triaxial fracturing on Berea sandstone sample-B.

The sample's results have been divided into three zones as was done for sample A. The same analysis can be used to explain the behavior here. One aspect that is different here is that overall sample's permeability declined by almost 40% even after fracturing. For sample A, the permeability was more or less restored after fracturing (it didn't increase though even though a large fracture was formed). This shows the effect of higher confining pressure – it closes the fracture more effectively keeping the permeability value lower in the process.

3. Berea Sandstone – Sample C.

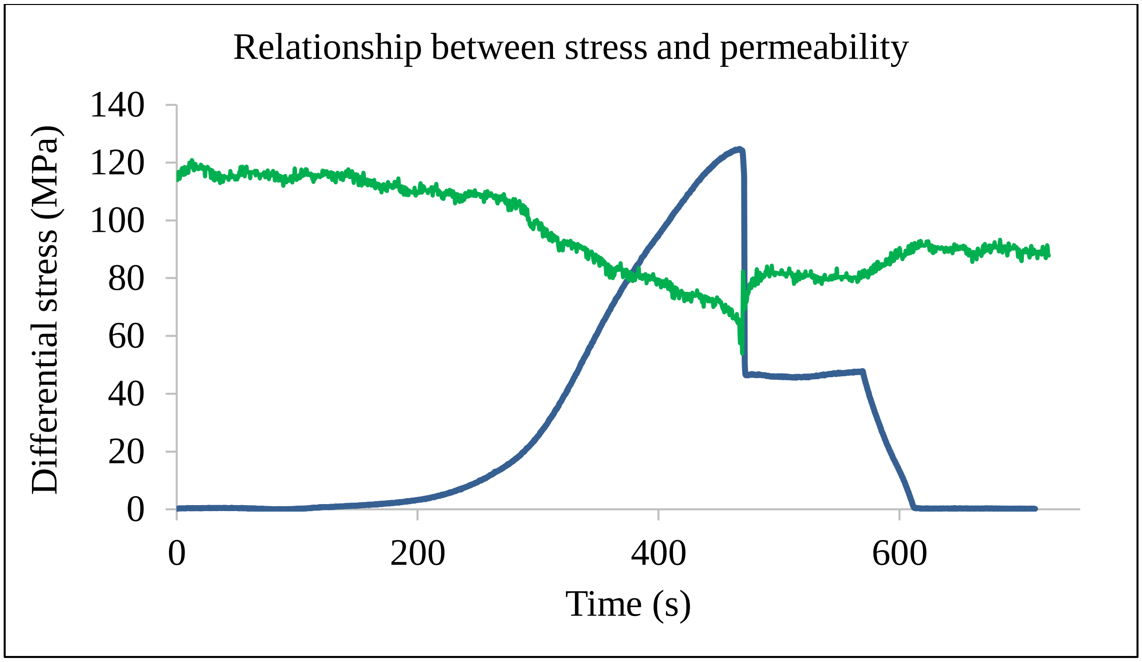

Figure 89: Plot showing relationship between stress and permeability for Berea sandstone sample-C.

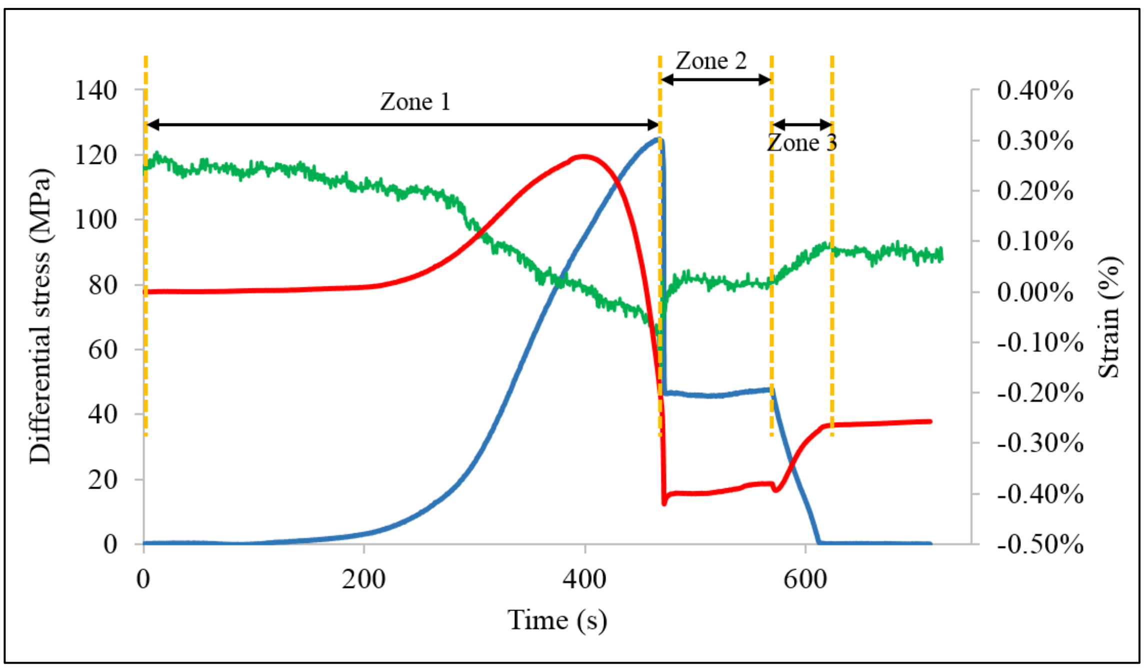

Figure 90: Volumetric strain and stress vs Permeability plot divided into three zones for analyzing behavior of triaxial fracturing on Berea sandstone sample-C.

The effective confining pressure was 3250 psi for this case. A similar pattern can be seen like the previous two samples although with two subtle differences. The permeability doesn't start stabilizing or increasing till the volumetric strain has gone beyond its initial value (at the beginning of the test). In earlier tests, it started changing once the volumetric strain reversed course from positive towards negative. Also, here in zone three we can see that once sample unloading starts, the permeability starts increasing.

Conclusion for Berea Sandstone – permeability seems to always decline in the loading phase before starting to stabilize and increase somewhat in the region where the volumetric strain becomes negative. After fracture, sample permeability remains stable even with more compression with fracture sliding creating more conductive pathways balancing out the compression of grains. Overall permeability declines during triaxial loading with decline larger in higher confining pressures. The results match those observed by Zhu et al,1997.

CORED ONE INCH PLUGS FROM THE GEO-N2 WELL

Porosity was also measured for these plugs at in-situ conditions of pressure. Table 17 below shows the values for all six samples. For GEO-N2-4180-H1, no data was available, so a different core plug (Sample GEO-N2-4180-H1) separated by just one inch from GEO-N2-4180-H1 in the core section was used.

Table 17: Porosity values at 2800 psi confining pressure before triaxial testing for the core plugs

Sample	Porosity (%)
OXY-72-3-3861.5-V2	1.7

GEO-N2-3858.5-H1	20.87
GEO-N2-4361-V2	0.13
GEO-N2-4361-V3	0.12
GEO-N2-4163-H1	18.41
GEO-N2-4180-H1	19.10

From the values in Table 17, we can see that the samples show a wide variety of porosity with one group (A and C section) with very low porosities (<3%) which is in contrast to the other sections (B, C and E) which have porosity values higher than 15%. A plot of the porosities vs confining pressure is shown below for all the samples.

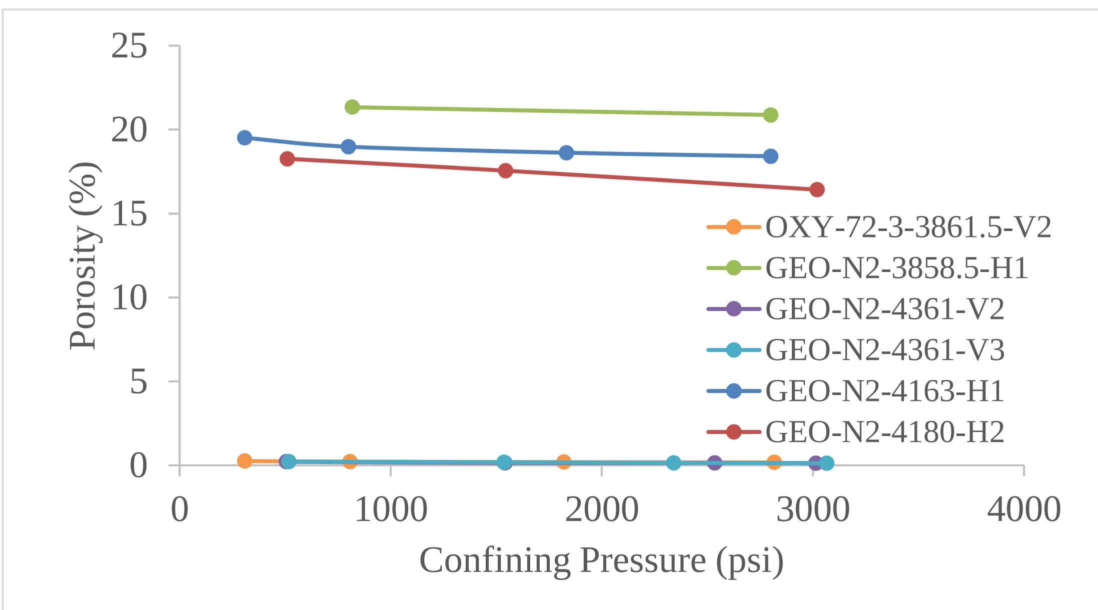

Figure 91: Porosities versus confining pressure data for plugged GEO-N2 and OXY 72-03 well samples

These six samples as described before in chapters 2 and 3 had similar differences in permeability with values varying from nano Darcy (nD) to milli Darcy (mD) ($1mD=10^6$ nD).

After triaxial testing, their permeability values changed – sometimes an increase was seen and sometimes a decrease was observed. For samples, GEO-N2-3858.5-H1, GEO-N2-4180-H1 and GEO-N2-4180-H1 permeability values were in the mD range and the changes in their permeability were measured on a real-time basis during triaxial testing. For the other three samples, permeability was in the nano Darcy range initially and hence real-time measurements could not be carried out. Permeability for these samples were measured at the beginning of the triaxial test and after failure. Observations and conclusions are also provided for each of these three samples below.

1. Sample GEO-N2-3858.5-H1

   Triaxial test plots have already been provided in Figure 70. As could be seen there, samples behave in a highly ductile manner. The effect on permeability due to triaxial compression is shown in Figure 92. The same figure has been divided into five stages in Figure 93 and details explained below.

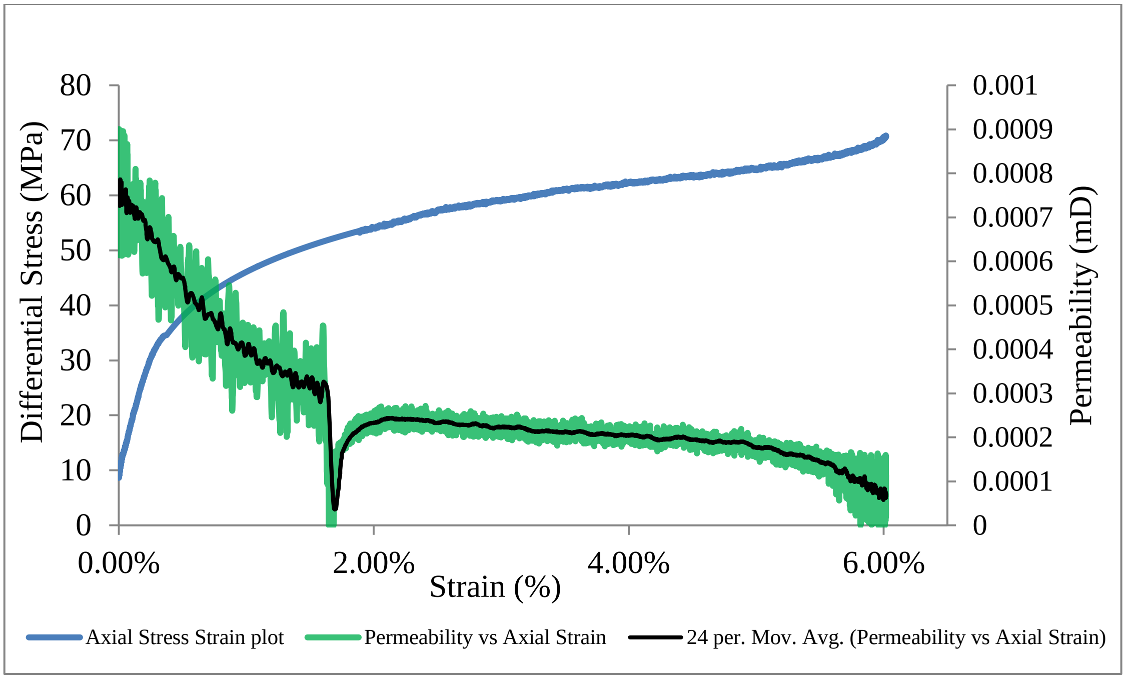

Figure 92: Effect of triaxial loading on Sample GEO-N2-3858.5-H1's permeability

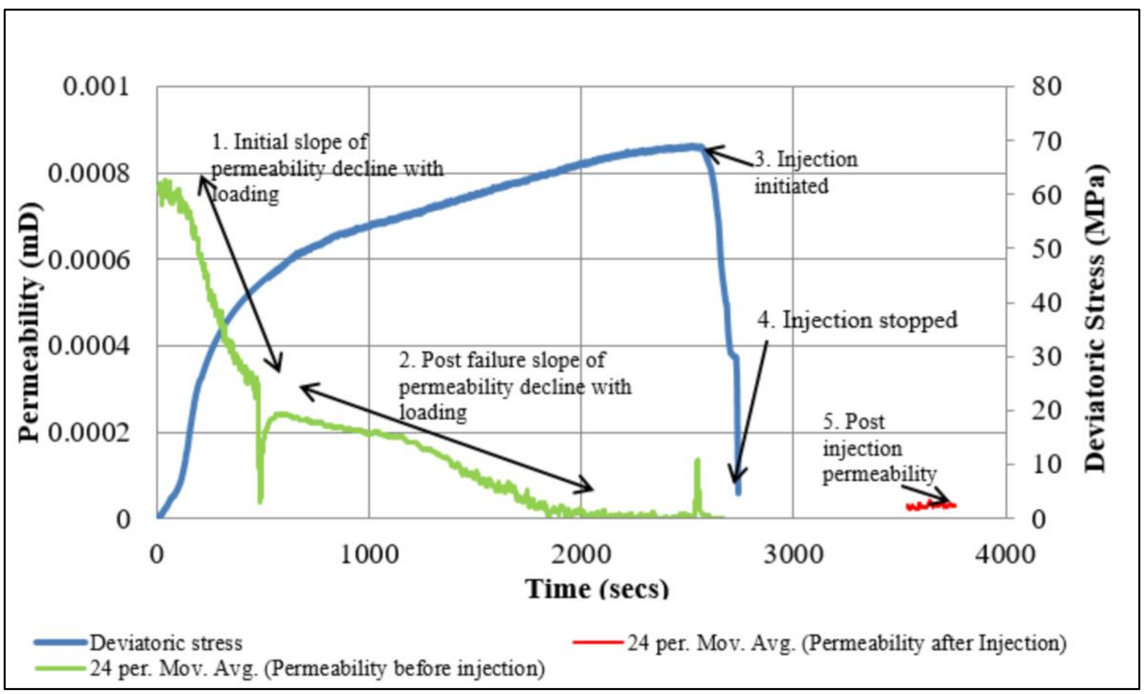

Figure 93: Relationship between differential stress and permeability for the triaxial part of the experiment for sample GEO-N2-3858.5-H1. The plot has been divided into five parts for the ease of explaining underlying phenomena.

The stages shown in Figure 93 are shown below:

1. Stage 1: Triaxial loading at confining pressure of 24.13 MPa (3500 psi) (up to 40 MPa differential stress -right axis). Permeability declines here as pores and some micro cracks close due to application of stress. The stress strain plot starts to concave upwards here. At about 44 MPa the permeability plot shows a sharp change in permeability. No corresponding effect is seen on the stress plot.
2. Stage 2: Sample starts exhibiting ductile behavior with increased loading. In terms of permeability, the slope of 'permeability decline' reduces considerably. This shows that post failure, permeability decline rate reduces considerably even with increased loading. This could be possibly due to combination of two factors – the pore closure reduces permeability while the formation of fractures increases it. Towards the end of this stage we can see that the permeability remains constant- this means that both processes start balancing out each other.
3. Stages 3, 4 and 5: These two stages are representative of injection being conducted on the sample which results in sample's brittle failure. It should be noted that injection had reduced the effective confining pressure from 3000 psi to 700 psi which causes the load bearing capacity of the sample to reduce considerably during this stage (down to 10 MPa from 70 MPa). The fracture permeability was measured here at effective confining pressure of 3000 psi and was found to be slightly higher (4 times) than earlier in stage 4. This is probably due to the increased fracture permeability achieved due to brittle failure.

Overall, we can observe that as the sample is compressed, permeability falls. After a certain strain is reached, we see that permeability decline reduces considerably and reaches a point where continued loading doesn't change sample permeability. However once effective confining pressure is reduced to 700 psi, samples fails with a brittle response. The last stage of triaxial injection results in increase of permeability – this shows that brittle failure will be more useful if it is intended to increase permeability in the reservoir for this rock. This is consistent with findings of Paola et al, 2008 and Zhu et. al. 1997 that brittle failure in granite and sandstone results in permeability enhancement. These results show that high porosity tuff has a similar behavior.

Sample GEO-N2-4180-H1

The porosity of the sample as a function of confining pressure (300 psi to 2800 psi) was measured and found to vary from 19.51%-18.41% and is shown below in Figure 94.

Table 18: Porosity vs confining pressure for GEO-N2-4180-H1

Confining pressure (psi)	Connected Porosity (%)
308	19.51
800	18.98
1832	18.62
2800	18.41

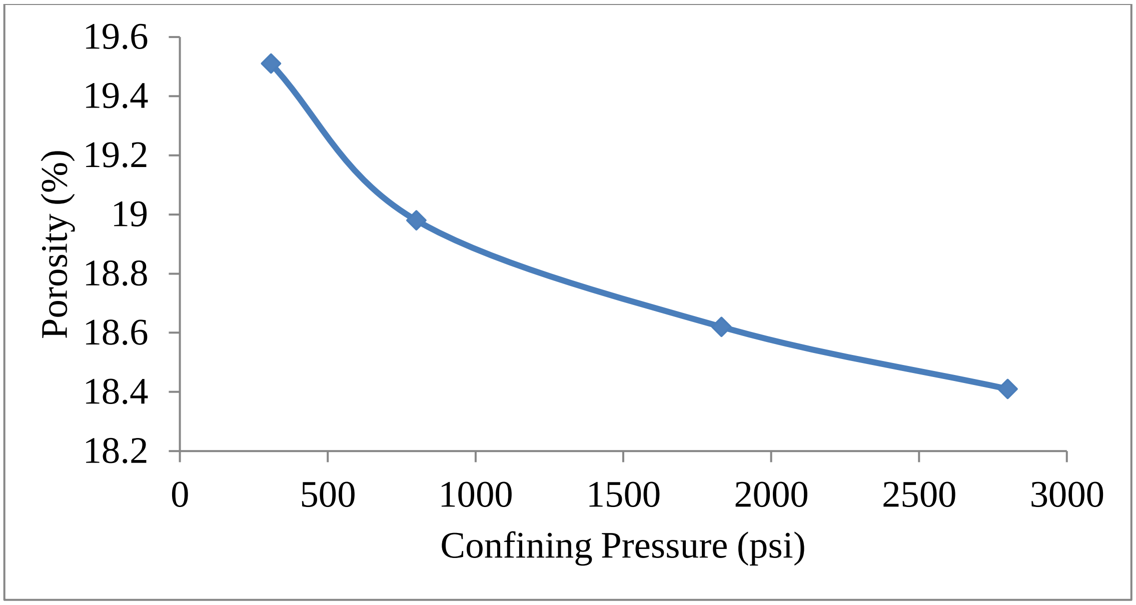

Figure 94: Porosity vs Confining pressure for sample GEO-N2-4180-H1 .

The permeability of the sample as a function of confining pressure (300 psi to 2800 psi) varies from 0.45 mD-0.11 mD and is shown below in tabular format. Note that these are Klinkenberg (slip) corrected values.

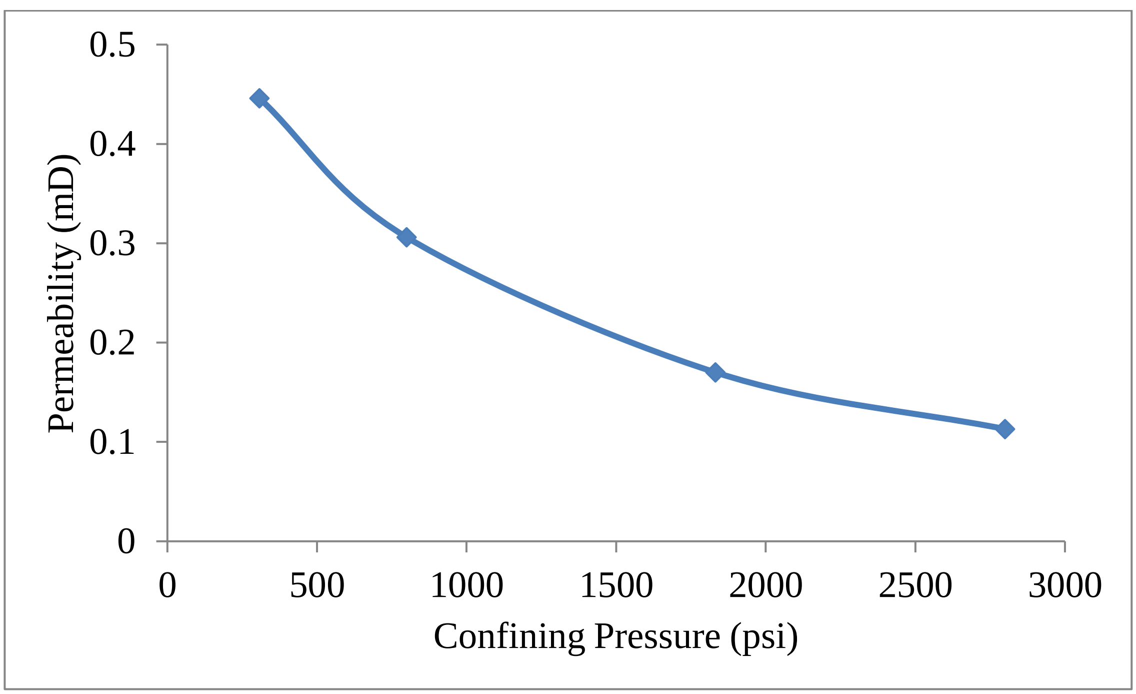

Figure 95: Permeability vs Confining pressure for GEO-N2-4180-H1

Table 19: Permeability vs confining pressure for GEO-N2-4180-H1

Confining pressure (psi)	Permeability (mD)
308	0.446
800	0.306
1832	0.170
2800	0.113

The porosity-permeability variation plot for the sample is shown below:

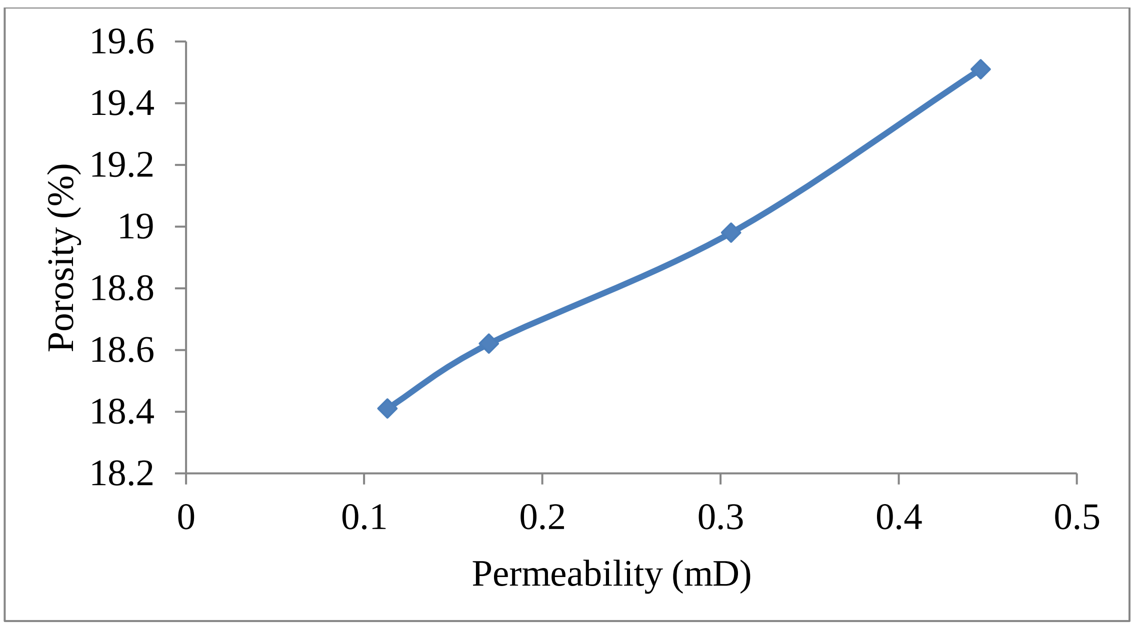

Figure 96: Porosity vs permeability for GEO-N2-4180-H1

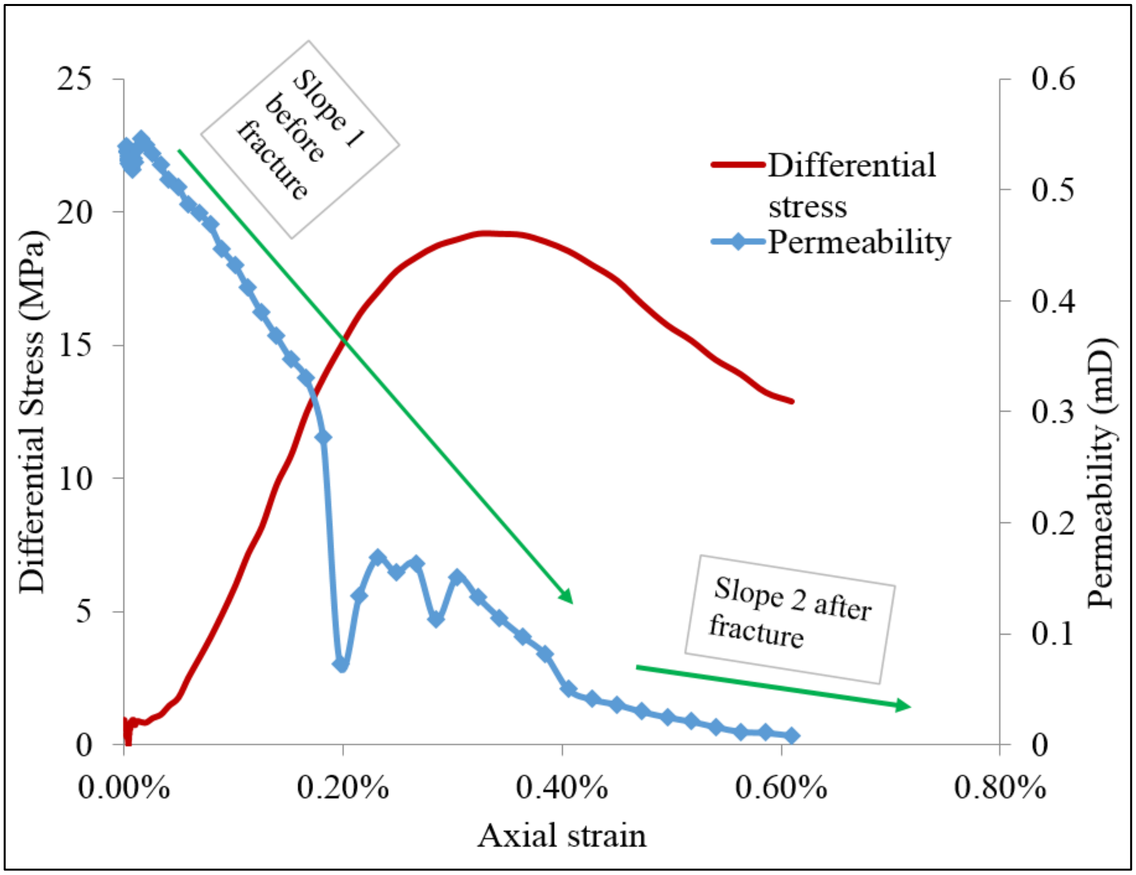

Figure 97: Relationship between Stress, axial strain and Permeability for sample GEO-N2-4180-H1 at an effective confining pressure of 1000 psi.

Specimen had no noticeable crack before testing as shown in Figure 9. The sample was brought to failure in triaxially compression using a confining pressure of 2500 psi and with a pore pressure (Nitrogen) of 1500 psi with a differential pressure of 100 psi across the sample making the effective pressure as 1000 psi. It failed with a single noticeable fracture running across the length of the sample at an angle (Figure 73). The fracture intersected the ends at the ends. Plots showing relationship between the three parameters of stress, permeability and strain is shown in Figure 98. The permeability declined while the sample was triaxially compressed. This is in-line with other results for the high porosity Newberry Tuff specimens (GEO-N2-3858.5-H1 and GEO-N2-4180-H1).

The results show that permeability reduction with increasing axial load has different trend before and after failure. The sample shows a lower decline post fracture with continued loading as compared to pre-failure loading as already been seen in Berea sandstones and in sample GEO-N2-3858.5-H1. This can be attributed to fracture permeability being higher and hence the decline is smaller. Overall, the sample doesn't show clear brittle or ductile failure – although it fails with a single large fracture, the stress capacity after failure doesn't fall by a large margin instantaneously. However, with increasing strain, it starts reducing again.

2. Sample GEO-N2-4180-H1

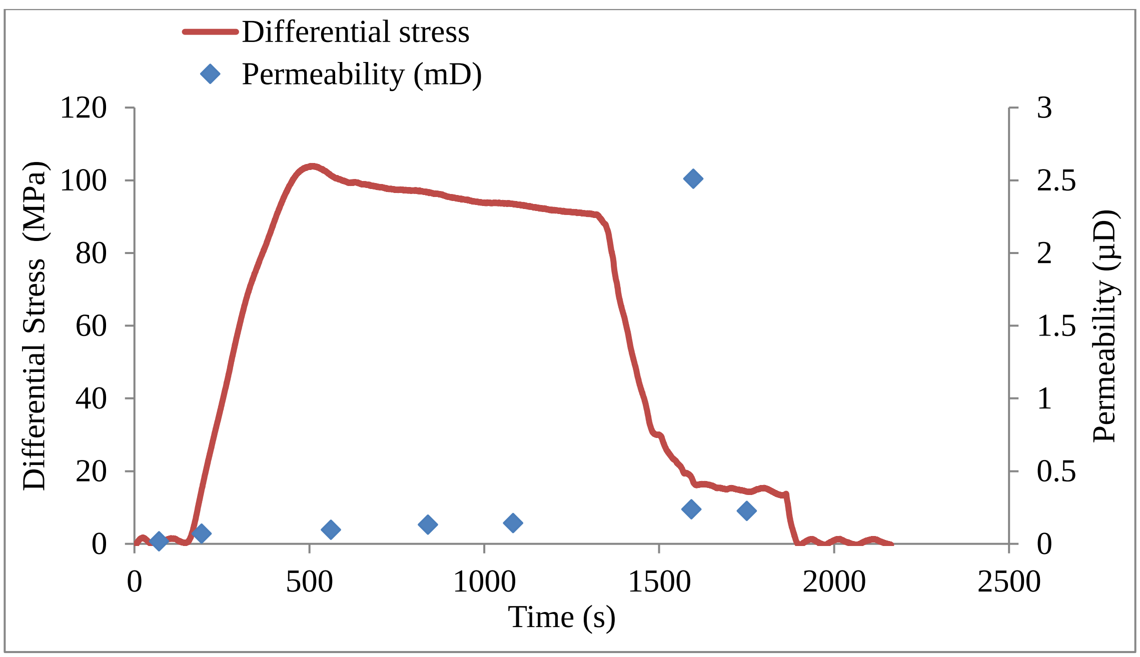

Figure 98: Stress and Permeability correlation for sample GEO-N2-4180-H1 .

The permeability of the sample GEO-N2-4180-H was low – ranging in microdarcy.

Overall the complete plot shows a weak correlation between loading and permeability. It stays constant more or less initially but as the sample reaches close to peak stress, the permeability shows a slight increase. This then maintains itself for the rest of the loading. The sample is ductile which is indicated by the stress strain plot.

Samples GEO-N2-4361-V2, GEO-N2-4361-V3 and OXY-72-3-3861.5-V2:

The permeability of these three samples wasn't measured continuously during the test but was measured at two defined intervals – these are:

1. Before beginning of triaxial test – this was observed to be in nano Dracy range at a confining pressure of 3500 psi.
2. After failure – this was measured at the same confining pressure as above. Values were then compared with the initial value.

The permeability was observed to increase in all three cases. It should be noted here that the fracture formed within the sample didn't intersect both ends of the sample – hence the permeability increase can be attributed to both the major fracture and possibly micro cracking spread throughout the sample. A transverse measurement of permeability would have been more apt for this case however couldn't be performed due to equipment limitations.

Table 20 shows the before and after permeability for all the six cored GEO-N2 samples.

Table 20: Permeability values before (k_o) and after triaxial testing (k_f) for the one inch core plugs from the GEO-N2 well

Plug	k_o (μD)	k_f (μD)	Ratio of final to initial permeability	Porosity (%)
OXY-72-3-3861.5-V2	10	150	15	1.7
GEO-N2-3858.5-H1	736000	12000	0.016304	21
GEO-N2-4361-V2	0.927	2.163	2.33	4.49
GEO-N2-4361-V3	22	2196	99.81818	5.8
GEO-N2-4180-H1	539000	800	0.001484	20.9
GEO-N2-4180-H1	17.1	226	13.21637	9.7

*-All permeability values above are at 3500 psi confining pressure

An interesting plot which shows the correlation between change in permeability at the end of triaxial experiment and porosity is shown below in Figure 99.

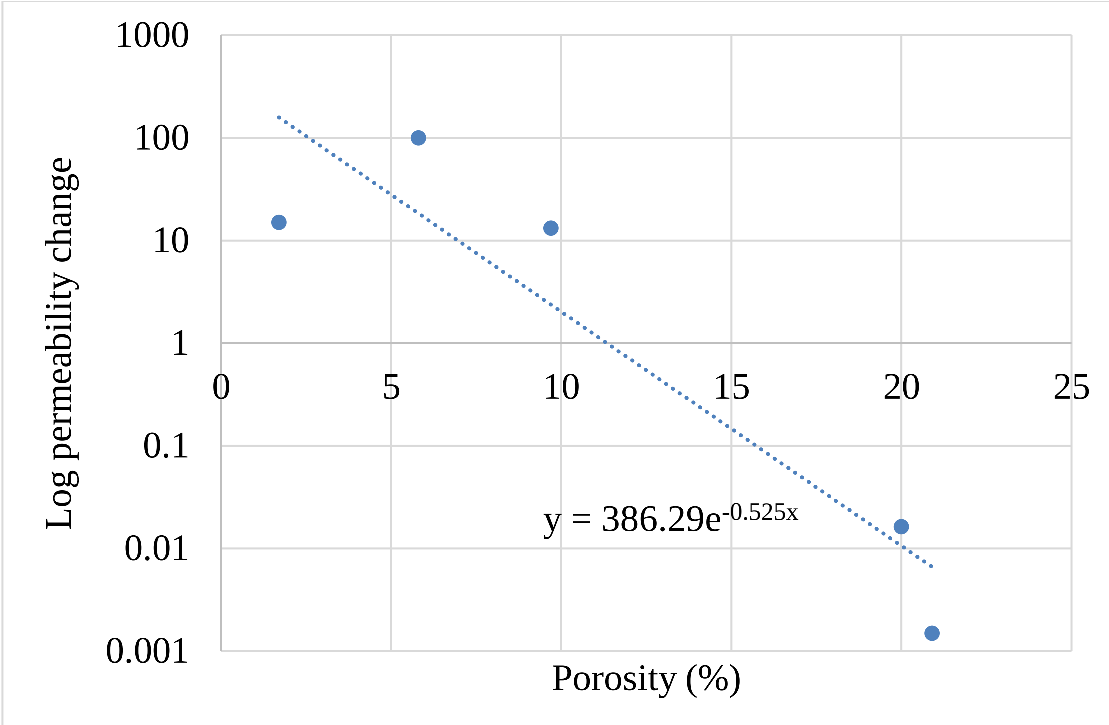

Figure 99: Relationship between permeability increase after triaxial fracturing and sample's porosity. An exponential relationship can be clearly seen with a 'transition' from increase to a decrease of permeability seen around 12%.

This figure shows that a possible increase in permeability due to triaxial failure is inversely proportional to the sample's porosity – higher porosity samples show a permeability decline while low porosity samples show a large increase. The amount of increase/decrease was also found out to be a function of porosity. Based on this, a cut off of ~12-13% can be estimated as the transition point between increase/decrease of permeability with loading.

Conclusion - It should be noted that typically, permeability may increase or decrease after triaxial testing. During sample loading, deviatoric stresses cause sample to compact. However, micro cracks or a major fracture formed as a result of sample failure enhances permeability. In general, research has shown that sample permeability increases for low porosity rocks due to dominance of fracture permeability while it decreases for high porosity rocks due to dominance of pore closures due to compaction as compared to permeability enhancement due to fractures. The work reported in this document demonstrates this behavior for the same class of rocks (Newberry Tuff). The reduction in permeability with loading for high porosity samples is strongly influenced by whether a major fracture has developed within the sample due to loading; after failure, the decline of permeability in the sample with higher loading is much lower as compared to pre-failure loading. This seems logical given the fact that fractures created due to failure intrinsically have higher permeability than matrix and even with further loading, make the sample less susceptible to permeability reduction. Overall, it can be seen that these samples have a range of porosity and permeability. Porosity and permeability are well correlated for the sample from the same section. Permeability of all samples is low – less than 1 mD in all cases and in nano darcy -10^6 times less than mD in many cases. Any EGS project on these rocks would require stimulation for its success.

SIERRA WHITE GRANITE

The porosity of a Sierra White granite sample was tested as a function of confining pressure (300 psi to 2800 psi) and found to vary from 0.98-0.65% and is shown below in tabular format in **Table 21**.

Table 21: Porosity vs confining pressure for Sierra White Granite

Confining pressure (psi)	Connected Porosity (%)
308	0.98

807	0.86
1820	0.72
2820	0.65

The crushed porosity was found to be 1.2% (no confining pressure). This is the total porosity of the sample (includes both connected and unconnected pores).

For the Sierra-White Granite, permeability was measured at two points in the triaxial test – before testing and after sample failure. Continuous measurements were attempted but were not successful due to the extremely small permeability of the sample (< 1μD). Every measurement therefore took several hours for steady state to be achieved. The stress strain plot has already been shown in chapter 3.

The overall permeability was observed to have increased from 0.821 μD to 181 μD after failure reflecting an increase of more than 200 times. It should be noted that the fracture didn't extend all the way to the two ends of the sample as shown in Figure 20. The porosity of the sample as measured earlier (no confining) was 1.2 %. The below table shows these results-they will be later used at the end of this section to derive more conclusions.

Table 22: Results of permeability changes for Sierra white granite

Plug	Total sample Porosity	Initial permeability (μD)	Final permeability (μD)	Ratio of Final to initial permeability
Sierra White Granite	1.2%	0.821	181.0	221

BARNETT SHALE

One 1"x2" sample from Barnett was tested. The porosity of the sample varied from 4.6%-5.7% as the confining pressure changed from 300 to 2800 psi. This is shown below.

Table 23: Porosity versus confining pressure for Barnett Shale sample 01-45

Confining pressure (psi)	Connected Porosity (%)
300	5.72
800	5.37
1800	4.72
2800	4.67

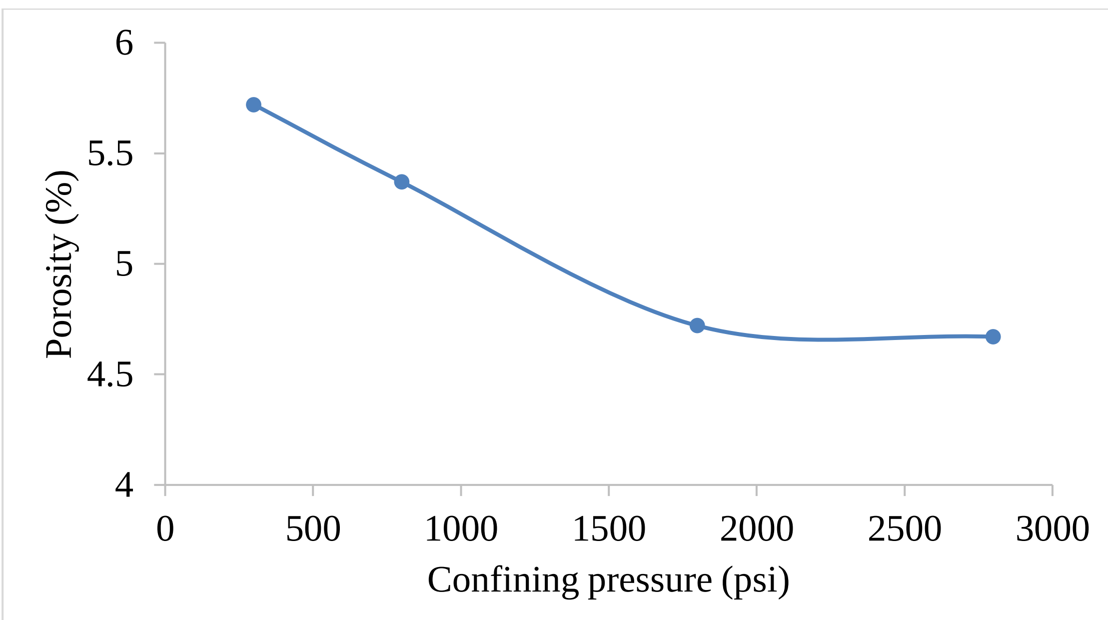

Figure 100: Influence of confining pressure on Porosity of the shale sample

Table 24: Results of permeability changes for Barnett shale

Plug	Total sample Porosity	Initial permeability (μD)	Final permeability (μD)	Ratio of Final to initial permeability
Barnett Shale	5.5	3.1	859.8	277

INEL-1 WELL SAMPLES

Porosity and Permeability were measured for all samples before triaxial testing using an automated Porosimeter-Permeameter. The Porosity was measured first using Boyle's law technique using Helium expansion at different confining pressures (AP-608 machine setup - described in Chapter 4). Figure 101 shows the variation of porosity with confining pressure, the deeper core from 10,365ft depth was found to have very low porosity of less than 1% while the shallower core had a porosity of >10%.

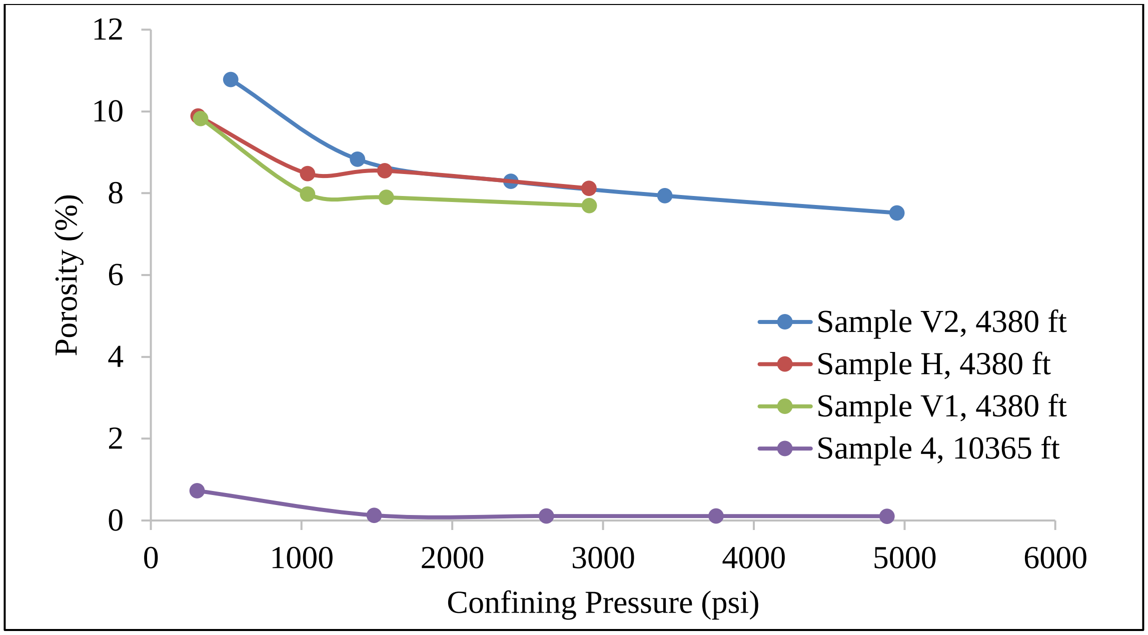

Figure 101: Porosity vs confining pressure for four core plugs from the INEL-1 core, sample depths are provided

Total porosity (crushed) was also measured using the displaced fluid method. The results are shown in Table 25.

Table 25: Density and total porosity for INEL core plugs

Sample	Bulk density (g/cc)	Grain density (g/cc)	Total porosity (%)
10365 ft	2.53	2.66	4.67
4830 ft	2.30	2.63	12.49

The values of crushed porosity (total porosity) are very different from the connected porosity for the deeper core section; this indicates the presence of unconnected pores. This is expected for igneous rocks.

Table 26: Permeability values before and after triaxial testing for the core plugs from the INEL-1 well

Plug	Total	Initial	Final	Ratio of Final to

	sample Porosity*	permeability (μD)	permeability (μD)	initial permeability
V-1, 4874 ft	12.49	18.2	1668.0	92
V-2, 4874 ft	12.49	0.068	0. 590	9
H, 4874 ft	12.49	0.197	10.138	44
INEL Sample 4, 10365 ft	4.67	0.086	17.357	201

*-Takes into account connected and unconnected pores

Table 26 describes the changes in permeability observed after fracturing. It should be noted that during compressional loading two processes compete – the sample compression reduces permeability due to pore closure, while micro fracturing or shear fracturing increases permeability. Permeability has been observed to decrease with increasing triaxial loading (even after fracture) for high porosity samples like sandstones and to increase for low porosity samples (Ohaka, 2010). The final permeability change is also a function of whether the fracture intersects the ends of the sample or more localized. It can be seen from below table that most of the samples showed large increases in permeability after fracturing which shows that injection experiments could be successful in creating improved fluid flow in these rocks. The final values of permeability though are still low (μD).

GEO-N2 FULL CORE SAMPLES

The value of porosity was found to be 1.4% for sample GEO-N2-4382-I1which varied very little with changes in confining pressure. This shows the highly-consolidated nature of this rock. These results are shown in Figure 102.

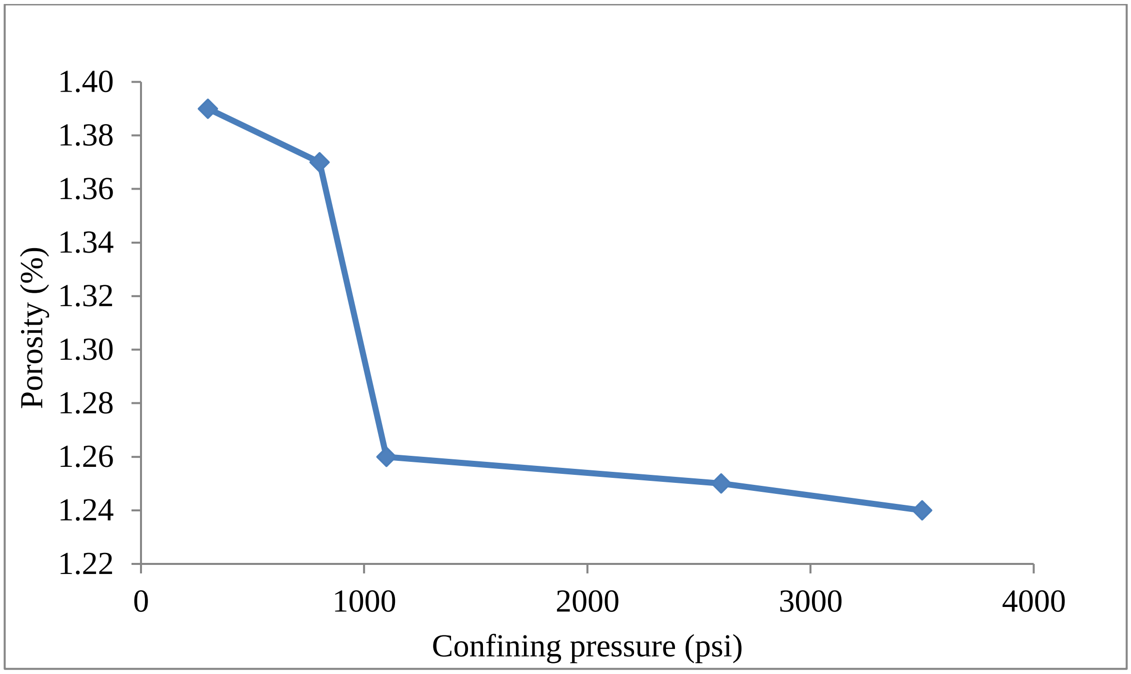

Figure 102: Porosity vs confining pressure for a core plug from the GEO-N2 core (GEO-N2-4382-I1), sample depth is provided. The effect of confining pressure can be seen to be very minimal.

Summary of Permeability measurements on the GEO N2 samples –For all the six full core samples from the GEO-N2 well, only before and after permeability was measured. The after-fracture permeability was observed to always increase for all the six samples after triaxial-injection or conventional triaxial failure. It increased the most for GEO-N2-4382-I1 due to large axial fractures although for the rest, a range of values were seen ranging from 10 times for GEO-N2-4243-I1 to 2330 times for GEO-N2-4300-I3.

Table 27 provides the before and after values for permeability for all the six samples along with comments.

Table 27: Permeability values before (k_o) and after triaxial testing (k_f) for the full core sections from the GEO-N2 well

Plug	k_o (μD)	k_f (μD)	Ratio of final to initial permeability	Comments
GEO-N2-4300-I1	0.027	0.340	13	Minor fracture formation-sample was completely intact after failure; Not representative
GEO-N2-4300-I2	0.037	22.6	610	Initially non-fractured rock – represents the impact of fracturing on a sample with no healed fractures. Most representative sample.
GEO-N2-4300-I3	0.098	228.3	2330	Had two large intersecting healed fractures initially. Sample failed along these pre-existing weak planes. Considered as a representative sample here especially as it shows the impact of fracturing on samples with existing fractures is to be considered.
GEO-N2-4300-I4	0.107	21	196	Had a healed fracture before testing. Sample failed along this fracture along with a new fracture. Also considered representative.
GEO-N2-4382-I1	0.047	-	-	Sample had no initial fracture, after fracture disintegrated – hence permeability measurements not reliable.
GEO-N2-4243-I1	1.12	10.2	10	Had several healed fractures before testing. Fracture was right at the center of the sample with both the ends of fracture away from the ends of the

				sample. Could have been considered representative if horizontal permeability measurements were available.

It can be seen here that for a sample without initial fractures, only GEO-N2-4300-I2 can be taken as a representative sample. As for samples, which failed along the pre-existing fractures, samples GEO-N2-4300-I3, GEO-N2-4300-I4 and GEO-N2-4243-I1 can be taken.

Overall 2-3 orders of increases in permeability values were seen after fracturing.

OVERALL CONCLUSION FOR ALL SAMPLES

Figure 103 was created using the results shown in this section.

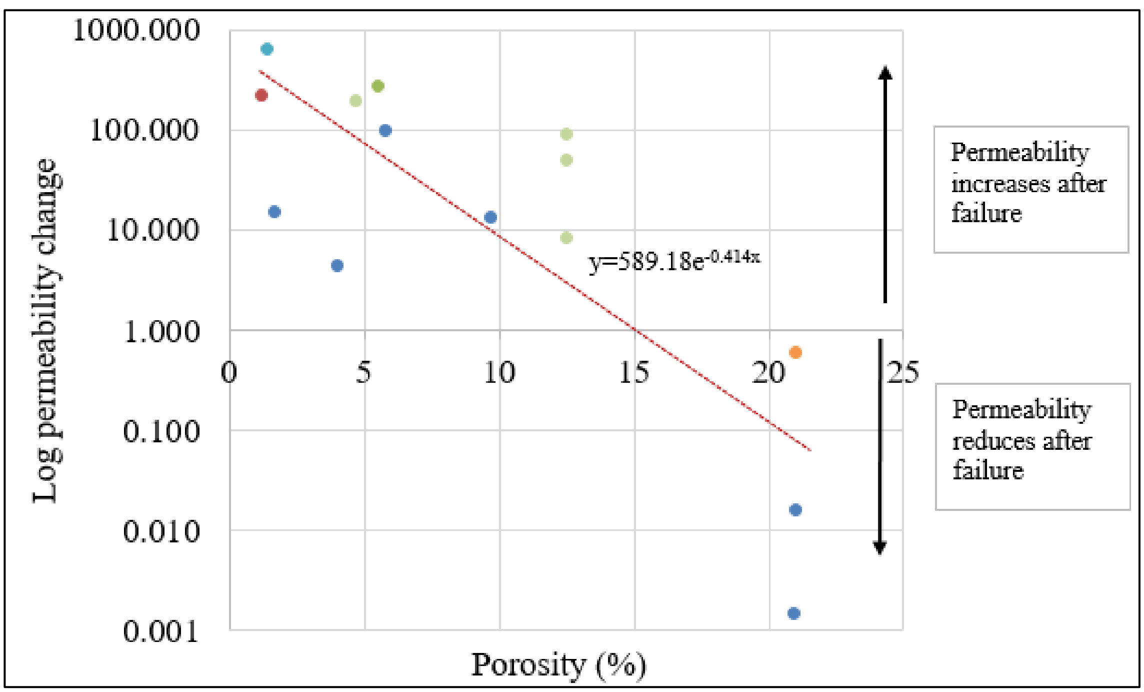

Figure 103: Relationship between permeability increase after triaxial fracturing and sample's porosity. An exponential relationship can be clearly seen with a 'transition' from increase to a decrease of permeability seen around 15%.

As can be seen from this figure, an exponential relationship can be seen between the ratio of post to pre-failure permeability and porosity of the sample. Around a value of 16 % porosity, we start to see that post triaxial failure, a decrease in permeability should be expected. The reasoning behind this has already been discussed here.

Variations between the Figure 103 and Figure 99 can be seen here – Figure 103 uses more data indeed but uses several types of rock specimens. All of these measurements were carried out at a confining pressure of 3500 psi – use of a different confining pressure may yield different results. No mention of any such plot was found in any other published research paper - a similar plot though comparing permeability values of sample before and after hydrostatic loading has been provided by Zhu et. al, 1997 for sandstones. In their highly-cited work, the authors arrived at a cutoff value of 16-17% porosity for increase/decrease of permeability using a set of sandstones and granite for data. This work demonstrates this behavior for igneous rocks (figure 100) using pre and post failure values of permeability for possibly the first time.

CHAPTER 5: ACOUSTIC EMISSIONS ANALYSIS

The intent of this chapter is to provide all information related to the Acoustic Emission testing of the samples. This includes the setup of equipment and sensors and results collected. The conventional reporting of the number of hits (cumulative and rate) are discussed, however additional results are also reported. A proposal on how energy released can be used as a qualitative and quantitative parameter in conjunction with number of hits for understanding acoustic emissions of every sample in a better fashion is provided. The location of AE events is discussed in both 2-D and 3-D space for most samples. Source analysis using first arrival waveform polarity method as well as using full moment tensor inversion process to identify source type is provided for a few samples to demonstrate the power of using AE as a way of understanding mechanical processes in intricate detail on a microscopic scale. This is an upcoming field where a lot of research is underway.

Experimental Setup

With the exception of two samples (GEO-N2-4163-H1 and GEO-N2-4300-I3) all of the rest that have been described in chapters 2,3 and 4 were tested with Acoustic Emissions (AE) set up. This consisted of the AE analysis system and the sensors for measuring them.

For the AE analysis system, the MISTRAS Express-24 channel, Acoustic Emission (AE) system with a frequency range of 1KHz - 1MHz was used. Differing number of AE sensors per sample were used depending upon the intended analysis. For example, for 3-D location analysis, a minimum of four sensors were used, for tensor analysis a minimum of six sensors were required-refer Appendix 2 for details. These sensors were attached to the sample using E-Z bound instant glue . A preamplifier of 40 dB was applied to all the sensors. The pre-amplifier amplifies the signal so that it can be processed by the AE recording equipment-original AE event energy is too low and a pre-amplifier must be therefore used. The amplitude cut off on these sensors varied from 45-60 dB for every test; any wave below this amplitude was discarded by the system as noise. Whenever MTS 315 system was used (most of the samples), the amplitude cut off were usually around 50 dB. However, whenever the 816 MTS system was used, the amplitude cutoffs were higher with values ranging between 55-62 dB. Several attempts were made to reduce noise in the MTS 816 system but the results achieved for MTS 315 in terms of noise reduction couldn't be replicated for MTS 816. A schematic of a sample with twelve sensors for illustration purposes is shown in Figure 104 below.

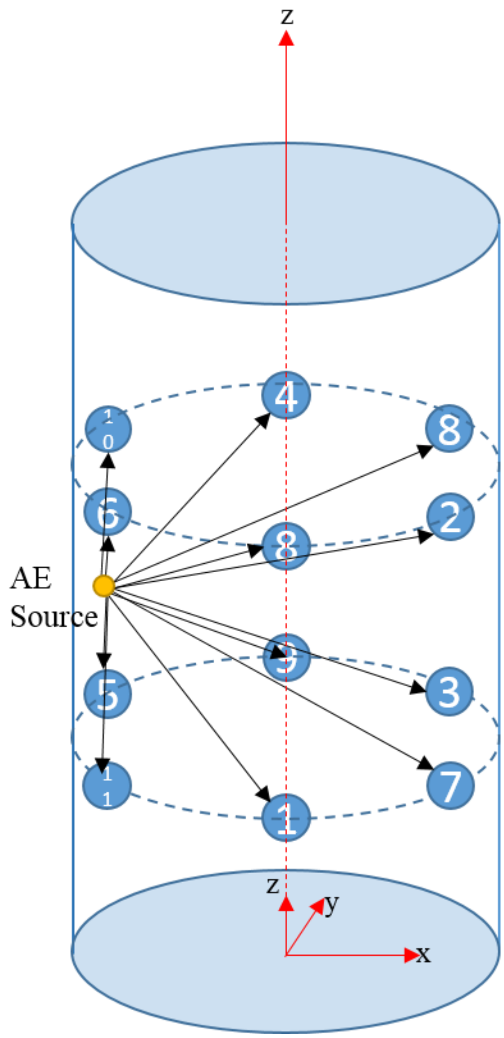

Figure 104: Schematic of the AE set up for all samples where 3-D location analysis was done (modified from Zang et al., 1998)

The frequency and the energy of AE events along with individual waveform data were also recorded during the tests using the software – these give more insights into the nature of failure. A sample rate of 1 MSPS (million samples per second) was used to record the AE information. This means that one waveform is taken every 1 µsec. Similarly, a sample rate of 2MSPS would mean that one waveform is taken every 0.5 µsec and so on. Increased samples rate typically improves location accuracy and allows for better waveform analysis but increases noise sensitivity – hence a balance must be struck between noise and signal quality. Based on this 1 MSPS provided an optimum balance. 3-D location analysis was performed using AE information – this technique uses the source amplitude and the differences in time it took the wave to reach the different sensors and to be recorded as an event. 3-D location is highly dependent upon the rock type – rocks which generate low amplitude AE (certain types of Tuff, limestone) typically do not give a good 3-D location response as compared to very brittle rocks which generate high amplitude AE waves during the failure process. Waveforms collected for analysis ranged in quality for every test. All waveforms were classified into three categories for analysis – the ideal one (Figure 105), the less than ideal waveform (Figure 106) and finally the discarded waveforms (Figure 107). Description is provided with each figure.

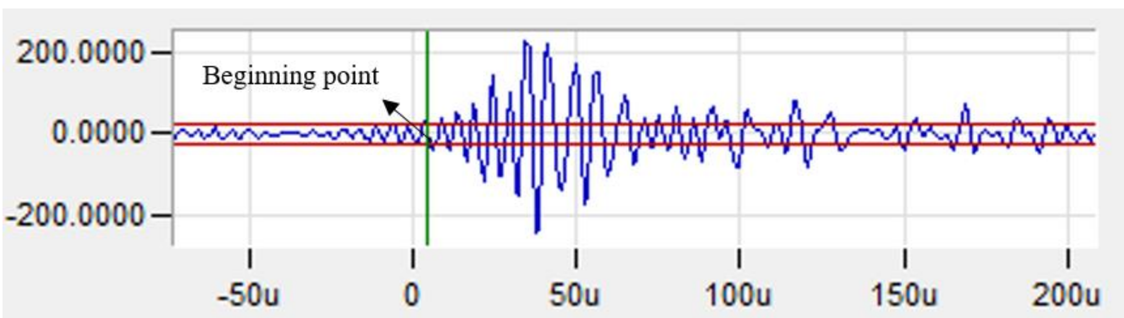

Figure 105: An ideal AE waveform. A clear beginning point can be seen with the pre-event area having very little noise. The signal 'dies' down also perfectly.

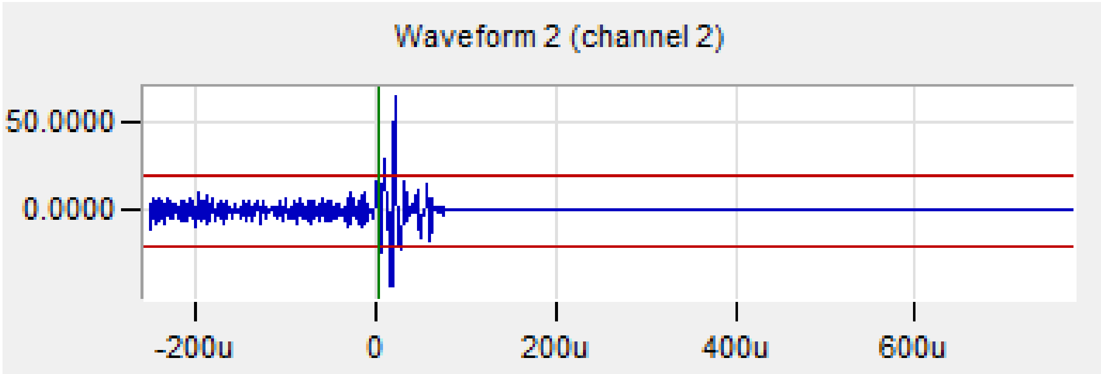

Figure 106: A less than ideal AE waveform- this can be used for analysis but errors can creep in if this is used for any analysis (location, source analysis or Moment tensor). Due to ambiguity in the waveform, if the incorrect beginning point is chosen, then location would be incorrect as time of the event will be affected. Similarly, if the wrong first waveform amplitude is chosen (required for source analysis), then source analysis will be incorrect. Beginning point and amplitude pick is subject to human error.

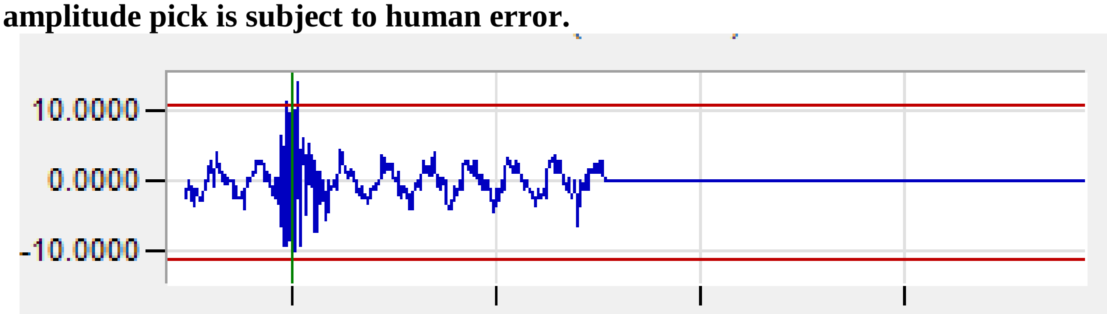

Figure 107:A poor waveform signal -this type of waveform wasn't used for any analysis and was deleted. It isn't clear as to where the waveform gets initiated and signal has lot of noise before the amplitude rise.

An amplitude filter was used for these experiments. This was selected based on the standard 'pencil break test'. This involves removing unwanted noise which may be present in the area due to various factors (machinery use, vibrations etc.). Although efforts are made to conduct the test such that the least noise is present, some of it is inevitable and must be removed lest it gets wrongly interpreted as an actual AE event generated due to changes in rock structure. In this case, a certain amplitude was chosen and the AE monitoring switched on. If noise is present, AE system will show events occurring at a fixed rate without any source to account for it. The source of these AE events is noise due to the sound sources present around the lab where the sample is kept (machines, human noise, pumps running etc). In this scenario, amplitude cut-off was raised higher to filter this noise. This was done until an amplitude was selected when no events were observed for a minute. To further confirm if the crystals were functioning properly, a pencil lead was taken close to the sample and broken. If a single AE event was observed for each crystal, then it indicates good quality setup. The quality of the signal is also checked to ensure it is of good quality.

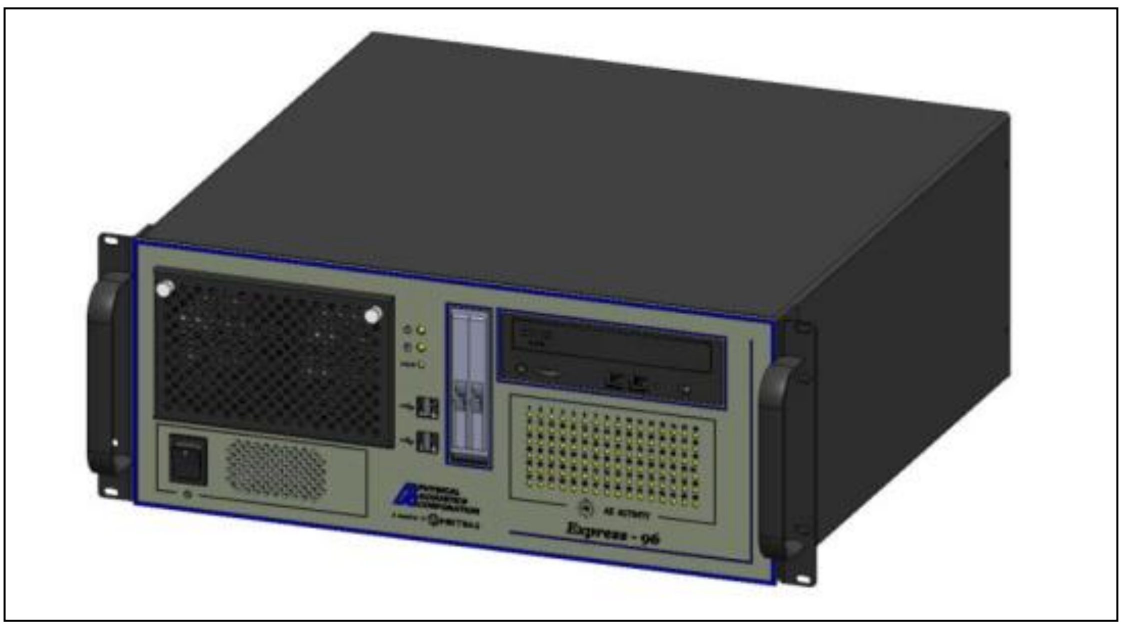

Figure 108: MISTRAS AE system

Figure 16 and Figure 30 shows the sample setup for both 1 inch samples (example GEO-N2 core plugs, INEL-1 well samples etc.) as well as 2.5 inch GEO-N2 full core samples, respectively. These show the Acoustic sensors that were used for measuring AE waveforms and associated information. The sensors were glued onto the copper jacket using E-Z bound instant glue. Whenever location analysis was to be done, a minimum of six sensors were used for each sample with a spacing of 60^{o} between adjacent crystals (Figure 30). The even spacing was used for ensuring that the location algorithm would perform well due to an adequate coverage of the sample's surface. Difficulties were encountered in one inch samples due to the limited area available after applying strain gauges and radial and axial LVDT's for strain measurements leaving very little room for applying acoustic sensors (Figure 16). The signal quality was then checked using the pencil break test described earlier. If satisfactory, triaxial tests were begun after closing the frame and applying required confining pressure. The application of confining pressure improves the connection between the copper jacket and sample which in turns improves signal quality.

At this point, it is pertinent to point out that AE energy is defined as the square of the amplitude of AE events generated. It is a parameter that quantifies the intensity of the AE signal.

AE ANALYSIS OF TRIAXIAL COMPRESSION OF BEREA SANDSTONE SAMPLES

The triaxial and permeability related aspects of testing the Berea sandstones have already been described in earlier chapters. In terms of Acoustic emissions, all Berea sandstones tested gave good AE signal. With the exception of the 2.5-inch sample, all samples were tested with only two crystals -one each placed in the top and bottom loading platens. Hence for these samples, 2-D or 3-D location testing was not done.

Berea Sample A: One inch Berea Sandstone with effective confining pressure 1000 psi. The results for this sample have already been described in terms of triaxial test parameters (Figure 18) and permeability effects (Figure 87). In terms of AE response, see Figure 109, Figure 110 and Figure 111.

In Figure 109, we can see that the AE started just before sample failure and then a high emission rate was seen during shear failure followed by which a reduced but constant response can be seen in the fracture sliding phase (refer Figure 111 for different stages). The signals die down once sample is unloaded (at ~700 seconds). It should be noted the number of hits shown here are using the sum of hits recorded by the two crystals.

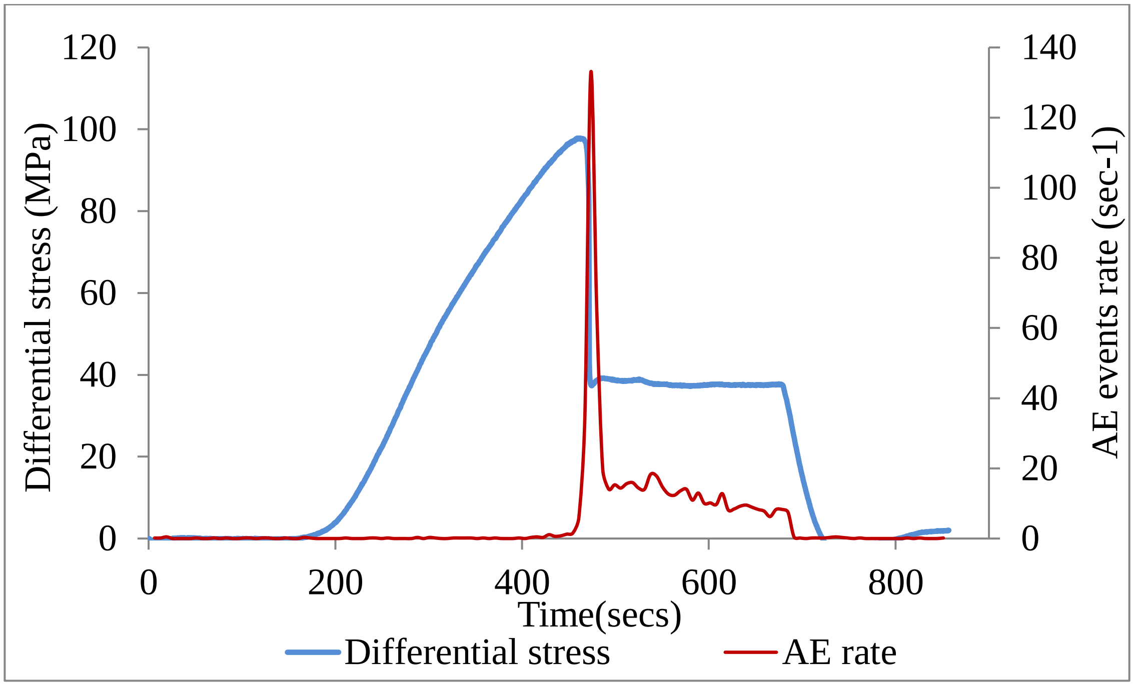

Figure 109: AE events rate when compared with differential stress for the triaxial- test. Most of the events were generated during fracturing.

The above figure is a standard way of evaluating AE response. An improved method of evaluating results in a better fashion is by using the ‘energy released’ in conjunction with the hits. This is not seen in literature but is proposed as part of this thesis.

For example, in Figure 110, we can divide the plot in three parts – elastic loading, fracturing phase and finally the sliding phase. This plots shows the 'energy released' on a logarithmic scale. From here two interesting observations can be seen:

1. The energy plot shows a trend broadly similar to the records of the acoustic hits. This is expected as energy gets released only when hits are generated.
2. There is a big difference -of three orders in fact between the energy released during fracturing and during sliding on fracture. So, while the number of hits falls by 1/6th from the fracturing phase to the sliding phase, the reduction in energy released is much more pronounced (1000 times).

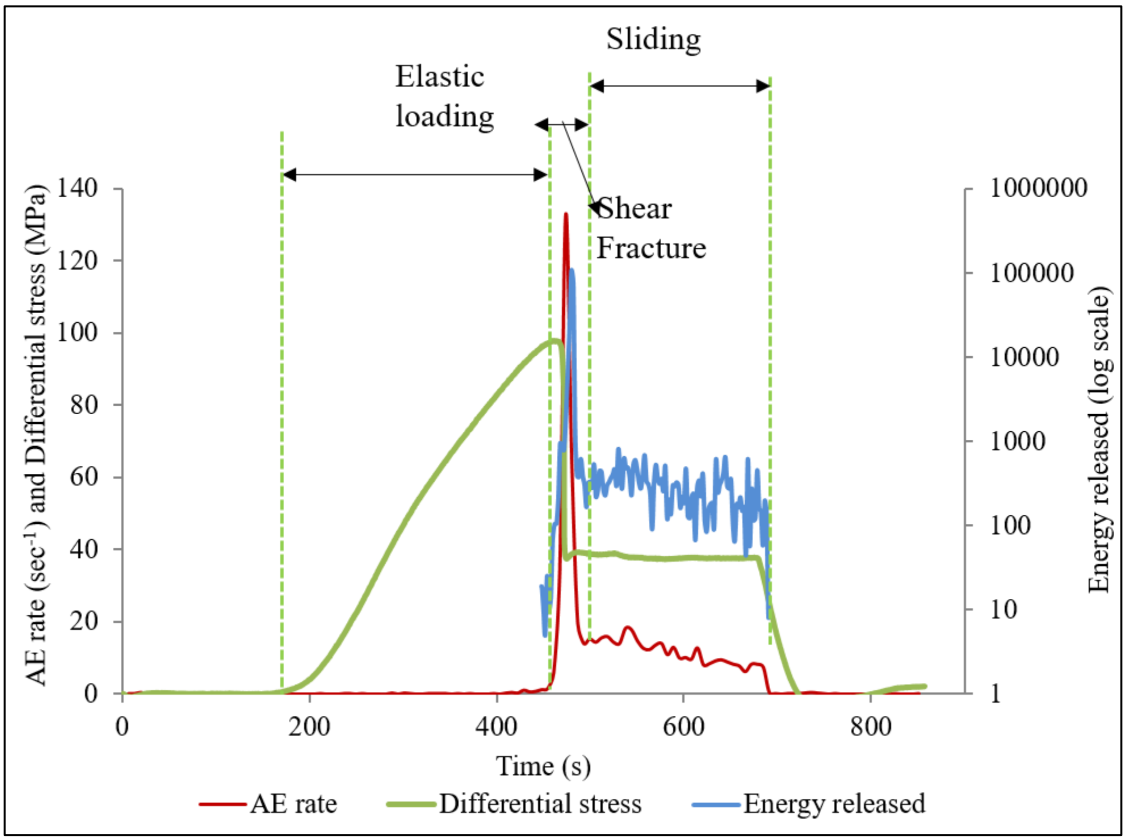

Figure 110: Stress and AE plot for Sample A Berea sandstone (hits rate and energy released) showing various sections for better understanding the micromechanical processes that the rock undergoes while triaxial loading.

This leads to an interesting conclusion – even though number of hits released during inelastic loading/fracture of sample is lower by a few times, energy released shows that sliding is a much lower energy process than fracturing and hits generated during sliding have a much lower amplitude. The amplitude may be so low that during actual fracturing operations, the AE signal may get attenuated before reaching the sensing equipment.

A comprehensive diagram stress, permeability and AE on a single plot has been shown in Figure 111. This figure linking these three parameters shows how well correlated these processes are with each other. The inelastic loading phase is where the permeability reduction occurs due to pore closure – in the same region, no AE is generated. Closer to failure, permeability starts increasing slightly and reaches a very high value for a brief moment when the sample fractures. AE follows the same fashion. Finally, in sliding, permeability stabilizes and AE starts reducing as well (but does get generated during sliding).

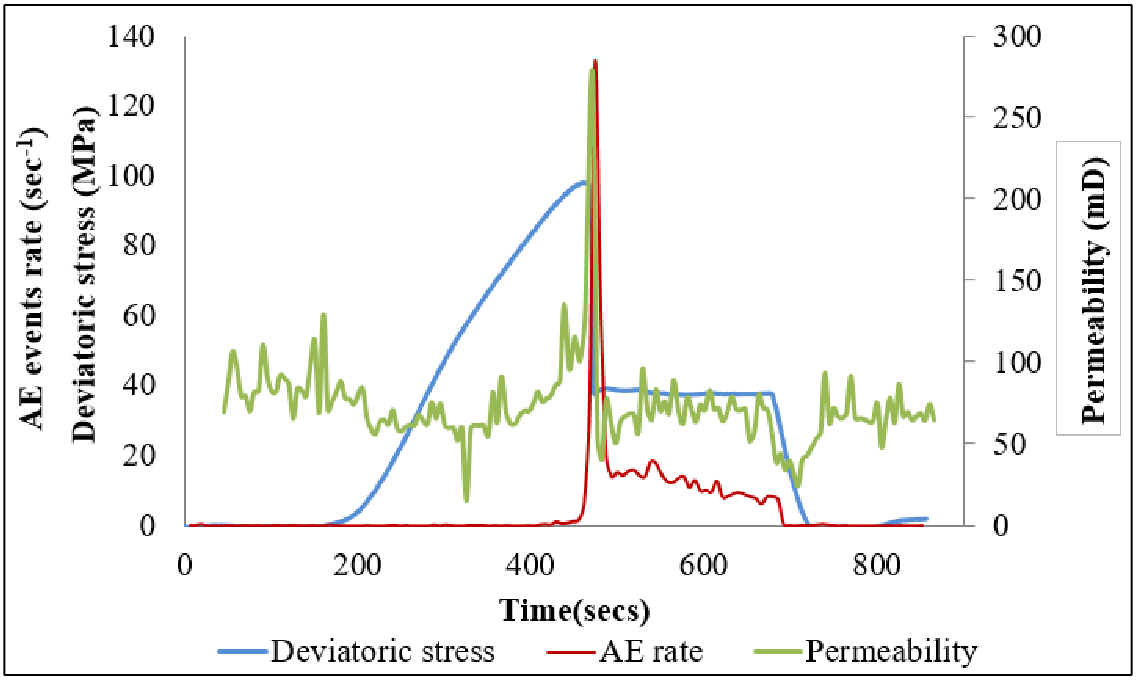

Figure 111: Plot showing differential stress, its impact on permeability as well as Acoustic emissions with time for Berea Sandstone sample A. A good correlation can be seen between all three.

Sample B: One inch Berea Sandstone with effective confining pressure 2000 psi.

The results for this sample have already been described in terms of triaxial test parameters (Figure 18) and permeability effects (Figure 89). In terms of AE response, see figures 112-114 below.

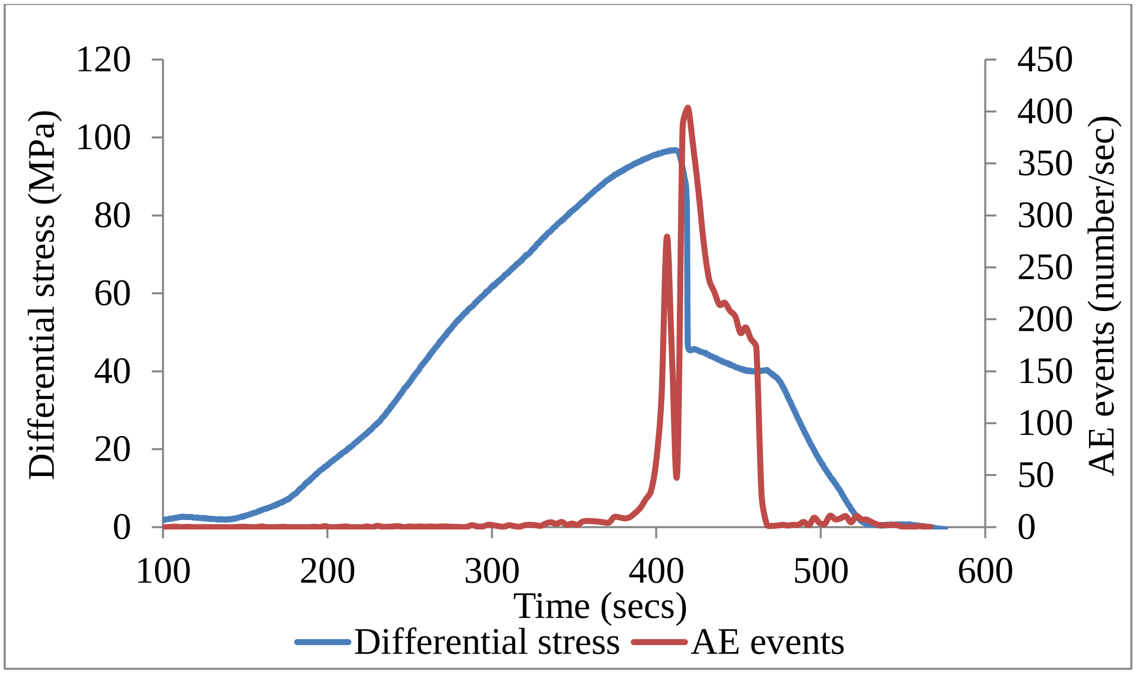

Figure 112: AE events rate when compared with differential stress for the triaxial-test for Sample B – Berea Sandstone. Most of the events were generated during failure.

The results seen for this rock are broadly similar to Sample A, but some differences do exist. For example, in Figure 112, instead of a single peak, we can see two peaks for AE during fracturing. This indicates that during fracturing probably two shear fractures were created. Since 3-D location analysis wasn't used, hence unfortunately this couldn't be verified as on visual observation, only a single major fracture was observed as shown in chapter 2.

The AE and energy released plot provides similar information as discussed for previous sample but a more pronounced inelastic region can be seen here. From the Figure 113, we can see that energy released close to failure is similar in magnitude to energy released during sliding. As in Sample A, three orders of magnitude difference can be seen between fracturing and sliding. This helps compare the two processes in a way that conventional stress, strain, permeability measurements or just counting number of AE events does not allow.

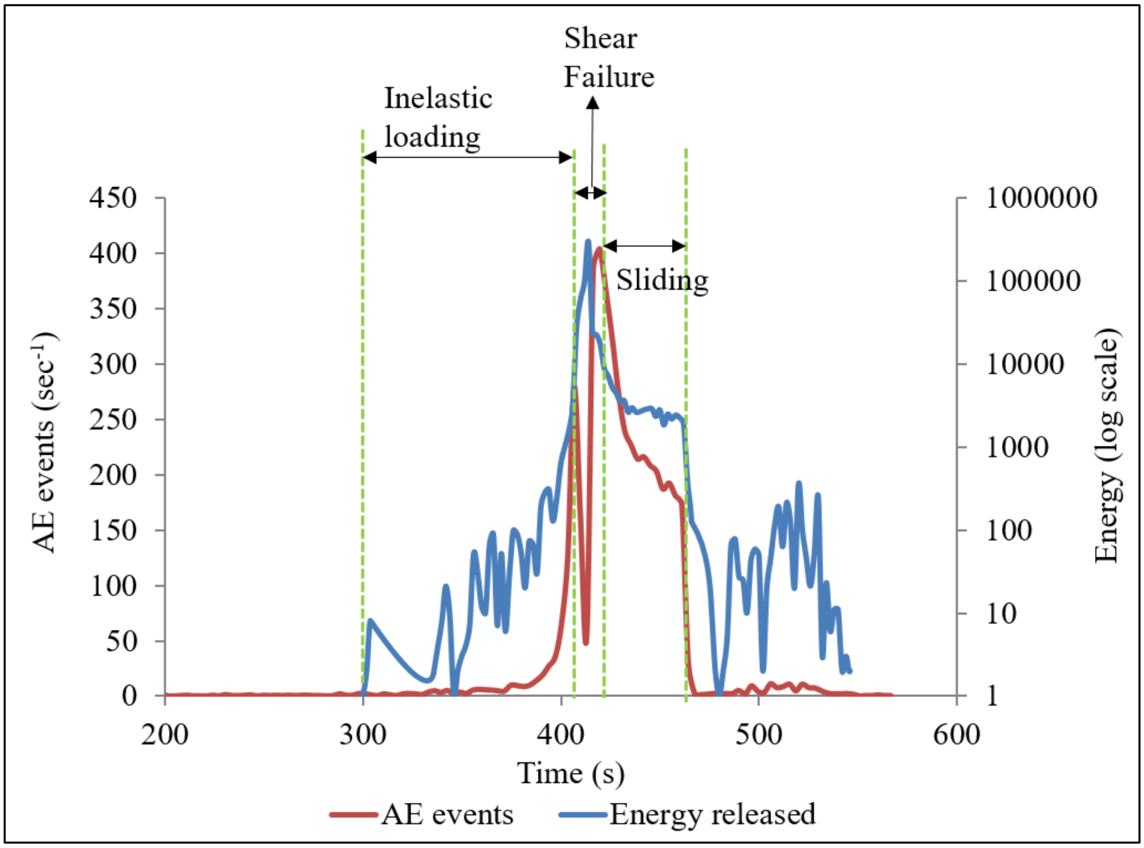

Figure 113: Stress and AE plot for Sample B Berea sandstone (hits rate and energy released) showing various sections for better understanding the micromechanical processes that the rock undergoes while triaxial loading.

Sample C: One inch Berea Sandstone with effective confining pressure 2500 psi.

The results for this sample have already been described in terms of triaxial test parameters and permeability effects. In terms of AE response, see Figure 114,Figure 115 and Figure 118. These figures show results consistent with what was seen in sample A and B (Berea Sandstone) – AE events start sometime before failure, reflecting the start of inelastic loading; most of events get generated during failure and finally some low energy events are also generated during sliding.

The results again support the conclusions derived in the previous two samples.

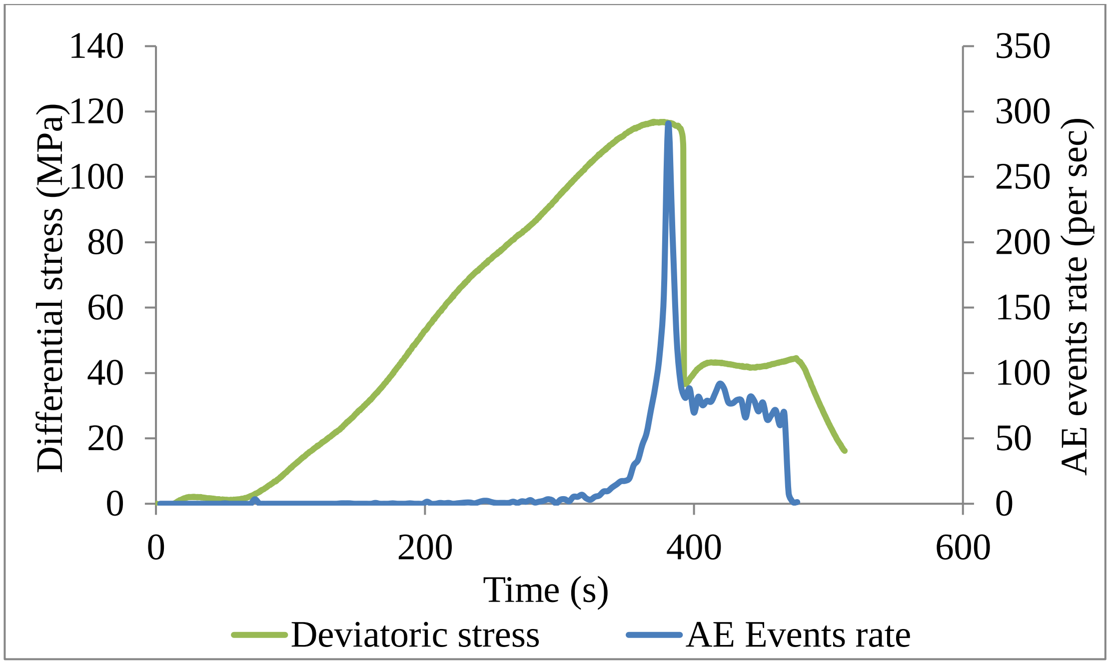

Figure 114: AE events rate when compared with differential stress for the triaxial-test for Sample C. Most of the events were generated during fracturing.

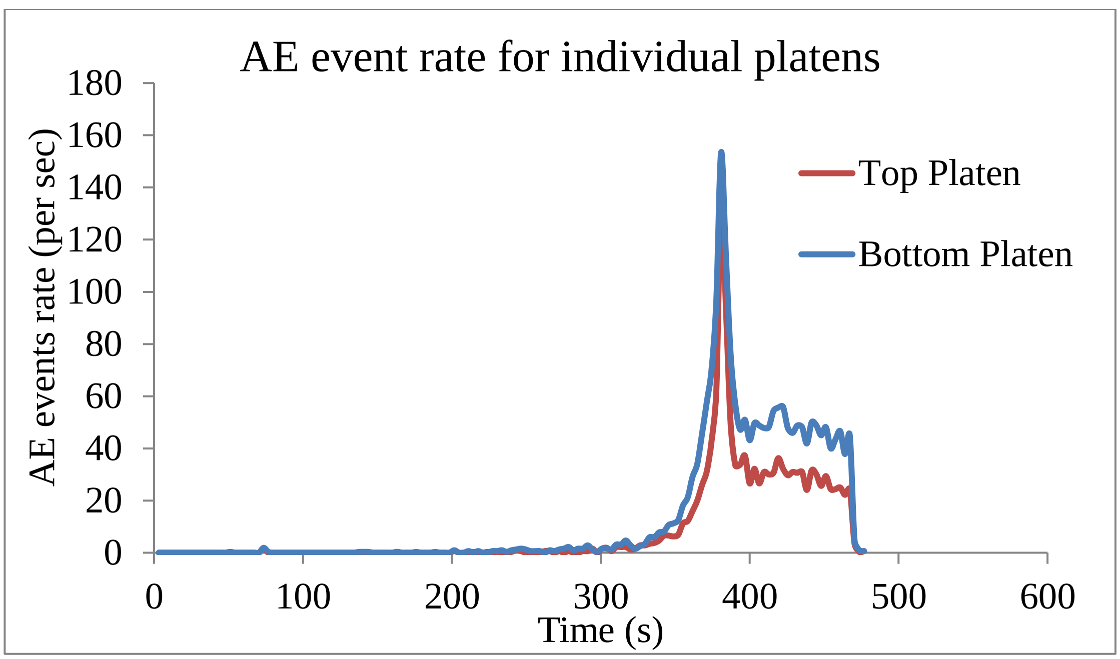

Figure 115: Number of hits registered at each individual crystal used for recording AE for Sample C. The number recorded by each crystal is almost same although

the trend has a better match. Possible reasons for difference could be closer proximity of more events to bottom platens as compared to top platen.

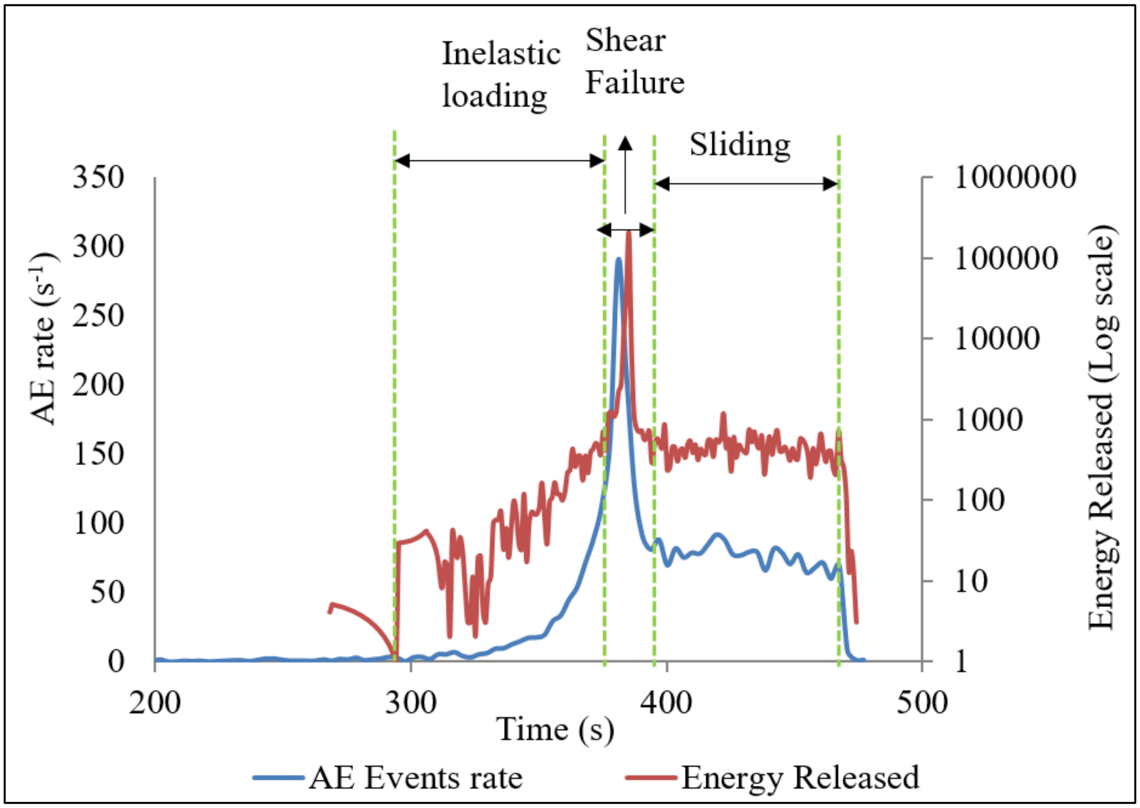

Figure 116: Stress and AE plot for Berea sandstone Sample C (hits rate and energy released) showing various sections for better understanding the failure processes that the rock undergoes while triaxial loading.

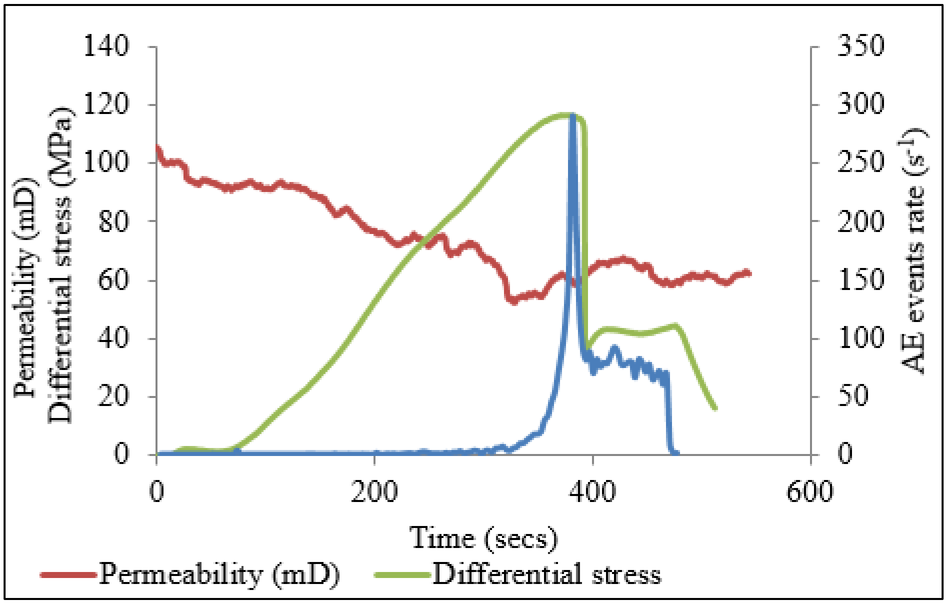

Figure 117: Plot showing differential stress, its impact on permeability as well as Acoustic emissions with time. A good correlation can be seen between all three.

Sample D: Two and half inch diameter Berea Sandstone with effective confining pressure 3500 psi.

The results for this sample have already been described in terms of triaxial test parameters and permeability effects. In terms of AE response, see Figure 118.

This sample was tested with six sensors for testing the accuracy of the 2-D and 3-D location algorithm. Results are seen in Figure 120 and Figure 121. As can be seen, an excellent correlation as obtained between actual fracture and its location using AE in both 2-D and 3-D space.

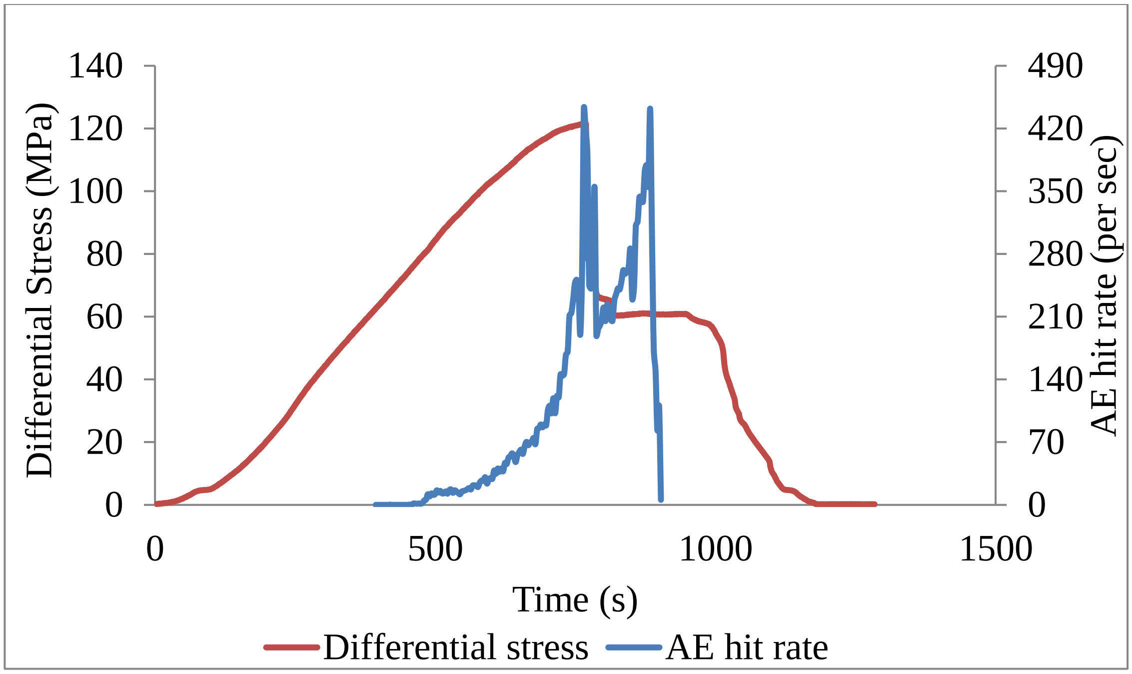

Figure 118: AE events rate when compared with differential stress for the triaxial-test. Most of the events were generated during fracturing.

The AE and energy released plot (Figure 119) provides similar information as discussed for previous sample but a very large inelastic region can be seen here. Measurements are more reliable here as sensors were attached all around the sample and hence attenuation based losses are expected to be minimal.

From the Figure 113, we can see that energy released close to failure is similar in magnitude to energy released during sliding. As in samples A, B and C, two- three orders of magnitude difference can be seen between fracturing and sliding. The number of hits here almost matches the number of hits generated during fracturing and it’s only the energy released plot which shows a clear distinction between sliding and fracturing. Once again, this helps compare the two processes in a way that conventional stress, strain, permeability measurements or just counting number of AE events doesn’t allow.

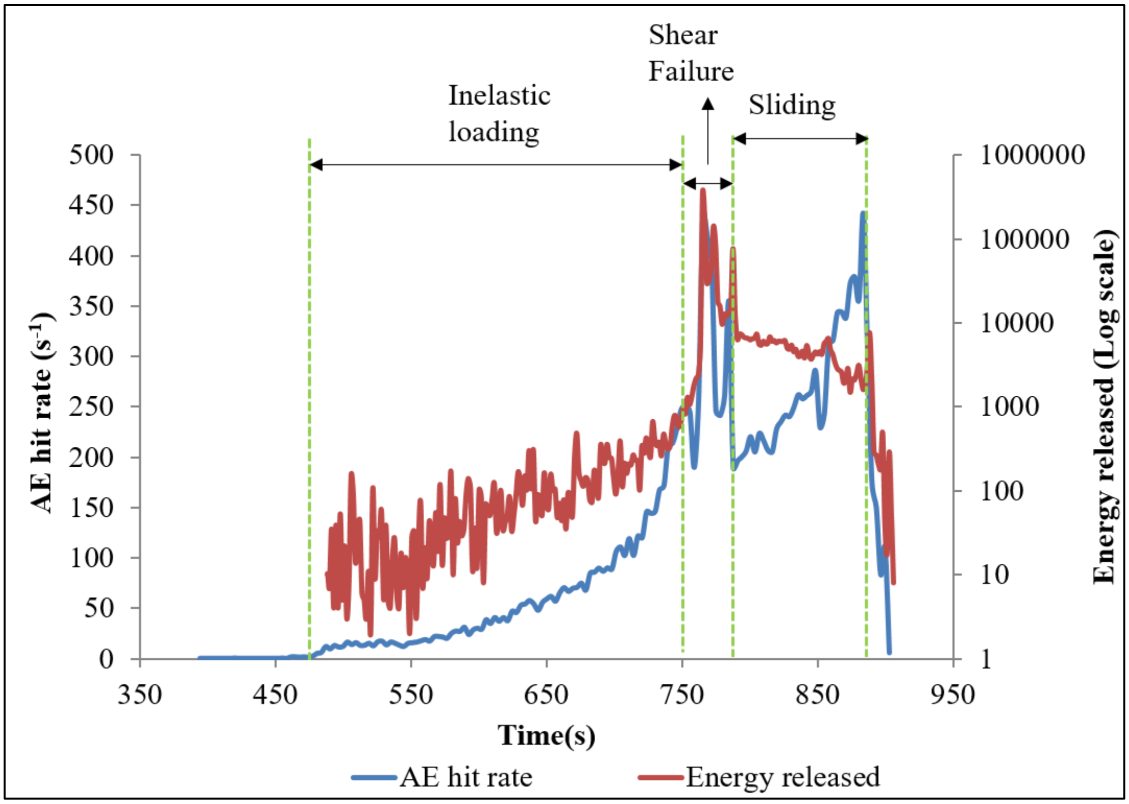

Figure 119: Stress and AE plot for Berea sandstone Sample D (hits rate and energy released) showing various sections for better understanding the micromechanical processes that the rock undergoes while triaxial loading.

2-D location and 3-D location plots are shown below.

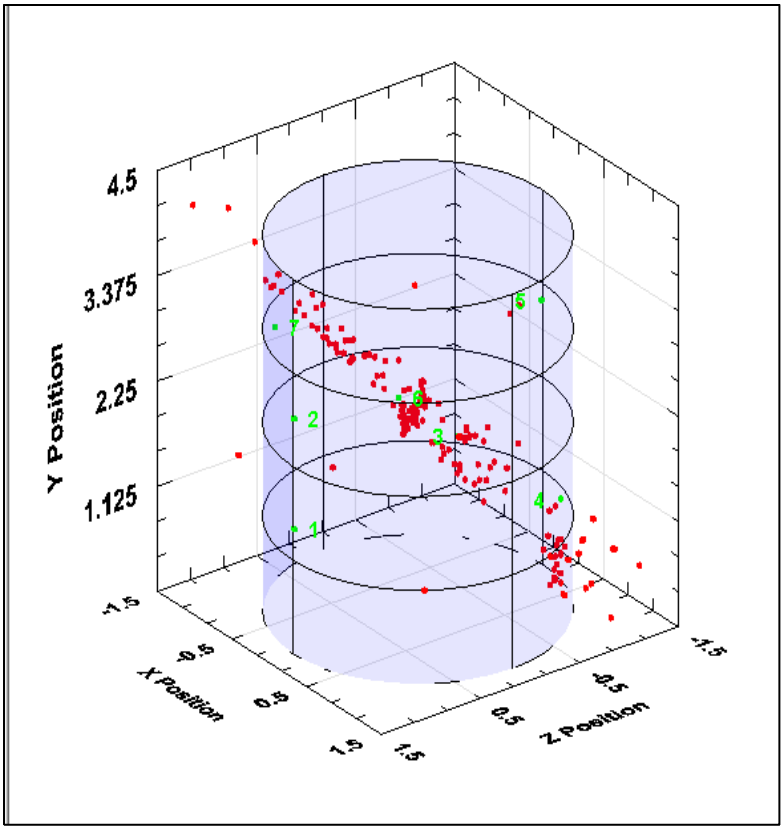

Figure 120: 3-D location of events using Acosutic emissions. A narrow shear fracture can be seen here. It should be noted that this is the original figure without any re-processing.

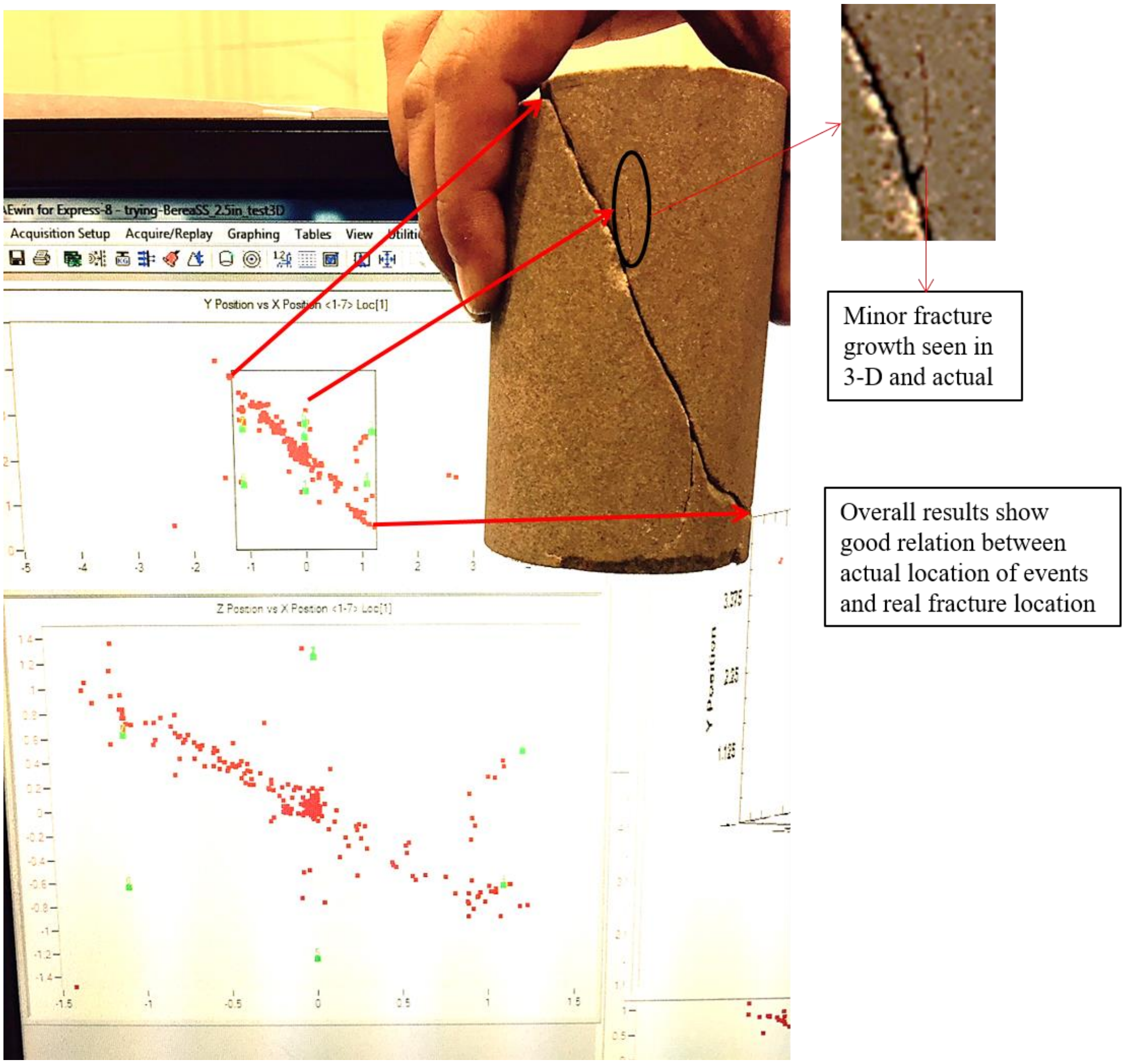

Figure 121: Correlation of location of calculated shear fracture versus actual location of fracture

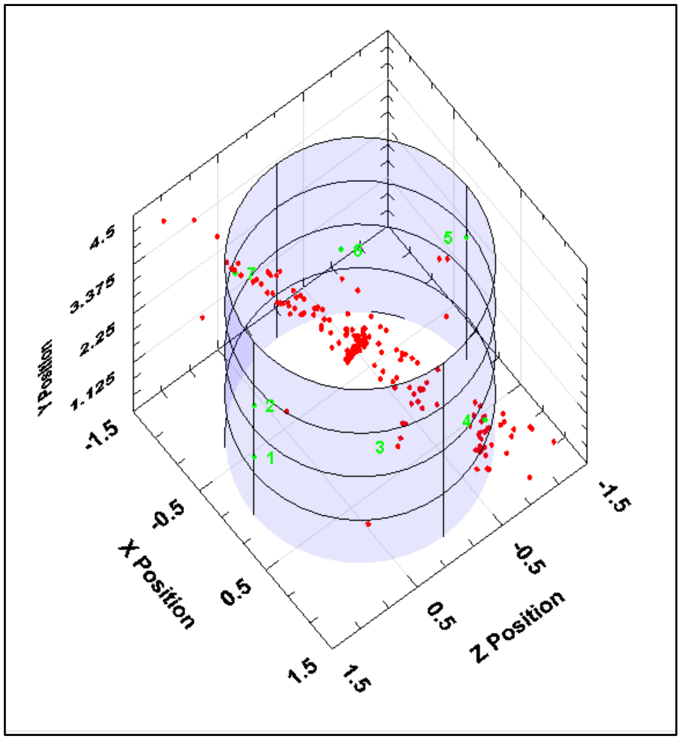

Figure 122: 3-D location of events with a different angle of view. A narrow shear fracture can be seen here

Monitoring the development of Shear Fracture using a time lapse plot of AE events for Berea Sandstone

Figure 123 below shows nine pictures with the associated timelines of how micro-cracking coalesces into a single large fracture can be understood using the AE events location technique.

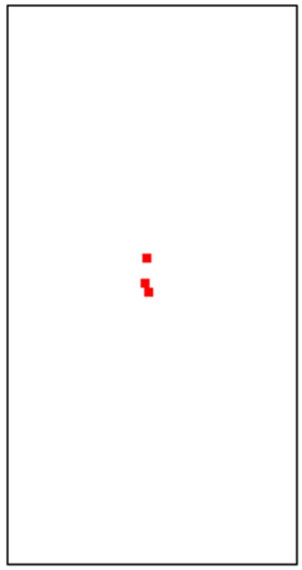

1:57

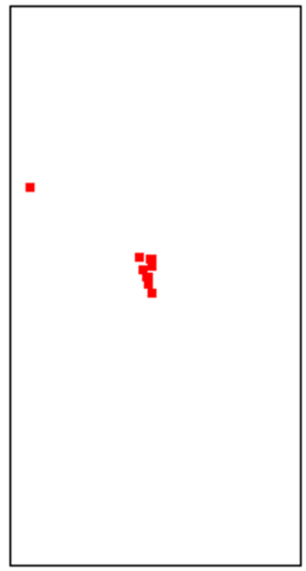

3:32

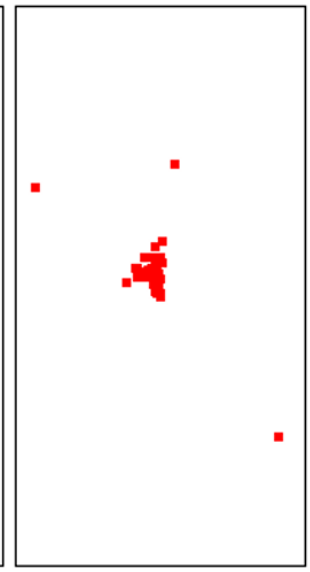

5:04

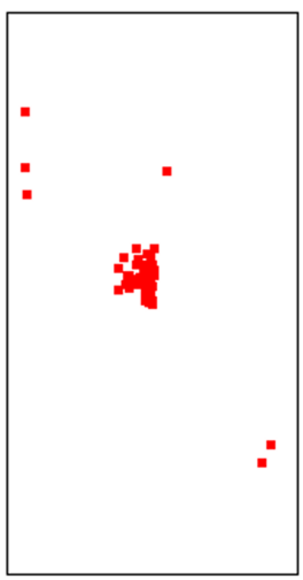

5:58

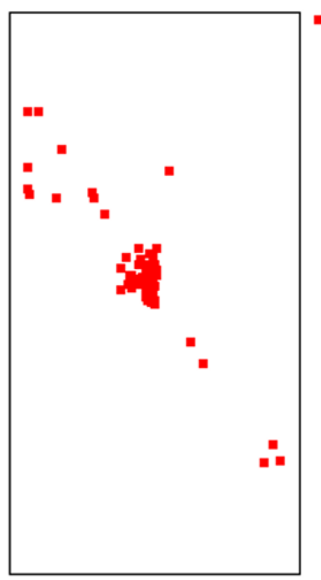

6:04

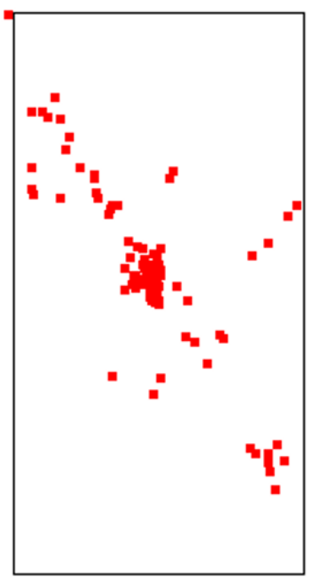

6:33

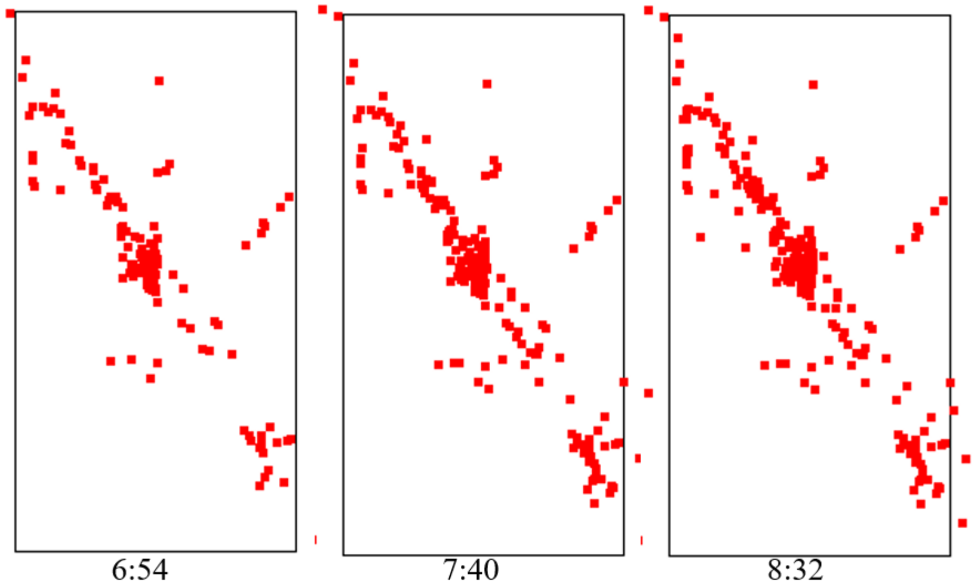

Figure 123:Time lapse plot showing development of shear fracture in the Berea Sandstone Sample D. It can be seen that the fracture develops at the center and then grows in both directions. Also, see the stress time plot below

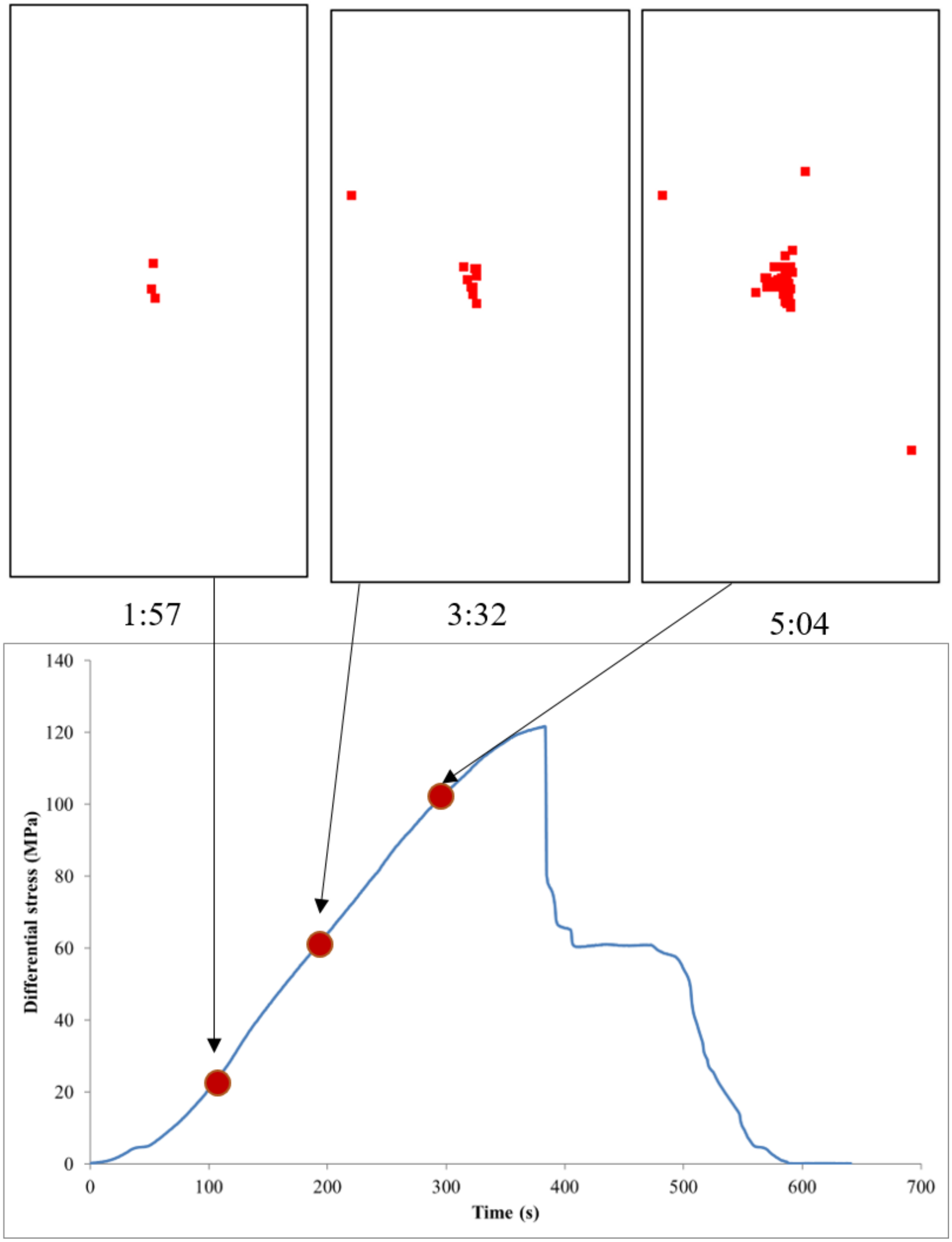
1:57
3:32
5:04
Differential stress (MPa)
Time (s)
0
20
40
60
80
100
120
140
0
100
200
300
400
500
600
700

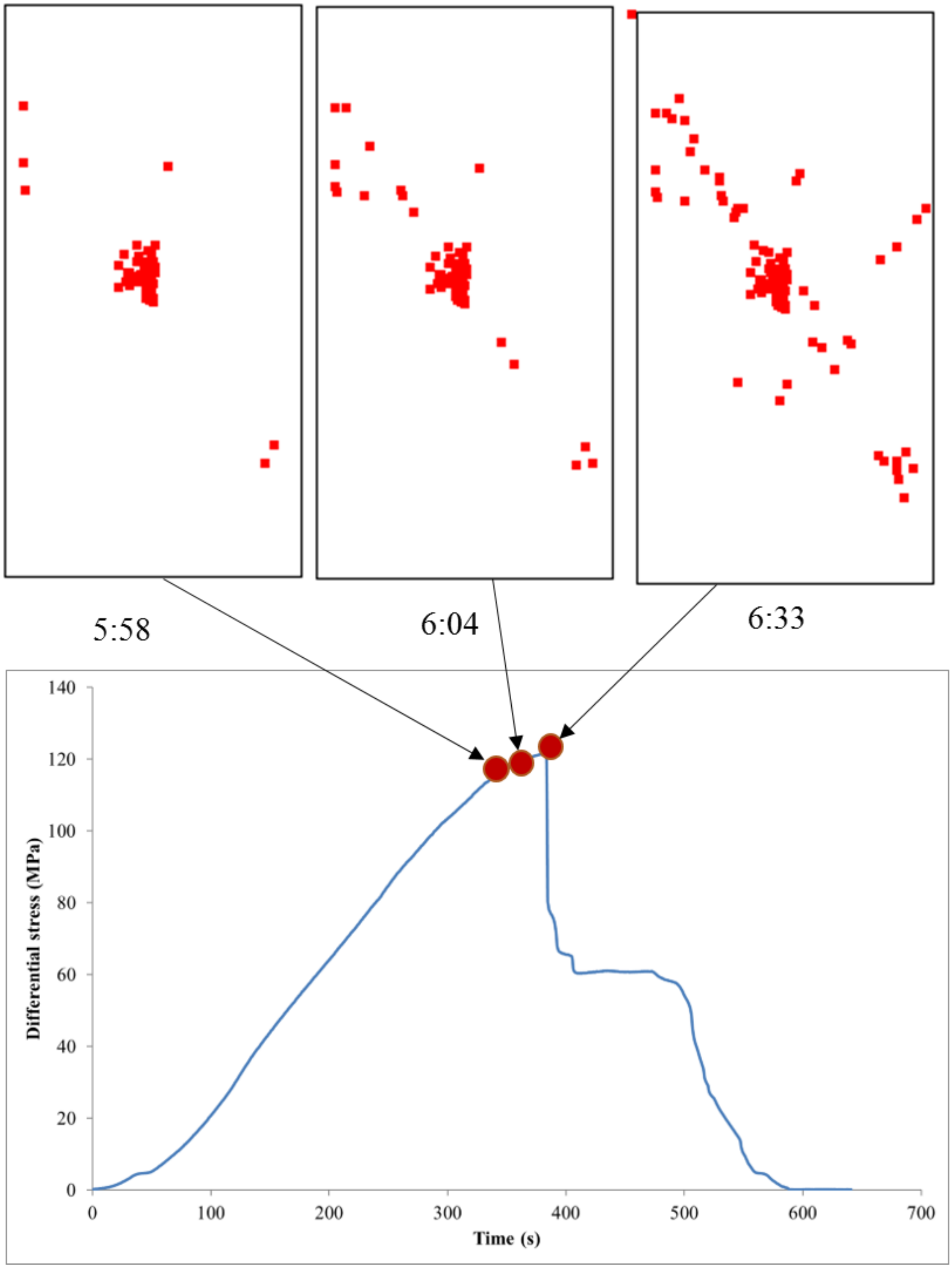
5:58
6:04
6:33
140
120
100
80
60
40
20
0
Differential stress (MPa)
0
100
200
300
400
500
600
700
Time (s)

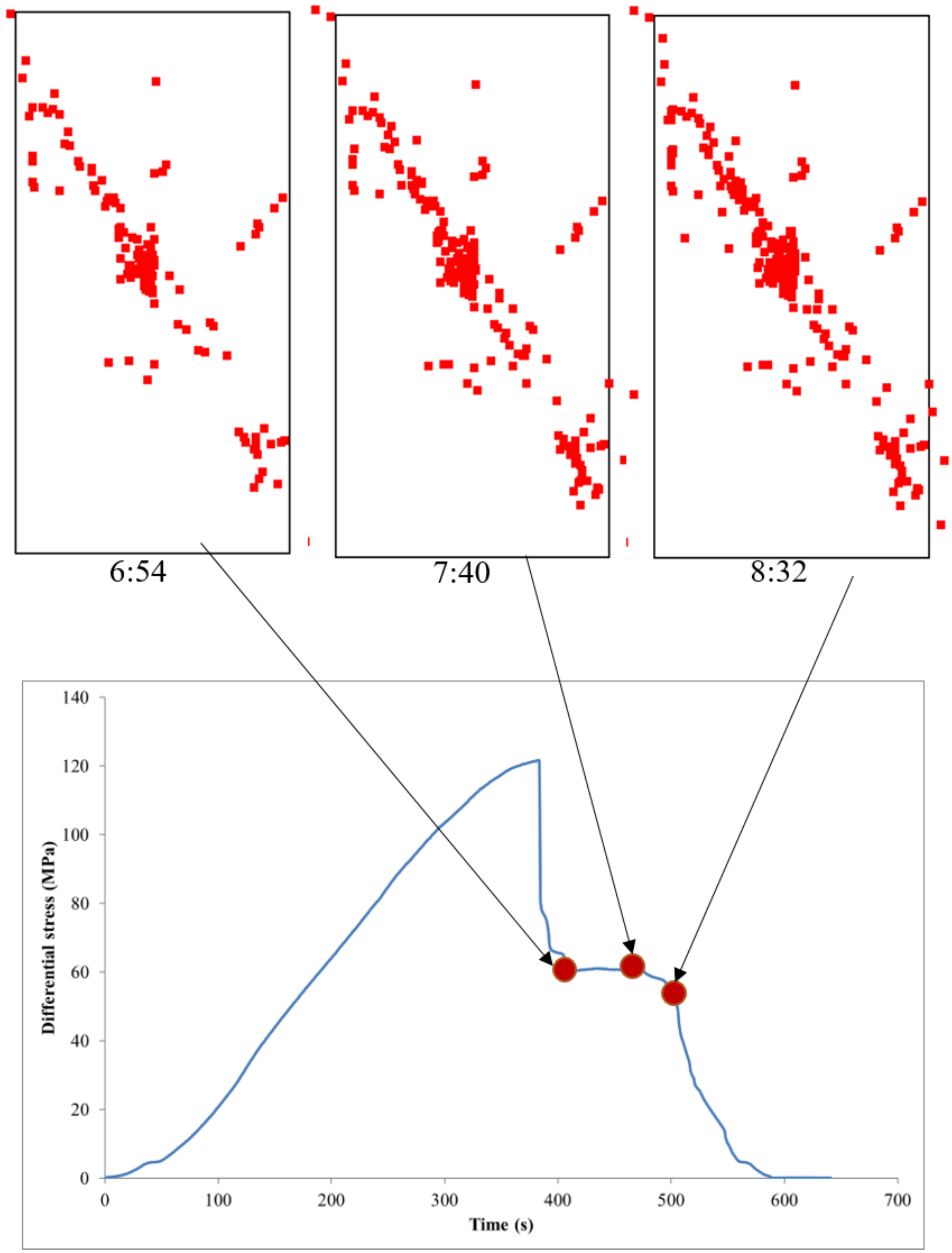

Figure 124: Time lapse plot for both differential stress and AE activity showing development of shear fracture in the Berea Sandstone Sample D.

As can be seen in this Figure 125, the shear fracture develops in the center fairly early into the loading of the sample. The top end bottom ends of the fracture develop almost simultaneously about 304 seconds into the process. The fracture reaches the top end at ~393 seconds and then develops fully in the next two minutes. As can be seen here, the failure is not sudden, the fracture development happens gradually. As will be seen later in this section for Sample GEO-N2-4243-I1 from GEO-N2 well, this isn't always true – sometimes fracture development may start just during failure and within 5-10 seconds develop fully.

SIERRA WHITE GRANITE

In the case of Sierra White granite sample, the triaxial test results have already been described in chapters 2 and 3. The Acoustic testing was done with nine sensors with an amplitude cut-off of 42-46dB. A digital filter was also used which restricted the frequencies only up to 100 kHz. Hence the results of the 3-D location became inaccurate as many of the signals from 100-400kHz were neglected.

Overall looking at the correlation between hit rate and stress, we can see that most of the events were generated during fracturing with very few generated close to failure. The total hit rate of ~400 hits during fracturing (Berea Sandstone had ~300) is higher than observed for any rock meaning that Granite has a good AE response.

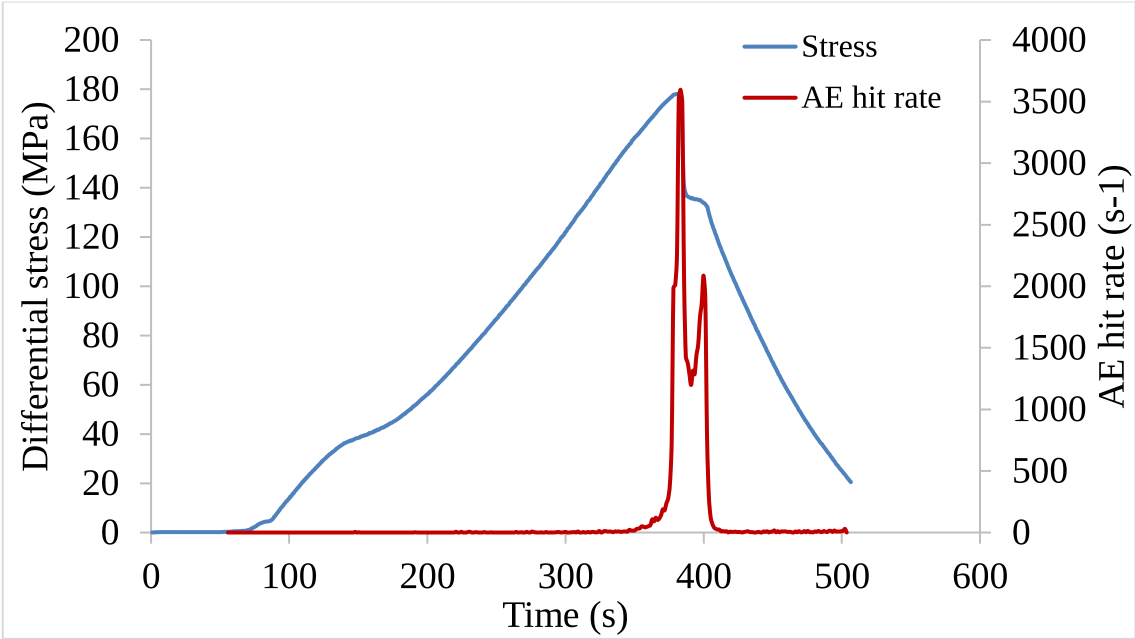

Figure 125: AE events rate when compared with differential stress for the triaxial-test. Most of the events were generated during fracturing.

From the Figure 126 and Figure 127, we can see that energy released close to failure is similar in magnitude to energy released during sliding. As in previous, two- three orders of magnitude difference can be seen between fracturing and sliding. The number of hits here almost matches the number of hits generated during fracturing and it's only the energy released plot which shows a clear distinction between sliding and fracturing.

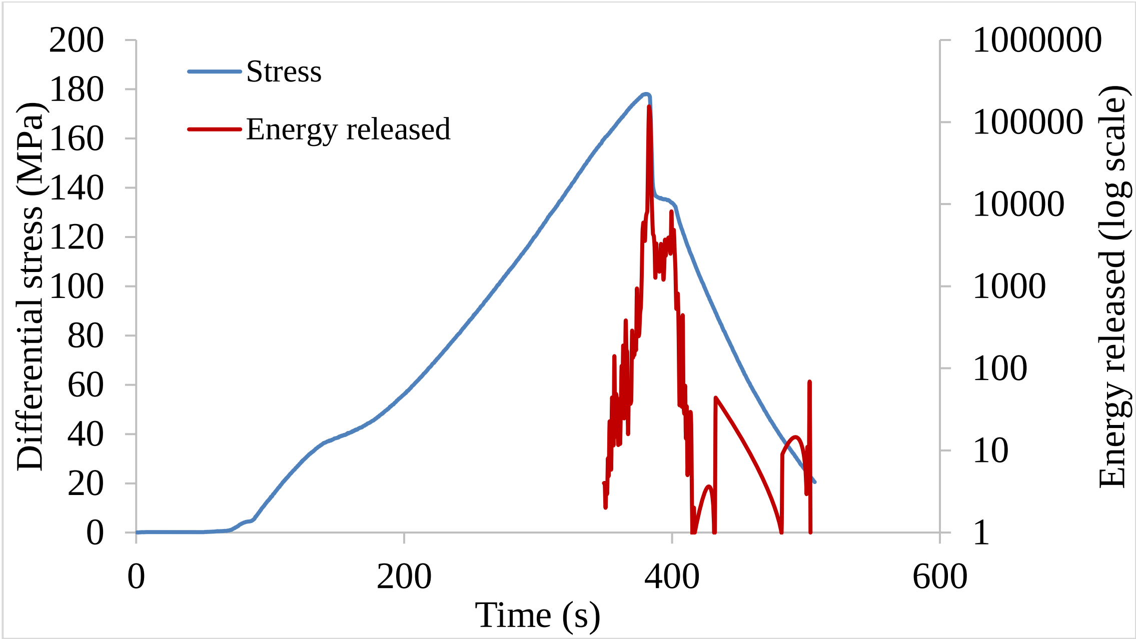

Figure 126: Differential stress versus energy released for Sierra White granite. Also see next figure for additional analysis on energy released.

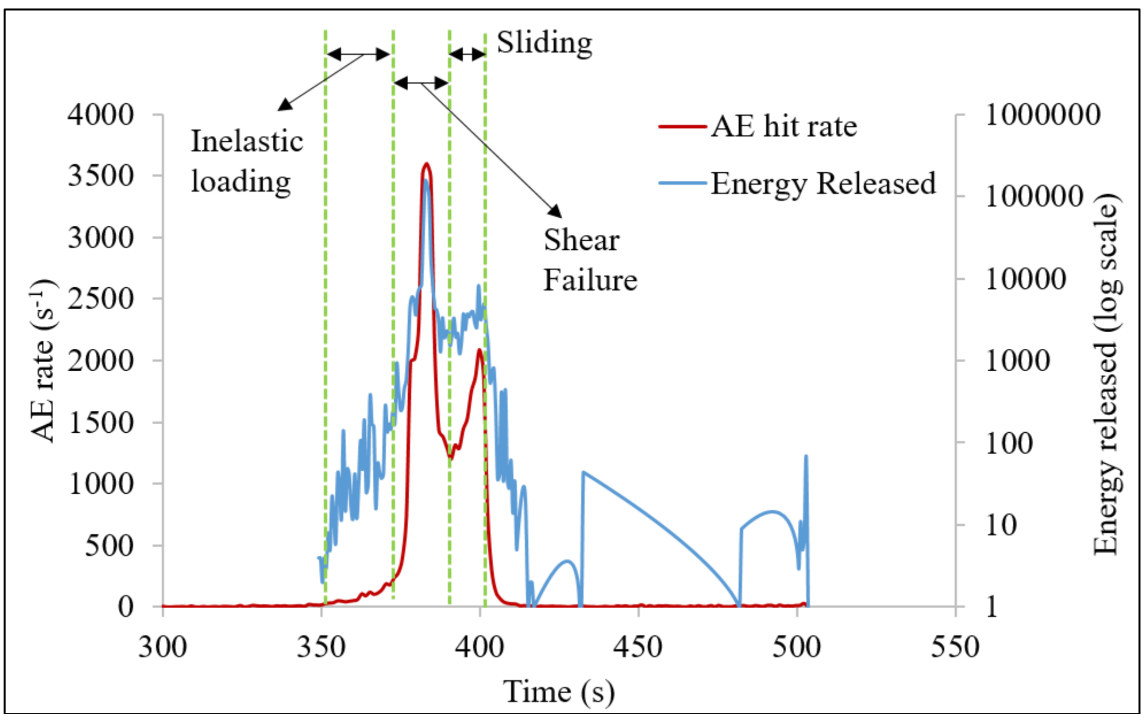

Figure 127: AE rate and energy released plot for Sierra white granite sample showing various sections for better understanding the micromechanical processes that the rock undergoes while triaxial loading.

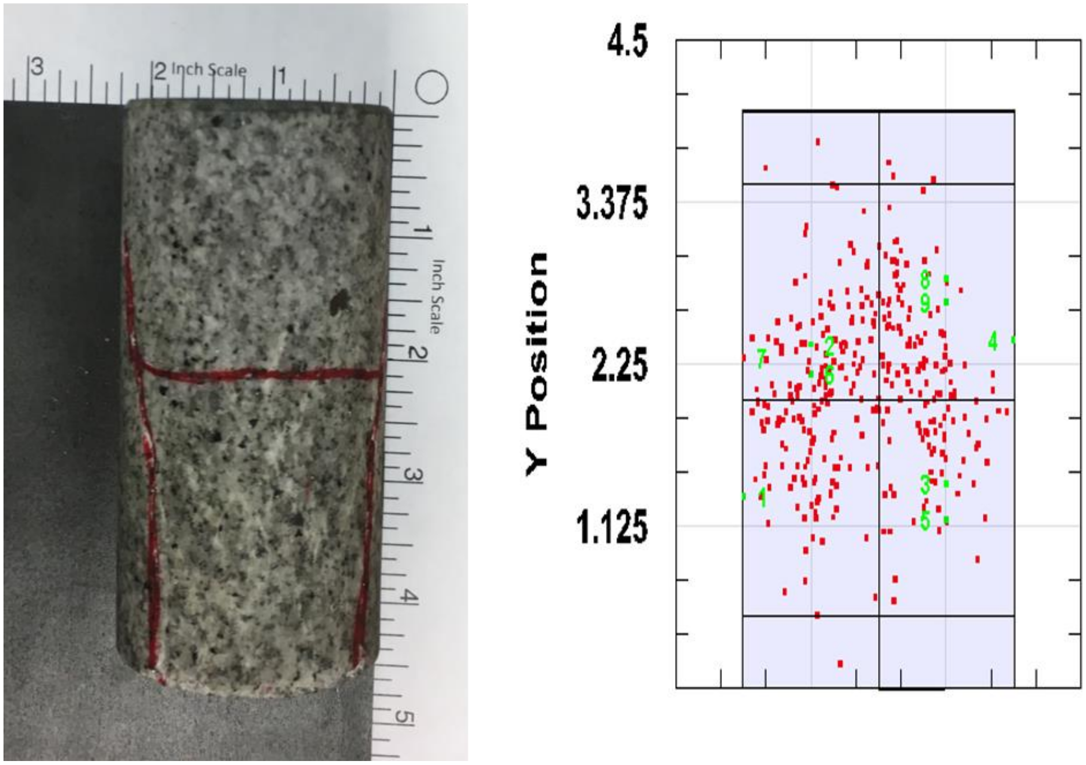

Figure 128: Figure showing a 2-D view of the location analysis done on the granite sample along with actual location of the fracture (marked using red, left figure). Due t confinig pressure being too low, fracture was not highly inclined.

BARNETT SHALE SAMPLE 01-45

AE plots for Barnett shale sample are shown in Figure 129 and Figure 130 below.

From the plots, we can see that this sample doesn't generate a lot of Acoustic emissions. For this sample, eleven AE crystals were used. Only eight worked satisfactorily though. This could be due to improper connections or non-adequate connection with the sample. Even then the AE rate per crystal is extremely low compared to other samples described earlier.

The energy and stress versus time plot shows the same, the factor here is one-two orders instead of three-four orders seen in earlier samples.

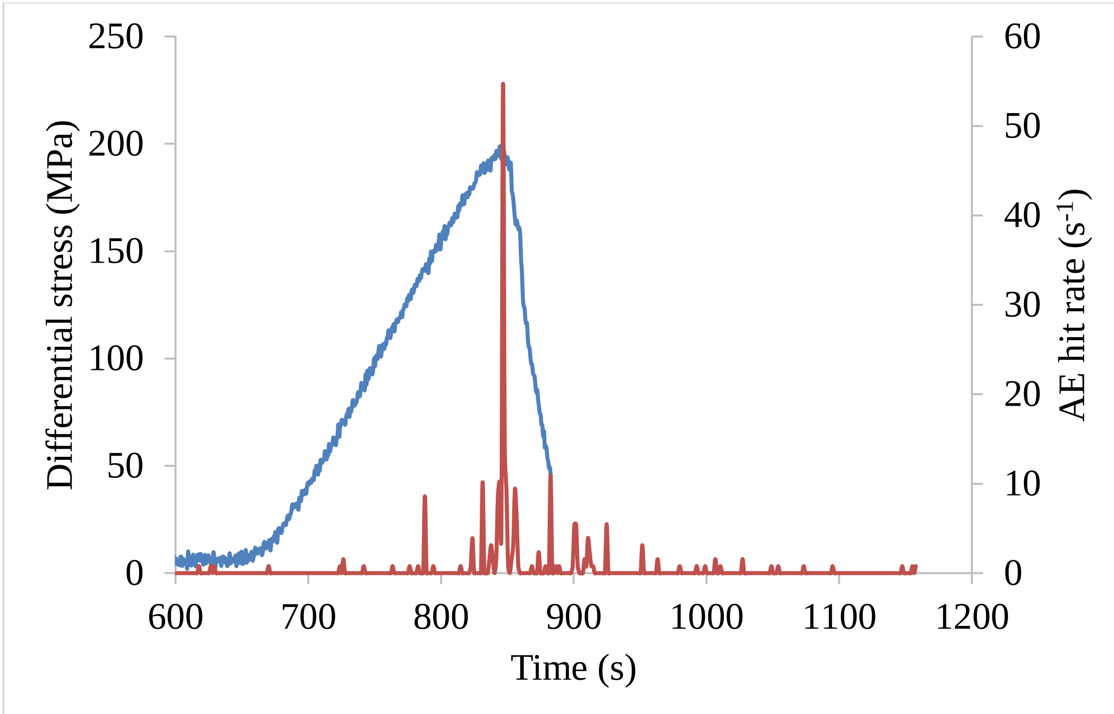

Figure 129: Stress and AE hit rate plot for Barnett shale sample 01-45

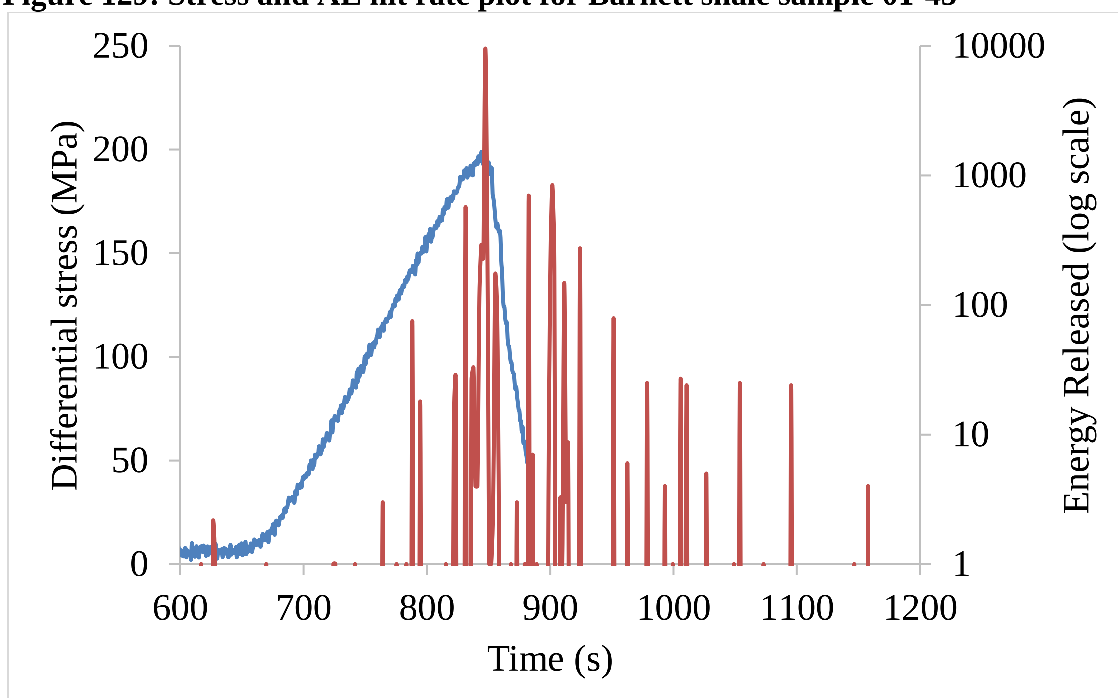

Figure 130: Stress and energy released plot for Barnett shale sample 01-45

No 3-D location plot is provided as the results were not satisfactory at all. This could be attributed to the very low number of hit/events observed with average number of hits observed at just 10 per crystals.

CORED SAMPLES FROM THE GEO-N2 AND THE OXY-72-03 WELL

Sample GEO-N2-4361-V3

Sample GEO-N2-4361-V3 was tested with eight sensors and at high temperature. Results for the triaxial testing have already been described in chapter 3. In terms of the AE response, a very weak response was seen despite the rock having a brittle failure. As can be seen from figure 105, the AE rate was restricted to 35 s^{-1}. These were generated using eight crystals which shows that the actual number of hits was very low. As will be seen later, all cored rocks from the GEO-N2 showed this type of behaviour. Nevertheless, a strong correlation between AE response and fracturing can be seen. It can be seen here that AE hits were also generated during loading of the sample in the 'elastic' region. These hits were however very few.

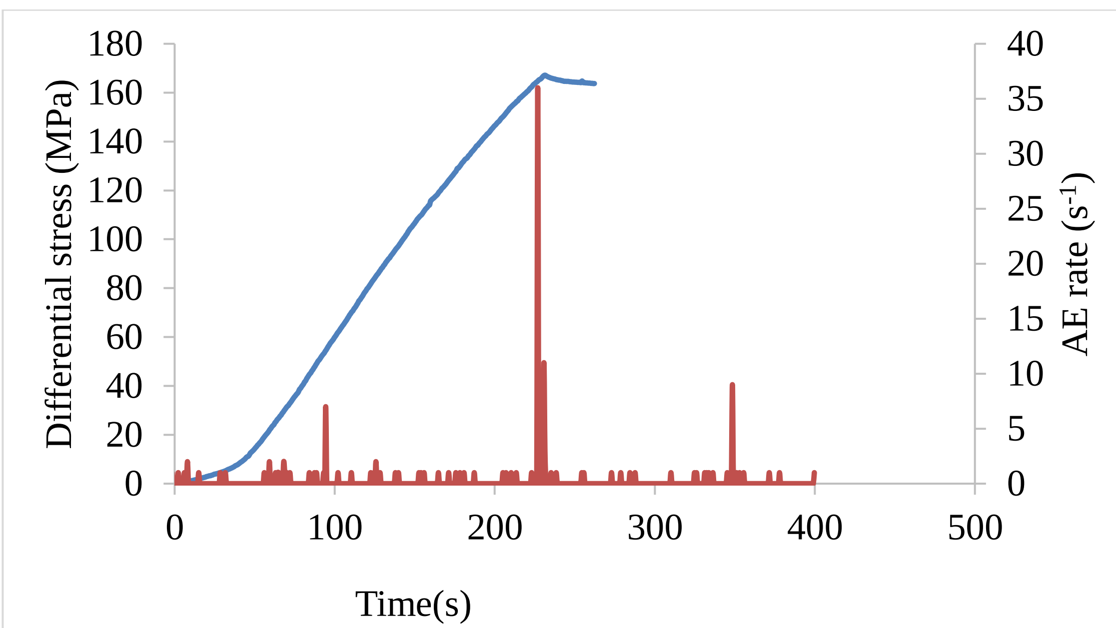

Figure 131: Stress and AE rate plot for sample GEO-N2-4361-V3.

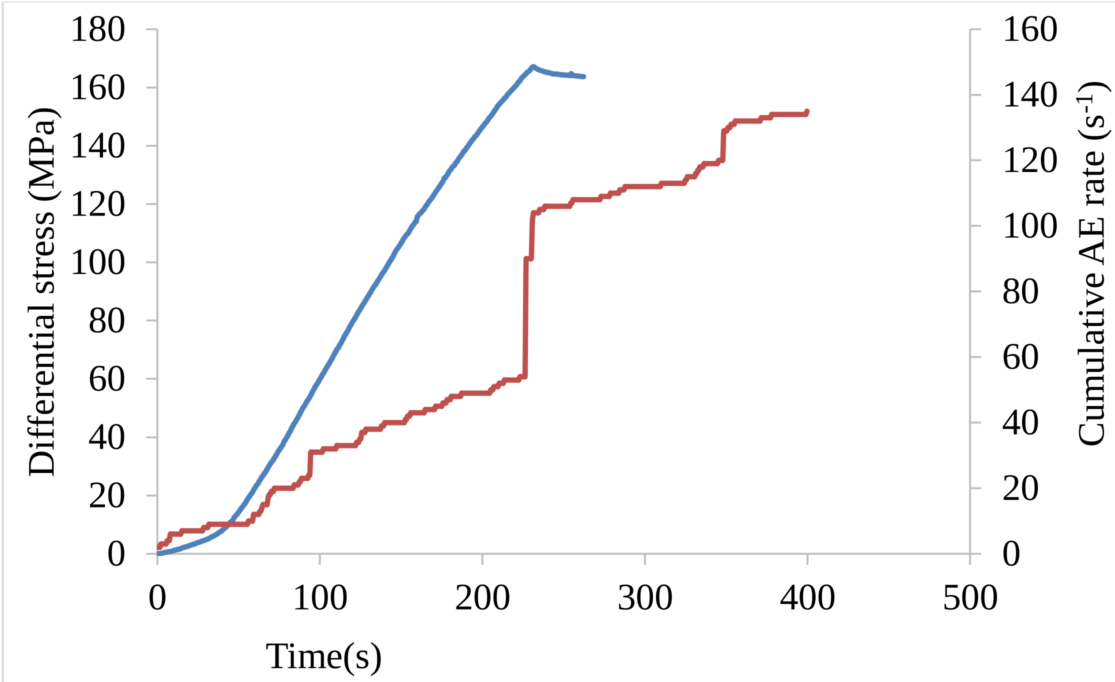

Figure 132: Cumulative AE and differential stress vs time plot for the GEO-N2-4361-V3 sample. The plot shows that even though most of hits are generated during fracturing event, many others are generated at different stages of loading as well. Also, refer fig 133 below. The overall number of hits is very low considering that these hits were recorded using eight AE crystals.

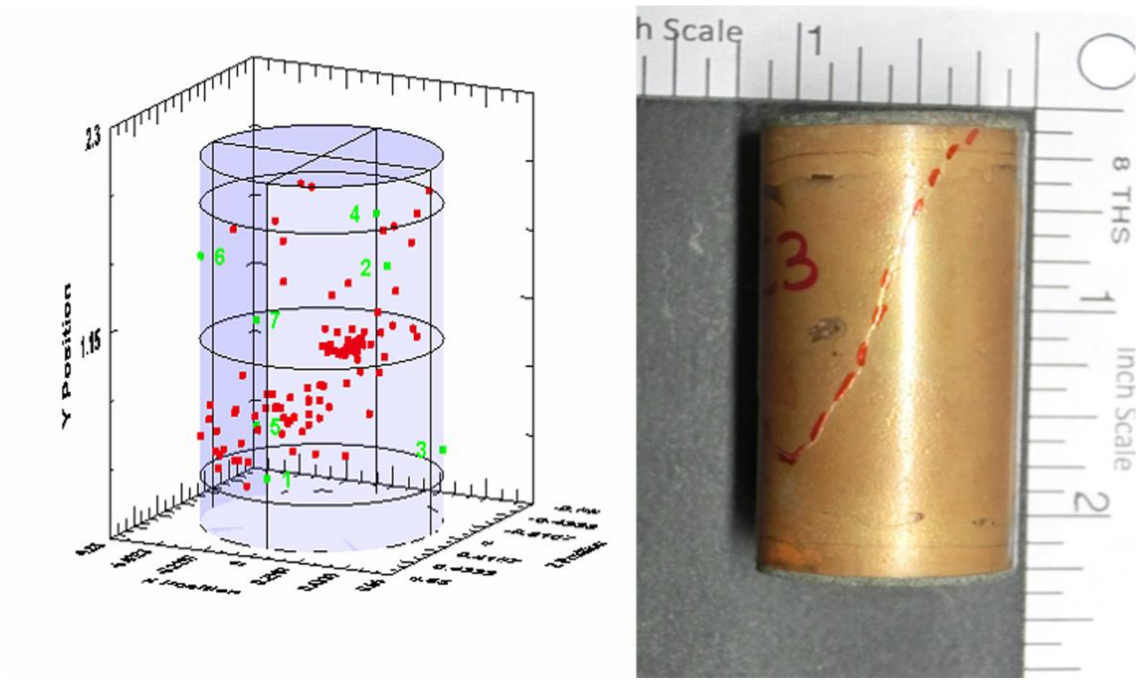

Figure 133: Figure shows Acoustic events recorded within the sample in 3-D using location analysis algorithm. An excellent correlation can be seen with the actual fracture location.

Sample GEO-N2-4361-V2

For the sample, GEO-N2-4361-V2, a very similar response as seen in sample GEO-N2-4361-V3 was seen. The total number of hits were 200 with the majority being generated during fracturing. These were also generated using 8 crystals. Loading can be seen to be inelastic from the beginning. These hits in the elastic region are due to the high temperature of the sample and may not have anything to do with the loading of the sample. The overall number of hits was low considering that this sample had 8 AE crystals.

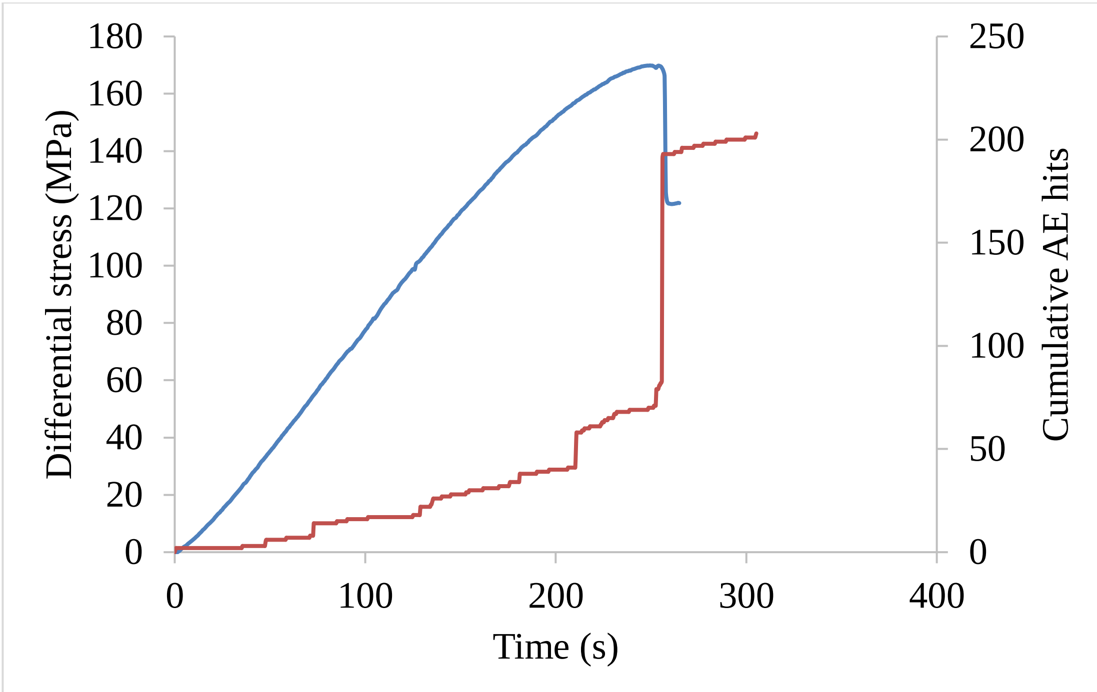

Figure 134: Cumulative AE events when compared with differential stress for the final triaxial-injection test. Similar to other samples, most of the events were generated during fracturing. Significant number of events were also generated during the initial part of the loading.

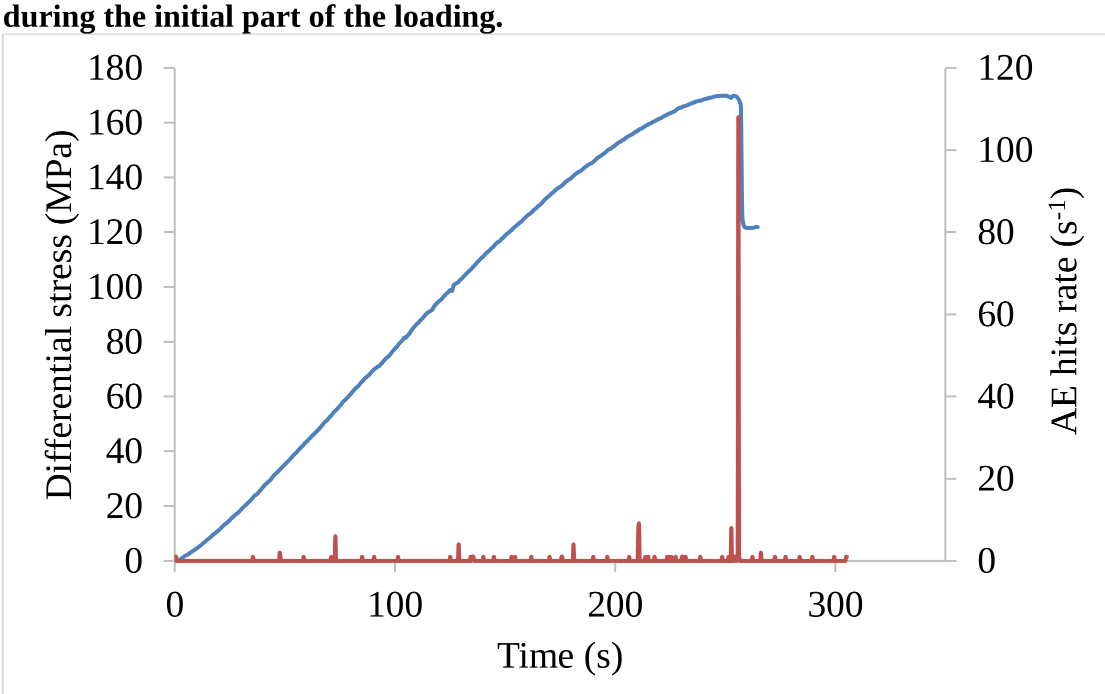

Figure 135: AE events rate when compared with differential stress for the final triaxial-injection test. Similar to other samples, most of the events were generated during fracturing.

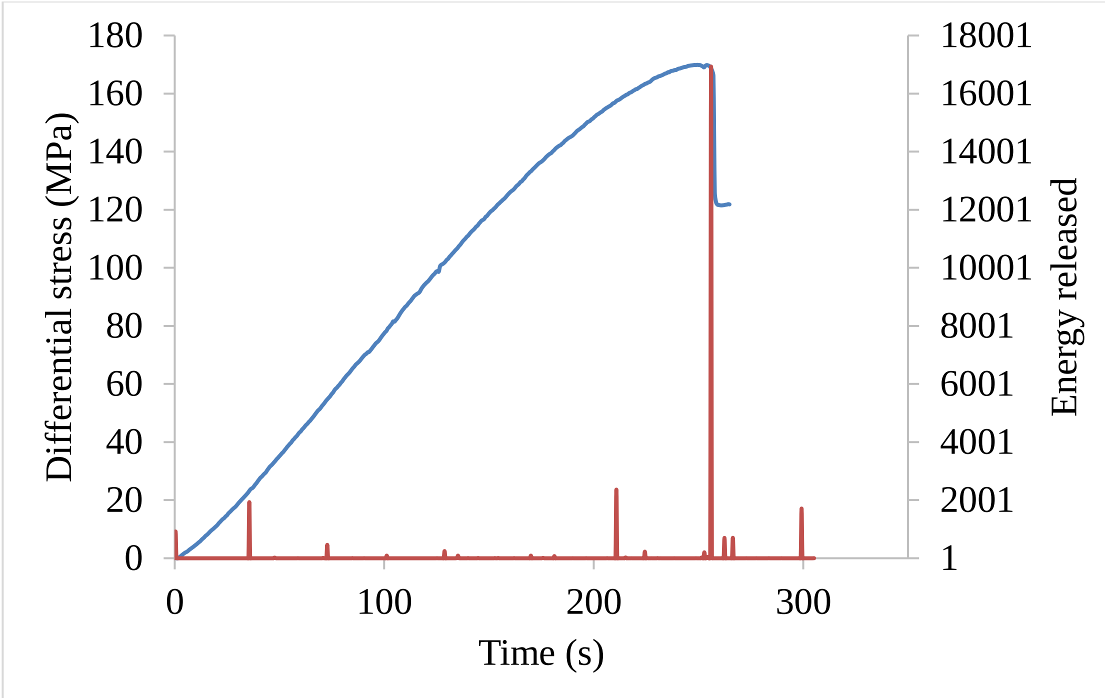

Figure 136: Energy vs stress differential stress for the final triaxial-injection test. This sample also released a large amount of energy on fracturing.

Observe Figure 136, this shows that the energy released during fracturing is only one order different than during fracturing. This behaviour was not seen in sandstone and granite where energy released early in the loading process or even close to failure was at least 2-3 orders lower than during fracturing. Combined with the low events detected, we can see that this rock's AE response is much lower as compared to other rock samples.

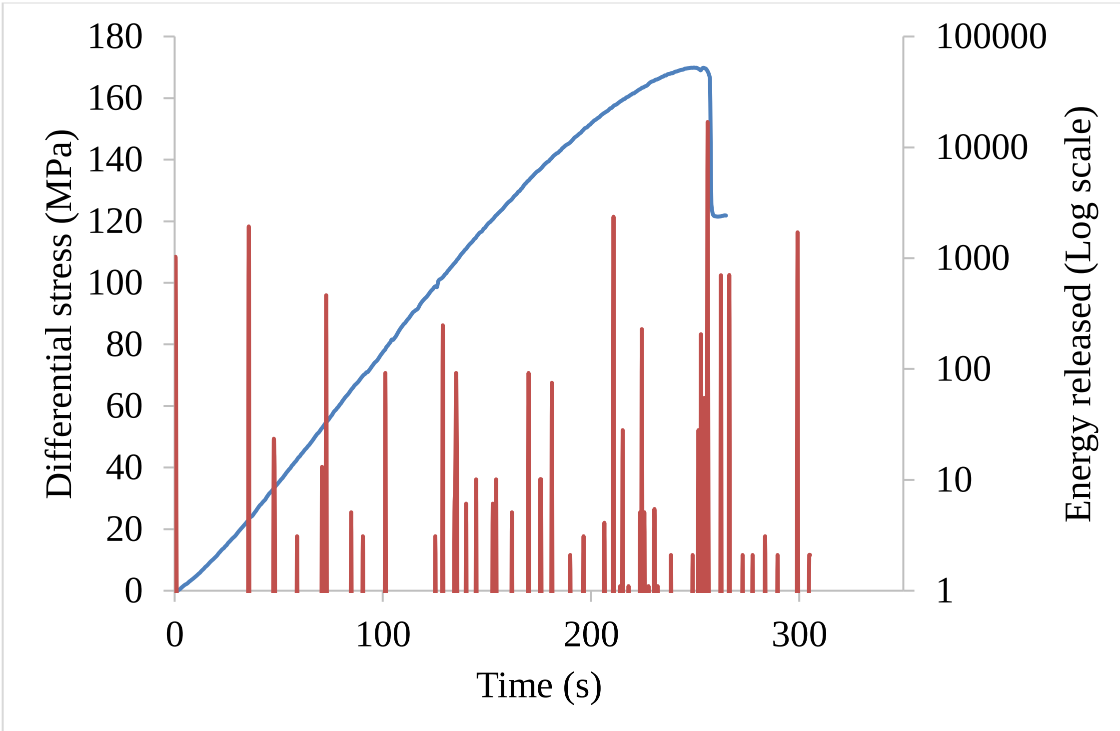

Figure 137: Stress and Energy released (log scale) during loading of the sample.

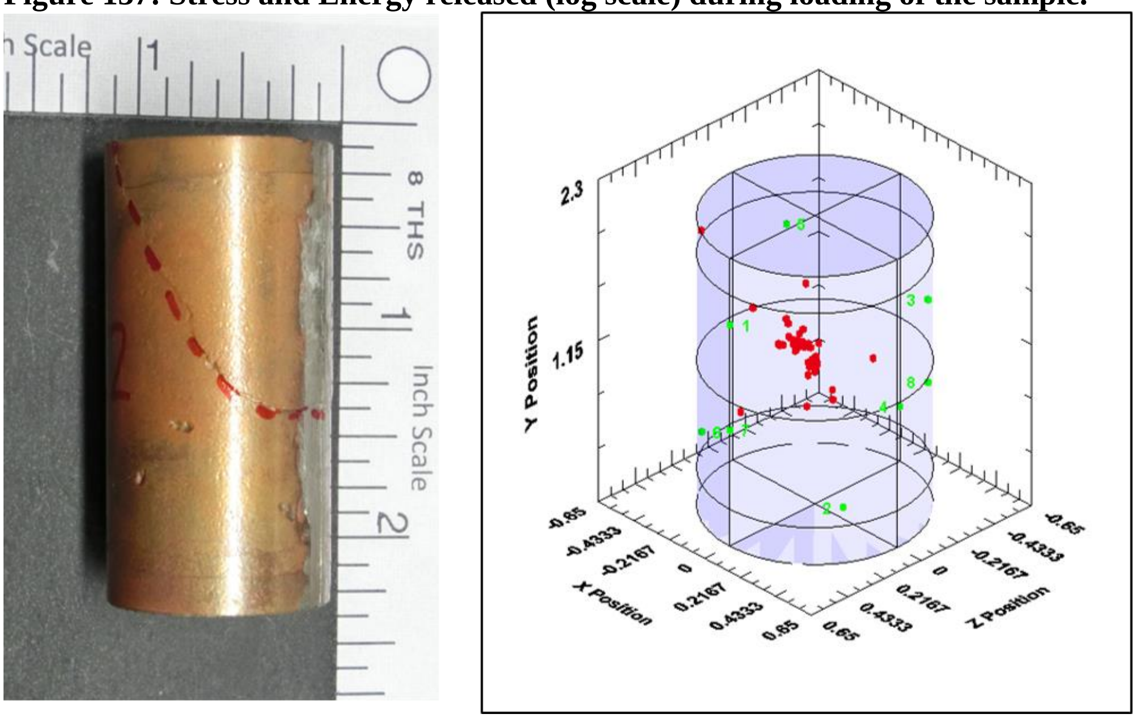

Figure 138:Comparison of actual fracture versus that predicted using AE data. A good correlation is not seen - this can be attributed to the very few events that got generated during the test.

Sample OXY-72-3-3861.5-V2

AE rate and cumulative number of events generated have been shown in below plots (Figure 139 and Figure 140). Following can be observed:

1. It can be noted that the number of AE events is very low (350 with 8 crystals) as compared to other rocks like sandstones or granites. Events were not continuously generated during loading of the sample and a larger number of events being generated closer to failure and after (sliding).
2. The largest number of AE events were registered when the sample failed. This is usually the case for most rocks.
3. 3-D location of events was carried out using AE information – the same is shown below in Figure 141. It should be noted that due to the very few events generated, this wasn't found to be representative when compared with the actual sample's fracture plane.

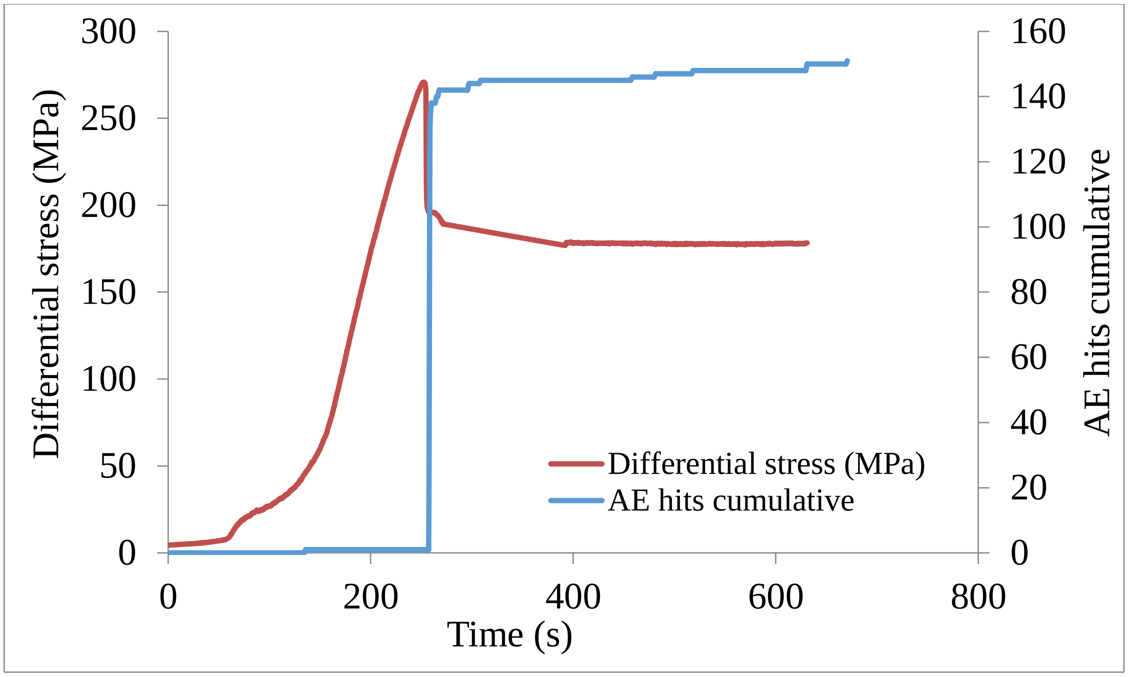

Figure 139: Differential stress and cumulative AE hits vs time for sample OXY-72-3-3861.5-V2. Note that's sliding based AE's can also be seen.

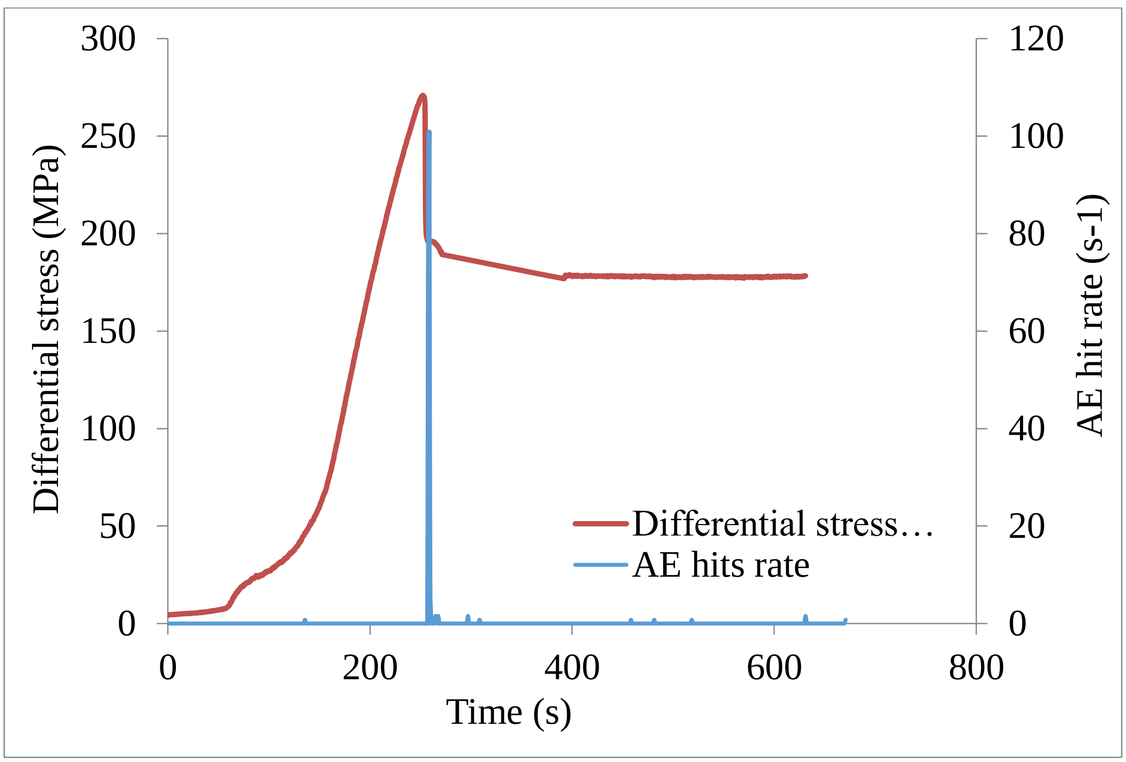

Figure 140: Differential stress and AE hits rate vs time for sample OXY-72-3-3861.5-V2

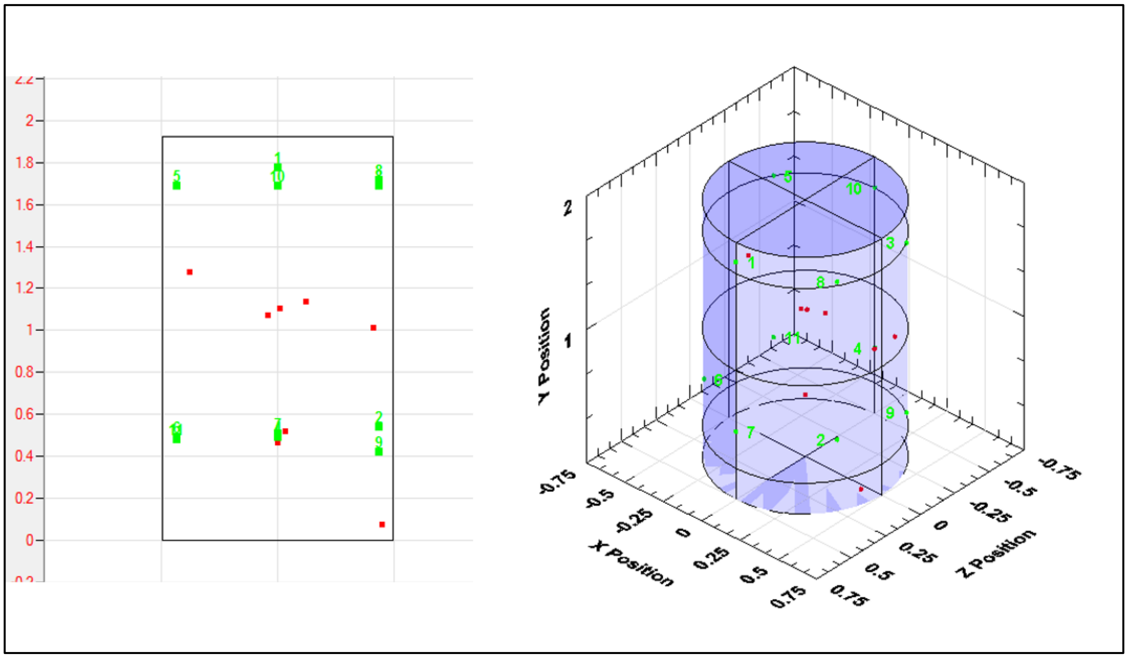

Figure 141: Figure shows Acoustic events recorded within the sample in 2-D (left) and 3-D using location analysis algorithm. The number of events can be seen to be very low. This is attributed to the rock type – very low events even though amplitude cut off wasn't very high (~50 dB).

Sample GEO-N2-4180-H1

The sample registered a very low number of Acoustic events and there isn't a strong correlation between AE and stress – even in the initial loading period some events are observed unlike Berea sandstone. However, the number of events increases substantially after failure which could be due to micro fractures formation after failure. An interesting feature can be observed when we look at the individual crystal response. One of the platens registers a high-energy event at about 1700 seconds into the test. The other platen doesn't register this event. Correlating the stress – strain plots with the permeability we can say with confidence that this is the time at which the local fracture was formed. On actual observation of the sample after the test it as observed that the fracture began from the end facing bottom platen and this platen was the one which recorded the acoustic event.

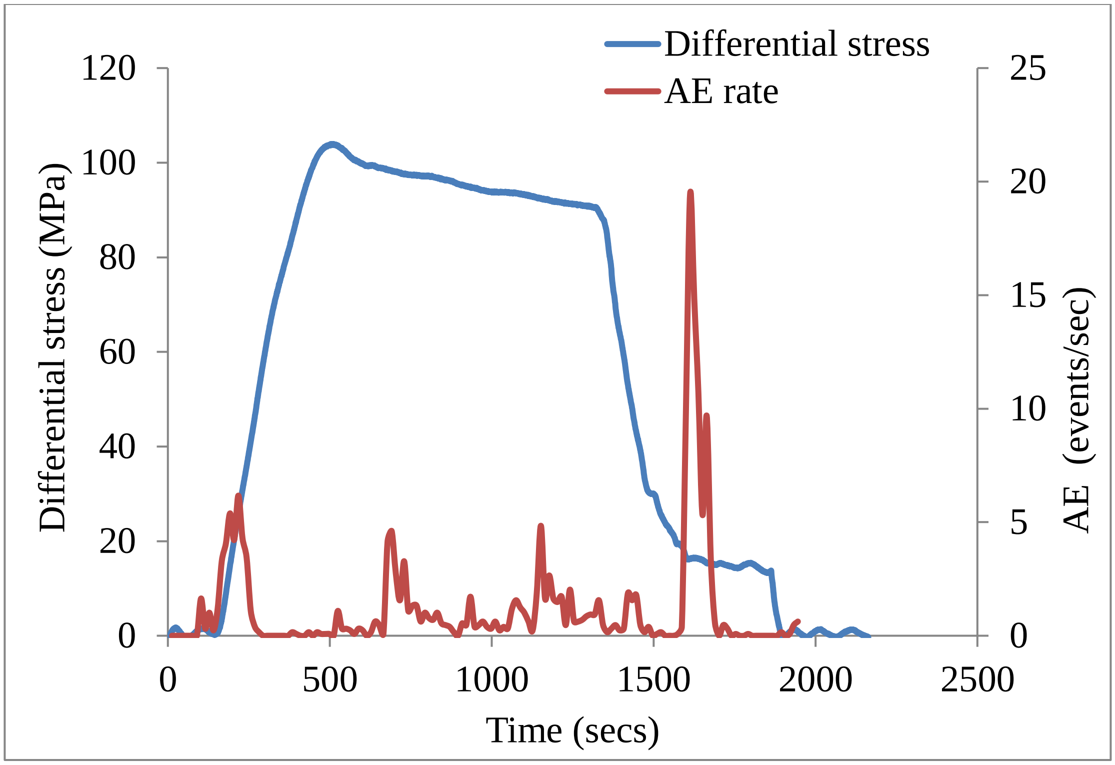

Figure 142: Relationship between Stress and AE events for sample GEO-N2-4180-H1.

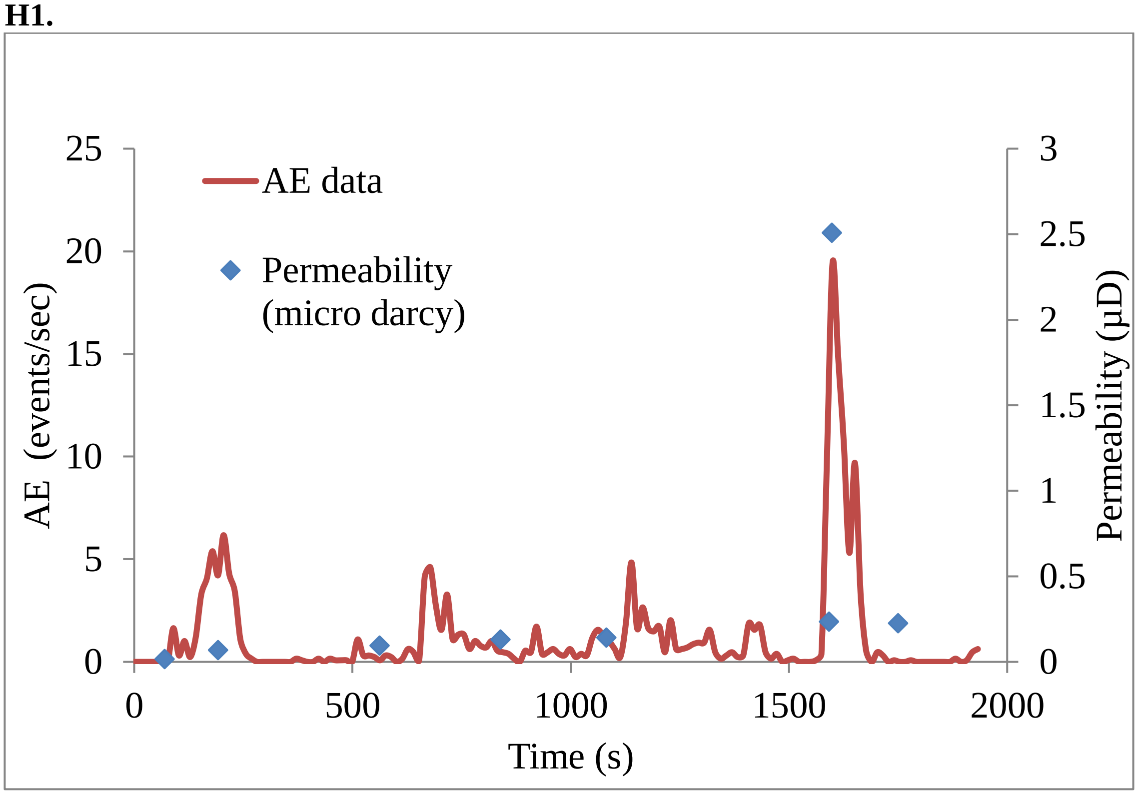

Figure 143: Relationship between Permeability and AE events

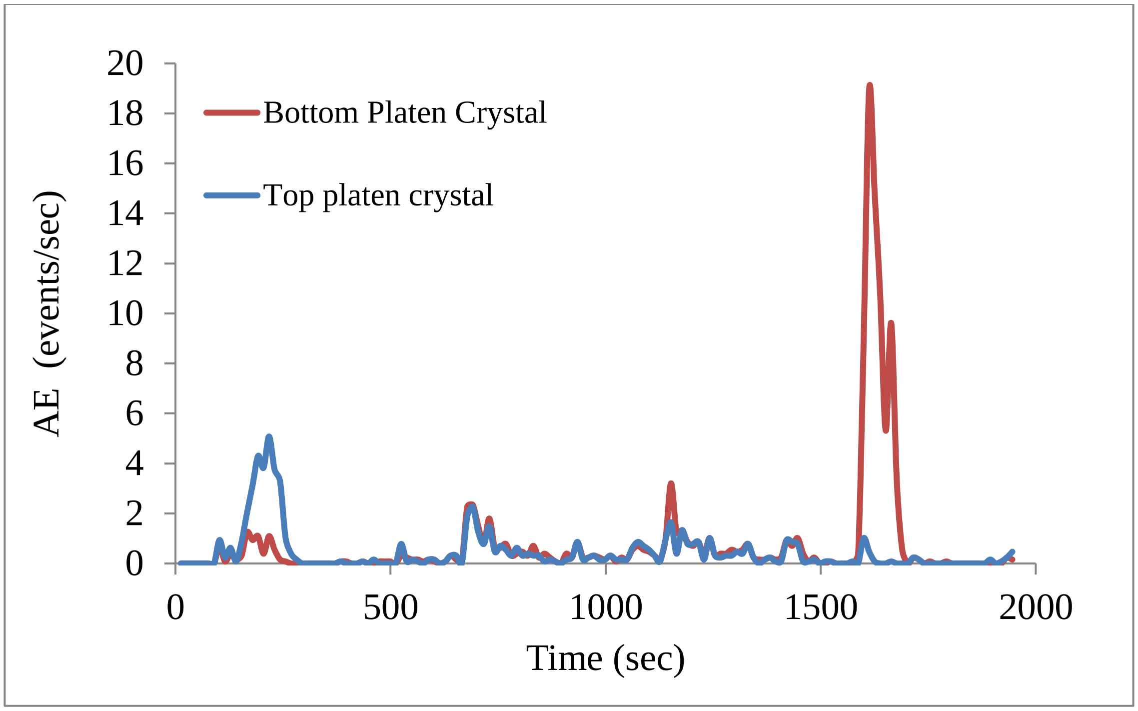

Figure 144: AE rate for individual platens for sample GEO-N2-4180-H1

Overall for cored GEO-N2 and OXY-72-03 samples, lower number of acoustic emissions were observed during testing of the samples. When the sample was brittle (section A, section C samples) the number of hits was higher but only marginally. The AE's correlated well with the generation of fracture. This shows that MEQ's can be expected to be generated during actual fracturing but their actual number will be far smaller (less by 10 times) as normally with sandstones. The location analysis worked well for only one out of three samples for which it was tried. One reason for this was the low number of AE events recorded during the test.

GEO N2 FULL CORE SAMPLES

All six of the samples with the exception of GEO-N2-4300-I3 were tested with AE monitoring. The large area of the cores made it much easier to use AE sensors on these samples as compared to cored plugs for which results have been described above. Results are provided along with description for each sample below.

Sample GEO-N2-4300-I1

This sample was tested with ten AE crystals – the triaxial and permeability results have already been discussed in chapters 2 and 3. A filter restricted the AE hits to frequencies less than 100kHz. An amplitude cut-off of 40-50 dB was applied during the testing. Plots 119 to 121 show the response of acoustics during loading – we can see that as the sample approaches failure, AE events are generated. This is especially true for when the actual fracturing takes place which generates the highest AE rate. It should be noted here that even though AE events were generated during the fracturing process, there number is quite small which is indicative of ductile behavior. The energy plot shows that most of the energy release was during fracturing (Figure 145). The magnitude of energy release when compared between different samples is a qualitative parameter which gives an indication of the irreversibility of the operation – larger energy release is associated with a more irreversible process then one with a low energy release.

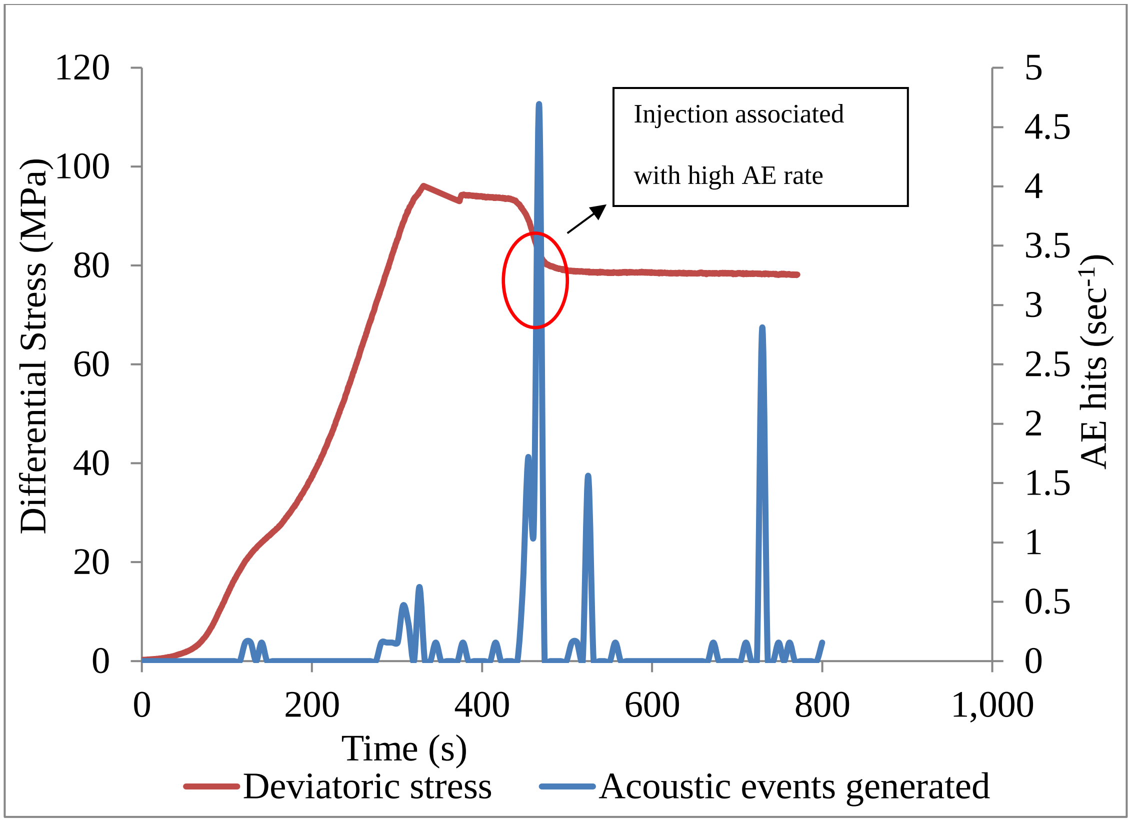

Figure 145: AE generation rate and corresponding stress versus time plot for sample number one. AE generation starts picking up as sample approaches failure. Clearly the AE rate even during fracturing is very low (<5 hits/sec).

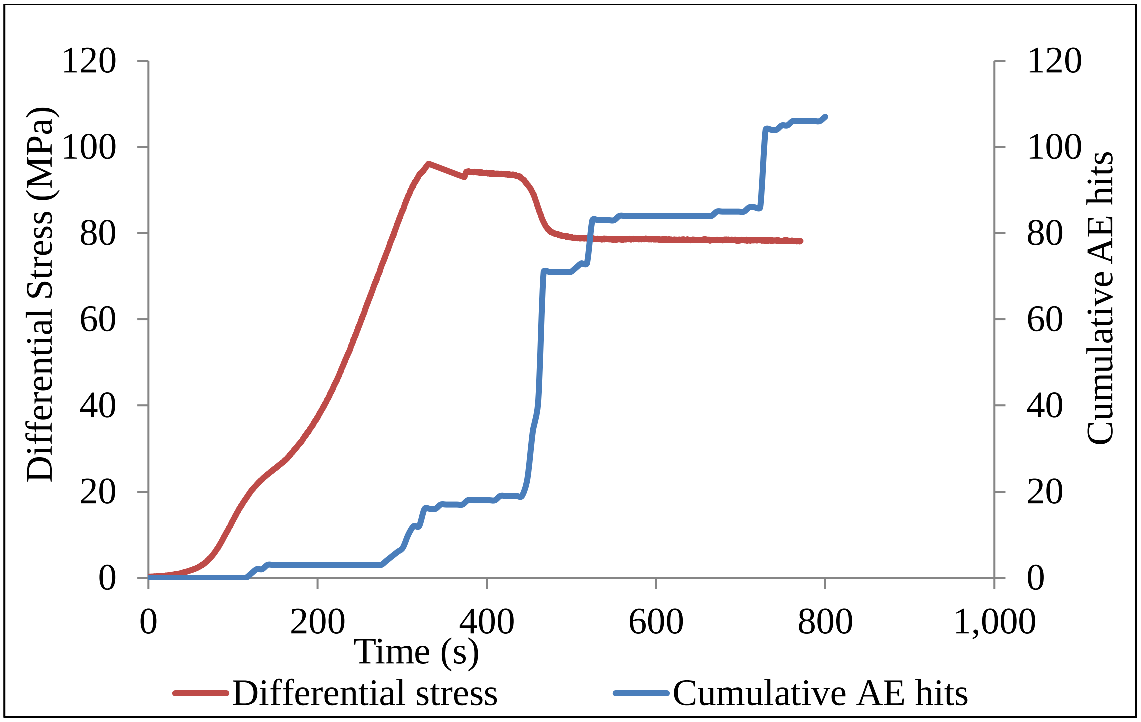

Figure 146: Cumulative AE generated and corresponding differential stress versus time.

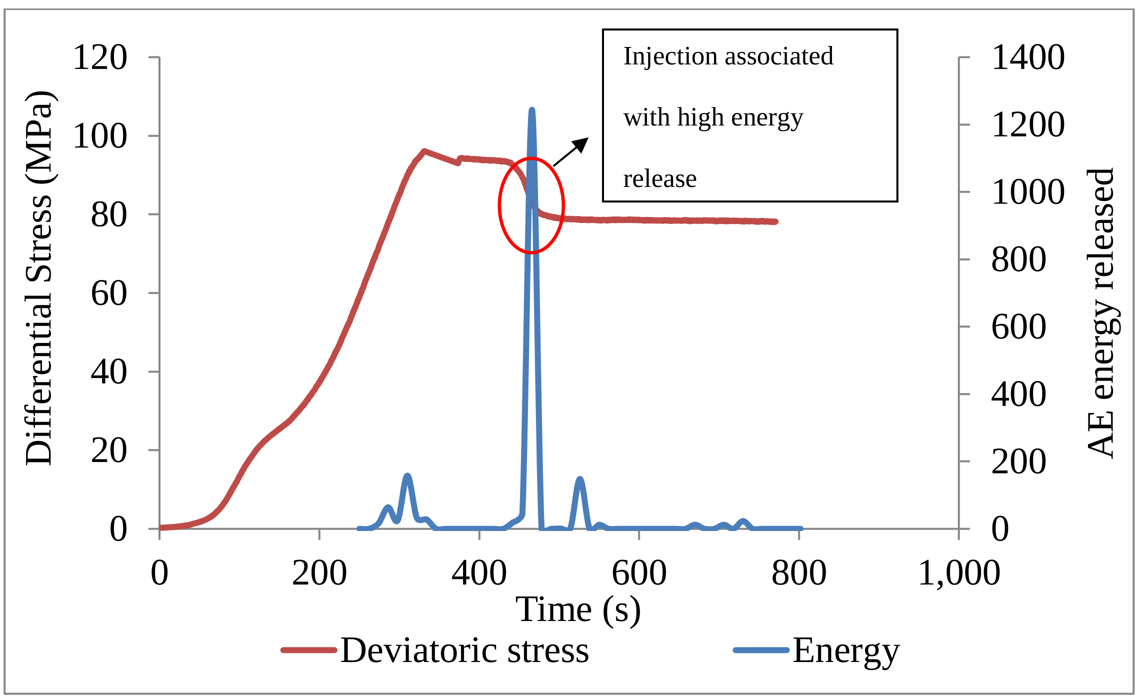

Figure 147: Stress and Energy released versus time for GEO-N2-4300-I1.

After the triaxial-injection test was complete, fluid flow at a high differential was maintained across the sample to evaluate its sliding characteristics. During this process, the 2-D and 3-D location of events was carried out while removing the frequency filter. Figure 122 shows the results of the location analysis. A reasonably good correlation can be seen with the actual location of the fracture. Figure 123 shows these results in 3-D space.

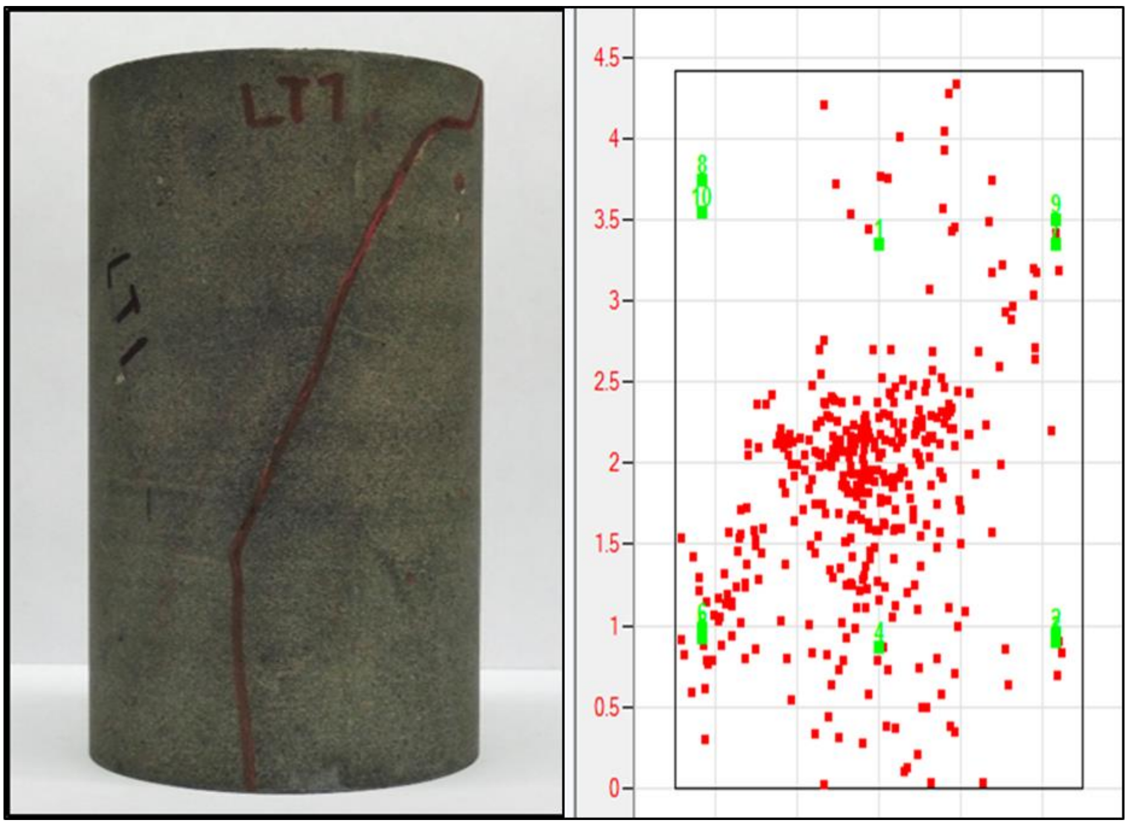

Figure 148: Figure showing 2-D location analysis plot as generated for GEO-N2-4300-I1. The prediction of fracture is reasonably accurate although the location analysis picks up points away from the fracture as well (more diffused). The 2-D plot juxtaposes the whole sample's AE events in 2-D space so while the back of the sample is not shown in the picture above, this plot shows those events as well.

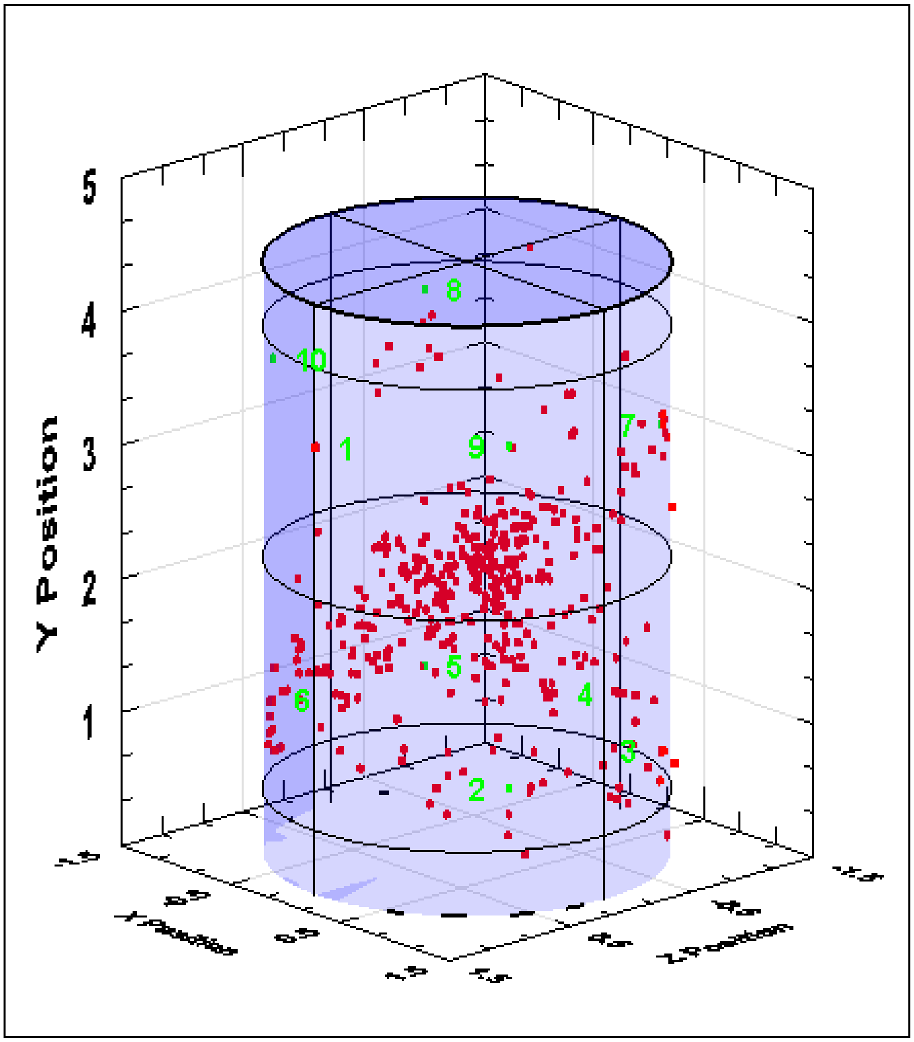

Figure 149: 3-D location analysis carried out on GEO-N2-4300-I1. We can see from the plot that the AE is mainly generated in the location of the existing healed fracture. This matches well with actual observations seen in the sample regarding fracture location.

Sample GEO-N2-4300-I2

This sample was tested with nine AE crystals – the triaxial and permeability results have already been discussed in chapters 2 and 3. A filter restricted the AE hits to frequencies less than 100kHz. An amplitude cut-off of 45-50 dB was applied during the testing for all crystals.

Plot 124 shows the response of acoustics during loading – we can see that as the sample approaches failure, AE events are generated. This is especially true for when the actual fracturing takes place which generates the highest AE rate.

It should be noted here that even though AE events were generated during the fracturing process, there number is quite small which is indicative of ductile behavior.

Just like GEO-N2-4300-I1, after the test was complete, fluid was flown through the sample which generated AE hits. These were analyzed to generate the 2-D and 3-D location figures as shown in Figure 151 and Figure 152. The location of events is not fully accurate – it predicts two major fractures instead of just one seen in the sample.

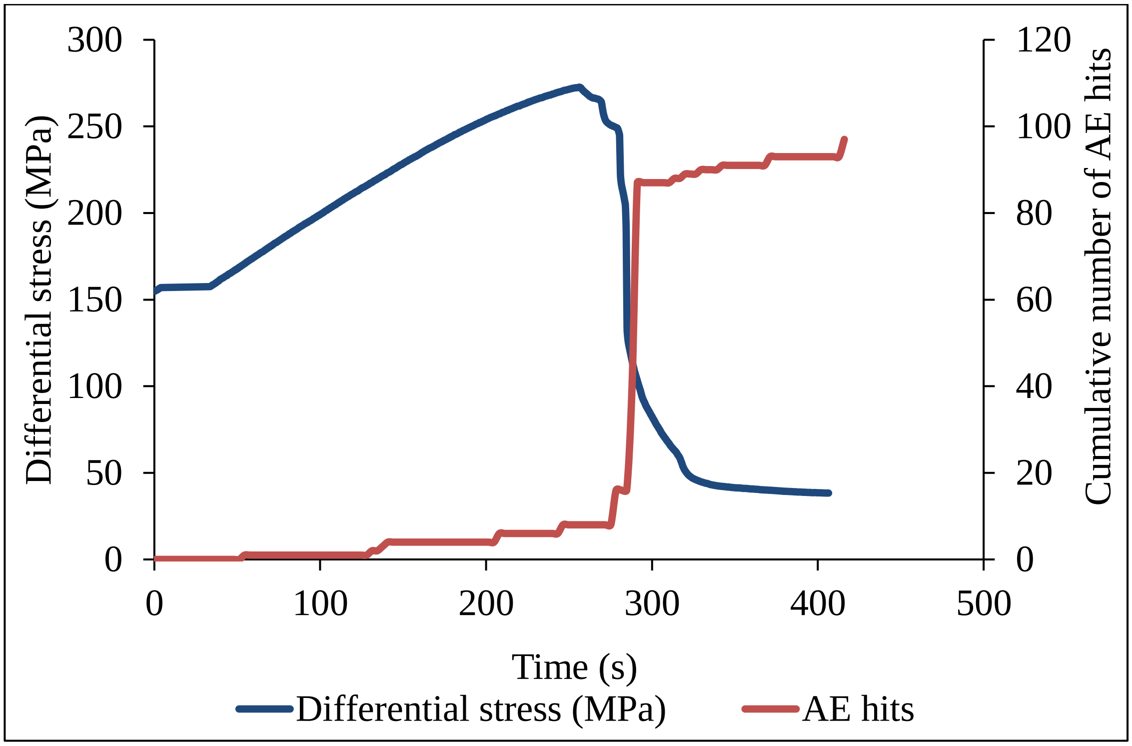

Figure 150: AE plot for GEO-N2-4300-I2 shows the Acoustic events generated during part two of the test (triaxial compression). The plot shows that most of the hits are generated during the fracturing process. The frequency response allowed for hits was restricted to 100 kHz.

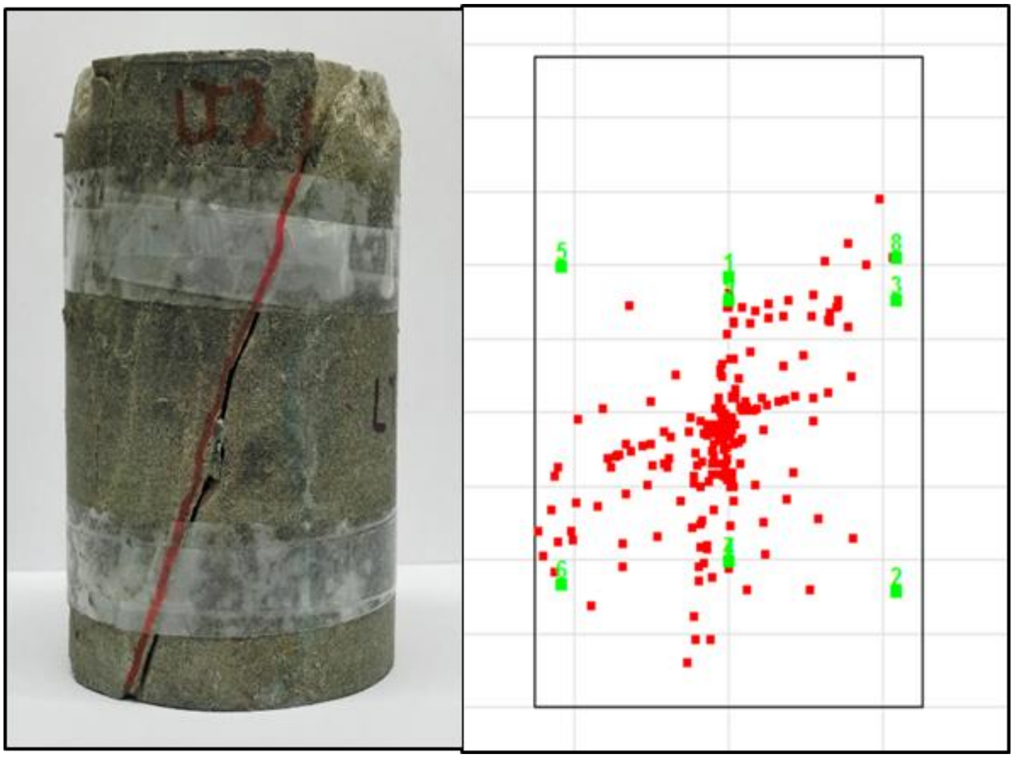

Figure 151: Figure showing 2-D location analysis plot as generated for GEO-N2-4300-I2. The prediction of fracture can be seen not to be fully accurate.

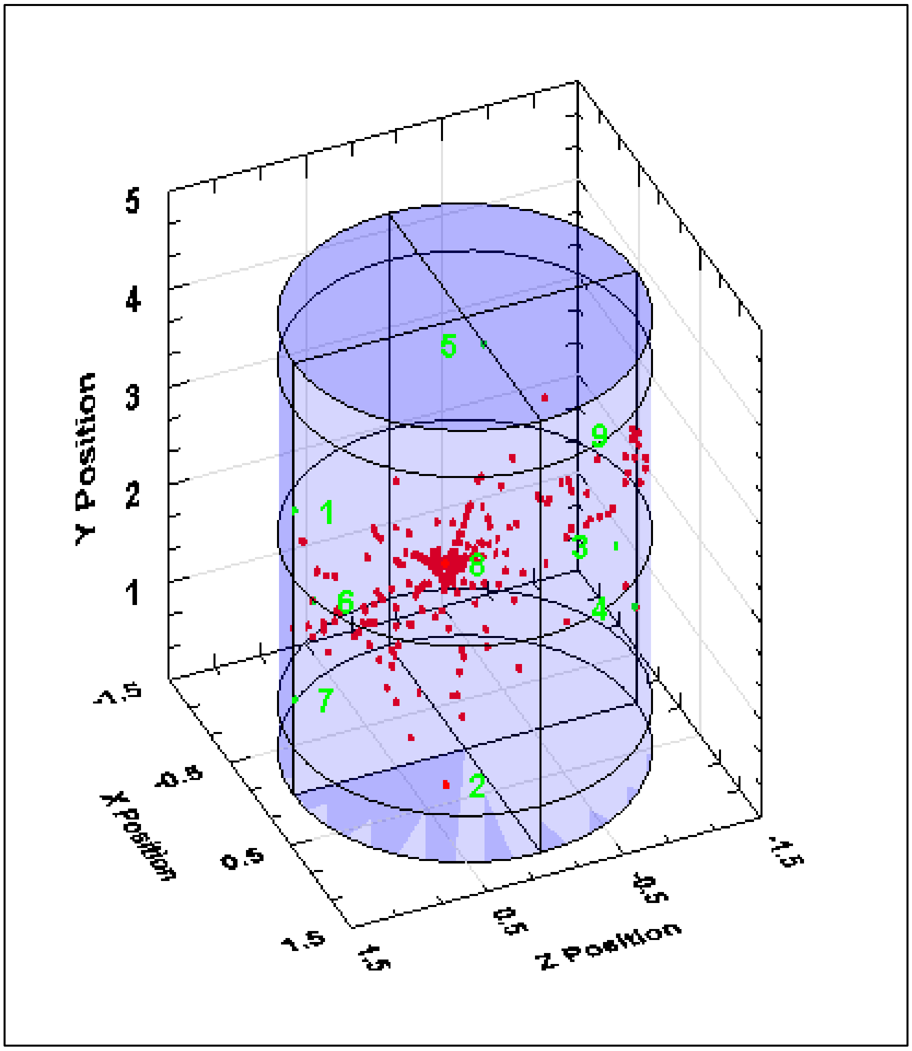

Figure 152: 3-D location analysis carried out on GEO-N2-4300-I2. We can see from the plots that the AE is mainly generated in the location of the fracture. The generated 3-D location is not completely accurate – it fails to pick up more events close to the ends.

Sample GEO-N2-4300-I4

This sample was tested with eight AE crystals – the triaxial and permeability results have already been discussed in chapters 2 and 3. No frequency filter was used for this test. An amplitude cut-off of 55-60 dB was applied during the testing to remove noise. Plots 119 to 121 show the response of acoustics during loading – we can see that as the sample approaches failure, AE events are generated. This is especially true for when the actual fracturing takes place which generates the highest AE rate. It should be noted here that even though AE events were generated during the fracturing process, there number is quite small which is indicative of ductile behavior. The energy plot shows that most of the energy release was during fracturing (Figure 145). The magnitude of energy release when compared between different samples is a qualitative parameter which gives an indication of the irreversibility of the operation – larger energy release is associated with a more irreversible process then one with a low energy release.

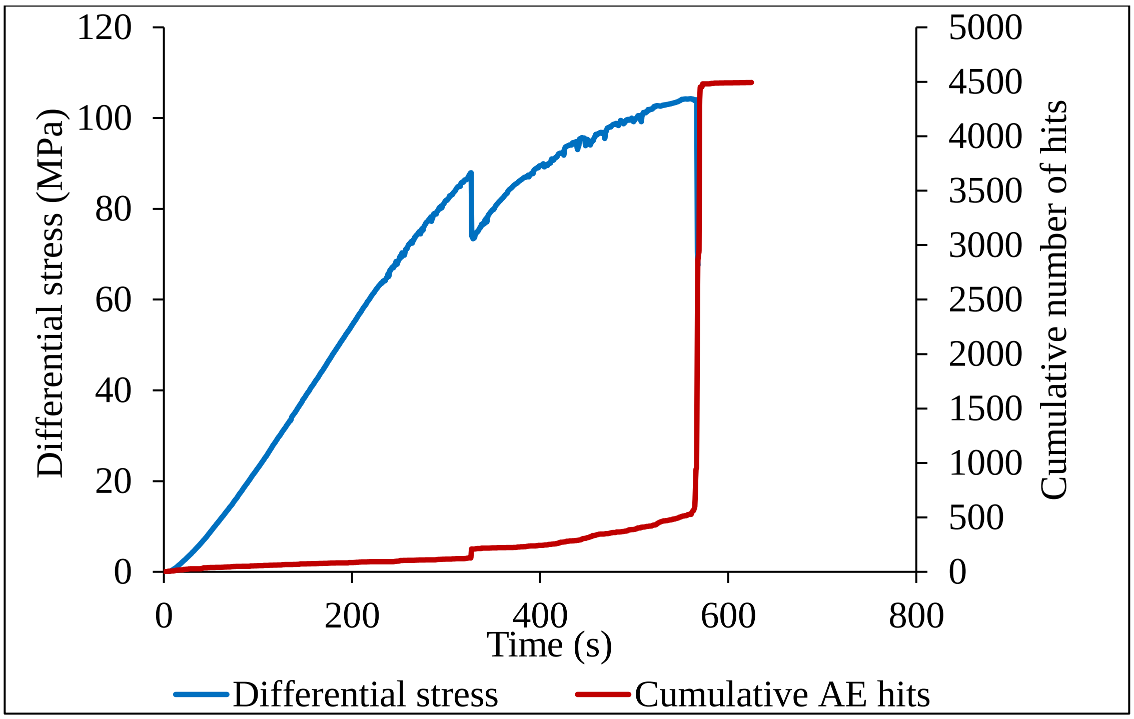

Figure 153: AE plot for sample GEO-N2-4300-I4 shows the Acoustic events generated during triaxial compression.

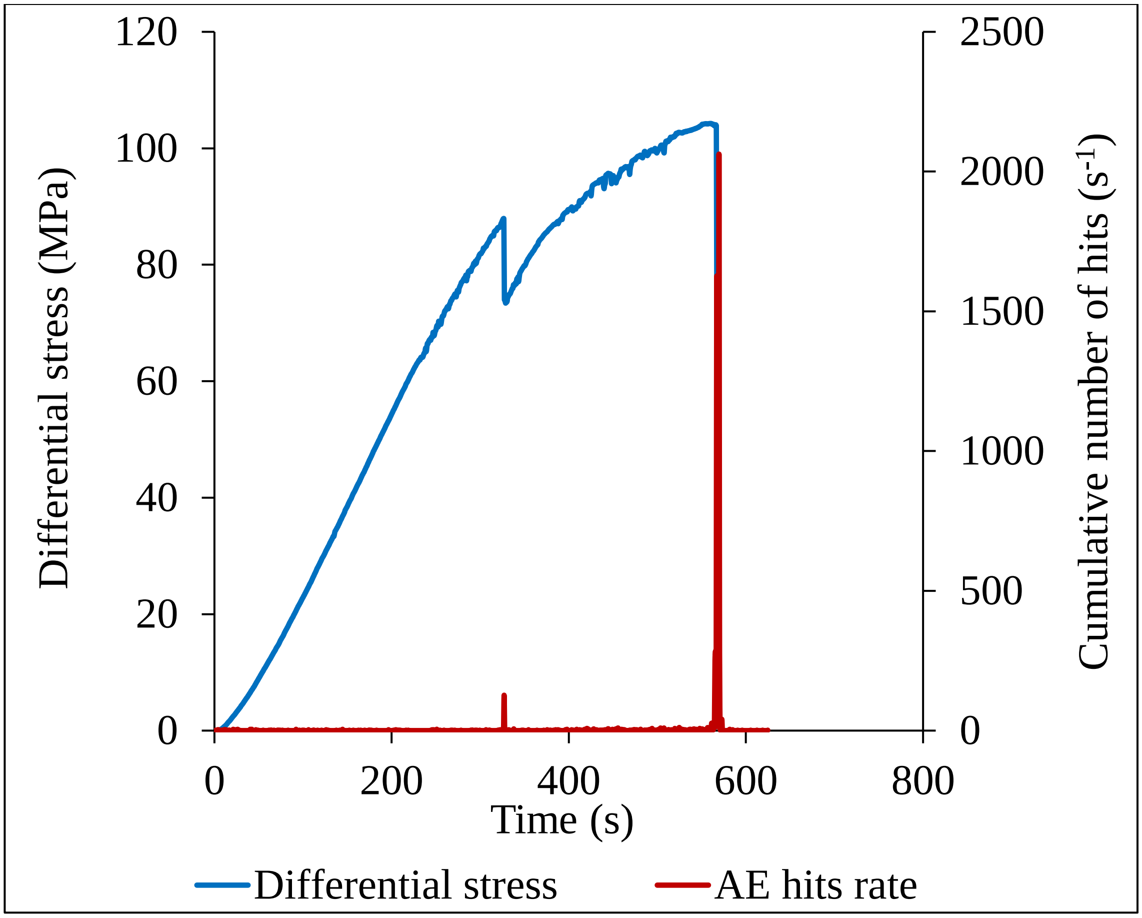

Figure 154: The above figure is a standard way of evaluating AE response. Once again, the reader is pointed out to the 'energy released' in conjunction with the hits plot shown on next page.

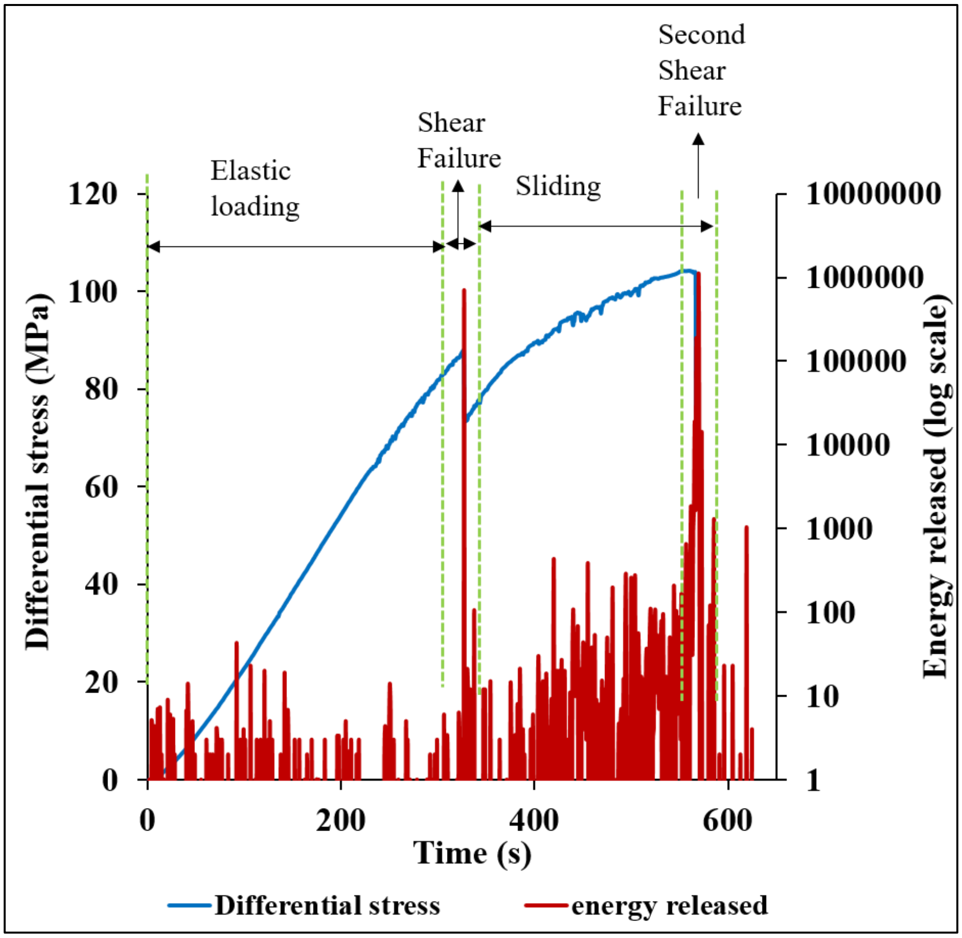

Figure 155: Stress and AE plot for GEO-N2-4300-I1 sample (hits rate and energy released) showing various sections for better understanding the micromechanical processes that the rock undergoes while triaxial loading. See figure 47 which shows the two fractures that developed during testing which correspond very well with observation of two fracturing events using AE

This is shown in Figure 155; here we can divide the plot in four parts – elastic loading, fracturing phase, the sliding phase and once again the shear fracture. This plots shows the 'energy released' on a logarithmic scale. On the liens of earlier samples, from here two interesting observations can be seen:

1. The energy plot shows a trend broadly similar to the Acoustic hits recorded. This is expected as energy gets released only when hits are generated.

2. There is a big difference -of three orders in fact between the energy released during fracturing and during sliding on fracture. The sample had an existing fracture along which this sliding is expected to be occurring. So, while the number of hits falls by 1/6th from fracturing phase to sliding phase, the reduction in energy released is much more pronounced (1000 times).

This confirms once again that even though number of hits released during inelastic loading/fracture of sample is lower by a few times, energy released shows that sliding is a much lower energy process than fracturing and hits generated during sliding have a much lower amplitude.

Using the location analysis, 3-D location plot was generated. This is shown below.

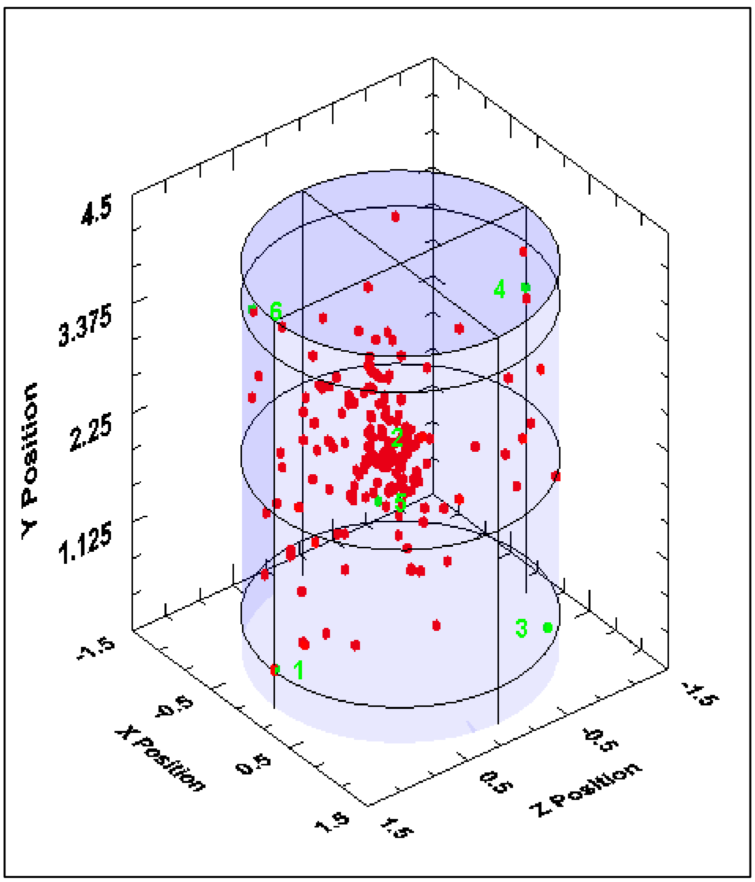

Figure 156: 3-D location plot for GEO-N2-4300-I4. We can see from the plots that the AE is mainly generated in the location of the fracture. The generated 3-D

location is not completely accurate – it fails to pick up the location of the fracture accurately.

Sample GEO-N2-4382-I1

Eight crystals spaced at 60^o to each other were placed across the sample (picture below). The amplitude cut off for all tests conducted on this sample was 60dB. The higher amplitude cut off for this test can be attributed to the use of the heat capable frame MTS 816 which has less noise cancelling capability than the larger and better sound insulated frame MTS 315.

The following figures (130, 131) show the results of the Acoustic emissions for the triaxial test with confining pressure 1500 psi – the final triaxial test which resulted in sample failure. As can be seen, most of the AE events are generated during failure due to the formation of fracture as expected. The location of these events was done in 2-D as well as 3-D using MISTRAS software. This is shown in fig 75 below. The location of events can be seen to match reasonably with the actual fracture although location algorithm also picks up some micro-cracking events within the sample at locations further away from the fracture.

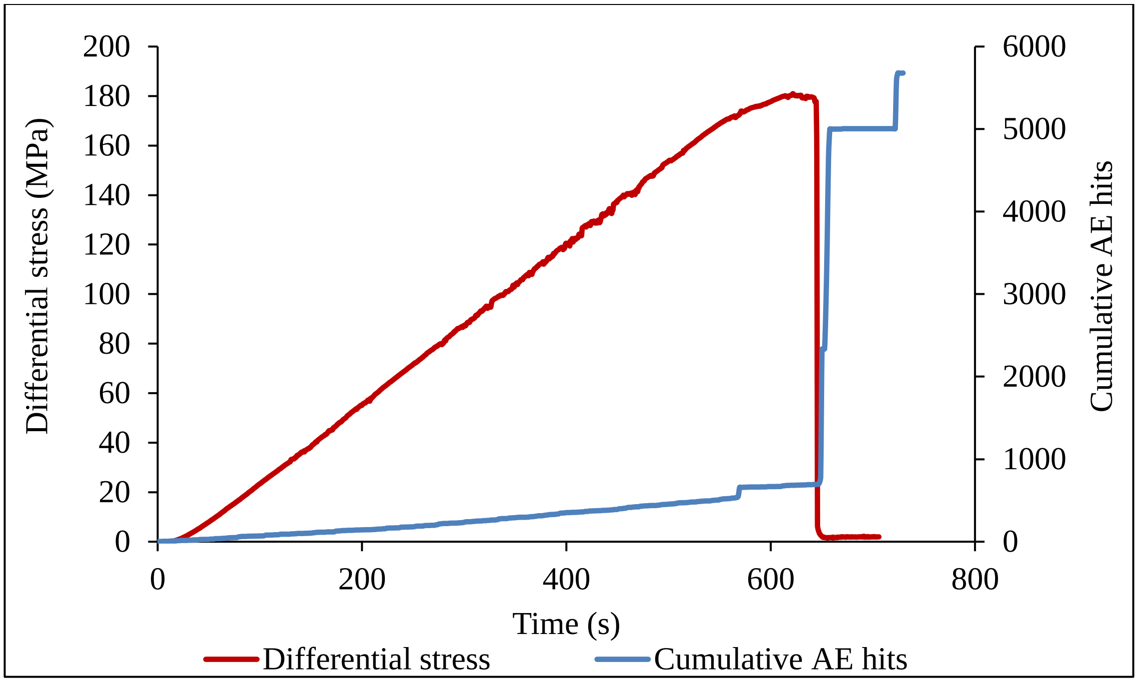

Figure 157: Cumulative AE events generated during triaxial loading of sample GEO-N2-4382-I1. AE was generated from the beginning of the sample but is mainly generated during fracturing of the sample.

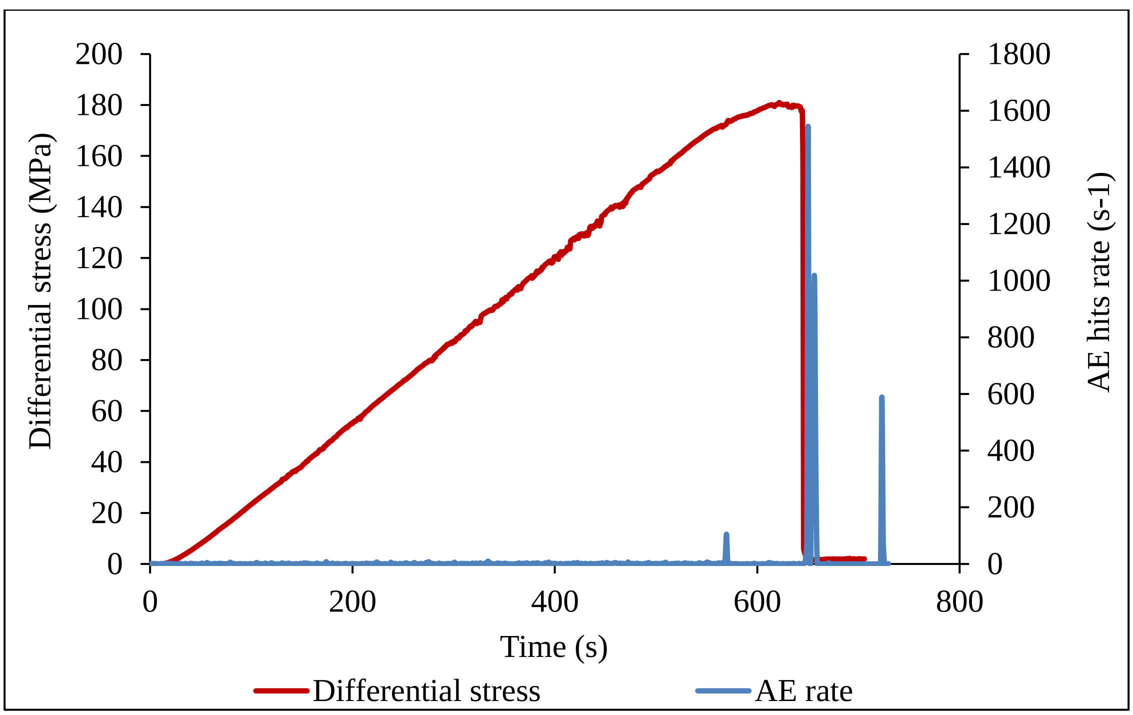

Figure 158: AE event rate generated during triaxial loading of sample GEO-N2-4382-I1.

From the Figure 159, we can see that energy released during failure is much larger than energy released at any point during the triaxial test. Also, while hits were generated throughout the test as was seen in figure 131, they were of little material significance since the energy released during the loading section of the test was lower than the that released during shear fracture by five orders of magnitude. No sliding test was done here as the sample jacket failed after the shear fracture. It’s only the energy released plot together with stress which shows a clear distinction between these aspects of the triaxial test.

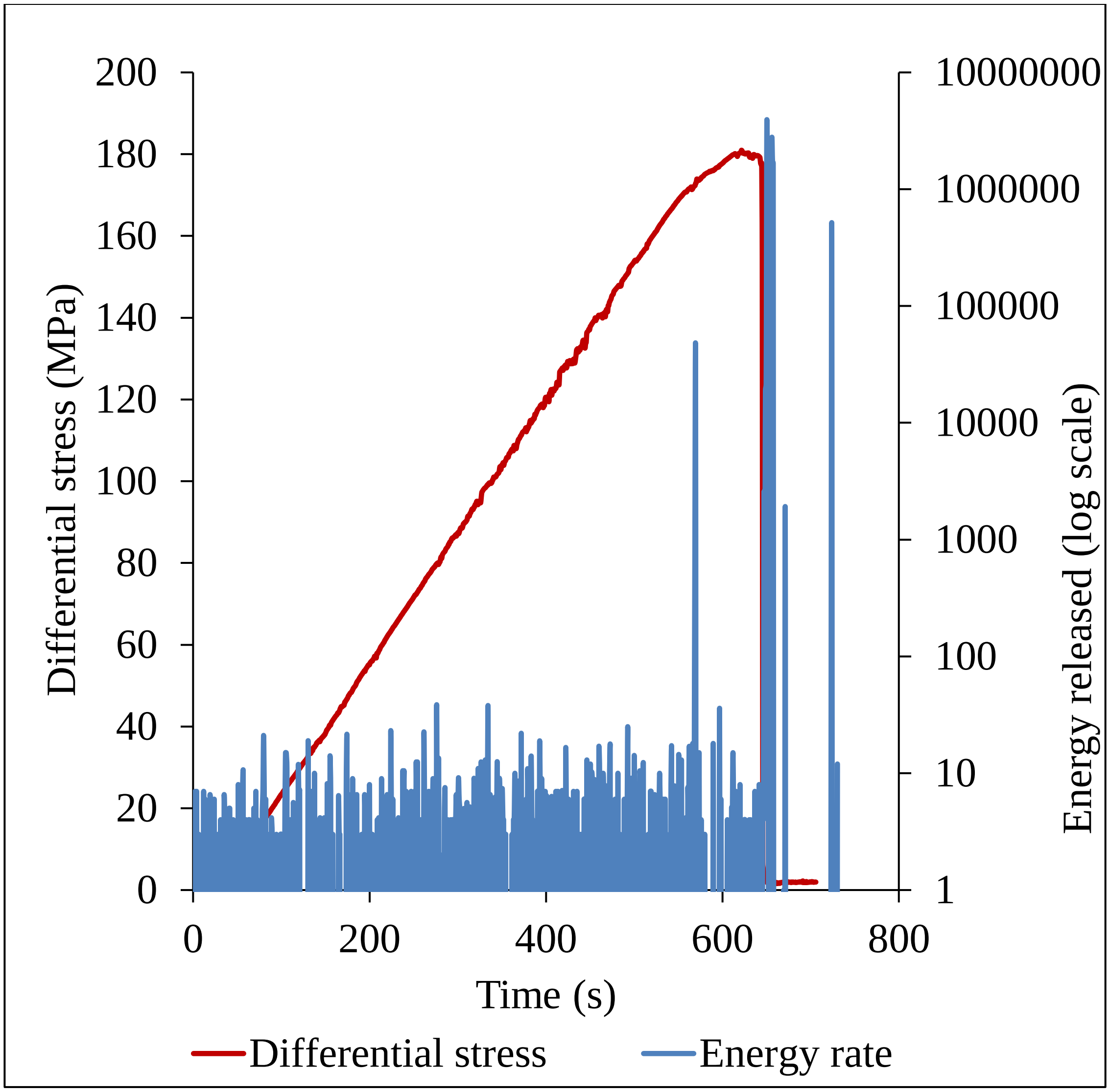

Figure 159: Differential stress and energy released (log scale) versus time for GEO-N2-4382-I1. When compared with other 5 samples, this failure released the highest amount of energy (Sample one, two, three had energy release of <10^5, Sample four had $1.1x10^6$ and sample six had $2.2x10^6$). This compares well with the actual observation of the fracture which appeared to be much more pronounced in GEO-N2-4382-I1 than all other samples (see fig below).

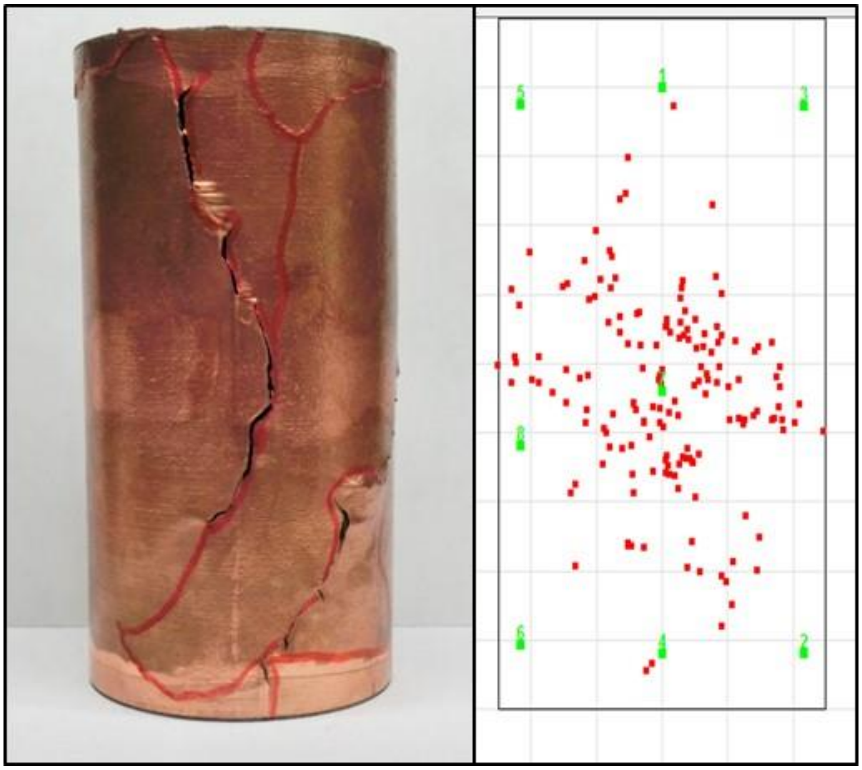

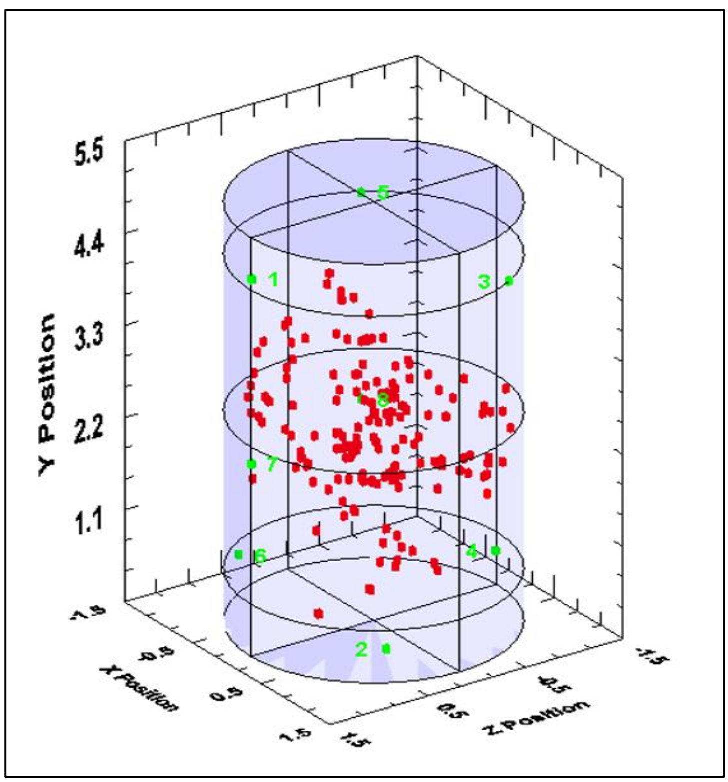

Figure 160: 2-D and 3-D location analysis carried out on sample GEO-N2-4382-I1. We can see from the plots that the AE is mainly generated in the location of the

fracture. The generated 3-D location is not completely accurate – it fails to pick up more events close to the ends.

Sample GEO-N2-4243-I1

Eight crystals, with six crystals spaced at 60° to each other and other two placed at carefully selected locations were attached to the sample. The amplitude cut off for all tests conducted on this sample was 60dB. The higher amplitude cut off for this test can be attributed to the use of the heat capable frame MTS 816 which has less noise cancelling capability than the larger and better sound insulated frame MTS 315.

The following figures (Figure 161,Figure 162 and Figure 163) show the results of the Acoustic emissions analysis for the triaxial test with confining pressure 2500 psi – the final triaxial test which resulted in sample failure.

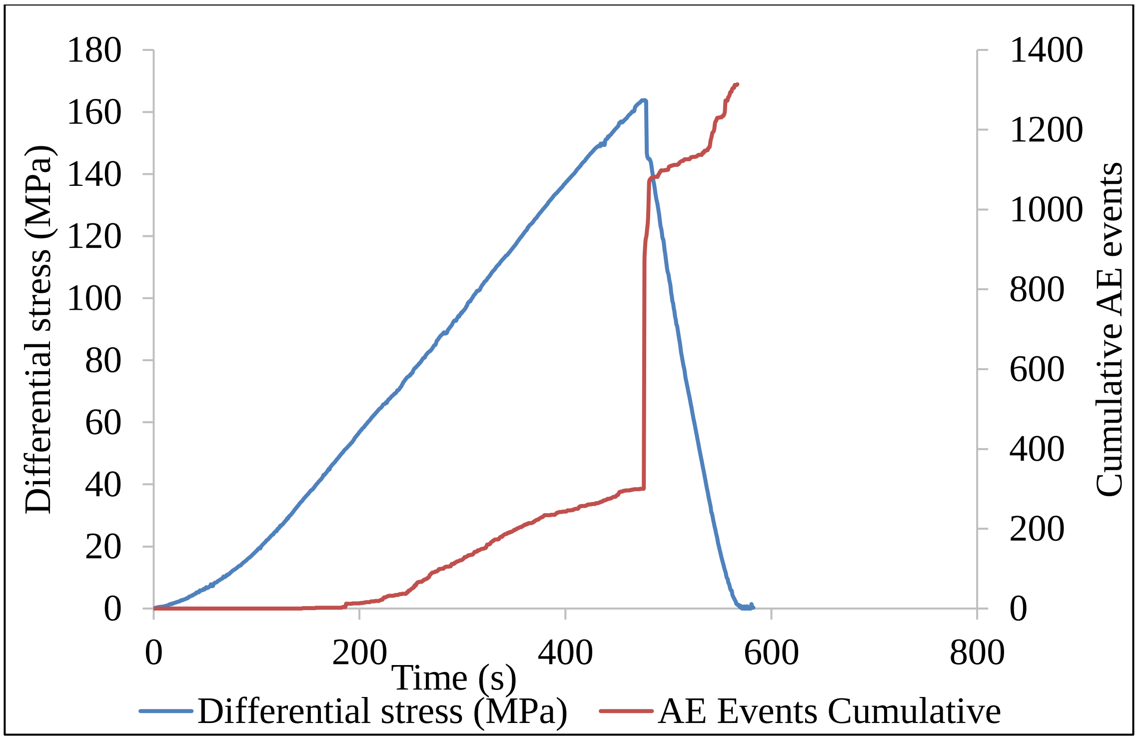

Figure 161: Cumulative AE events when compared with differential stress for the final triaxial-injection test. Similar to other samples, most of the events were generated during fracturing. Significant number of events were also generated during the initial part of the loading.

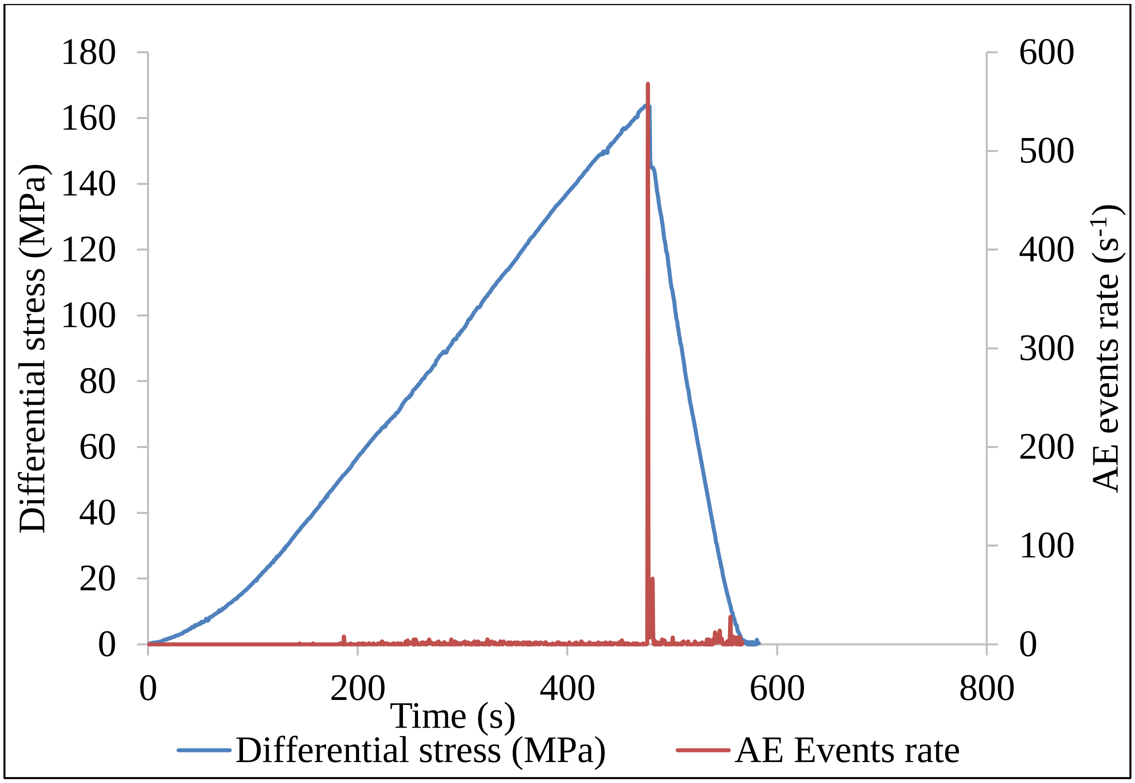

Figure 162: AE events rate when compared with differential stress for the final triaxial-injection test. Similar to other samples, most of the events were generated during fracturing.

From the Figure 163, we can see that energy released close to failure is similar in magnitude to energy released during sliding. As in previous, two- three orders of magnitude difference can be seen between fracturing and sliding. The number of hits here almost matches the number of hits generated during fracturing and it's only the energy released plot which shows a clear distinction between sliding and fracturing.

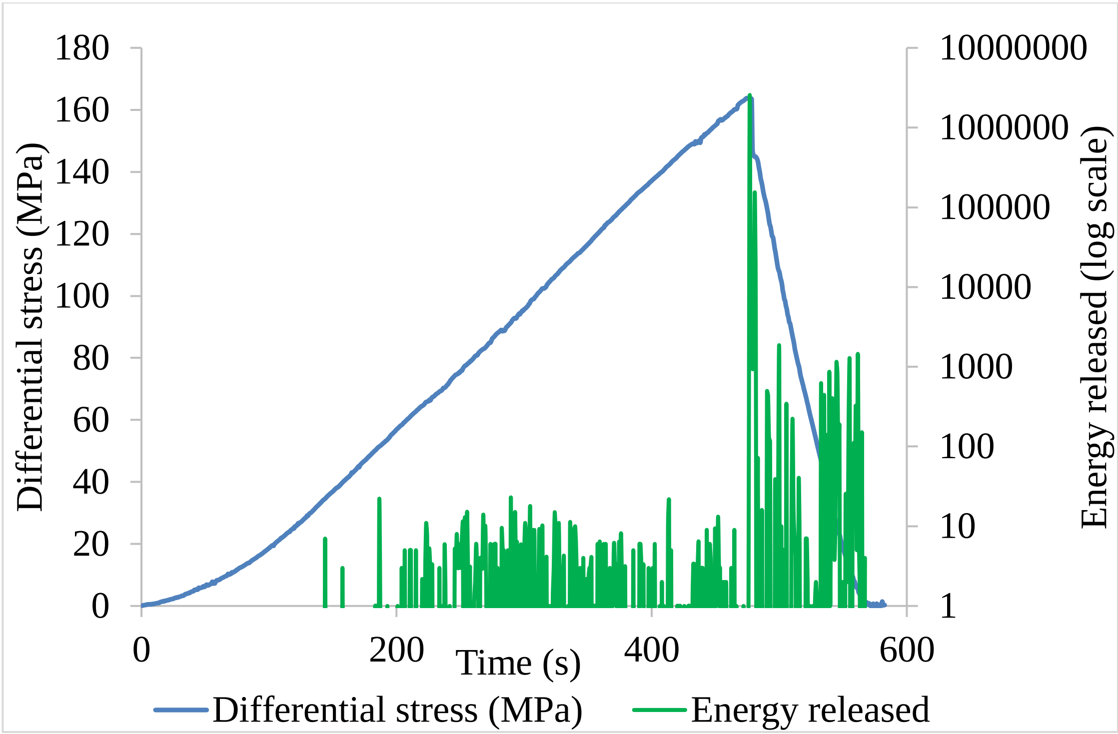

Figure 163: Energy vs stress differential stress for the final triaxial-injection test. This sample also released a large amount of energy on fracturing.

As can be seen, most of the AE events are generated during failure due to the formation of fracture as expected. The location of these events was done in 2-D as well as 3-D. This is shown in Figure 164 below. The location of events can be seen to match reasonably with the actual fracture although location algorithm also picks up some micro-cracking events within the sample at locations further away from the fracture.

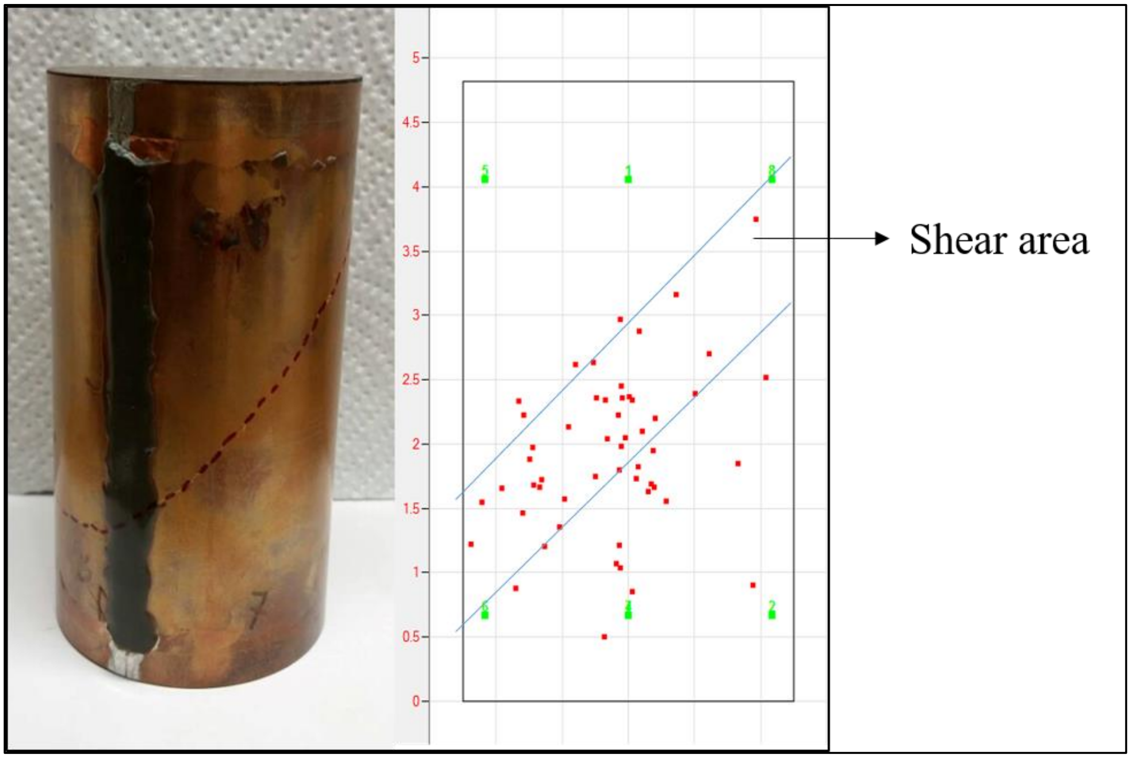
Shear area

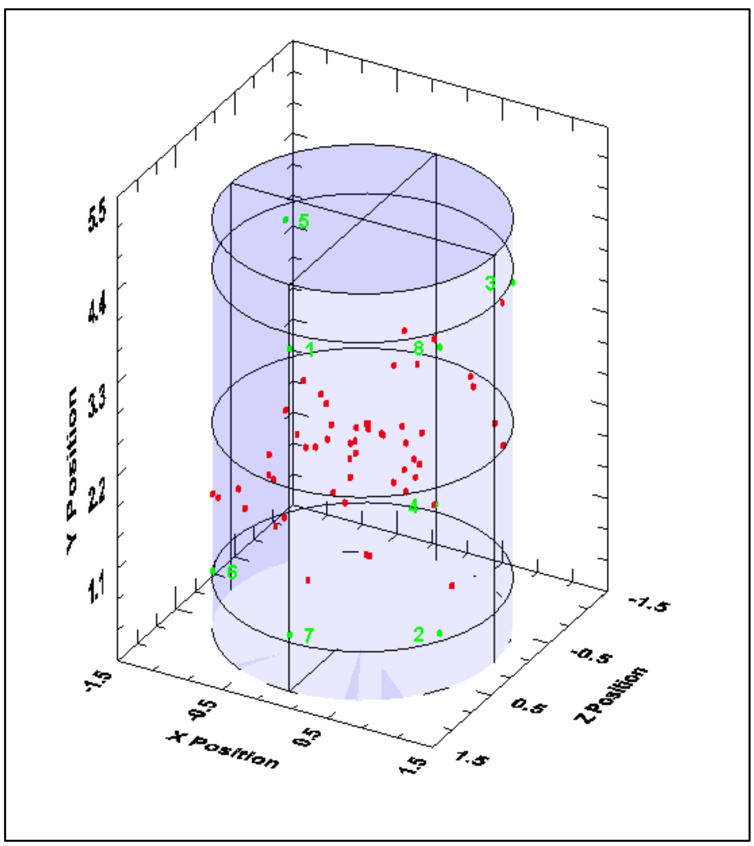
Y Position
X Position
Z Position

Figure 164: 2-D and 3-D location analysis carried out on sample number 6. We can see from the plots that the AE is mainly generated in the location of the fracture. The generated 3-D location is reasonably accurate – it picks up more events close to the ends. However, the located events show up as a thick band whereas in reality the fractured area is more narrow.

Fracture development analysis for GEO-N2-4243-I1

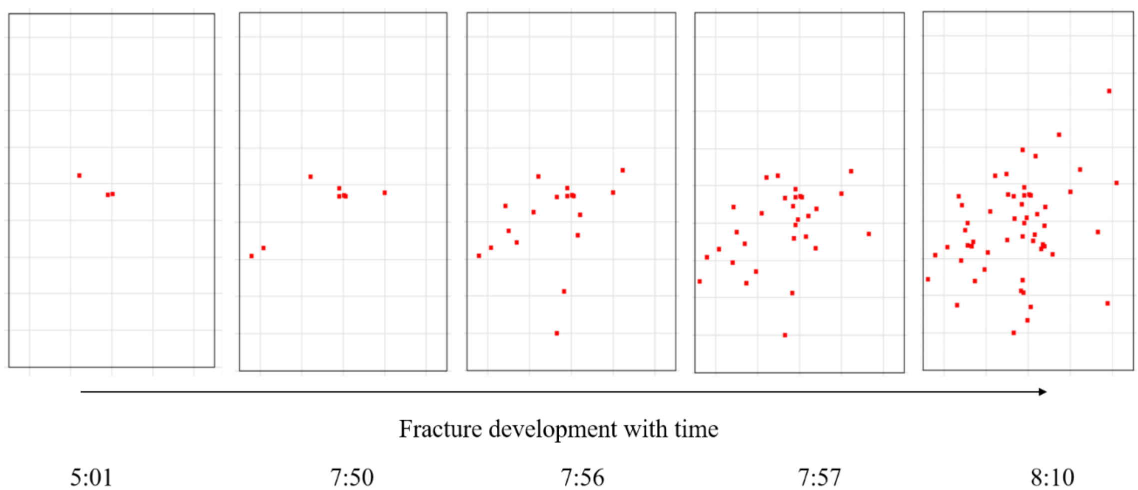

Figure 165: Figure showing development of shear fracture with time for GEO-N2-4243-I1.

Figure 165 shows the time-based development of fracture in the GEO-N2-4243-I1. We can see that for the first half of loading of sample (half of maximum strain), no event gets generated (event being defined as a hit registered by four or more sensors). At 301 seconds into loading the shear fracture development gets initiated at the center of the sample. In an interval of seven seconds (from 470-477 seconds), we see that the fracture gets developed in the lower half of the sample and gets created at an angle of approx. 40 with the vertical axis. After about 15 seconds from here the shear fracture can be seen well developed across the sample. This time lapse plot shows that the development of a shear fracture gets initiated at the center and develops from there. This helps understand the micromechanical processes that go on to create major fracture planes within a sample in a triaxial (or any other) test.

Frequency Response Analysis

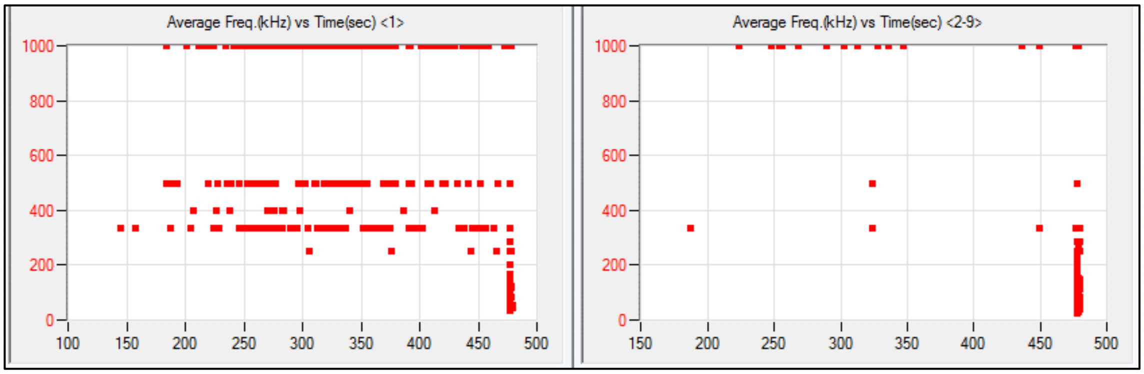

Figure 166: Average frequency response for Sample 6. Fracture is associated with an average frequency of 477 kHz for all nine sensors.

Figure 140 shows the frequency analysis that can be done for a sample using AE information. The fracture development for this sample happened at ~477 seconds from the start of the test (Figure 163). Looking at the frequency response using Fig 140, we can see that all sensors register the fracture development with a frequency response ranging from 10-350 kHz with the event generating a range of frequencies within a single second or so. Loading of the sample otherwise generates frequencies ranging from 300-500 kHz only. This type of frequency analysis can help identify the nature of failure in the field where fractures may be associated with a more 'complex' frequency response' within a short span of time as compared to the rest of the fracturing job. This same response has been seen in all rocks studied so far and it is the intent to develop a more robust theory on this topic and understand the reasons for this behaviour and compare with field results (not a part of this thesis).

AE Moment Tensor and source analysis for GEO-N2-4243-I1.

For the GEO-N2-4243-I1, source analysis as well as moment tensor inversion was carried out to identify source type as well as identify moments directions and values. Source analysis was done using both first wave arrival method (described earlier) as well as moment tensor inversion technique.

Using first wave arrival source analysis method (Appendix 2, the following statistics were obtained:

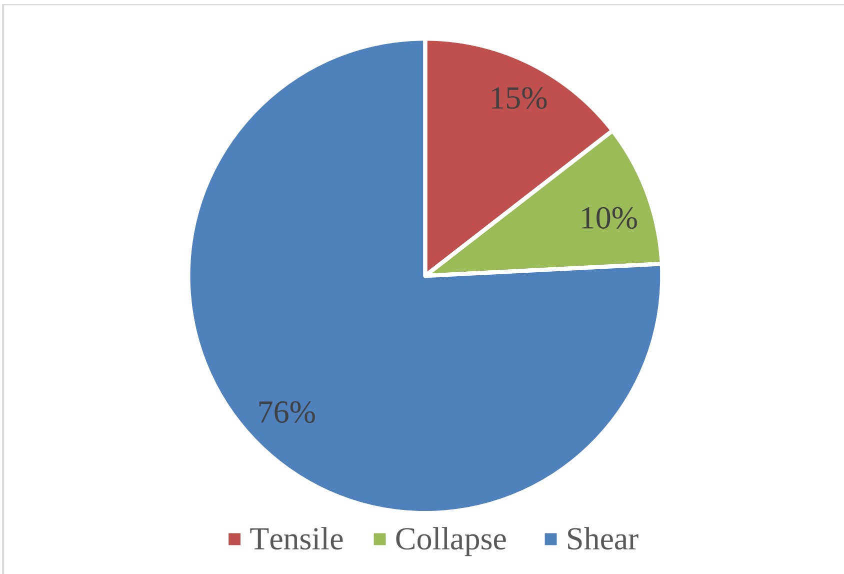

Figure 167: Source analysis using first arrival wave polarity method

A total of 310 events were analyzed for this purpose. The results are on expected lines – in a triaxial test the majority of hits are expected to be shear in nature. For this rock, most of the tensile failure events were seen (90%) before sample failure. During fracturing shear failure dominates with few collapse type events. During sliding, most of the events (>90%) are shear in nature with some compressive (8%) and very few tensile events (2%) also seen.

Full moment tensor inversion

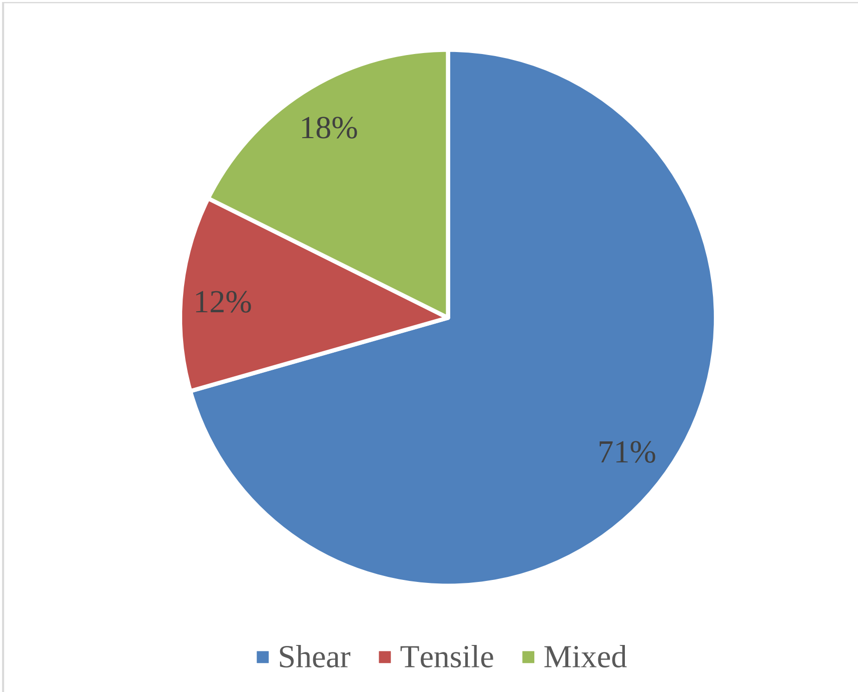

Figure 168: Source analysis using full moment tensor inversion

The moment tensor technique used here has been described in Appendix 2, its results are considered as the most accurate method of determining source type and full moment tensor for the sample. Its main limitation is the requirement for a single hit to be registered by at least six independent sensors and certain assumptions that have been mentioned in Appendix 2 (chief being the requirement that sample is homogeneous and isotropic).

The results of source analysis using this technique are shown in Figure 168.

Comparing to results using the first wave polarity method in Figure 167, we can see that the results are close to each other. The following table compares the results:

Table 28: Comparison of two source analysis methods for GEO-N2-4243-I1 of GEO N2 sample

Source Type	First wave polarity method	Full Moment tensor inversion
Tensile	15 %	12 %
Compressive	10 %	-
Shear	76 %	71 %
Mixed	-	18 %

The moment tensor method can also be used for calculating the location of an event. This method is more refined than the original method described earlier as it uses only high quality signals with a minimum of six sensors for calculating position rather than four sensors in the other technique. The results of the same are shown in Figure 169.

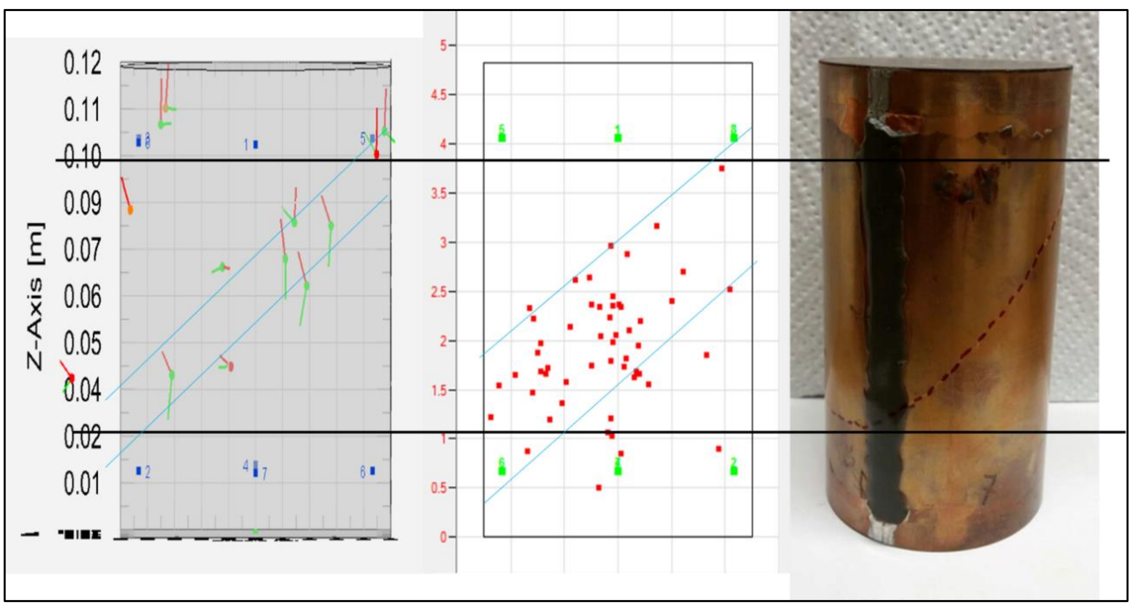

Figure 169: Plot showing location analysis using AE events with moment tensor inversion (left) as well as wave time analysis method (center) with the actual fracture plane on the sample marked in red (right).

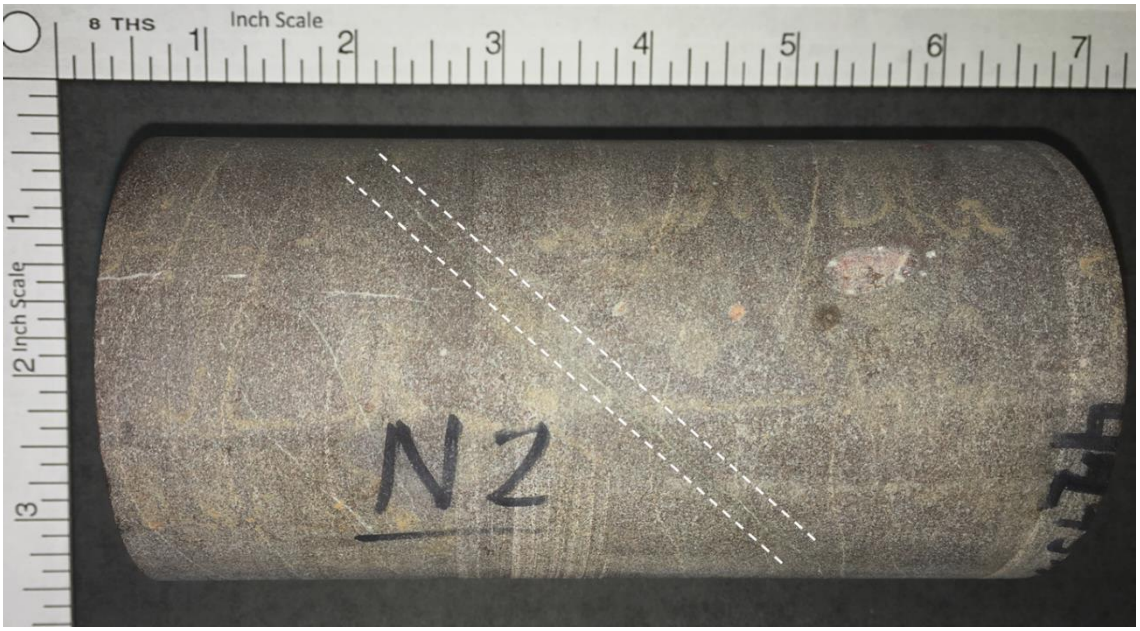

Figure 170: Figure shows the healed fracture along which the sample failed contained within the dashed white lines

We can see that the shear band predicted using moment tensor inversion is much narrower and matches actual fracture plane much better than the wide band obtained using wave time analysis method. In the tensor inversion process, crack motion and crack surface normal directions can also be determined. Also calculated is the eigenvalue and eigenvectors in the X, Y and Z direction of the solution. The direction of the crack opening corresponds to the first eigenvector. In case of the shear crack, the second and third eigenvector gives orientation and crack surface sliding direction. These are out of scope of this thesis work. These are shown in Figure 171 for sample six.

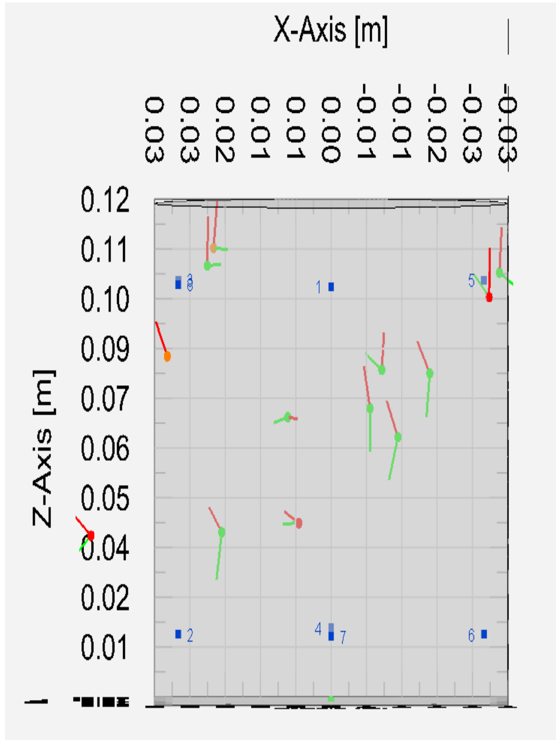

Figure 171: Plot showing location of fracture and crack motion and crack surface normal directions of events

The solution obtained for a random event (event number 15) for sample six showing what kind of information can be extracted is shown below:

1. Moment tensor solution:

-0.0545	-0.0582	1
	0.1671	-0.7834
		-0.0941

2. Source location:

X (m)	Y (m)	Z(m)
0.022	0.006	0.107

3. Eigen vectors and vector solutions:

	Maximum	Midiate	Minimum
Eigen Value	1	-0.0197	-0.9947
Eigen Vector X	-0.5758	0.6209	0.5319
Eigen Vector Y	0.3707	0.7781	-0.5071
Eigen Vector Z	0.7287	0.0948	0.6782

4. Composition Ratio of Eigen Value (%)- refers to the percentage of a shear component of the event:
   Value for event-97.5%

5. Crack Motion & Crack Surface Normal Directions

	X	Y	Z
Motion	-0.04	-0.089	0.995
Normal	-0.784	0.62	0.047

Such results are available for all events.

INEL-1 WELL SAMPLES

For the INEL-1 well's four samples, the sample description and results of the triaxial tests have already been described in chapters 2 and 3.

8 to 12 AE sensors per sample for recording acoustic emissions generated during the triaxial tests were used. These sensors were attached to the sample using epoxy. A preamplifier of 40 dB was applied to all the sensors. The amplitude cut off on these sensors varied from 45-55 dB; any wave below this amplitude is discarded by the system as noise. Frequency and energy of failure events were also recorded during the tests – these give insights into the nature of failure; typically, higher confining pressures result in lower energy released during the failure if the rocks become more ductile. A sample rate of 1 MSPS (million samples per second) was used to record the AE information. 3-D location analysis was also performed using AE information – this technique uses the source amplitude and the differences in time it took the wave to reach the different sensors to arrive at the location of the event.

Figure 172 below shows the time - stress responses in conjunction with AE information for each of the four tests. The figures show the rate and number of hits observed during the respective tests. It can be observed that generally the rocks tested have a good AE response with the strongest AE response observed close to and during failure. Also, low AE activity is observed after failure when slip takes place on the shear surface. Samples V1 generated low AE after failure while samples V2, H, and 4 show good AE response to fracture slippage. Overall the highest number of events were recorded for sample H and followed closely by V1, and 4 and far less for V2. This can be explained as follows:

1. Sample INEL-H has the highest strength and is more brittle (sharp drop in stress after failure) than all other samples. This clearly contributed to its high AE rate and total number of events.

2. Sample INEL-V1 and sample no 4 both generated similar number of hits, however in terms of rate of AE generation, sample INEL-V1 had double the rate at fracture initiation as compared to INEL-Sample 4. This is because INEL-Sample 4 had several healed fractures before testing and deformation localized on those prior to the formation of a new fracture plane. On actual observation after failure, INEL-Sample 4 had several failure planes – it failed along the healed fractures in addition to newly generated failure planes resulting in a more gradual failure process than V1 which failed in a highly brittle manner.

3. Sample INEL-V2 had the lowest AE response, this despite it having almost the same strength and coming from the same exact depth as INEL-V1 and almost similar dynamic and elastic modulus. This can be attributed to presence of micro cracks in V1 which contributed to a good initial permeability value (more than 250 times that of V2). As a result, the pore pressure within V1 was able to increase more rapidly throughout the sample, causing a more brittle failure as compared to V2 which had a very ductile failure. It can be seen in table 6 that even the final permeability in V2 after failure is lower than the initial permeability in V1.

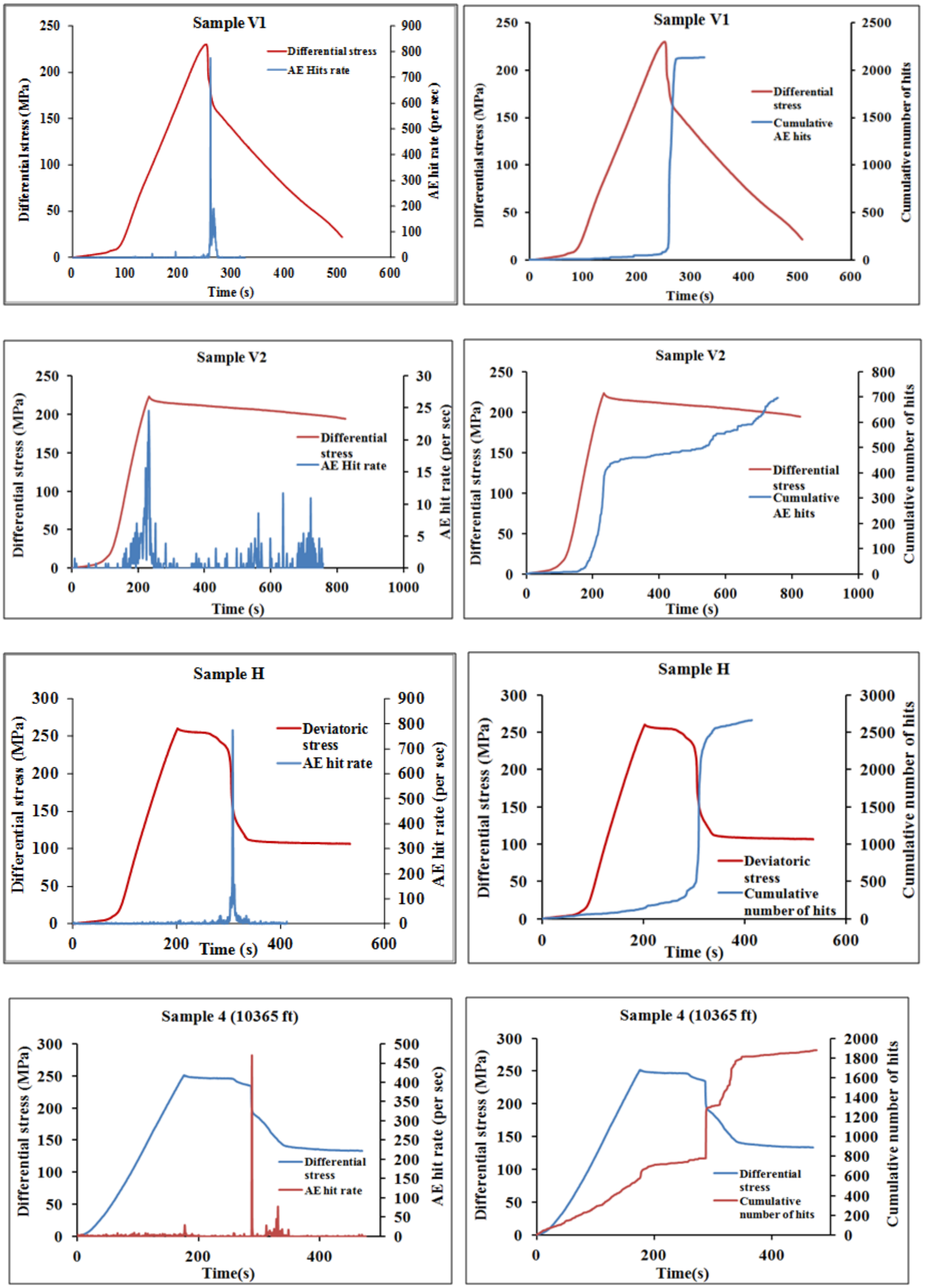

Figure 172: AE hits rate and cumulative number of hits correlated to axial stress during triaxial testing observed in the four INEL -1 well core plugs. More brittle

failure (V1, H and sample no 4) show high number of hits as compared to sample V2 (ductile failure – observe stress plot). Most of the hits are generated during fracturing although some are generated just before and during fracture sliding.

It should be noted that the AE was recorded using 8-12 sensors and these rocks were observed to generate far less AE activity when compared with sandstones (for example Berea sandstone in a similar experiment generated over 10000 hits).

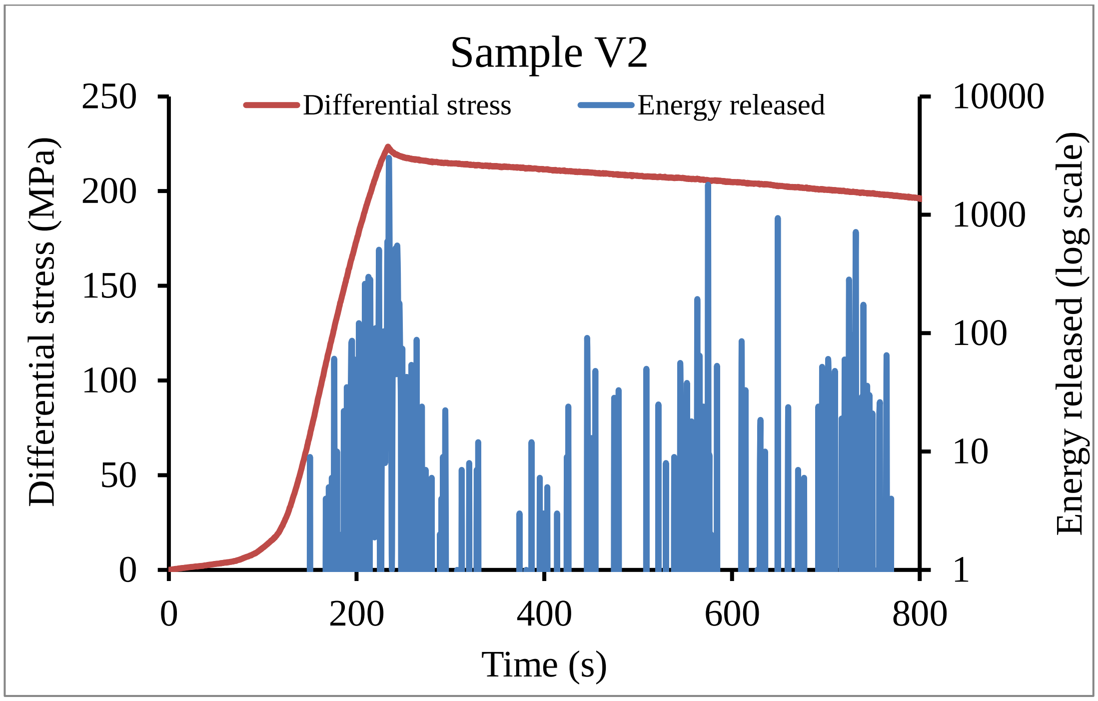

Figure 173: Stress and Energy released during triaxial testing of sample INEL-V2 showing comparison of energy released during shear fracture versus gradual failure of sample as pore pressure gets increased in an triaxial-injection experiment.

The following plots show the 2-D and 3-D location analysis of AE events for all the four samples. The figures show the failed sample next to the 2-D location plot and a three-dimensional plot showing location of events. It should be noted that the red lines on the sample show the fracture location. Also, location analysis shows the location of micro-fracturing in addition to the large shear fracture locations.

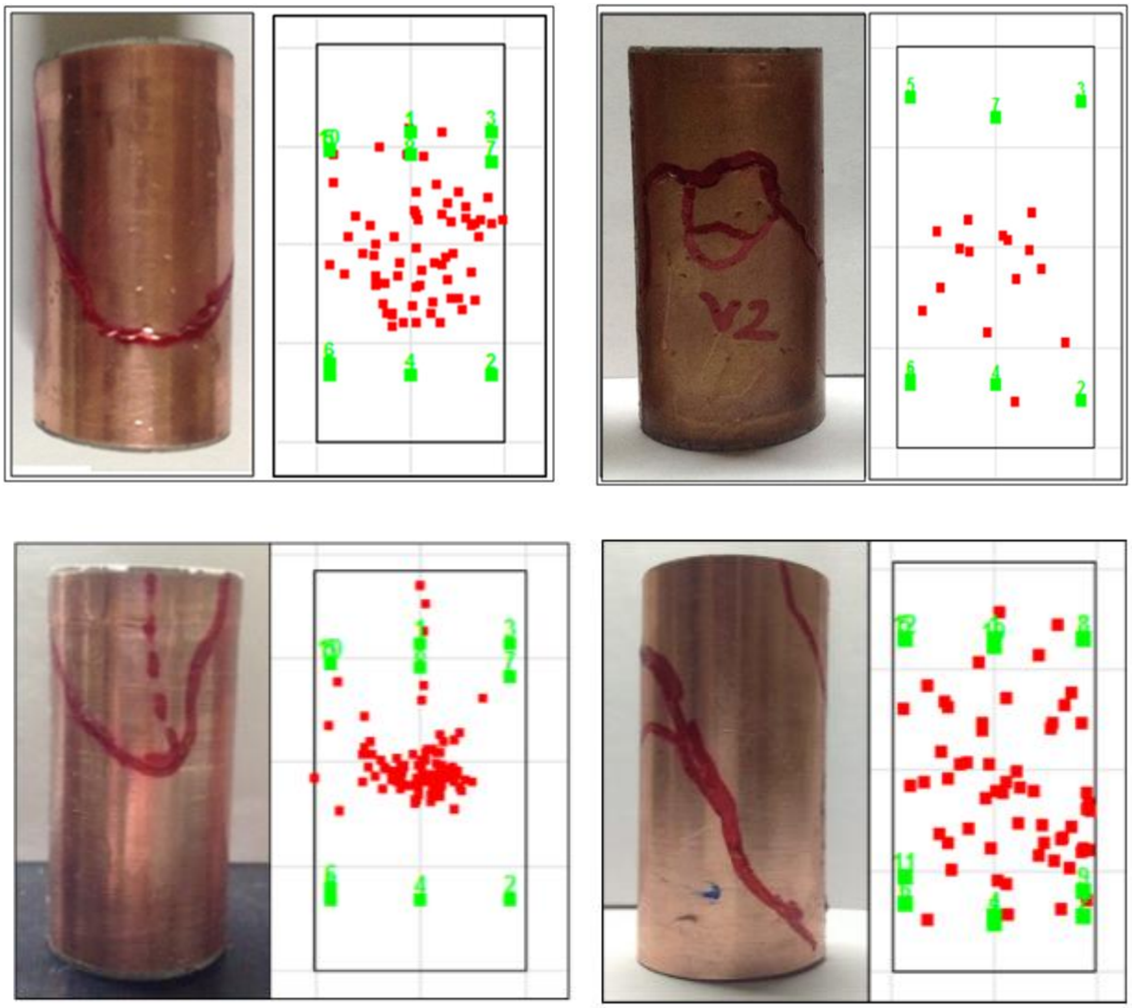

Figure 174: INEL sample 2-D location plots with Sample INEL-V1 (top left), sample V INEL-2 (top right). Sample INEL-H (bottom left) and INEL-Sample 4 (bottom right) in showing event locations in 2-D within the sample as compared with the fracture location in the respective samples (marked red). Location algorithm picks up micro cracking as well within the sample.

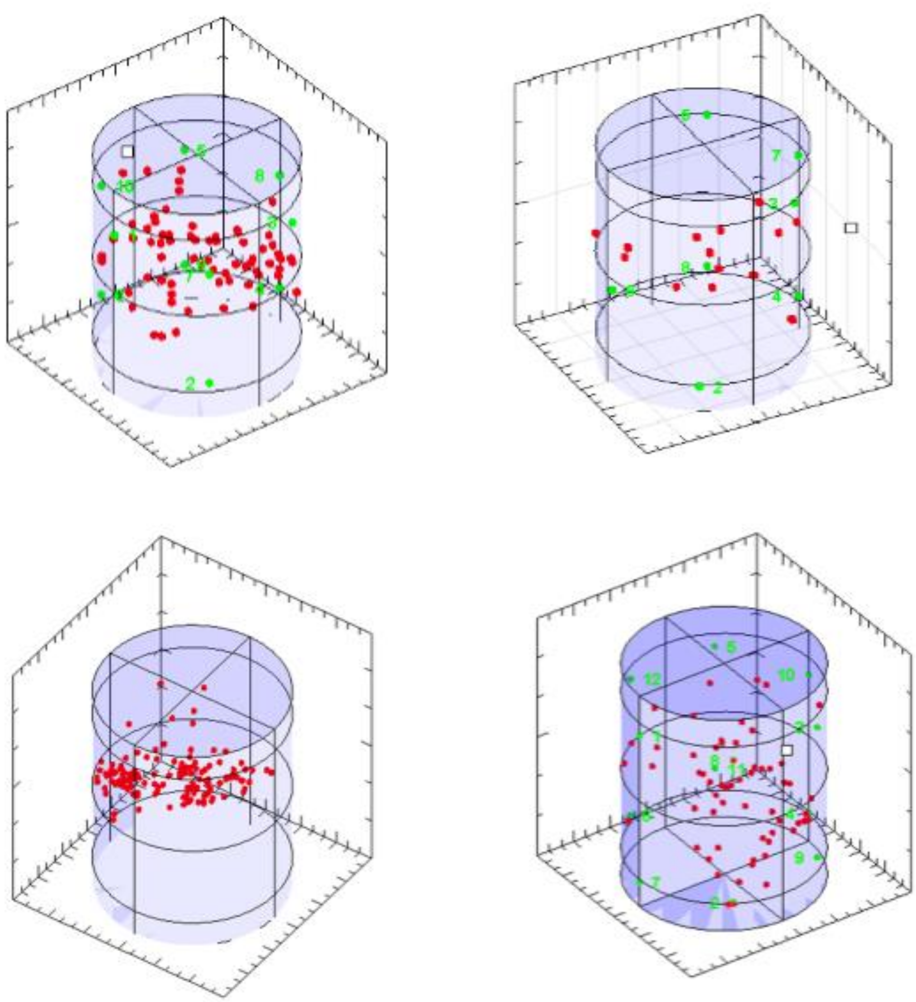

Figure 175: INEL samples 3D location plots showing event locations in 3-D within the sample - Sample INEL-V1 (top left), sample INEL-V2 (top right). Sample INEL-H (bottom left) and INEL-Sample 4 (bottom right)

Source Analysis for Sample V2 and a Brazilian Test sample from INEL-1 well

Based on first waveform arrival method described earlier, source analysis was conducted on the AE events. Events were filtered on signal quality (described earlier) and a minimum of six sensors receiving the same hit albeit at different time for a higher confidence.

The analysis revealed the following statistics:

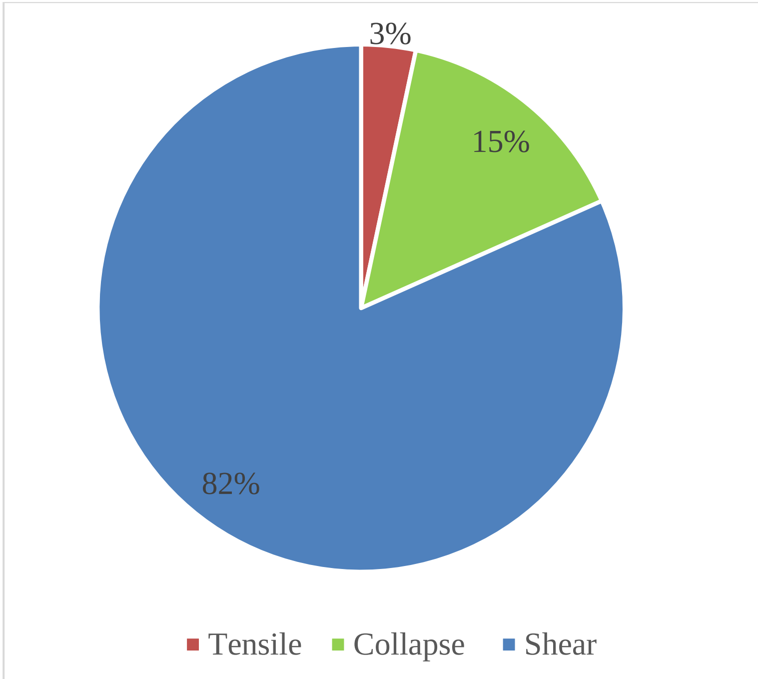

Figure 176: Source analysis of Sample V2's AE events showing the majority of events were shear in nature.

The results are on expected lines – in a triaxial test the majority of hits are expected to be shear in nature. For this rock, about 50 of the total 700 events were generated before sample failure. Here shear failure dominates with few collapse type events. During Shear fracture (350 events) the majority are shear again with very few tensile and compressive. During the sliding phase, only shear type events are seen based on this analysis.

Source analysis on a Brazilian Test from the INEL-1 well

A Brazilian sample from the INEL-1 well was tested with AE as well. A picture of the sample is shown below:

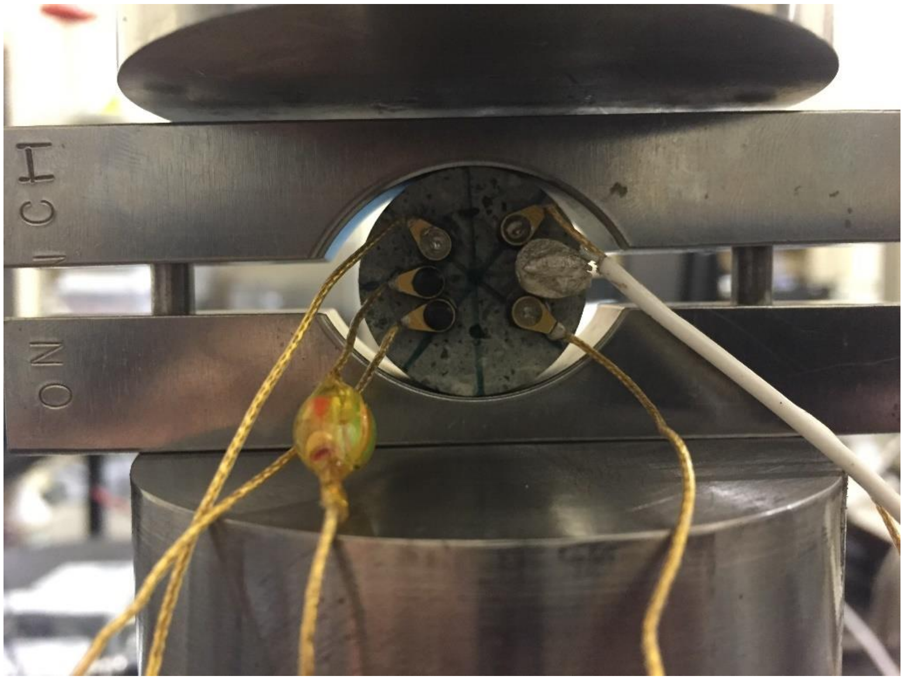

Figure 177: Picture of a sample for the Brazilian test with AE sensors.

No examples of Brazilian tests were found in literature with AE testing especially with source analysis. This is probably due to the very small sample area on which very limited sensors can be added. The hit rate versus time plots are shown in figure 152. An interesting observation made here was that the AE hit rate was very high – when compared with the triaxial tests – overall, they were slightly higher than triaxial tests. The energy released difference is even more striking – the energy released for the triaxial test from GEO-N2-4300-I4 peaked at 2300/crystal, whereas the energy released here was ~18000 reflecting a difference of 7 times. Exactly same trend was seen for the other three other Brazilian tests conducted on the samples from INEL-1 well. In conclusion – Brazilian tests have similar AE hit rate but release a higher energy than triaxial testing. Since Brazilian testing is in an indirect tension process, and triaxial testing is a compressive process- we can say that tensile fractures release more energy. However, an additional analysis that should be done would be to test release of energy with a larger range of confining pressures; in this case due to only four samples only a single confining pressure of 3500 psi was used.

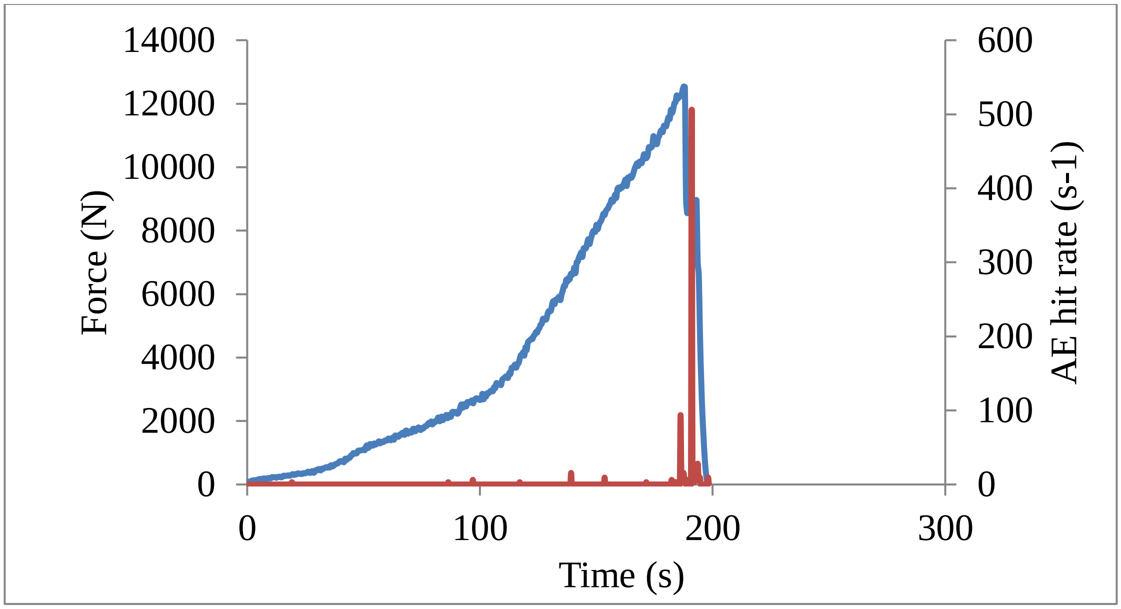

Figure 178: AE hit rate and Total axial force acting on Sample S2 (Brazilian test)

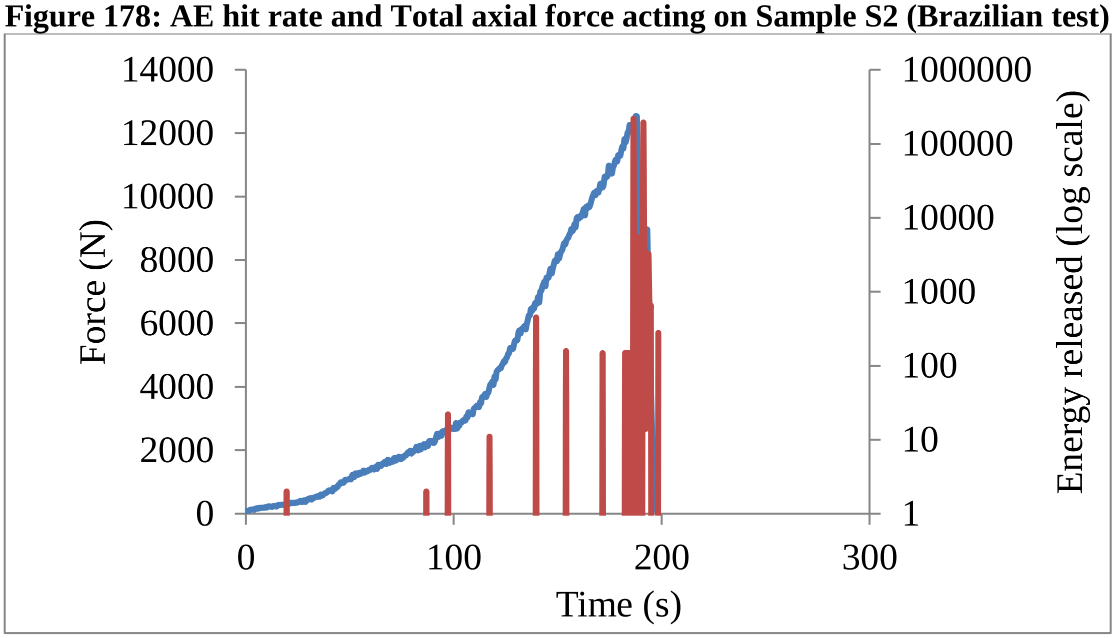

Figure 179: Total axial force and Energy released versus time for Sample S2.

Source analysis for Sample S2-Brazilian test

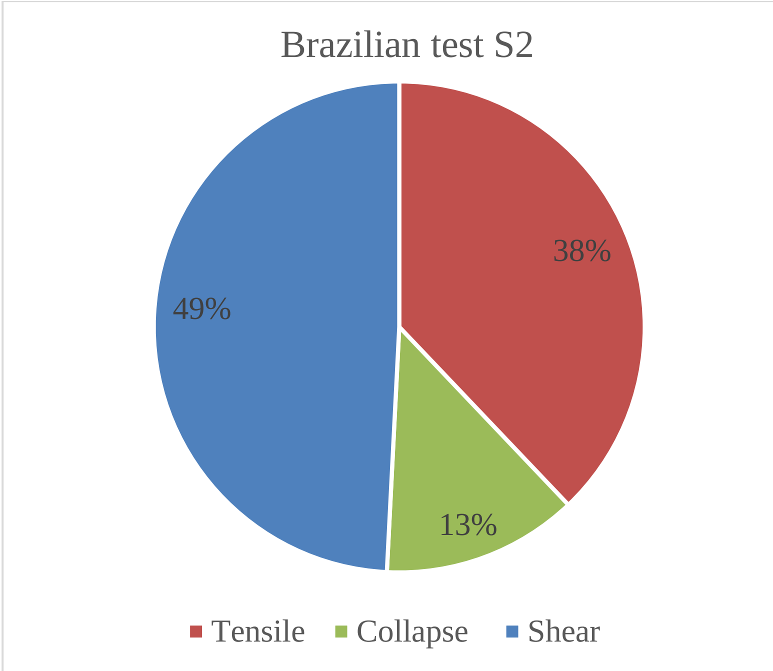

Figure 180: Source analysis for Sample S2 tested as an indirect tension test (Brazilian test)

Source analysis done on the AE events registered during the testing reveal that only about 40% events were tensile in nature and half were actually shear. It is known that Brazilian testing isn't a fully tensile test – hence the name indirect. But this test's results calls into question if this test accurately reflects a tensile test. It is known that there are a variety of tensile tests used for measuring tensile strength – it is therefore recommended to conduct more testing on different tensile tests to find out which one is more representative – this is out of scope of this thesis work.

CHAPTER 6: CONCLUSIONS

In this thesis, the objective of conducting a triaxial (or triaxial-injection) test with or without heating, velocity, permeability monitoring and Acoustic analysis has been demonstrated. Such a comprehensive testing can help create a much more insightful analysis that a simple triaxial test can do. The impact of various parameters within the domain of triaxial test, permeability measurements, velocity measurements and Acoustic emissions analysis has been demonstrated.

Several triaxial-injection tests were completed successfully for a range of rocks. The results show that there are differences in results obtained while using this test instead of the standard triaxial test. Several high temperature tests were also performed and associated parameters calculated. All the elastic parameters were calculated and Mohr-Coulomb strength envelops added whenever multistage tests were done.

The objective of evaluating permeability alterations due to triaxial loading have been studied in detail and a correlation has been derived which links the sample's increase or decrease of permeability post failure, with its initial porosity. Also, for several samples a real time behaviour analysis of rock permeability versus triaxial loading strain has been provided which shows that volumetric strain determines the changes in permeability more strongly than any other parameter. It has been demonstrated that our setup can measure permeability at extremely low scales with values as low as 10 nano Darcy -this has helped us test ultra-low permeability rocks like rhyolites, shales and granites.

Finally, a detailed AE analysis has also been presented which links together stress and strain of a sample with Acoustic emissions. It has been shown that the hit rate should be used in conjunction with the energy released as differentiating parameter in understanding acoustic emissions during sample testing. Using this it has been shown that for all classes of rocks tested here, there was always a difference of energy by a factor of 100-1000 during shear failure when compared with sliding. 2-D and 3-D location analysis has been shown. For two samples – Berea Sandstone and Basalt, a more comprehensive analysis has been provided to show the full extent of possibilities of using AE to derive information on a microscopic as well as macroscopic scale for any sample. As part of this time lapse plots have been provided which show the development of a shear fracture versus time which shows how a fracture first develops at the center and then ‘grows’ out. For Berea sandstone, this is more gradual, while for basalt, a more brittle failure is seen and the fracture develops in a short period of time. A source analysis based on both first wave arrival method has been conducted on these samples. The results show that most of the events are shear in nature although significant number of tensile and collapse events are also seen. In the beginning, tensile events are more while compressive events are more towards the end – in both cases shear events are always in majority. A full-scale tensor inversion has also been done for one sample and the results described as well. This has been used for doing a more accurate source analysis and location analysis. The results of the source analysis using both the techniques show a close match which is similar to what has been found in recent literature (only one such study was found-Graham, 2008). 3-D location was seen to have improved with moment tensor analysis rather than the usual waveform arrival time analysis. Hence wherever possible it is recommended to use this method for location analysis.

REFERENCES

1. Bargar, Keith E. and Terry E.C. Keith. 1999. Hydrothermal mineralogy of core from geothermal drill holes at Newberry Volcano, Oregon.

2. Bakshi, R., M.E. Halvaei, A. Ghassemi. 2016. Geomechanical Characterization of Core from the Proposed FORGE Laboratory on the Eastern Snake River Plain, Idaho.

3. Crawford, A. and D. Wylie. 1987. A modified multiple failure state triaxial testing method. 28th US Rock Mechanics Symposium, 133-140.

4. Dobson, Patrick F., T.J. Kneafsey, J. Hulen, A. Simmons. 2003. Porosity, permeability, and fluid flow in the Yellowstone geothermal system, Wyoming. Journal of Volcanology and Geothermal Research, Volume 123, Issues 3–4, 1 May 2003, Pages 313-324, ISSN 0377-0273.

5. Goodman, R.E. 1989. Introduction to Rock Mechanics. 2nd ed.

6. Kovari, K., A. Tisa, H. Einstein, and J.A. Franklin. 1983. Suggested methods for determining the strength materials in triaxial compression, Int. J. of Rock Mech. & Min. Sci. & Geomechs Abs. 20: 283-290.

7. INL/EXT-06-11746 report by MIT. 2006. The future of geothermal energy, Impact of Enhanced Geothermal Systems (EGS) on the United States in the 21st century.

8. Kim, M. M., and H. Y. Ko. 1979. "Multistage triaxial testing of Rocks," Geotechnical Testing 2: 98-105.

9. Kwasniewski, M. Mechanical behavior of rocks under true triaxial compression conditions; volumetric strain and dilatancy. Archives of Mining Sciences [0860-7001] yr:2007 vol:52 iss:3 pg:409

10. Li, Yawei, J. Wang, W. Jung, A. Ghassemi. 2012. Mechanical properties of intact rock and fractures in welded Tuff from Newberry volcano.

11. Lutz, S. J., S. Hickman, N. Davatzes, E. Zemach, P. Drakos and A. Robertson-Tait. Rock mechanical testing and petrologic analysis in support of well stimulation activities at the Desert peak geothermal field, Nevada

12. Miller, L.G., S.M. Prestwich and J.L. Griffith, 1978. INEL/Snake River Geothermal Drilling and Testing plan – INEL-1 Well

13. Moos, D., C. A. Barton. 1990. In-situ stress and natural fracturing at the INEL site, Idaho.

14. Ohaka, S. 2010. Evolution of porosity and permeability during brittle faulting.

15. Sruoga, N. P., G. H. Rubinstein. 2004. Porosity and permeability in volcanic rocks: a case study on the Serie Tobfera, South Patagonia, Argentina, Journal of Volcanology and Geothermal Research, Volume 132, Issue 1, 15 April 2004, Pages 31-43.

16. Tran, D.T., Pagoulatos, A., C.H. Sondergeld. 2010. Quantify uncertainty of rock failure parameters from laboratory triaxial testing using conventional and multistage approaches, 44th U.S. Rock Mechanics Symp., June 27 - 30, 2010, Salt Lake City, Utah.

17. Williams, C.F., M.J. Reed, and R.H. Mariner. 2008. A review of methods applied by the U.S. Geological Survey in the assessment of identified geothermal resources: U.S. Geological Survey Open-File Report 2008-1296 [http://pubs.usgs.gov/of/2008/1296/].

18. Y. Bernabe´, U. Mok, and B. Evans. 2003. Permeability-porosity Relationships in rocks subjected to various evolution processes. Pure Applied Geophysics. 160 (2003) 937–960

19. Bartlett W.H. C. Experiments on the expansion and contraction of building stone. Am.J. Sci. 22,136 (1832).

20. Adie A.J. ON the expansion of different kinds of stone from an increase in temperature with a description of the pyrometer used in making the experiments. Trans.Roy.Soc. Edinburgh 13, 366 (1836).

21. Wheeler N.E. On the thermal expansion of rock at high temperature. Trans.Roy.Soc. Canada3, 4 (1910).

22. Todd T. Effect of cracks on elastic properties of low porosity rocks. Ph.D. thesis, Mass. Inst. of tech., 320 (1973).

23. Hockman A. and Kessler D. W. thermal and moisture expansion of some domestic granites. U.S. Nat. Bur. Of Standards, RP 2087, 395 (1950).

24. Warren N.W. and Latham G.V. (1970) An experimental study of thermally induced microfracturing and its relation to volcanic seismicity. J. geophys. Res. 75, 4455-4464.

25. Todd T., Richter D., Simmons G. and Wang H. Unique characterization of lunar rocks by physical properties. Proc. Fourth Lunar Sci. Conf. 3, Pergamon Press, 2663 (1973).

26. Saiang, Christine. Influence of heat on the physical and mechanical properties of selected rock types. Avd. for geoteknologi, Lulea tekniska Universitet. Stockholm (2012)

27. Geology of the Bedford Shale and Berea Sandstone in the Appalachian Basin. Science 16 Apr 1954: Vol. 119, Issue 3094, pp. 512-513

28. Greenkorn, R.A. and Johnson, C.R: “Directional permeability of Heterogeneous Anisotropic porous media.” Society of petroleum Engineers Journal, pp.124-132, 1964.

29. Brace, W.F.: “permeability from Resistivity and pore shape.” Journal of Geophysical research, Vol.82, pp.3343-3349, 1977.

30. Freeze, R.A. and Cherry, J.A.: “Groundwater”, prentice-Hall, Inc., Englewood Cliffs, New Jersey, USA, 1979.

31. Biot, M.A.: “General theory of Three-Dimensional Consolidation.” J. Appl. Phys., Vol.12, pp.155-164, 1941

32. Stavrogin, AN, Tarasov, B & Fairhurst, C (ed.) 2001, Experimental Physics and Rock Mechanics (Results of Laboratory Studies). CRC Press/Balkema, Lisse.

33. Dautriat, J., Gland, N., Guelard, J., Dimanov, Alexandre., Pure appl. geophys. (2009) 166: 1037. doi:10.1007/s00024-009-0495-0

34. RI Korsnes, R Risnes, I Faldaas, T Norlan., End effects on stress dependent permeability measurements. Tectonophysics, 426 (1/2) (2006), pp. 239–251

35. Miller, L.G., Prestwich,S.M., Griffith,J.L., 1978, INEL/Snake River Geothermal Drilling and Testing plan – INEL-1 Well

36. Rodgers, D.W., H.T. Ore, R.T. Bobo, Nadine McQuarrie, and Nick Zentner, 2002, Extension and subsidence of the eastern Snake River Plain, Idaho, in Bill Bonnichsen, C.M. White, and Michael McCurry, eds., Tectonic and Magmatic Evolution of the Snake River Plain Volcanic Province: Idaho Geological Survey Bulletin 30, p. 121-155.

37. Kuntz, M.A., Anderson, S. R., Champion, D.E., Lanphere, M.A., Grunwald, D.J., tension cracks, eruptive fissures, dikes, and faults related to late Pleistocene-Holecene basaltic volcanism and implications for the distribution of hydraulic conductivity in the eastern Snake River Plain, Idaho. Geological Society of America, special paper 353, 2002

38. Welhan, J.A., Johannesen, C.M., Reeves, K.S., Clemo, T.M., Glover, J.A., Bosworth, K.W., Morphology of inflated pahoehoe lavas and spatial architecture of their porous and permeable zones, eastern Snake River Plain, Idaho. Geological Society of America, special paper 353, 2002

39. Zhu, W., and T. Wong (1997), The transition from brittle faulting to cataclastic flow: Permeability evolution, J. Geophys. Res., 102(B2), 3027–3041, doi:10.1029/96JB03282.

40. De Paola, N., D. R. Faulkner, and C. Collettini (2009), Brittle versus ductile deformation as the main control on the transport properties of low-porosity anhydrite rocks, J. Geophys. Res., 114, B06211, doi:10.1029/2008JB005967.

41. X.-L. Lei ,K . Kusunose, O. Nishizawa, A. Cho and T. Satoh. On the spatio-temporal distribution of acoustic emissions in two granitic rocks under triaxial compression: the role of pre-existing cracks. Geophysical Research letters, vol. 27, no. 13, pages 1997-2000, July 1, 2000

42. S.-H. Changa, C.I. Leeb. Estimation of cracking and damage mechanisms in rock under triaxial compression by moment tensor analysis of acoustic emission. International Journal of Rock Mechanics & Mining Sciences 41 (2004) 1069–1086

43. Goebel, T. H. W., T. W. Becker, D. Schorlemmer, S. Stanchits, C. Sammis, E. Rybacki, and G. Dresen (2012), Identifying fault heterogeneity through mapping spatial anomalies in acoustic emission statistics, J. Geophys. Res., 117, B03310, doi:10.1029/2011JB008763.

44. Chen Yong and Chi-yuen Wang. Thermally Induced Acoustic Emission in Westerly Granite. Geophysical Research Letters, Vol. 7, No. 12, Pages 1089-1092, December 1980

45. A. Maji and S.P. Shah. Process Zone and Acoustic-Emission Measurements in Concrete. SEM Spring Conference on Experimental Mechanics hem in New Orleans, LA, 1986

46. Rice J.R. (1979), "Theory of precursory processes in the inception of earthquake rupture", gerl. Beitr. Geophys., 88, 91-127

47. Ricer J.R. (1980), "the mechanics of earthquake rupture", in: Physics of the earth's Interior (proceedings of the International School of Physics "Enrico Fermi", Course 78, 1979), A.M. Dziewonski and E. Boschi (eds.), Italian Physical Society, North-Holland Publ. Co., pp.555-649.

48. C. H. Scholz. Microfracturing and the Inelastic Deformation of Rock in Compression, 1968.

49. Thompson, B. D., R. P. Young, and D. A. Lockner (2009), Premonitory acoustic emissions and stick-slip in natural and smooth-faulted Westerly granite, J. Geophys. Res., 114, B02205, doi:10.1029/2008JB005753.

50. Bakshi, Rohit, Mostafa Eskandari Halvaei, and Ahmad Ghassemi. "Geomechanical Characterization of Core from the Proposed FORGE Laboratory on the Eastern Snake River Plain, Idaho."

51. Bakshi, Rohit, Mostafa Eskandari Halvaei, and Ahmad Ghassemi. "Injection Experiments on Basaltic Tuffs under Triaxial and Heated Conditions with Acoustic

Emissions Monitoring." 50th US Rock Mechanics/Geomechanics Symposium. American Rock Mechanics Association, 2016.

52. Aki K, Richard PG. Quantitative seismology Sausalito: University Science Books;2002.

53. Ohtsu M. Simplified moment tensor analysis and unified decomposition of acoustic emission source: Application to in situ hydrofracture test. J Geophys Res 1991;96(B4):6211–21.

54. Lockner DA, Byerlee JD, Kuksenko V, Ponomarev A, Sidorin A. Quasi-static fault growth and shear fracture energy in granite. Nature 1991;350:39–42.

55. Shigeishi M, Ohtsu M. Acoustic emission moment tensor analysis: develop- ment for crack identification in concrete materials. Constr Build Mater 2001;15:311–9.

56. Dahm T, Manthei G, Eisenblatter J. Automated moment tensor inversion to estimate source mechanisms of hydraulically induced micro-seismicity in salt rock. Tectonophysics 1999; 306:1–17.

57. James Andrew Fetterman and Nicholas C. Davatzes. Evolution of Porosity in Fractures in the Newberry Volcano Geothermal System, Oregon, USA: Feedback between Deformation and Alteration, 2011

58. Jihoon Wang, Woodong Jung, Yawei Li, Ahmad Ghassemi, Geomechanical characterization of Newberry Tuff. Pages 74–96. Geothermics Volume 63, September 2016, Pages 74–96

59. Al-Shayea NA (2004) Effects of testing methods and conditions on the elastic properties of limestone rock. Eng Geo 74:139–156.

60. ASTM D 3148–96 (1996) Standard test for elastic moduli of intact rock core specimens in uniaxial compression, p 21.
61. Christaras B, Auger F, Mosse E (1994) Determination of the moduli of elasticity of rocks. Comparison of the ultrasonic velocity and mechanical resonance frequency methods with direct static methods. Mater Struct 27:222–228
62. Ciccotti M, Mulargia F (2004) Differences between static and dynamic elastic moduli of a typical seismogenic rock. Geophys J Int 57:474–477
63. Gue´guen Y, Palciauskas V (1994) Introduction to the physics of rocks. Princeton University Press, New Jersey, p 294
64. Rodrıguez Sastre MA, Calleja L (2004) Caracterizacion del comportamiento elastico de materiales pizarrosos del Sinclinal de Truchas mediante ultrasonidos (In Spanish). Trabajos de Geologıa, Universidad de Oviedo 24:153–164
65. Saenger EH, Kruger OS, Shapiro SA (2006). Effective elastic properties of fractured rocks: dynamic vs. static considerations. Int J Fracture 139:569–576
66. Schon JH (1996) Physical properties of rocks: fundamentals and principles of petrophysics. In: Helbig K, Treitel S (eds). Handbook of geophysical exploration, section I, seismic exploration, vol 18. Oxford, Pergamon, p 583
67. Song I, Suh M, Woo YK, Hao T (2004) Determination of the elastic modulus set of foliated rocks from ultrasonic velocity measurements. Eng Geo 72:293–308
68. Zang A, Wagner FC, Stanchits S, Dresen G, Andresen R, Haidekker MA (1998) Source analysis of acoustic emissions in Aue granite cores under symmetric and asymmetric compressive loads. Geophis J Int 135(3):1113–1130.

69. Brace, W. F., J. B. Walsh, and W. T. Frangos, Permeability of granite under high pressure, J. Geophys. Res. 73, 225, 1968.

70. Zoback, M.D., and J. D. Byerlee, The effect of microcrack dilatancy on the permeability of Westerly Granite, J. Geophys. Res. 80, 752-755, 1975.

71. Stanley C. Jones, Two-Point Determinations of Permeability and PV vs. Net Confining Stress. SPE Formation Evaluation, March 1988

72. Bernabe´, Y., U. Mok, and B. Evans (2006), A note on the oscillating flow method for measuring rock permeability, Int. J. Mech. Min. Sci. Geomech. Abstr., 43, 311 – 316, doi:10.1016/j.ijrmms.2005.04.013.

73. Kranz, R. L., J. S. Saltzman, and J. D. Blacic (1990), Hydraulic diffusivity measurements on laboratory rock samples using an oscillating pore pressure method, Int. J. Mech. Min. Sci. Geomech. Abstr., 27, 345–352, doi:10.1016/0148-9062(90)92709-N.

APPENDIX 1: SAMPLE DETAILED DESCRIPTION

BEREA SANDSTONE- DETAILED PORE STRUCTURE DESCRIPTION

The Berea sandstone's pore structure using a thin section is shown below for reference.

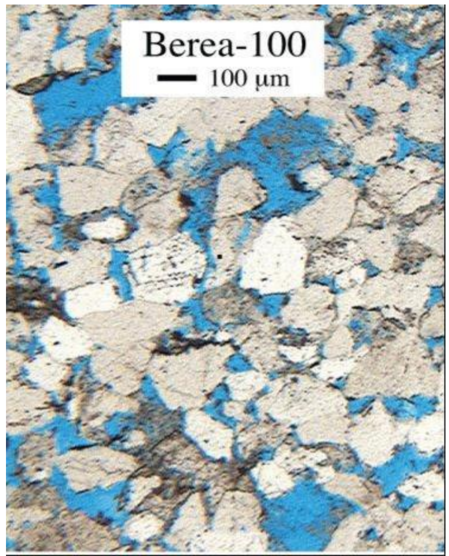

Figure 181: Thin section image of Berea Sandstone. Pore spaces are colored in blue. Grains are angular and usually larger than 100 µm. Pore spaces are well connected.

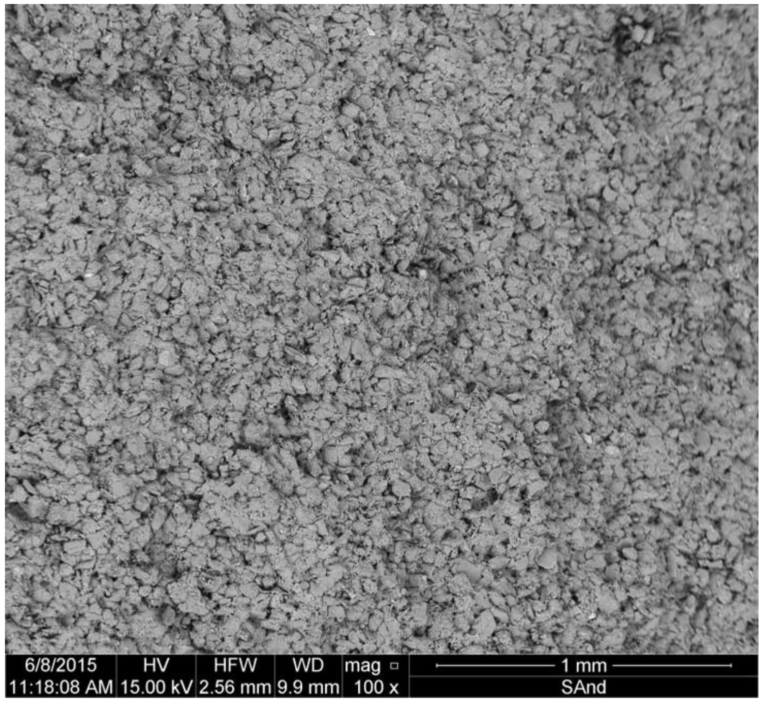

Figure 182: SEM image with a magnification of 100x. Scale is shown for reference; the grains are angular and connected pore spaces (black) can be seen spread throughout the sample. Sample can be seen to be highly homogeneous.

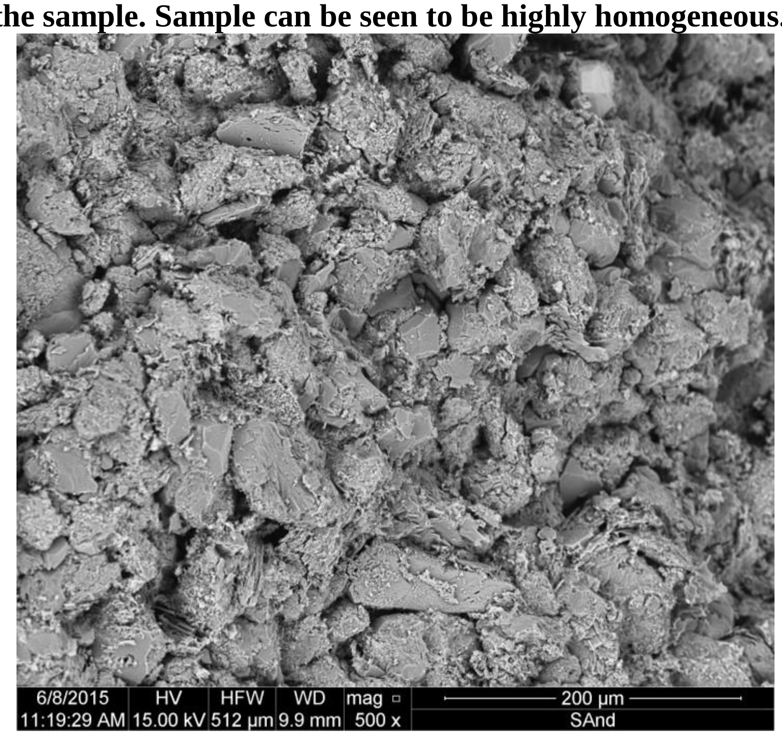

Figure 183: SEM image with a magnification of 500x. Scale is shown for reference; the silica grains are angular and connected pore spaces (black) can be seen as well. The grains have clay particles on them.

It can be seen that sample grain size is usually greater than 100μm and sample seems homogeneous with well-connected pore spaces uniformly present all across the sample. Clays can be seen on the magnified view of the sample (below) and these line the silica grains.

SIERRA WHITE GRANITE PORE STRUCTURE

Sierra white's pore structure was studied by using both thin sections as well as SEM analysis. Following plots show both. A SEM based mineralogical analysis was also done which helps identify mineralogical composition at very small scales. This is also shown.

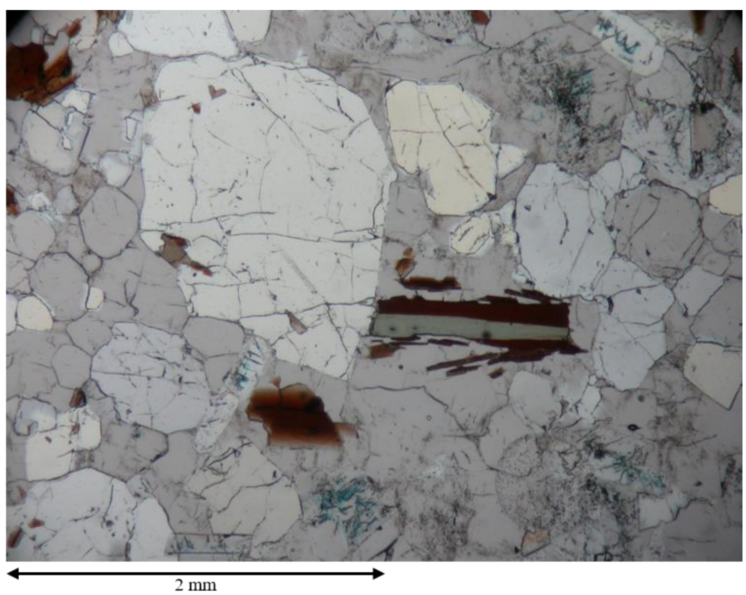

Figure 184: Thin section image of Sierra white granite. Large grains can be seen which are well interlocked into each other resulting into no pores that can be seen here.

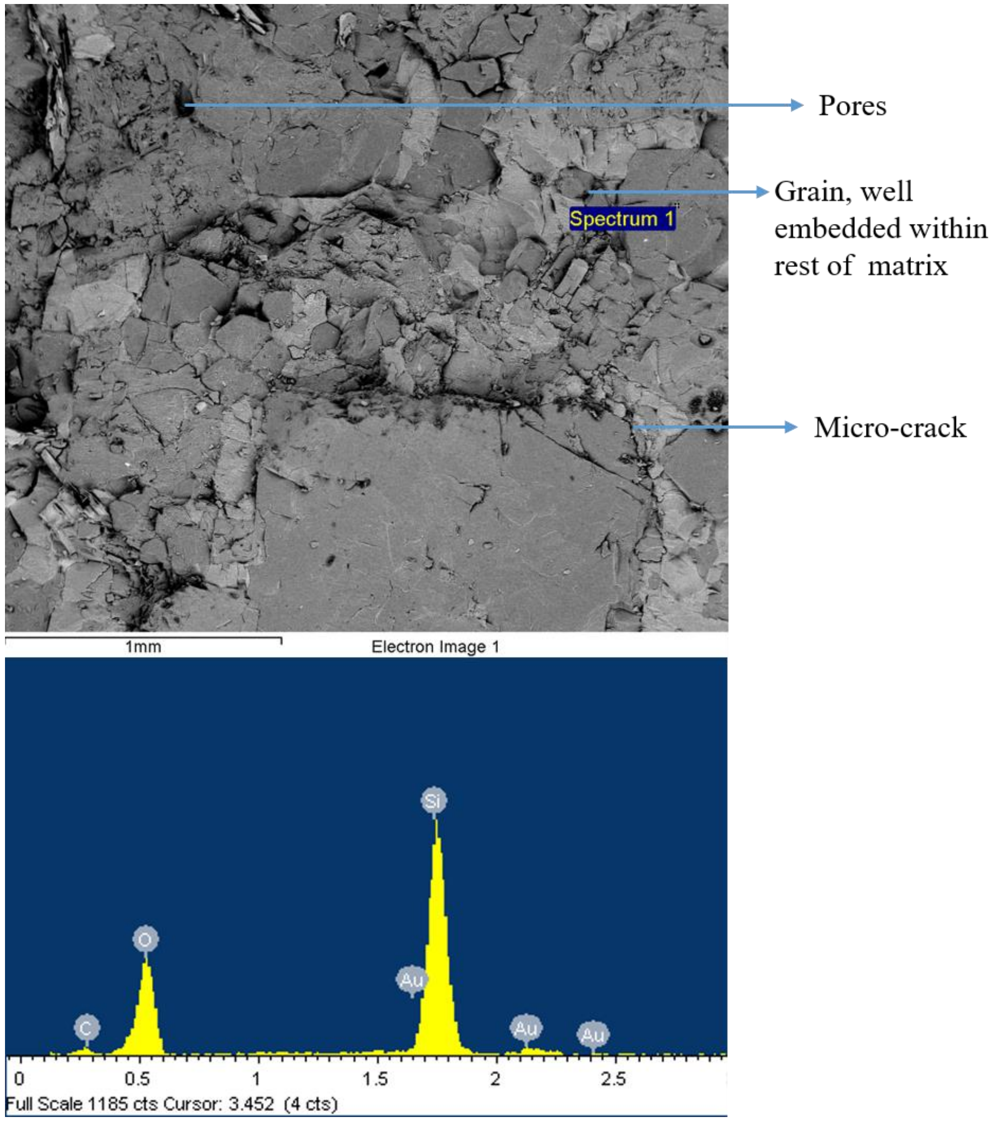

Figure 185: SEM image for Sierra White granite showing absence of pores and a well cemented matrix. Mineralogy of the area marked as 'Spectrum1' in the above picture is shown in the lower section showing presence of mainly silicates.

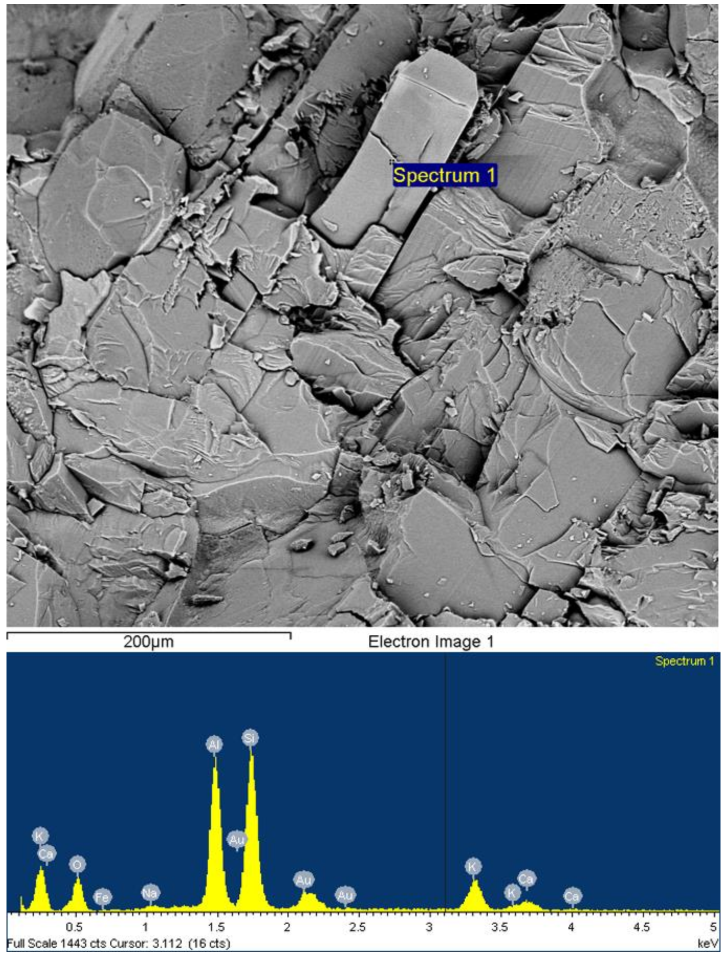

Figure 186: Another SEM image for Sierra White granite showing absence of pores and a well cemented matrix. Mineralogy of the area marked as 'Spectrum1' in the above picture is shown in the lower section showing presence of silicates, calcium, iron, and sodium oxides.

INEL-1 WELL SAMPLES – PORE STRUCTURE DESCRIPTION

For the INEL-1 well samples, both thin section imaging and SEM pore structure imaging was done. The SEM sections weren't high quality and as such, high quality images weren't obtained. Still the pore structure can be seen to be very heterogenous and with hardly any porosity for the deeper core. These are shown below.

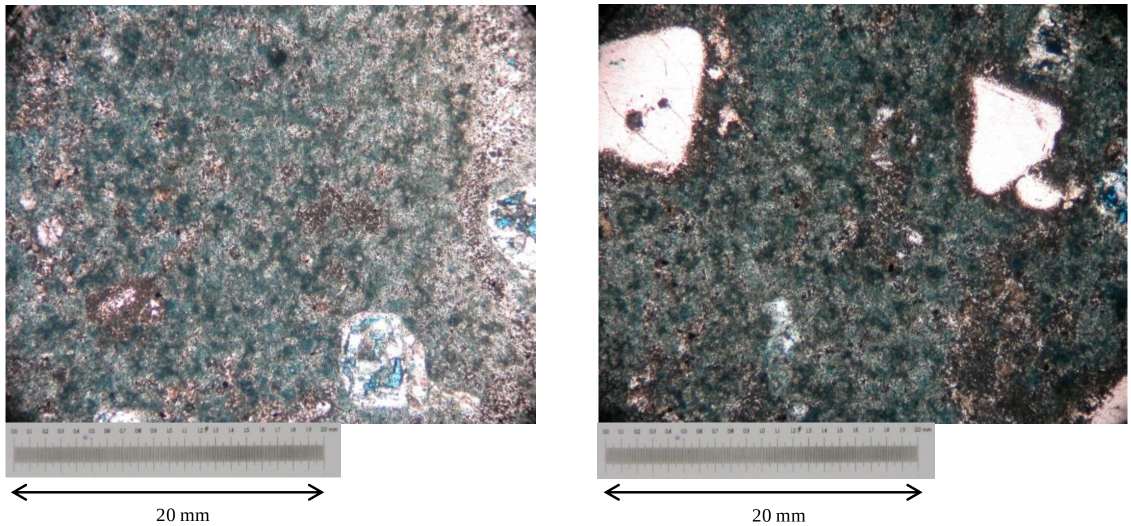

Figure 187: Thin section images of the core plugs from 4874 ft show a largely aphanitic texture with a few large quartz grains interspersed across. Porosity is not clearly observed suggesting small size pores which are described in detail in the SEM images.

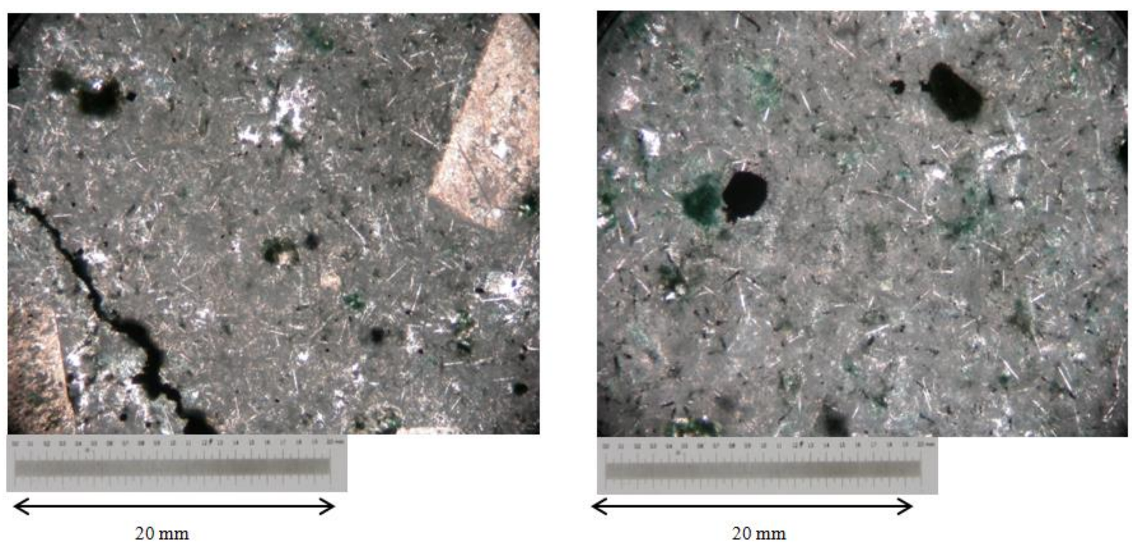

Figure 188: Thin section images of the core plugs from 10,365 ft, these also show a more aphanitic texture with a few large quartz grains interspersed across. Unconnected porosity and a micro-crack can be seen here (both black).

The following images show the pore structure using SEM at two different magnification levels. The core from 4830 ft shows pores of 20-100 μm at a 35x magnification. Most of the pores appear to be small though. Several large quartz grains (1-2 mm) can be seen interspersed within the sample (marked as green circles in figure 3). Pore connectivity is good. No micro cracks are seen here.

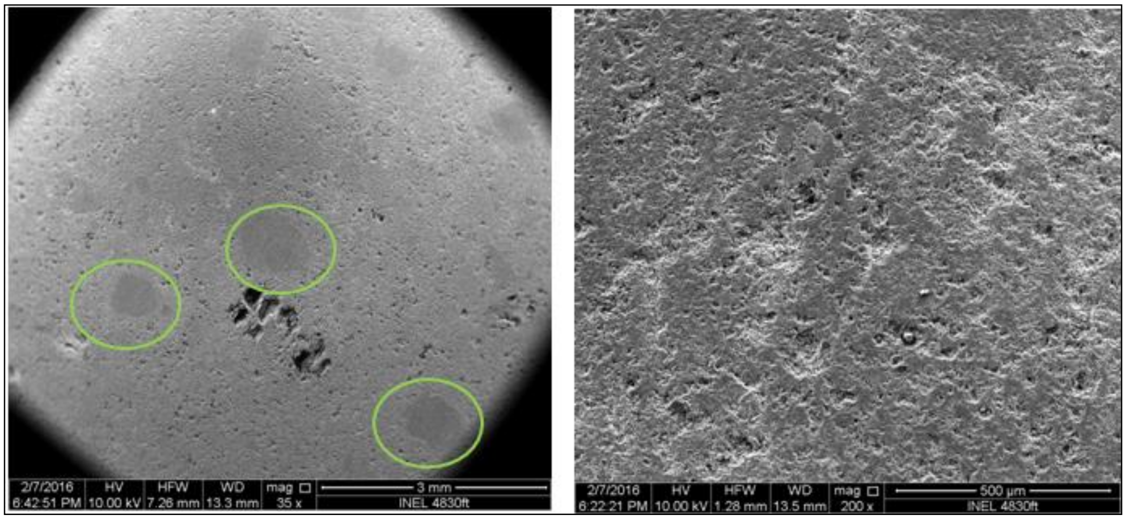

Figure 189: SEM images of the 4830 ft core. The left picture has a magnification of 35x while the right one has a 200x magnification. The green circles on the left show embedded grains within the matrix. The right picture shows pore spaces spread uniformly throughout the sample.

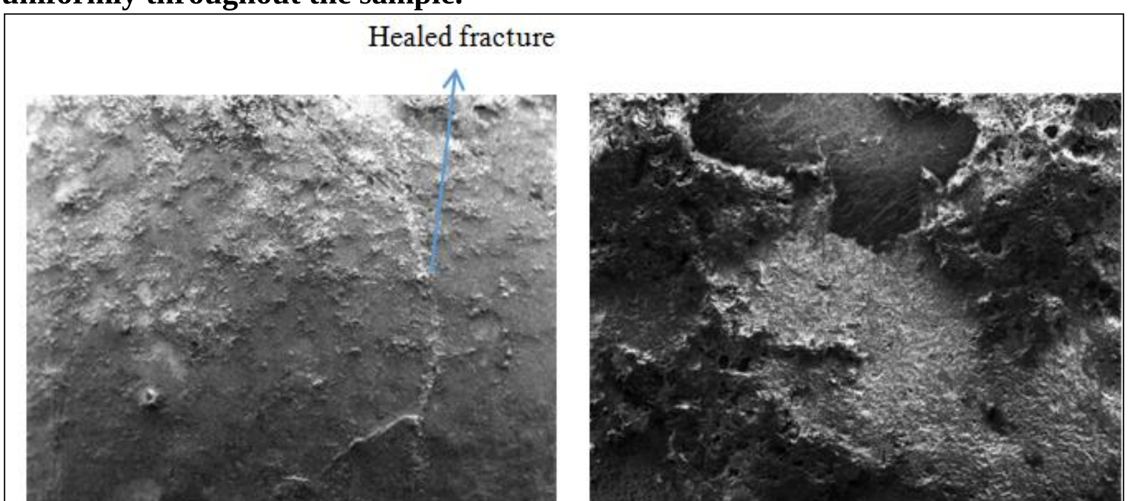

Figure 190: SEM images of the 10,365ft core plug. We can see that no porosity is evident in either picture and matrix looks denser. A healed fracture can be seen here – this was found to be filled with calcite.

For the 10,365ft core, the structure is markedly different. No porosity is evident here in the 35x magnification. In the 240x magnified image though, a few pores can be seen with sizes less than 50 μm. A healed fracture is seen here; many more can be seen throughout the sample.

LOCATION OF THE GEO-N2 AND OXY 72-03 WELLS, OREGON, USA

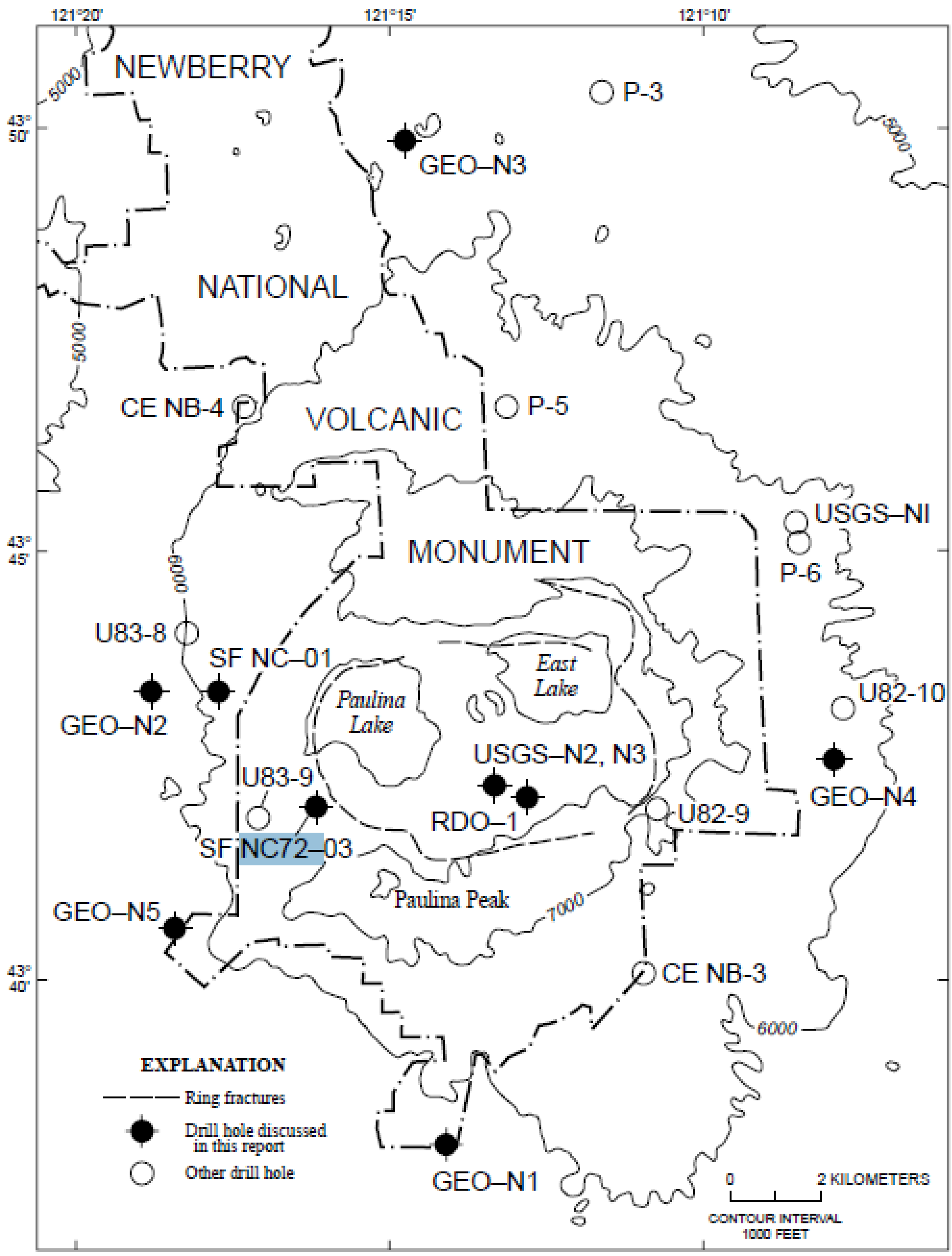

Figure 191: Map showing location of geothermal exploration drill holes at Newberry volcano (after Olmstead and Wermiel, 1988)

GEO-N2 (CORED) AND OXY 72-03 WELL CORED SAMPLES - DETAILED DESCRIPTION

Core sections from the GEO-N2 well and the Oxy 72-03 well

Five core sections were initially provided (Figure 192). The sections of whole core from where these were taken vary in depth from 3858 - 4364.5 ft. Four-Five plugs were extracted from each core section – a total of 23 plugs were extracted; the details of the same are described in table 1 below. While four plugs were tested in A&M university, four were broken or chipped (D1, D2, DH2, E1 and B1), leaving 14 samples for testing. Out of these fourteen, six have been tested for the purpose of this report (one from each depth section at least).

Figure 192: Five core sections along with their respective coring depths and diameters as provided

A core section wise detailed description is provided below:

1. Core section 3861-3862ft (Section A): Taken from the Oxy 72-03 Well. It had a diameter of 1.88 in and 1 feet length.

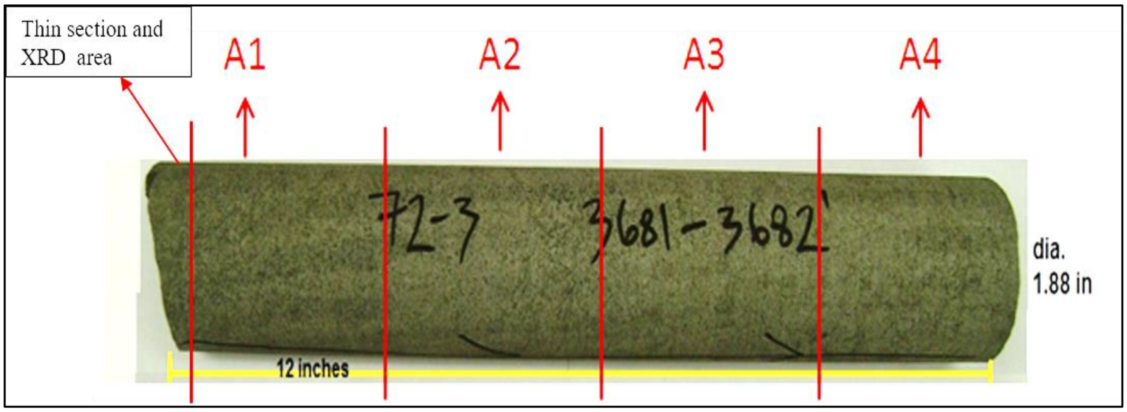

Figure 193: Core section 3861-3862 ft. Four plugs were extracted from this section -their locations are shown above

Figure 194: The four extracted core plugs from 3861-3862 ft section of the Oxy 72-03 well.

The core plugs were similar to each other in appearance with a dark gray color and very fine grain structure with grains not visible to the eye. A thin section image of the above is shown below in fig 4 and 5 (zoomed further).

Overall grains are angular with brownish color which indicates that these are rich in iron/magnesium. XRD results can confirm this.

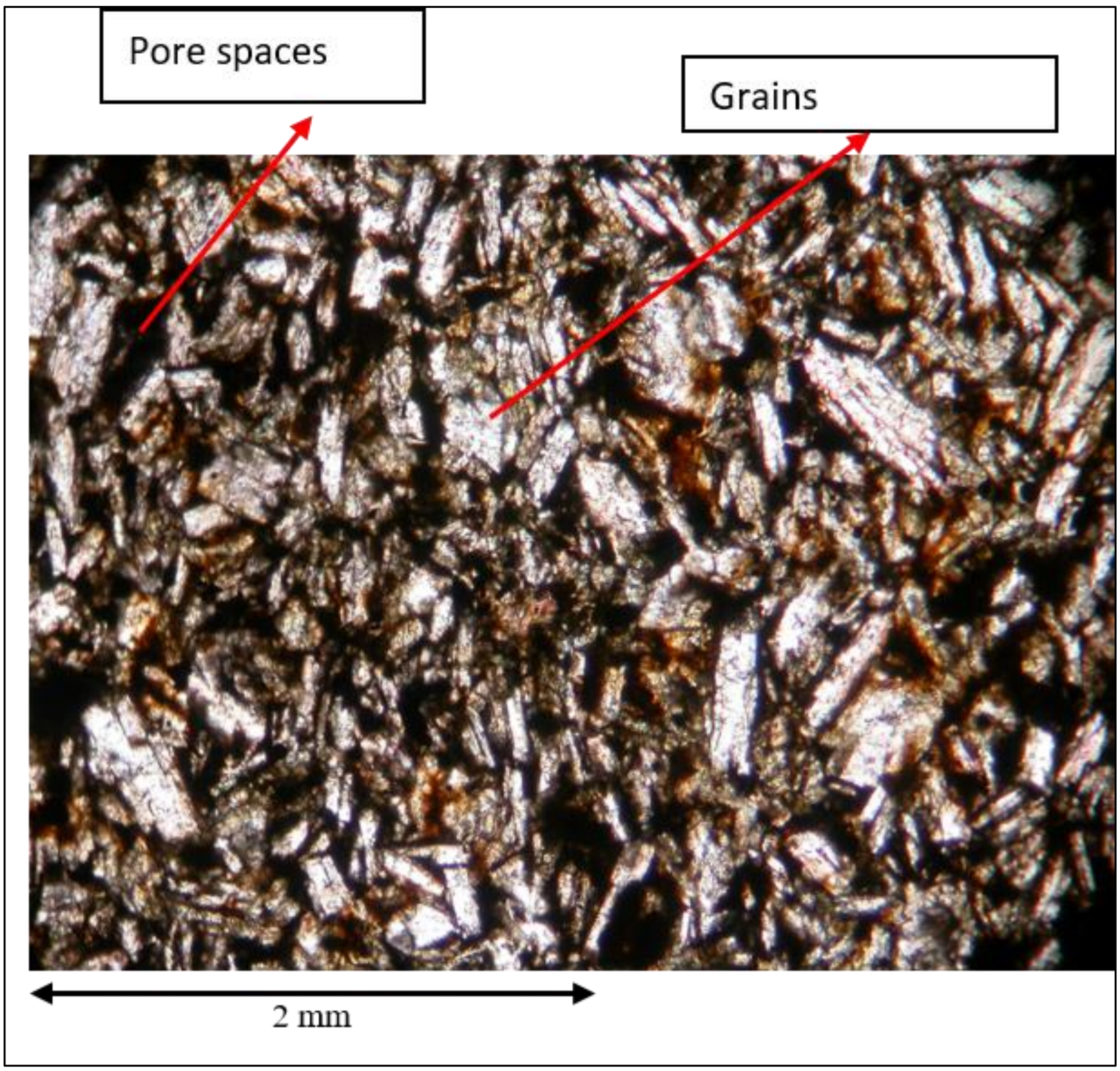

Figure 195: Thin section image of sample A. We can see small grains (<0.5mm), angular with pore spaces in black. The dark-colored crystals (brownish) are usually rich in iron/magnesium. The connected porosity is low at ~3% (table 3) but

the pore spaces are more here; this indicates that there are lots of unconnected pore spaces within the sample

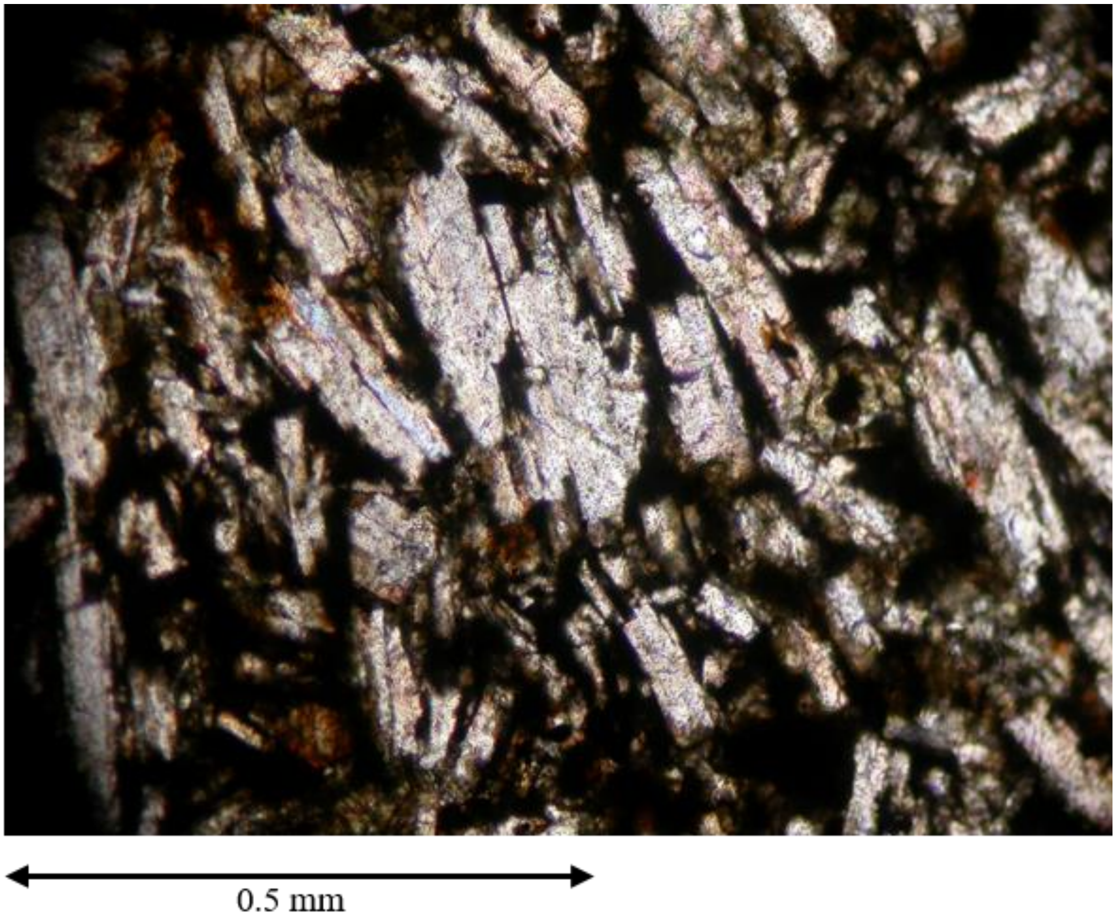

Figure 196: Zoomed in thin section image (scale provided) of sample A. We can see small grains interlocked with each other. Pore spaces are in black.

2. Core section N2 3858-3859 ft (Section B):

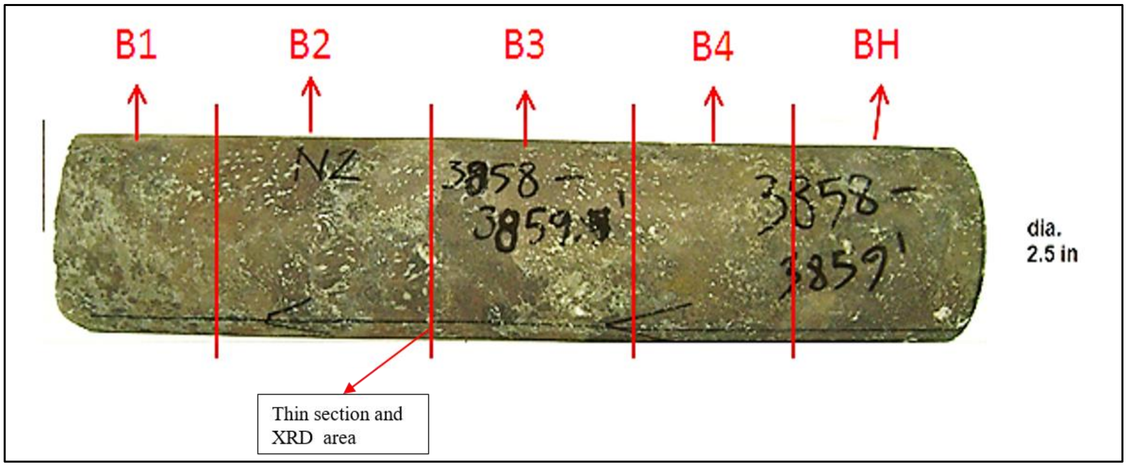

Figure 197: Core section 3858-3859 ft. Four plugs were extracted from this section - their locations are shown above

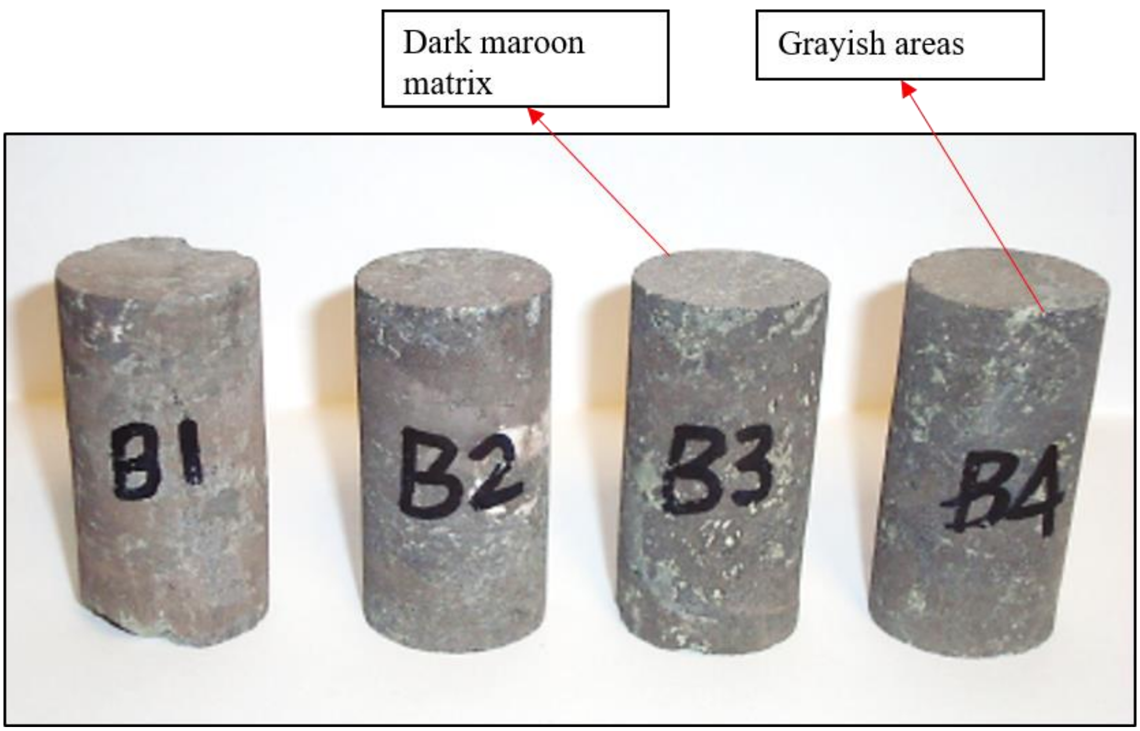

Figure 198: The four extracted core plugs from 3858-3859 ft section of the GEO-N2 well.

The core plugs were similar to each other in appearance with a dark maroon color interspersed with grayish areas in between. A thin section image of the above is shown below in Figure 199. Due to the very soft nature of the material, the thin sections were not of a good quality and not much data can be inferred from them.

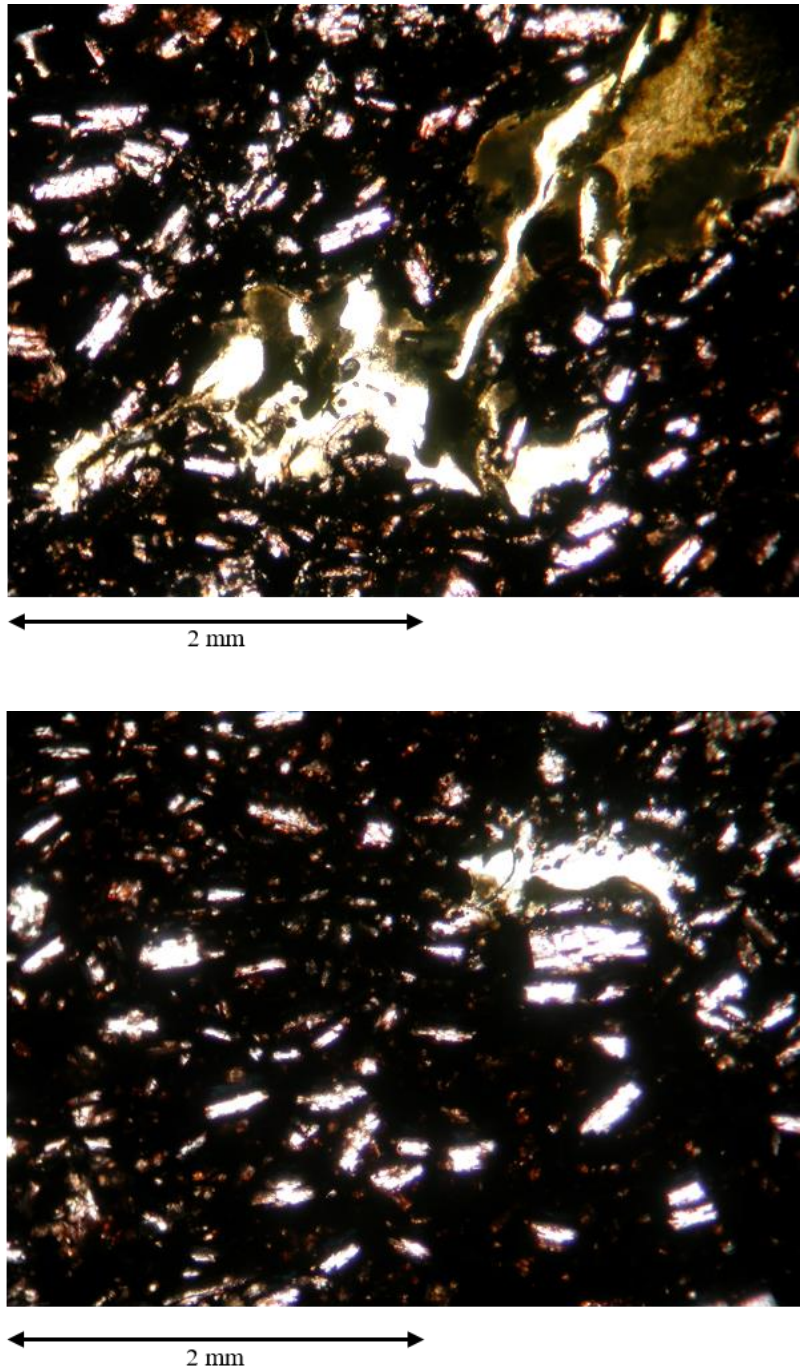

Figure 199: Thin section image of section B core. The quality of the thin section isn’t good and not much can be inferred from it. Grains do appear angular with a horizontal orientation. The grain size is usually < 0.5mm.

3. Core section 4360.5 – 4361.5 ft (Section C)

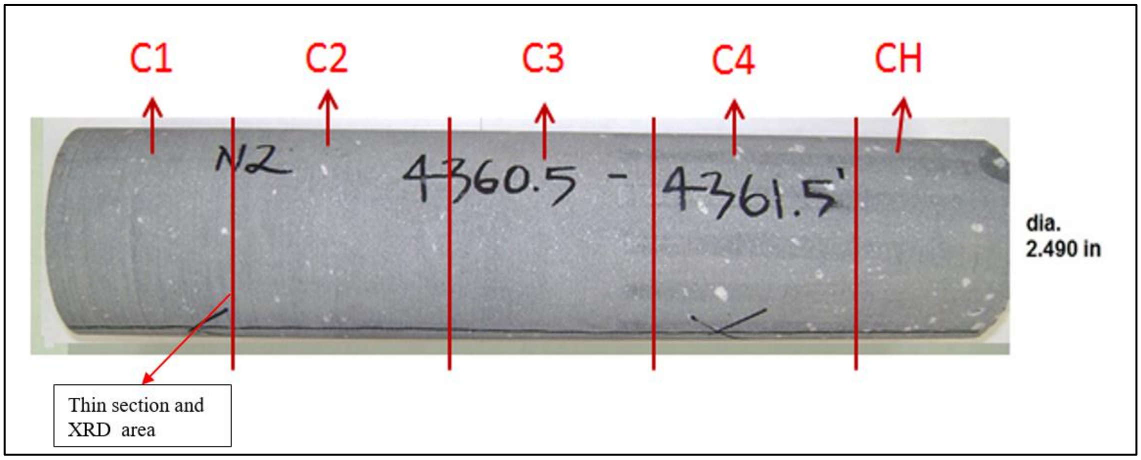

Figure 200: Core section 4360.5-4361.5 ft. Four plugs were extracted from this section -their locations are shown above

Figure 201: The four extracted core plugs from 4360.5-4361.5 ft. section.

The core plugs were similar to each other in appearance with a gray color and few white crystals interspersed between them. All of them have a very fine grain structure with grains (except the embedded white ones) not visible to the eye. A thin section image of the above is shown below in Figure 202 and Figure 203 (zoomed further).

Overall grains are angular with brownish color which indicates that these are rich in iron/magnesium.

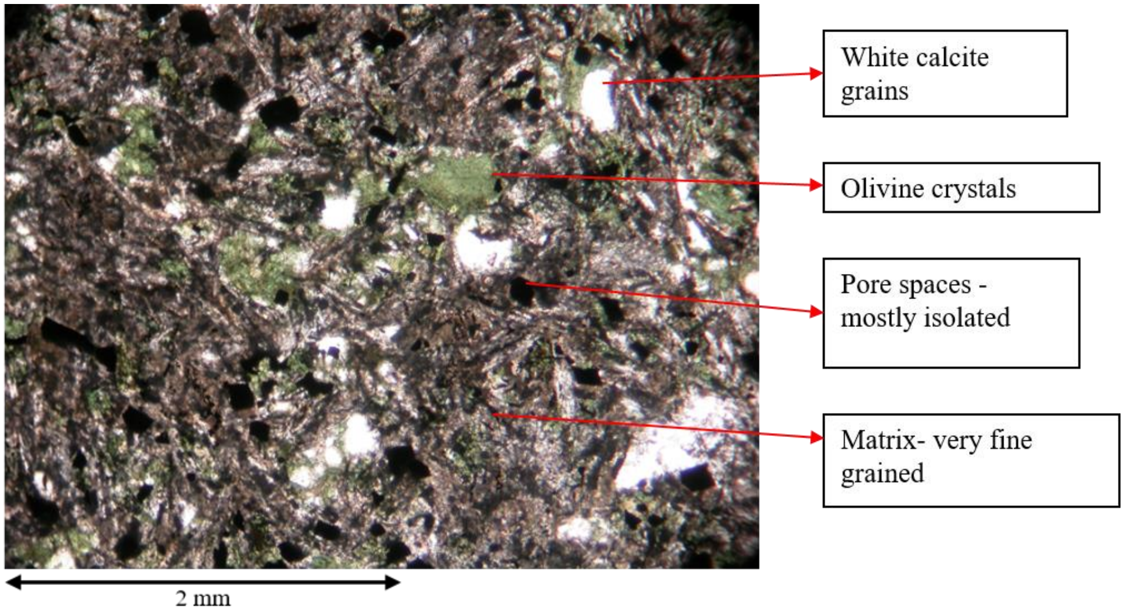

Figure 202: Thin section image of Section C of the core. The green crystals are olivine – very commonly present in igneous rocks. They give the sample its characteristic light green color. The white large grains seen in the sample can be clearly seen here – these are calcite crystals. The rest of the matrix is very fine grained with all grains less than 0.1 mm in size. The pore spaces are few and randomly spread throughout the sample and not connected. This indicates that both porosity and permeability of the sample should be very low.

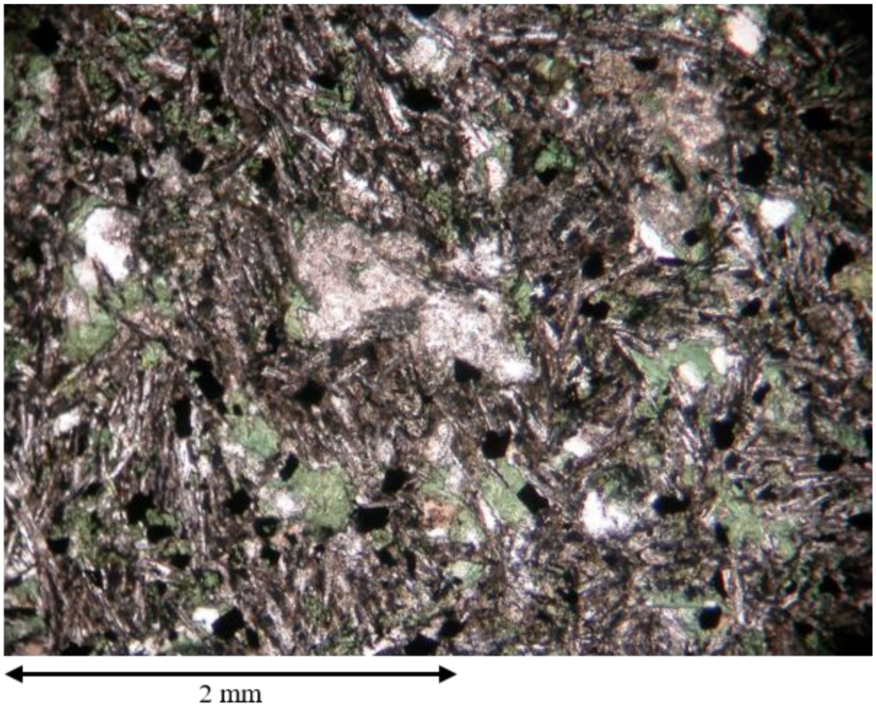

Figure 203: Another thin section of Section C. An explanation is already provided in the above figure.

4. Core section 4163.5 – 4164.5 ft

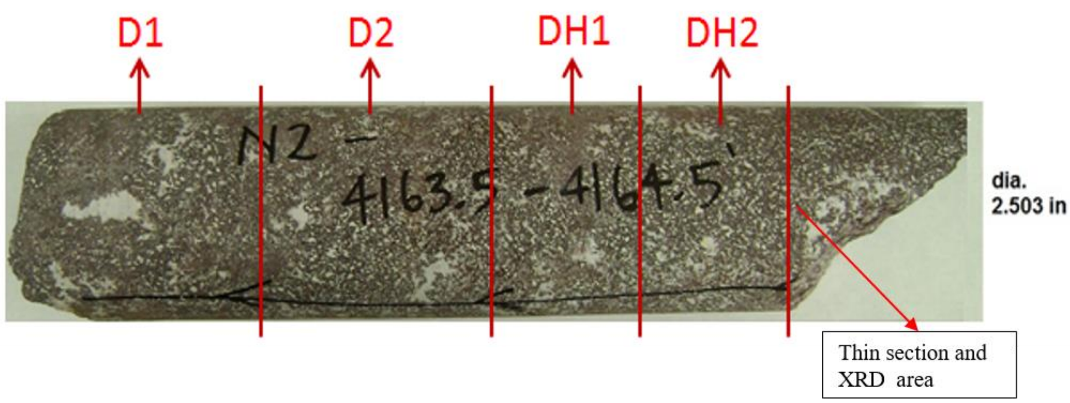

Figure 204: Core section 4163.5-4164.5 ft. Four plugs were extracted from this section -their locations are shown above

Figure 205: The four extracted core plugs from 4163.5-4164.5 ft section.

D1 and D2 broke into two parts and hence were taped as shown above. The recovery of GEO-N2-4180-H1 and DH2 was also not complete and both GEO-N2-4180-H1 and DH2 were less than 1.5 inch in length (instead of 2 inches).

The core plugs were similar to each other in appearance with a maroon color and several white crystals interspersed between them. All of them have a very fine grain structure with grains (except the embedded white ones) not visible to the eye. A thin section image of the above is shown below in Figure 206 and Figure 207.

Overall grains are angular with brownish color which indicates that these are rich in iron/magnesium. XRD results can confirm this.

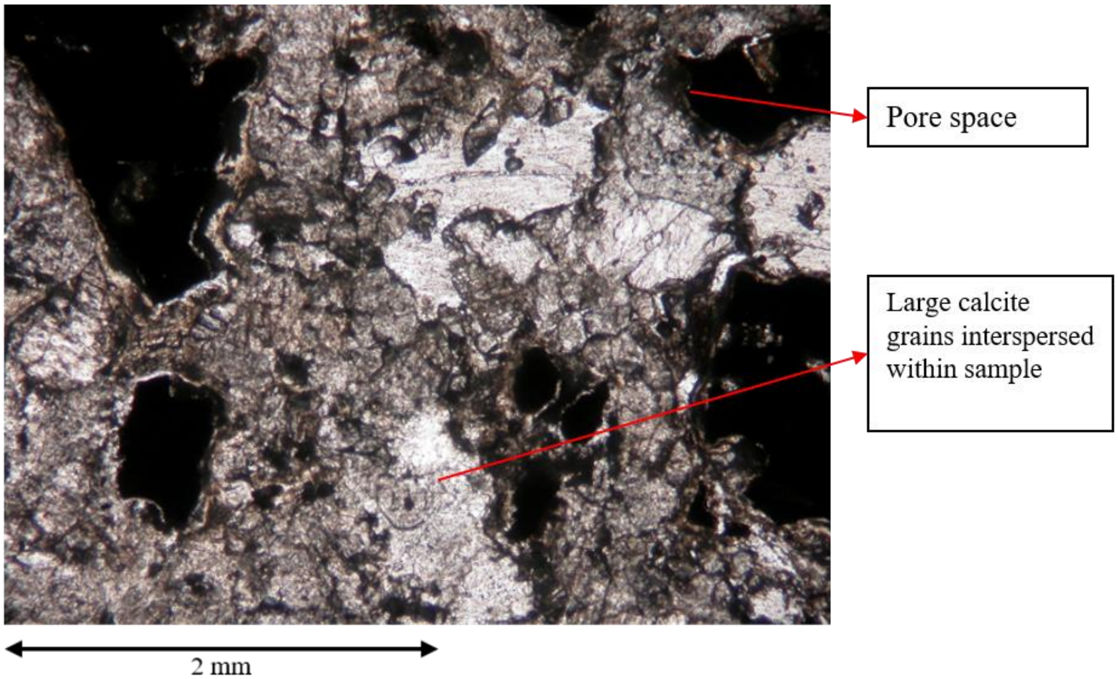

Figure 206: Thin section image of core section D. We can see several large grains well interlocked into the rest of the matrix with large unconnected porosity present within the sample. Grain size is described in next figure.

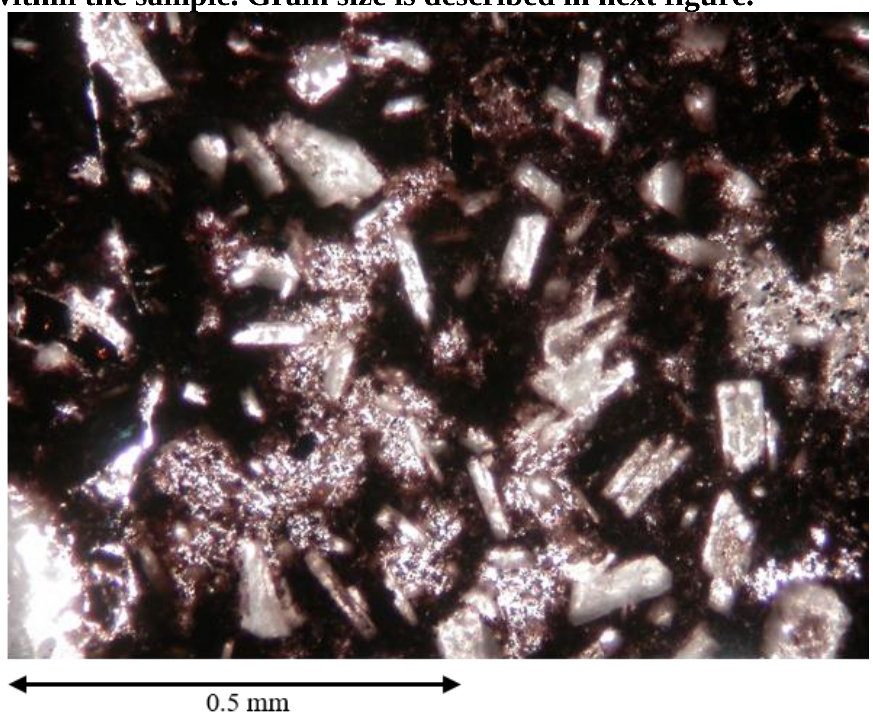

Figure 207: Zoomed in thin core section D (scale provided). Pore spaces are in black. Several angular grains and pore spaces can be seen clearly here. These are reasonably well connected as well which indicates that sample permeability should

be higher than the previous samples. Grains are less than 0.5 mm in length and don't show any particular orientation.

5. Core section 4179.5 – 4180.5 ft (Section E):

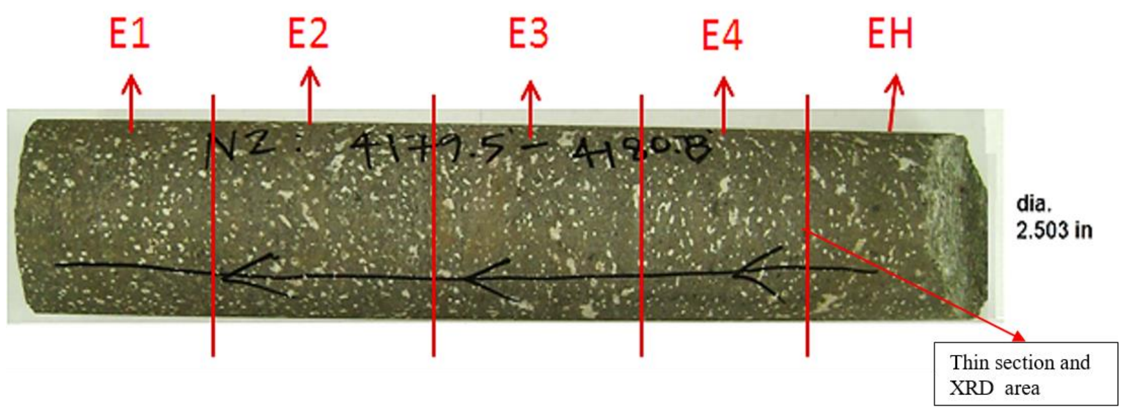

Figure 208: Core section 4179.5-4180.5 ft. Four plugs were extracted from this section -their locations are shown above

Figure 209: The four extracted core plugs from 3861-3862 ft section.

The core plugs were similar to each other in appearance with a gray color and several white crystals interspersed between them. All of them have a very fine grain structure with grains (except the embedded white ones) not visible to the eye. A thin section image of the above is shown below in Figure 210 and Figure 211.

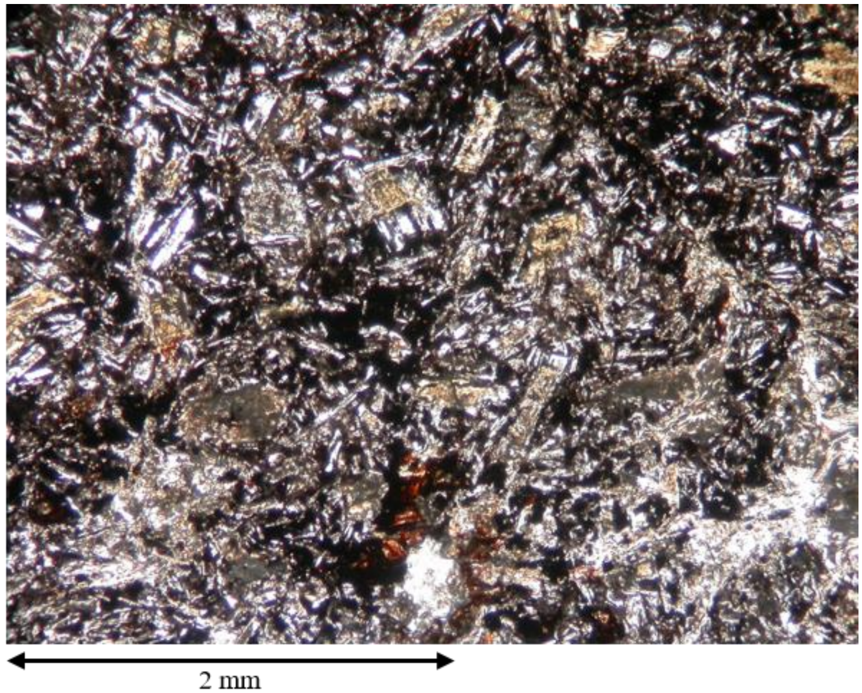

Figure 210: Thin section image of section A core. We can see small grains (<0.5mm), angular and well interlocked with pore spaces in black. The dark-colored crystals (brownish) are usually rich in iron/magnesium. Pore spaces are clearly visible although not always well connected. This indicates that sample has a >20% total porosity but lower connected porosity.

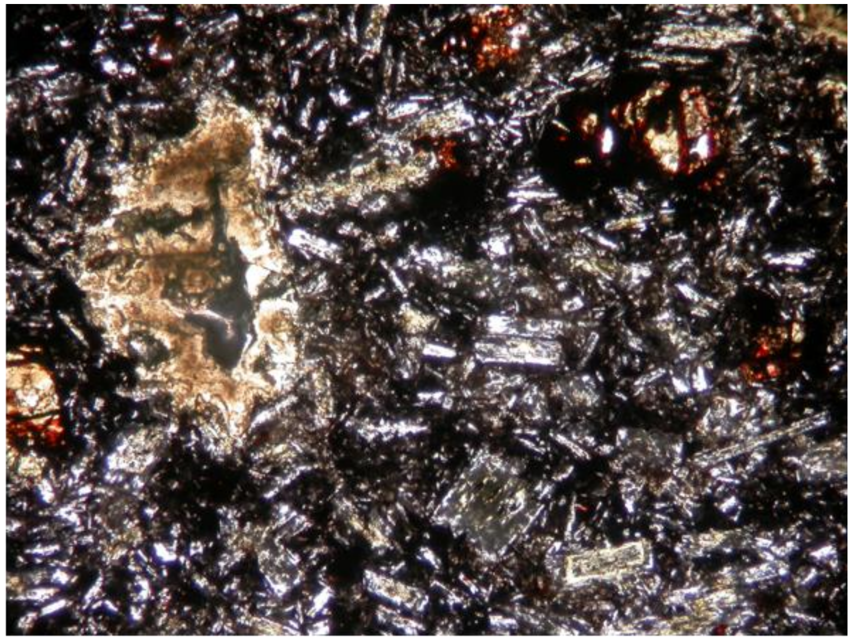

0.5 mm

Figure 211: Zoomed in version of above image. Description has already been provided.

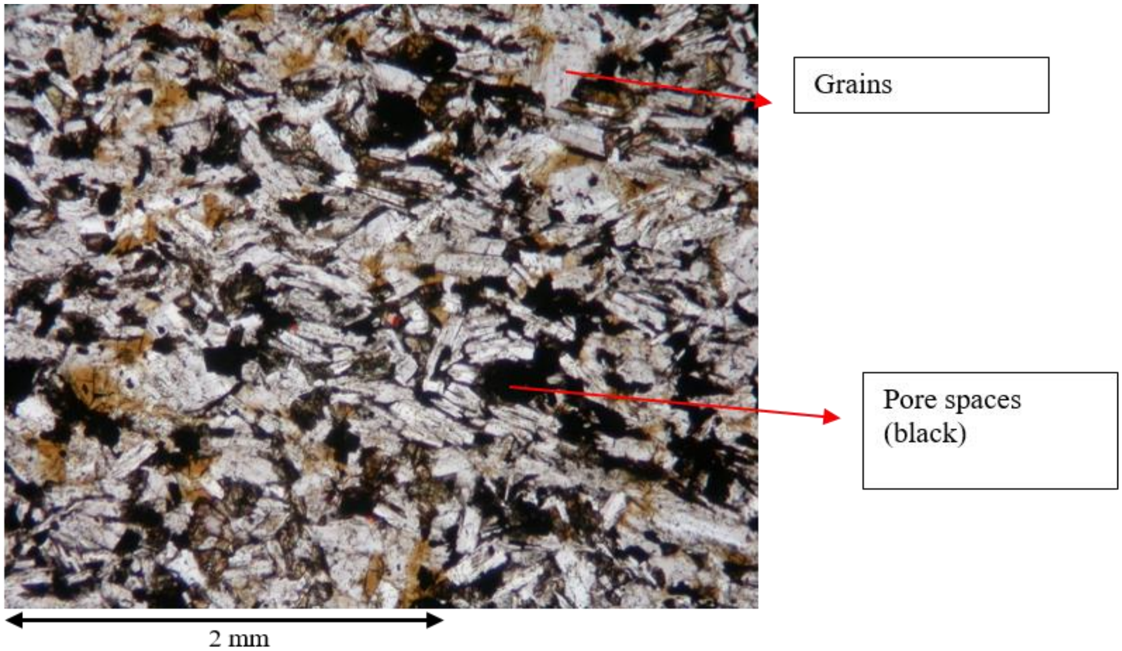

Figure 212: Thin section image of GEO-N2-4300-I1. We can see small crystals, interlocking in nature and angular with pore spaces in black. The dark-colored crystals (brownish) are usually rich in iron/magnesium. Grains are less than 0.5 mm in length.

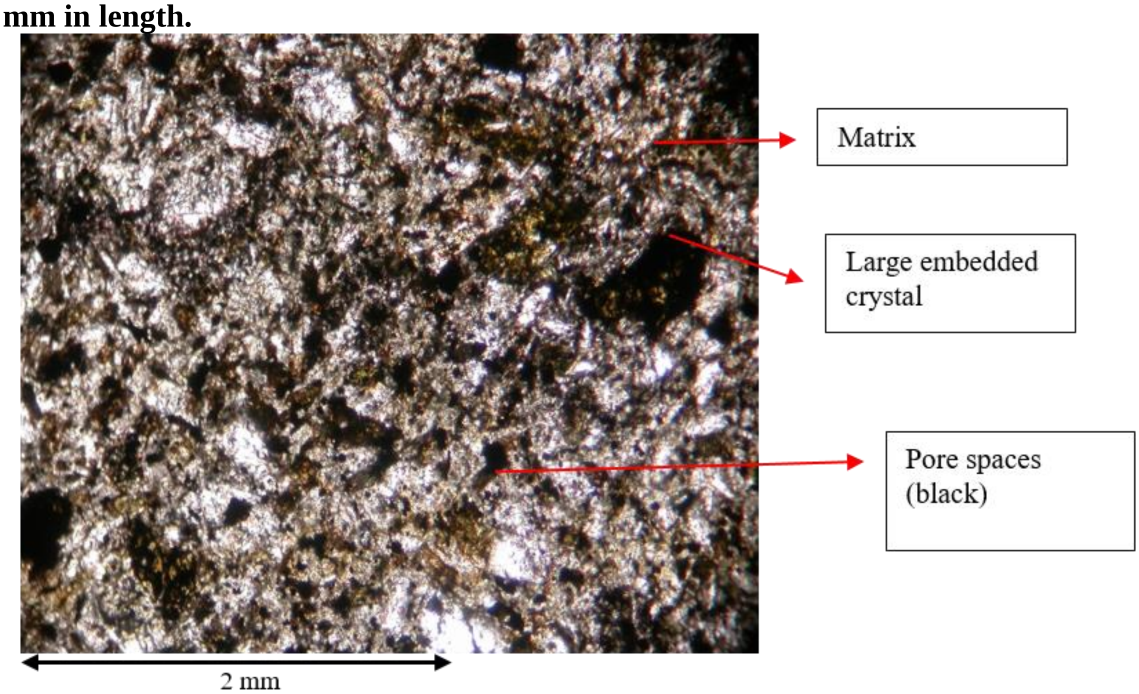

Figure 213: A thin section image for Sample number 5 in non-polarized light. Scale is provided for reference. We can see a very fine grained structure in comparison

to GEO-N2-4300-I1 with non-connected pores (black color) distributed throughout the sample. Grains are angular and less than 0.5 mm in size with the exception of a few large grains.

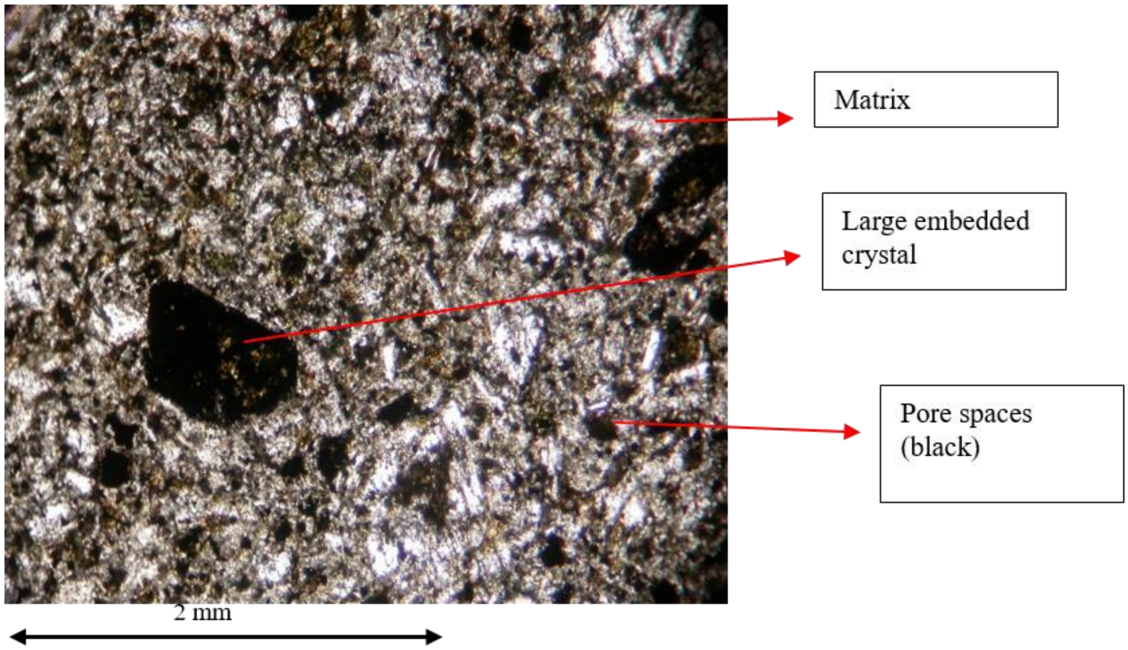

Figure 214: A thin section image for Sample number 6 in non-polarized light. Scale is provided for reference. We can see a very fine grained structure with non-connected pores (black color) distributed throughout the sample. Grains are angular and less than 0.5 mm in size with the exception of few large grains.

GEO-N2 full core sections - dynamic velocity and textural descriptions

<u>**Sample one**</u>

Table 29: Compressional and shear velocities for GEO-N2-4300-I1.

	P-wave velocity (m/s)	S-wave velocity (m/s)	Elastic modulus (GPa)	Poisson's ratio
500 psi	5154.55	2961.21	59.58	0.25
3500 psi	5309.19	3085.58	64.35	0.24

Figure 215: Closer view of the healed fractures within the GEO-N2-4300-I1 (top left) and Magnified view of sample showing inclusions (red and white) within the sample. Bottom view of sample showing the healed fracture intersecting one end of the sample.

<u>Sample description</u>

Sample is dark grey in color and has a length of 126.7 mm in length and a diameter of 63.5 mm (L/D ratio = 2). With a largely aphanitic structure it looked very similar to sample one and two with the exception of having many large embedded crystals within the sample. Sample had a large healed fracture (vein) running across the length intersecting one end of the sample. It had an angle of about 20^{o} with the vertical axis. Several inclusions can be seen in the sample. These are shown in figure above. Apart from the major fracture, there were several small localized fractures spread throughout the sample.

<u>Sample GEO-N2-4300-I2</u>

Figure 216: Pictures of GEO-N2-4300-I2. No healed fractures are visible. A few white calcite inclusions can be seen in the top two pictures.

Table 30: Compressional and shear velocities for sample GEO-N2-4300-I2

Confining pressure	P-wave velocity (m/s)	S-wave velocity (m/s)	Elastic modulus (GPa)	Poisson's ratio
500 psi	5261.50	3027.41	62.22	0.25
3500 psi	5143.20	2916.58	58.23	0.26

<u>Sample GEO-N2-4300-I3</u>

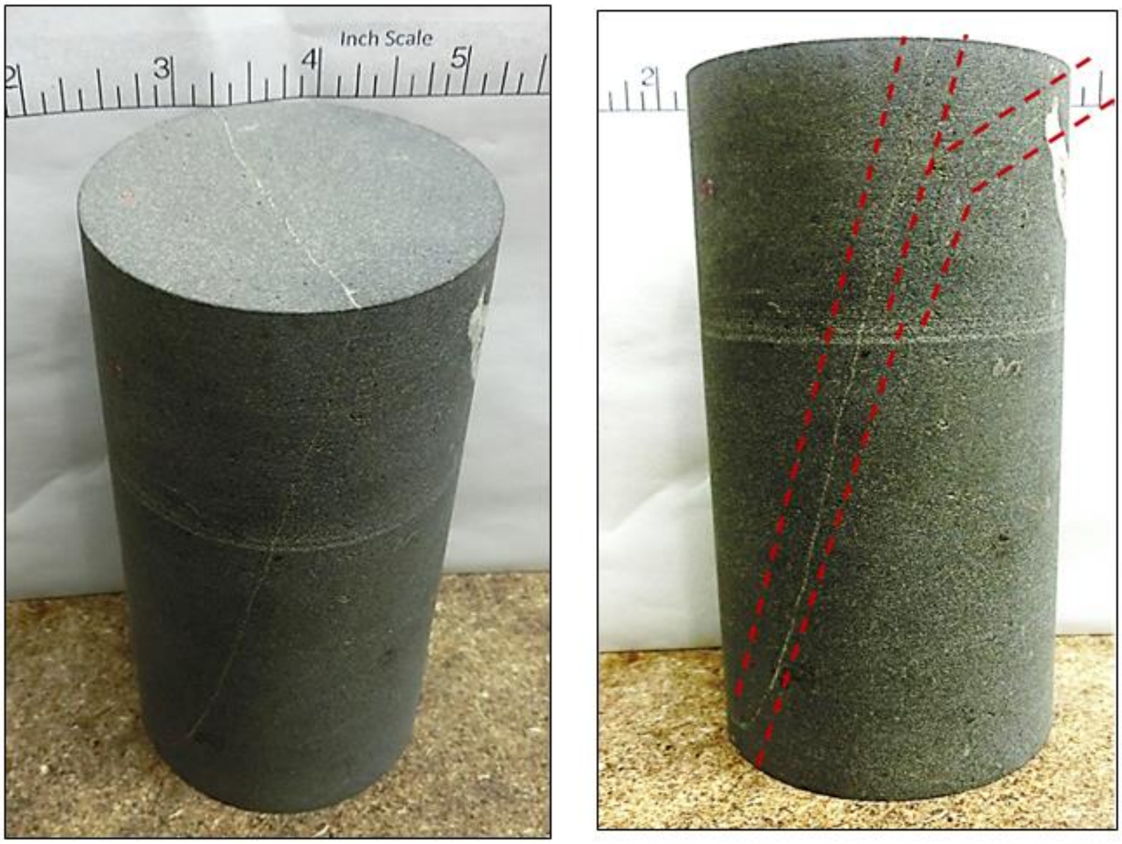

Figure 217: Sample GEO-N2-4300-I3pictures. A large healed fracture (vein) can clearly be seen running throughout the sample. Sample is aphanitic with large crystals embedded within the sample (see below pictures). Red lines enclose the healed fracture (veins) which are calcite in nature.

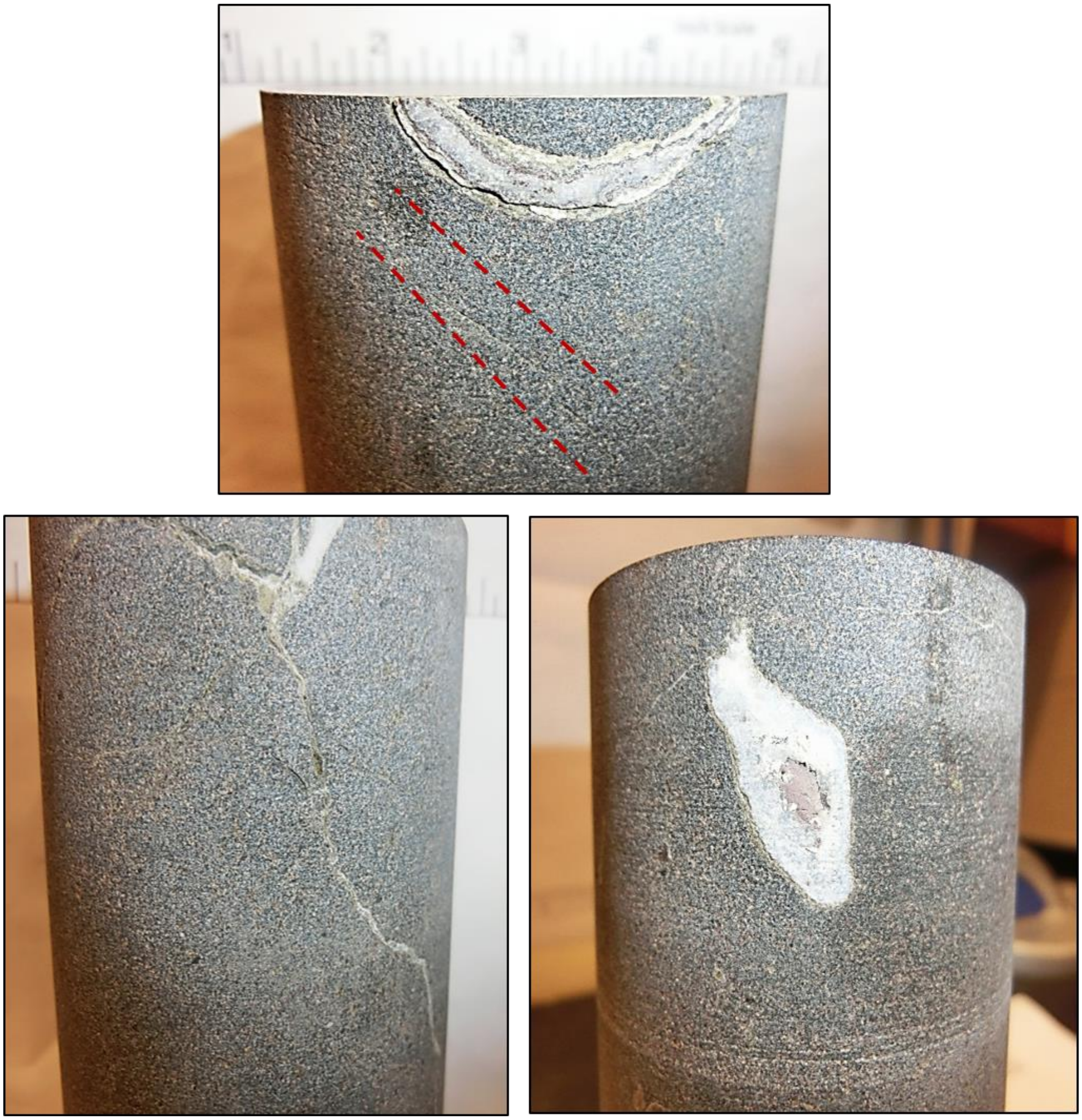

Figure 218: Pictures showing the various crystals embedded within the sample GEO-N2-4300-I3. All are 0.5- 1 inch in length and were not loose. We can also see a localized fracture in the top figure (within red lines).

<u>Sample Description</u>

Sample is light gray in color and has an average depth of 4381.75 ft (uncut core depth of 4378.4 – 4385 ft). It has a length of 127.51 mm (5.02 in) and 63.4 mm (2.5 in) in diameter (L/D ratio of 2:1). It also has reddish and white lines running across the sample (fig 59). It shows no visible fractures – minor or major. It does show few white colored inclusions (similar to other samples) which vary in size from <1 mm – 5mm in length (figure 59). Grain structure is same as sample - GEO-N2-4300-I1 but even more fine grained (thin section image; figure4) and very well consolidated. Its mineral content is provided below (ref Table 34-Table 40).

Table 31: Velocity measurements on Sample GEO-N2-4300-I3.

Confining Pressure	P-wave velocity (m/s)	S-wave velocity (m/s)	Elastic modulus (GPa)	Poisson's ratio
500 psi	4994.65	2766.57	52.85	0.28
3500 psi	5254.37	2935.33	59.24	0.27

Sample GEO-N2-4300-I4

Figure 219: Figure showing pictures of Sample GEO-N2-4300-I4. Healed fracture is visible running across the sample from one end to almost the other end.

Table 32: Dynamic velocity measurements for sample GEO-N2-4300-I4.

Confining Pressure	P-wave velocity (m/s)	S-wave velocity (m/s)	Elastic modulus (GPa)	Poisson's ratio
500 psi	5083.27	2659.63	49.98	0.31
3500 psi	5225.61	2758.04	53.56	0.31

Sample GEO-N2-4382-I1

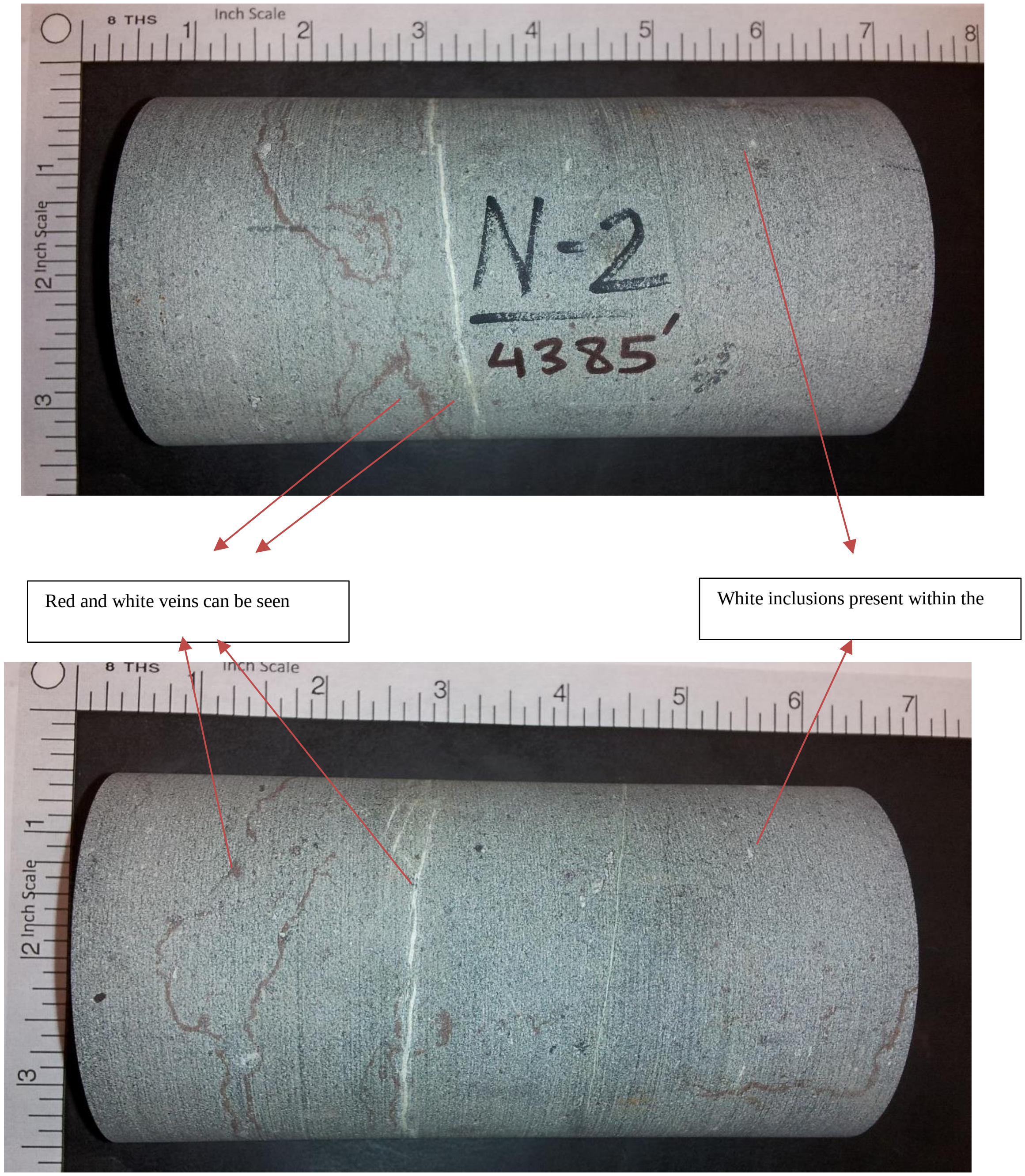

Figure 220: Figure shows pictures of GEO-N2-4382-I1. This sample differed from other samples in appearance – it can be seen to have a light grey appearance (compared to dark grey color for all other samples) with very pronounced reddish veins across the sample. White inclusions (calcite) can also be seen present in the sample.

Sample Description

Sample is purplish in color and has an average depth of 4382 ft. It has a length of 122.4 mm (4.8 in) and 63.5 mm (2.5 in) in diameter (L/D ratio of 1.9:1). Sample has white calcite veins (confirmed with XRD) running across the sample (fig 76). It shows no visible fractures – minor or major. It does show few white and colored inclusions (similar to other samples) which vary in size from <1 mm – 5mm in length (figure 76). Grain structure is same as sample - GEO-N2-4300-I1, fine grained and very well consolidated. Its mineral content is provided below (ref Table 34-Table 40).

Table 33: Velocity measurements for GEO-N2-4382-I1.

Confining Pressure	P-wave velocity (m/s)	S-wave velocity (m/s)	Elastic modulus (GPa)	Poisson's ratio
500 psi	4724.73	2946.59	54.11	0.18
3500 psi	4913.72	3073.29	58.71	0.18

<u>Sample GEO-N2-4243-I1</u>

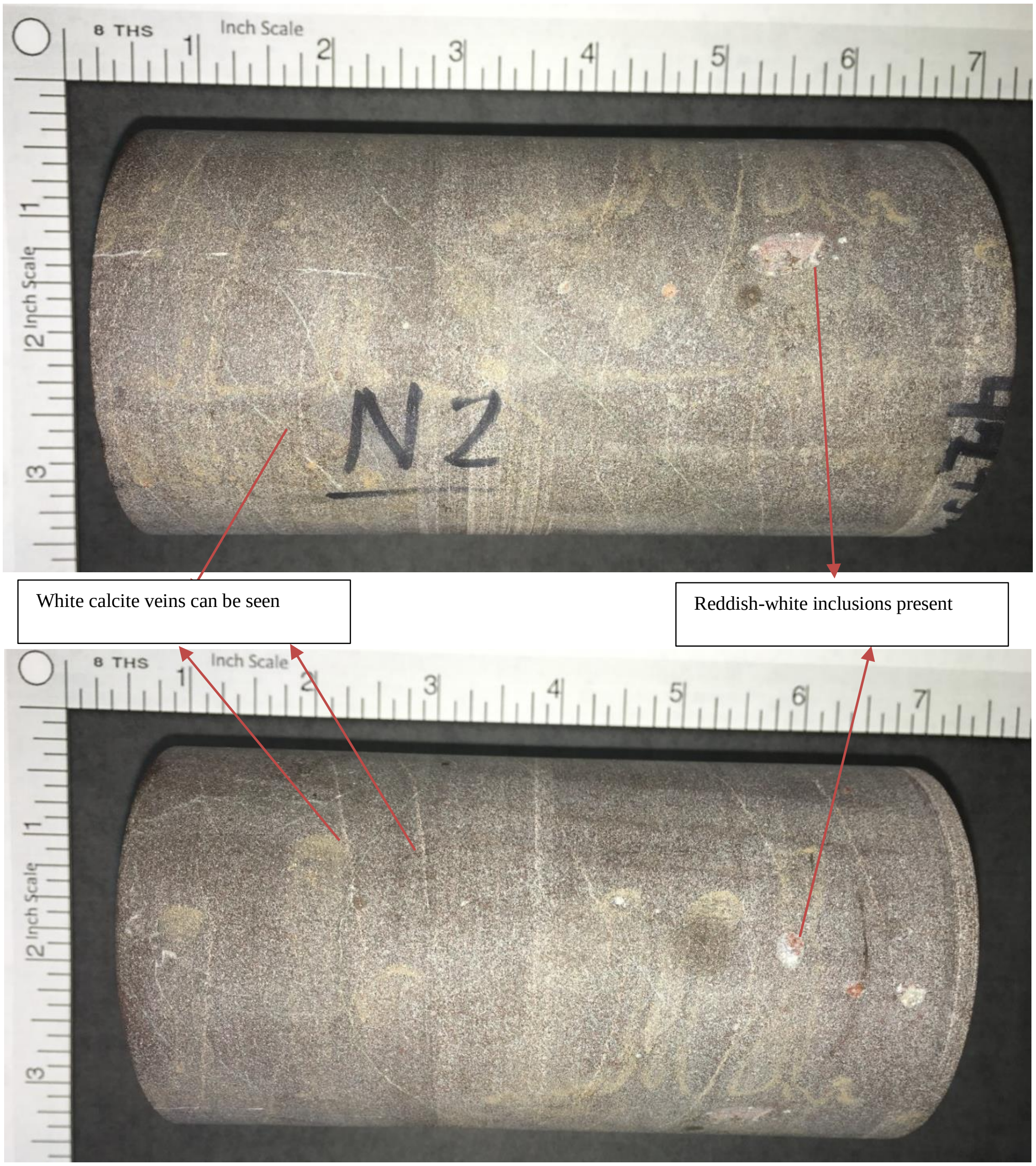

Figure 221: Figure shows pictures of GEO-N2-4243-I1. This sample differed from other samples in appearance – it can be seen to have a light grey appearance (compared to dark grey color for all other samples) with very pronounced reddish white veins across the sample. White inclusions (calcite) can also be seen present in the sample.

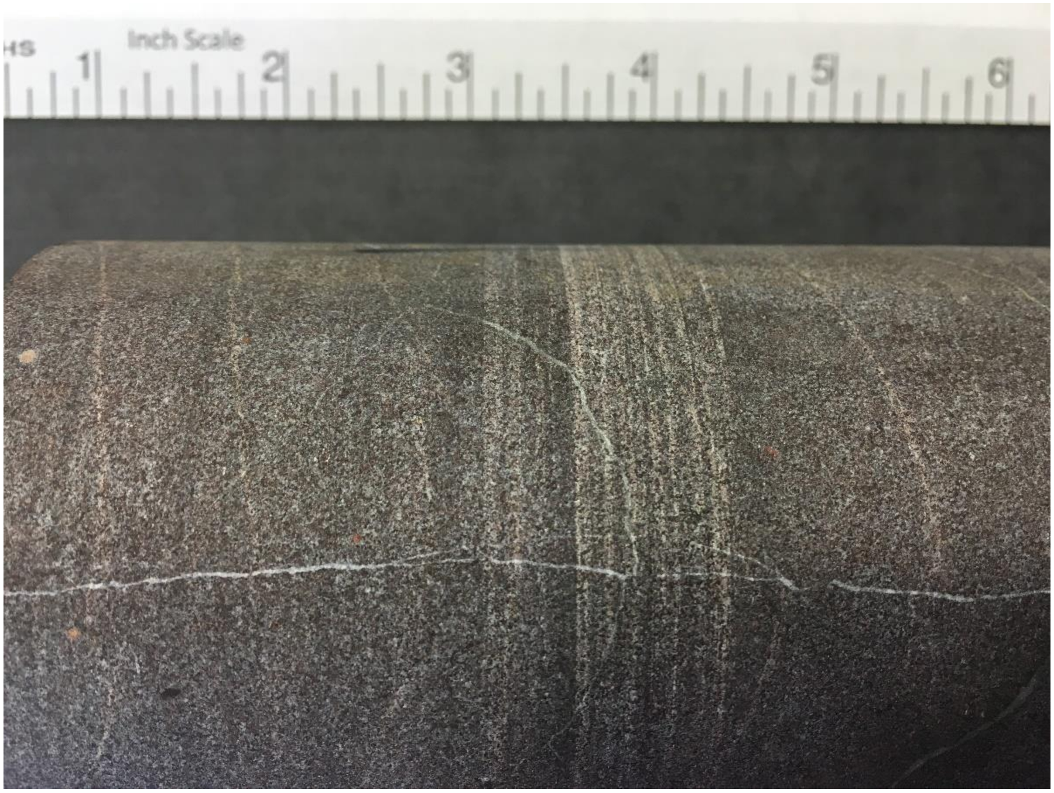

Figure 222: Zoomed in version of sample showing the calcite veins present in the sample clearly. This sample had the largest number of such veins crisscrossing the sample both horizontally and vertically.

Compound based classification of igneous rocks – few reference items:

Observe the two plots below taken from Johnson et al and University of Auckland's Geology page respectively, which help classify igneous rocks. Based on the fact that the samples tested (GEO N2 full core samples) had 44-53% silica, high feldspar content, were fine grained and high calcium content, we can conclude that these rocks lie somewhere between Basalts or Andesites. A closer match however based on all the properties mentioned above is Basalt. It should be noted that XRD analysis involves a very small portion of the sample (less than 5 gms). Hence it can't be considered representative of the entire core – variations may occur.

Useful information on classifying Igneous rocks on the basis of chemical composition

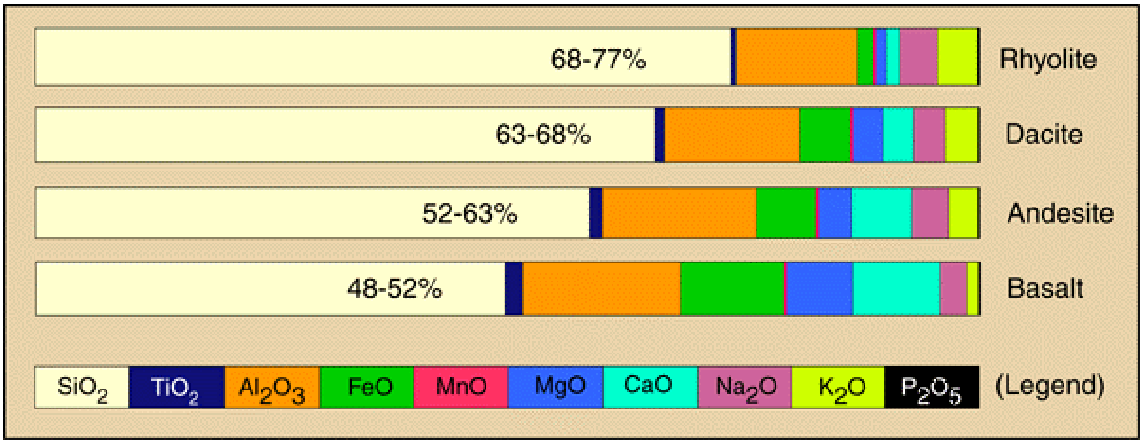

Figure 223: Compound based classification of igneous rocks (Johnson, 2005)

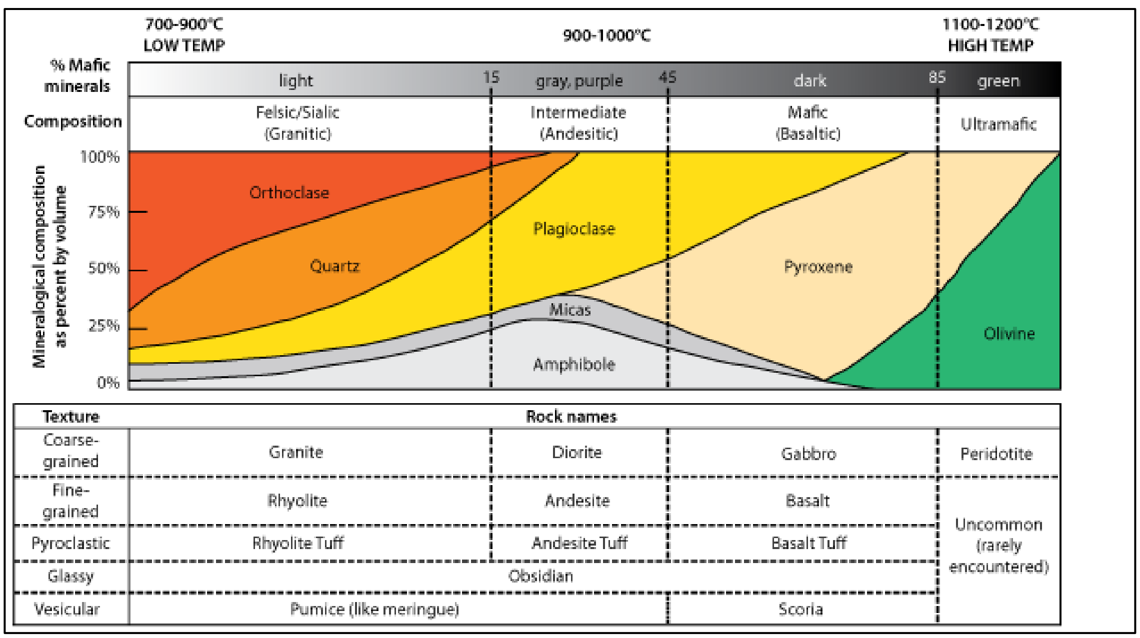

Figure 224: Mineral, grain size and texture based classification of igneous rocks (University of Auckland).

Mineral content description for GEO-N2 full core samples

A tabular description of the mineral and compound content is provided below:

Table 34: Mineral content in GEO-N2-4300-I2

Sample no 2	
Minerals	**Weight (%)**
Albite	38.3
Anorthite	21.9
Anorthite (Sodian, intermediate)	8.6
Pigeonite	9.3
Augite	7.8
Vermiculite	4.2
Quartz	3.8
Ferrosillite	2.9
Ilmenite	3.3

Table 35: Mineral content in GEO-N2-4382-I1

Sample GEO-N2-4382-I1	
Minerals	**Weight (%)**
Anorthite	28.5
Albite	25.7
Clinochlore	23.2
Corrensite	5.8
Quartz	9.8

Hematite-Ti	2.9
Ferrosillite	3
Fluorite	1

Table 36: Mineral content in GEO-N2-4243-I1

Sample GEO-N2-4243-I1	
Minerals	**Weight (%)**
Labradorite	42.1
Albite	33.1
Vermiculite	15.0
Quartz	6.6
Hematite	3.2

Table 37: Mineral content in healed fractures (white)

Healed fracture (Vein)	
Minerals	**Weight (%)**
Quartz	49.8
Ankerite	36.7
Dolomite	12.5
Albite	0.7
Calcite	0.2

Table 38: Compound composition in GEO-N2-4300-I2

Compound	**Weight (%)**
SiO_2	52.8%
Al_2O_3	21.3%

CaO	9.4%
Fe_2O_3	4.5%
Na_2O	4.3%
MgO	4.1%
TiO_2	1.7%
NiO	1.6%

Table 39: Compound composition in GEO-N2-4382-I1

Compound	Weight (%)
SiO_2	47.4%
Al_2O_3	25.9%
Fe_2O_3	10.5%
Na_2O	4.7%
MgO	4.1%
CaO	3.7%
TiO_2	0.2%

Table 40: Compound composition in GEO-N2-4243-I1

Compound	Weight (%)
SiO_2	44.1
Al_2O_3	31.7
Fe_2O_3	3.2
Na_2O	3.8
MgO	4.0
CaO	8.7

GEO-N2 core plug individual descriptions (textural and porosity) and compressional and shear velocity detailed information:

Sample-GEO-N2-4361-V2

Sample is light gray in color and has a length of 51.99 mm and diameter of 25.39 mm. Sample has a porphyritic structure with large white grains (>3mm) interspersed within an otherwise fine grained sample. No fractures or cracks can be seen within the sample with naked eye. Sample has a Length to Diameter ratio of 2.05. Thin section images of this sample have already been provided in section 1.

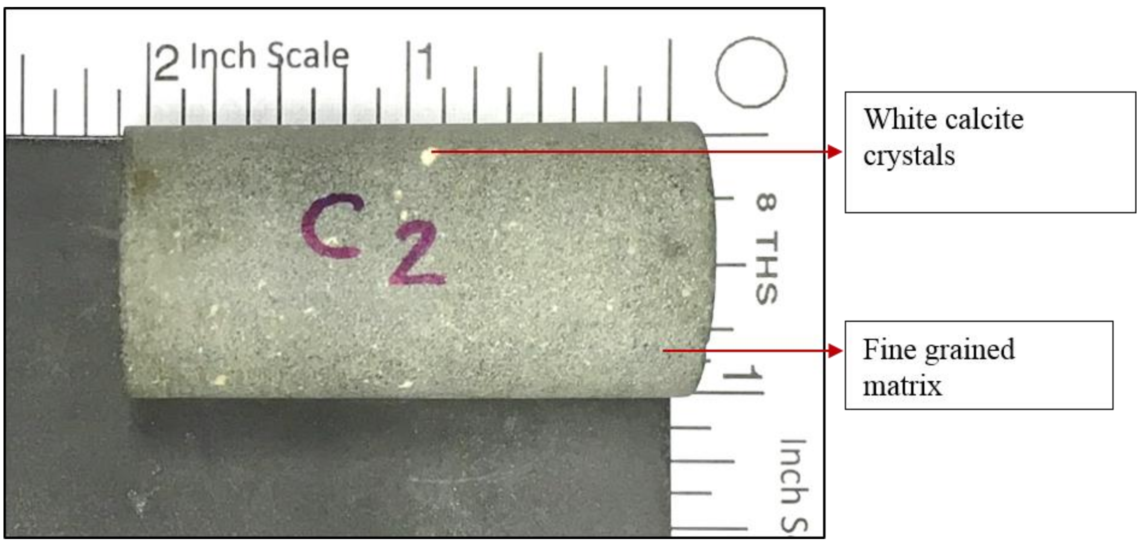

Figure 225: Front view of sample showing a fine-grained matrix, grayish-green in color with white calcite crystals interspersed within the sample.

Dynamic Velocity measurements for Sample GEO-N2-4361-V2

Dynamic velocity tests were carried within the triaxial cell just before and after the test. These were measured at confining pressures of 0 to 3500 psi - these are reported below. The reason for these pressures is that ideally, velocities should be measured at the in-situ conditions although measuring them at low confining pressures and then comparing those to higher pressures gives a qualitative idea of the compressibility of the material as well as its porosity. Very large differences (>10%) are seen in unconsolidated rocks while lower differences are found in consolidated rocks (<5%). Presence of large crystals like seen in this sample can also strongly affect these readings as the velocity of wave within these grains may be very different from the rest of the matrix.

In the case of sample GEO-N2-4361-V2, a difference of 3% was observed between the compressional velocities measured between 100 psi or 3500 psi, while the difference for shear velocities was lower at 8% over the same confining pressure range. This shows the well consolidated nature of these rocks. Average V_p/V_s ratio of 1.60 was observed for this sample. Tests were carried out with axially placed compressional and shear crystals, both of frequency 500 Hz, placed within the top and bottom platens. Results are tabulated below:

Table 41: Compressional and shear velocities for sample GEO-N2-4361-V2

Confining Pressure	P-wave velocity (m/s)	S-wave velocity (m/s)	Dynamic Elastic Modulus (GPa)	Dynamic Poisson's ratio
0	4782	2971	53.03	0.19
1000	4908	3176	58.27	0.14
2500	5091	3212	61.15	0.17
3500	5100	3224	61.49	0.17

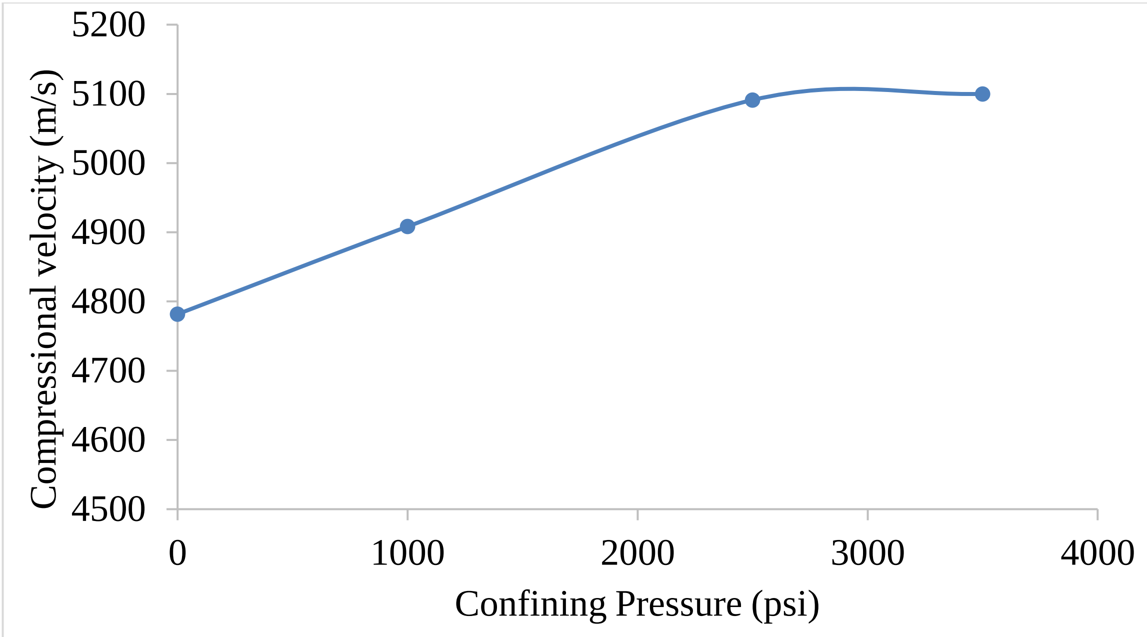

Figure 226: Figure showing variation of compressional velocity for sample GEO-N2-4361-V2 with change in confining pressure. Results show about 2% variation in velocities as confining pressure changes from 0 to 3500 psi.

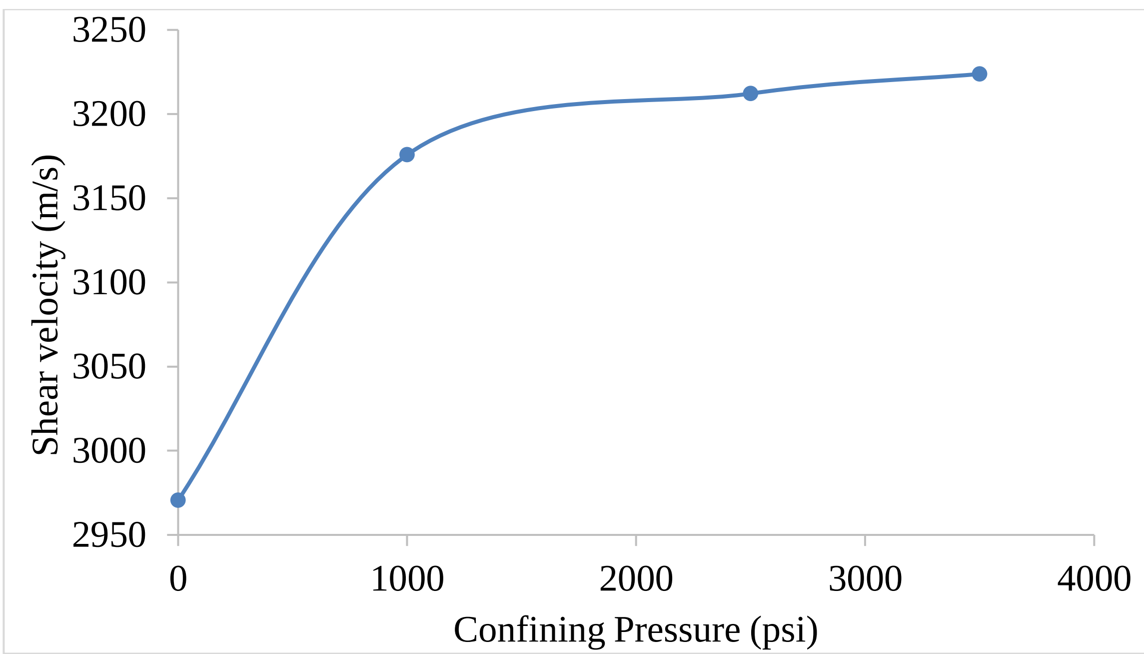

Figure 227: Figure showing variation of shear velocity for sample GEO-N2-4361-V2 with change in confining pressure. Results show about 8% variation in velocities as confining pressure changes from 0 to 3500 psi.

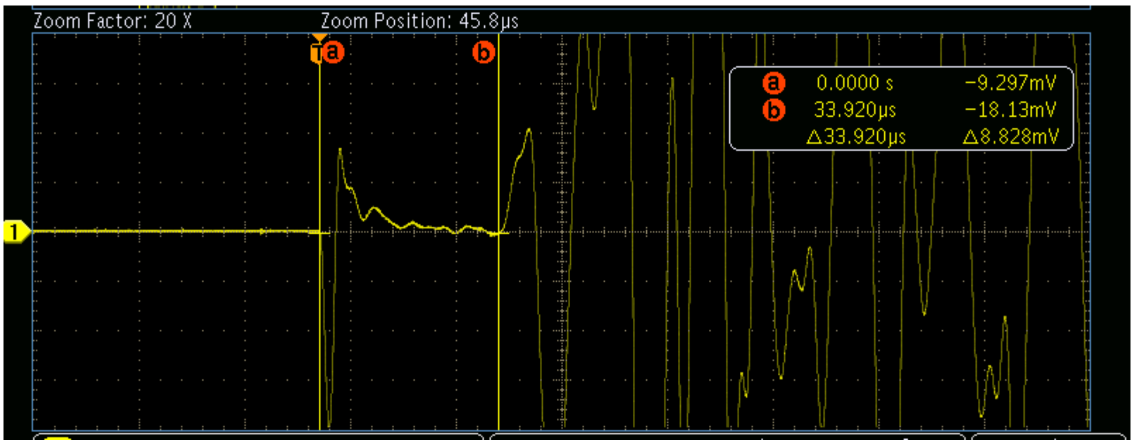

Figure 228: Above two figures show compressional (top) and shear waves for sample GEO-N2-4361-V2. Corrections were applied to these waves to remove effect of platen travel time.

Variation of Porosity with changing confining pressure: The porosity –permeability relationship with changes in confining pressure was measured using a AP-608 Automated Permeameter-Porosimeter

The porosity of the sample as a function of confining pressure (500 psi to 4000 psi) was measured and found to vary from 0.22%-0.12% and is shown below:

Table 42: Porosity vs confining pressure for GEO-N2-4361-V2

Confining pressure (psi)	Connected Porosity (%)

506	0.21
1541	0.14
2534	0.14
3014	0.13
4055	0.13

The extremely low values of porosity show the highly compacted nature of this rock.

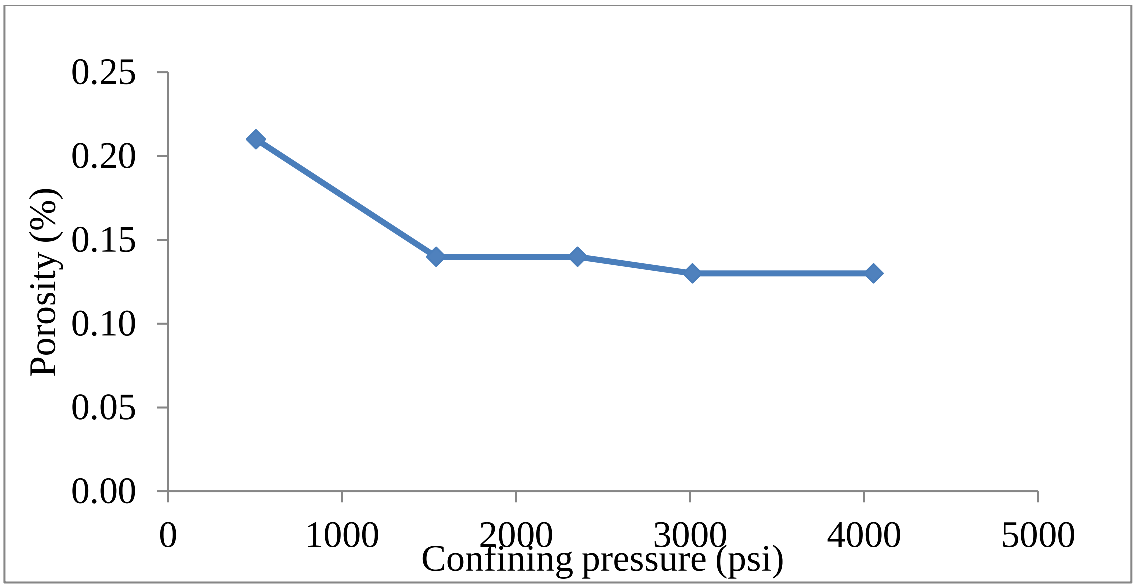

Figure 229: Porosity vs confining pressure for sample GEO-N2-4361-V2.

Sample OXY-72-3-3861.5-V2

Sample is dark gray to black in color and has a length of 51.98 mm and diameter of 25.39 mm. Sample has a aphanitic structure with few small red grains (<1 mm). No fractures or cracks can be seen within the sample with naked eye. Sample has a Length to Diameter ratio of 2.05. Thin section images of this sample have already been provided in section 1. They confirm that this sample is fine grained with angular grains,

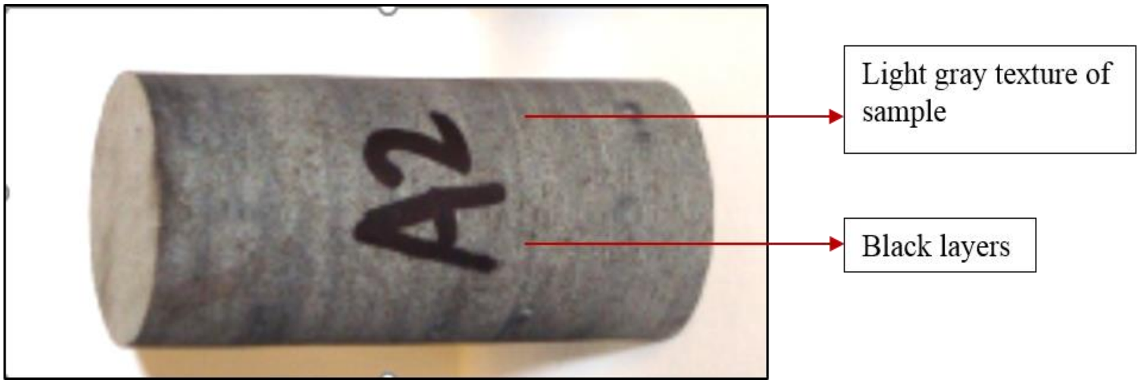

Figure 230: Front view of sample showing a fine grained matrix, grayish-green in color with white calcite crystals interspersed within the sample.

Dynamic Velocity measurements

Dynamic velocity tests were carried within the triaxial cell just before and after the test. These were measured at confining pressures of 0 to 3100 psi - these are reported below. The reason for these pressures is that ideally, velocities should be measured at the in-situ conditions although measuring them at low confining pressures and then comparing those to higher pressures gives a qualitative idea of the compressibility of the material as well as its porosity. Very large differences (>10%) are seen in unconsolidated rocks while lower differences are found in consolidated rocks (<5%). Presence of large crystals like seen in this sample can also strongly affect these readings as the velocity of wave within these grains may be very different from the rest of the matrix.

In the case of sample OXY-72-03-3861.5-V2, a difference of 4.1% was observed between the compressional velocities measured between 1 psi or 3100 psi, while the difference for shear velocities was higher at 7.3% over the same confining pressure range. This shows the well consolidated nature of these rocks. Average V_p/V_s ratio of 1.76 was observed for this sample. Tests were carried out with axially placed compressional and shear crystals, both of frequency 500 Hz, placed within the top and bottom platens. Results are tabulated below:

Table 43: Compressional and shear velocities for sample OXY-72-3-3861.5-V2

Confining Pressure (psi)	P-wave velocity (m/s)	S-wave velocity (m/s)	Dynamic Elastic Modulus (GPa)	Dynamic Poisson's ratio
1	5675	3173	70.11	0.27
1100	5763	3284	74.31	0.26
3500	5834	3308	75.62	0.26

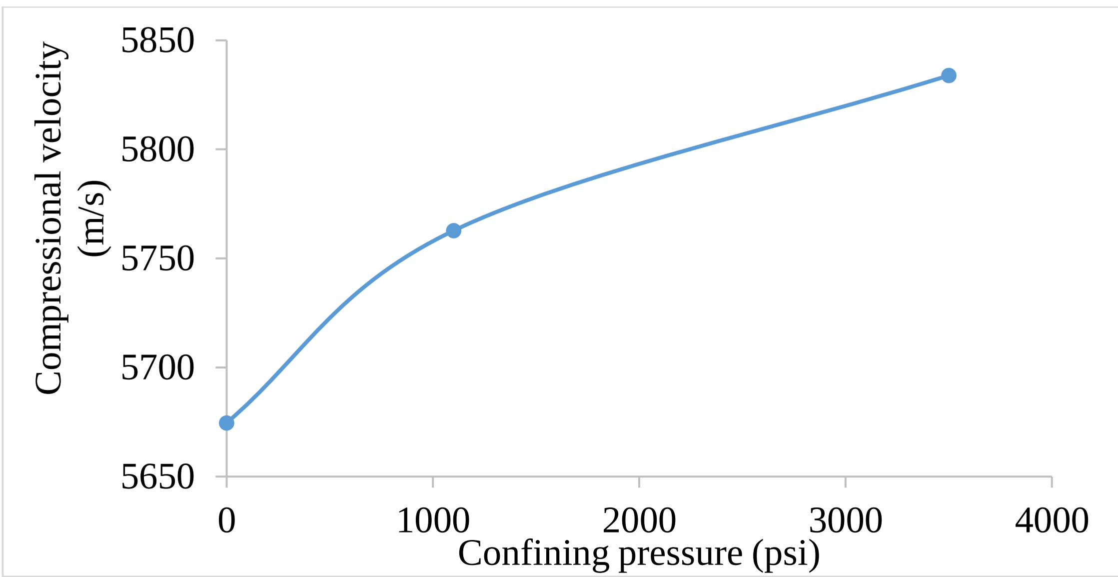

Figure 231: Figure showing variation of compressional velocity for sample OXY-72-3-3861.5-V2 with change in confining pressure. Results show about 6% variation in velocities as confining pressure changes from 0 to 3500 psi.

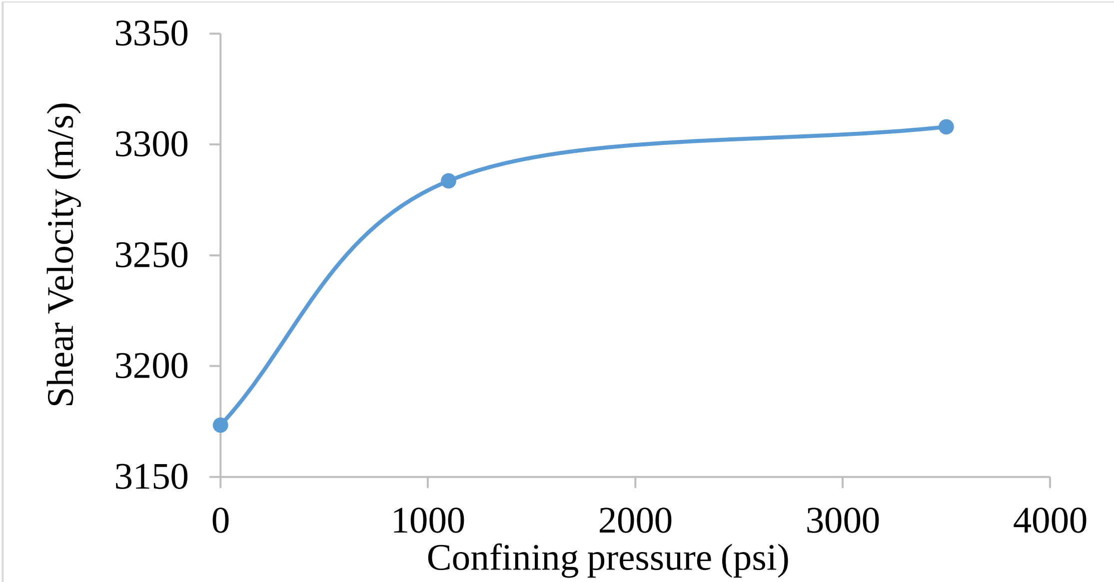

Figure 232: Figure showing variation of shear velocity for sample OXY-72-3-3861.5-V2 with change in confining pressure. Results show about 2% variation in velocities as confining pressure changes from 0 to 3500 psi.

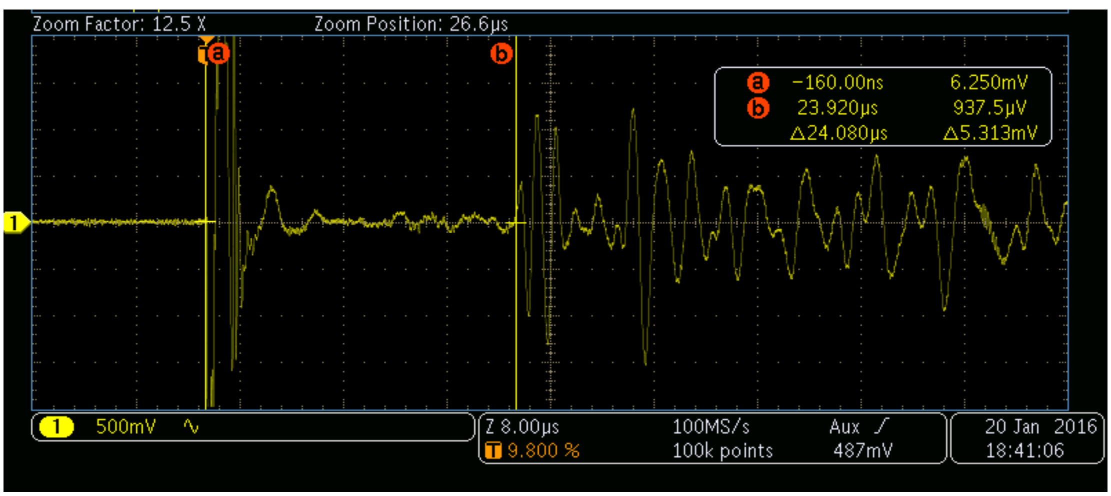

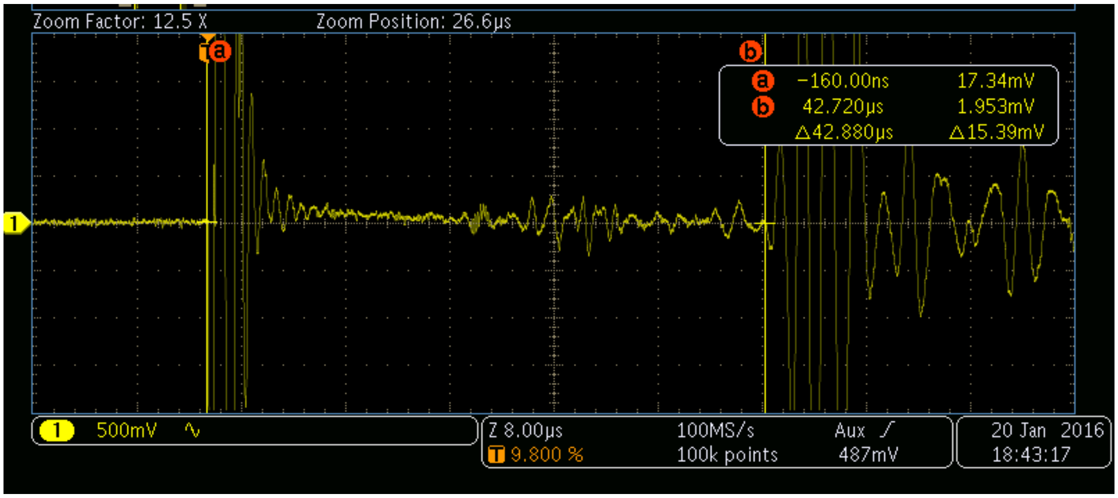

Figure 233: Above two figures show compressional (top) and shear waves for sample OXY-72-3-3861.5-V2. Corrections were applied to these waves to remove effect of platen travel time.

Sample GEO-N2-4361-V3

Sample is light gray in color and has a length of 52.17 mm and diameter of 25.43 mm. Sample has a porphyritic structure with large white grains (>3mm) interspersed within an otherwise fine grained sample. No fractures or cracks can be seen within the sample with naked eye. Sample has a length to diameter ratio of 2.05. Thin section images of this sample have already been provided.

Figure 234: Front view of sample GEO-N2-4361-V3 showing a fine grained matrix, grayish-green in color with white calcite crystals interspersed within the sample.

Dynamic Velocity measurements

Dynamic velocity tests were carried within the triaxial cell just before and after the test. These were measured at confining pressures of 0 to 3500 psi - these are reported below. The reason for these pressures is that ideally, velocities should be measured at the in-situ conditions although measuring them at low confining pressures and then comparing those to higher pressures gives a qualitative idea of the compressibility of the material as well as its porosity. Very large differences (>10%) are seen in unconsolidated rocks while lower differences are found in consolidated rocks (<5%). Presence of large crystals like seen in this sample can also strongly affect these readings as the velocity of wave within these grains may be very different from the rest of the matrix.

In the case of sample GEO-N2-4361-V3, a difference of 6% was observed between the compressional velocities measured between 100 psi or 3500 psi, while the difference for shear velocities was lower at 2% over the same confining pressure range. This shows the well consolidated nature of these rocks. Average V_p/V_s ratio of 1.67 was observed for this sample. Tests were carried out with axially placed compressional and shear crystals, both of frequency 500 Hz, placed within the top and bottom platens. Results are tabulated below:

Table 44: Compressional and shear velocities for sample GEO-N2-4361-V3

Confining Pressure	P-wave velocity (m/s)	S-wave velocity (m/s)	Dynamic Elastic Modulus (GPa)	Dynamic Poisson's ratio

100	4516	2751	45.84	0.20
250	4516	2762	46.06	0.20
1000	4632	2768	47.08	0.22
2000	4723	2781	48.00	0.23
3500	4787	2788	48.56	0.24

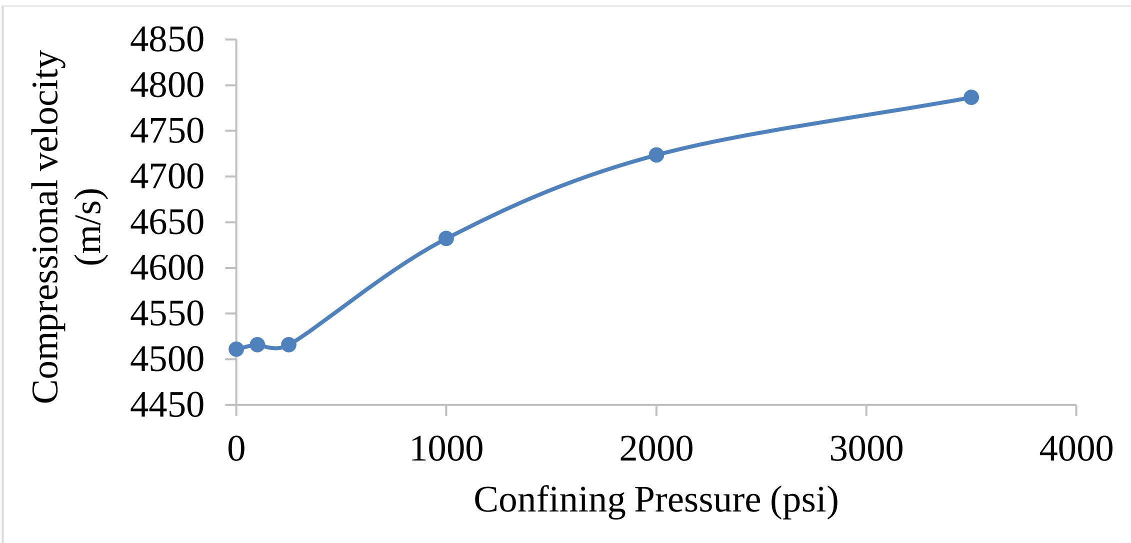

Figure 235: Figure showing variation of compressional velocity for sample GEO-N2-4361-V3 with change in confining pressure. Results show about 6% variation in velocities as confining pressure changes from 0 to 3500 psi.

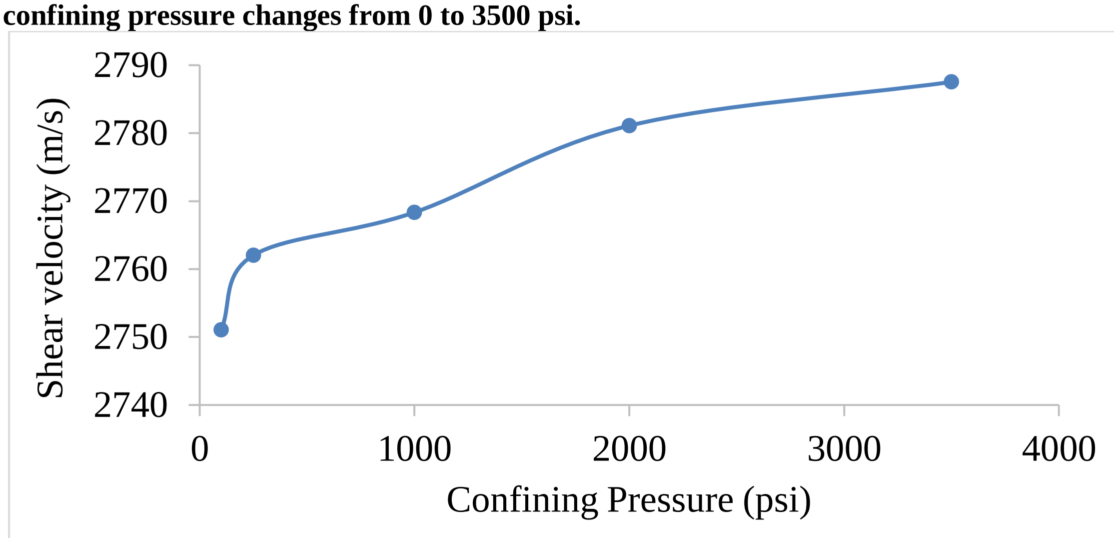

Figure 236:Figure showing variation of shear velocity for sample GEO-N2-4361-V3 with change in confining pressure. Results show about 2% variation in velocities as confining pressure changes from 0 to 3500 psi.

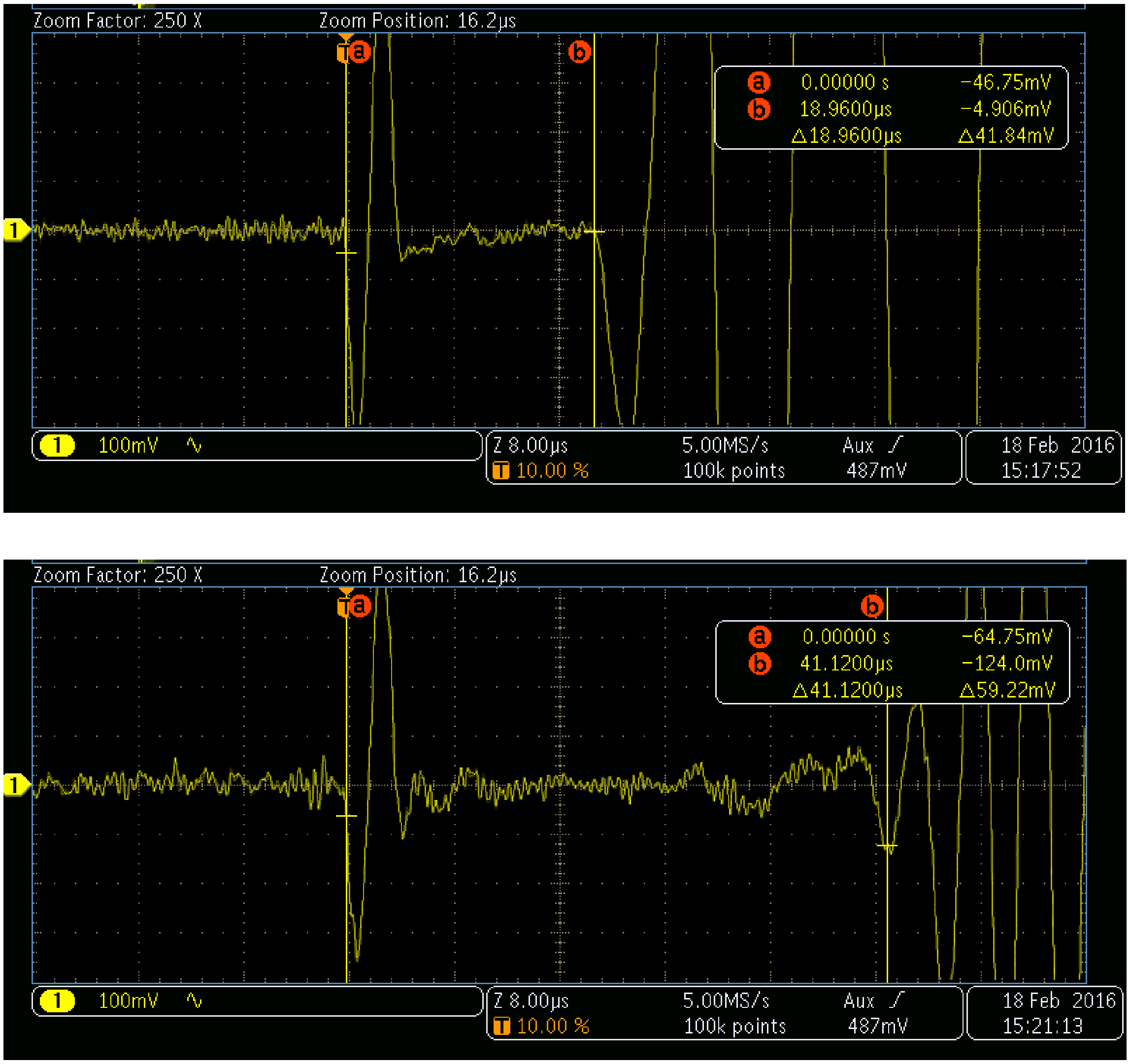

Figure 237: Above two figures show compressional (top) and shear waves for sample GEO-N2-4361-V3. Corrections were applied to these waves to remove effect of platen travel time.

Variation of Porosity with changing confining pressure

The porosity –permeability relationship with changes in confining pressure was measured using a AP-608 Automated Permeameter-Porosimeter (Described in detail earlier).

The porosity of the sample as a function of confining pressure (500 psi to 4000 psi) was measured and found to vary from 0.22%-0.12% and is shown below:

Table 45: Porosity vs confining pressure for sample GEO-N2-4361-V3

Confining pressure (psi)	Connected Porosity (%)
517	0.22
1536	0.18
2341	0.15
3066	0.12
4040	0.12

The extremely low values of porosity show the highly compacted nature of this rock.

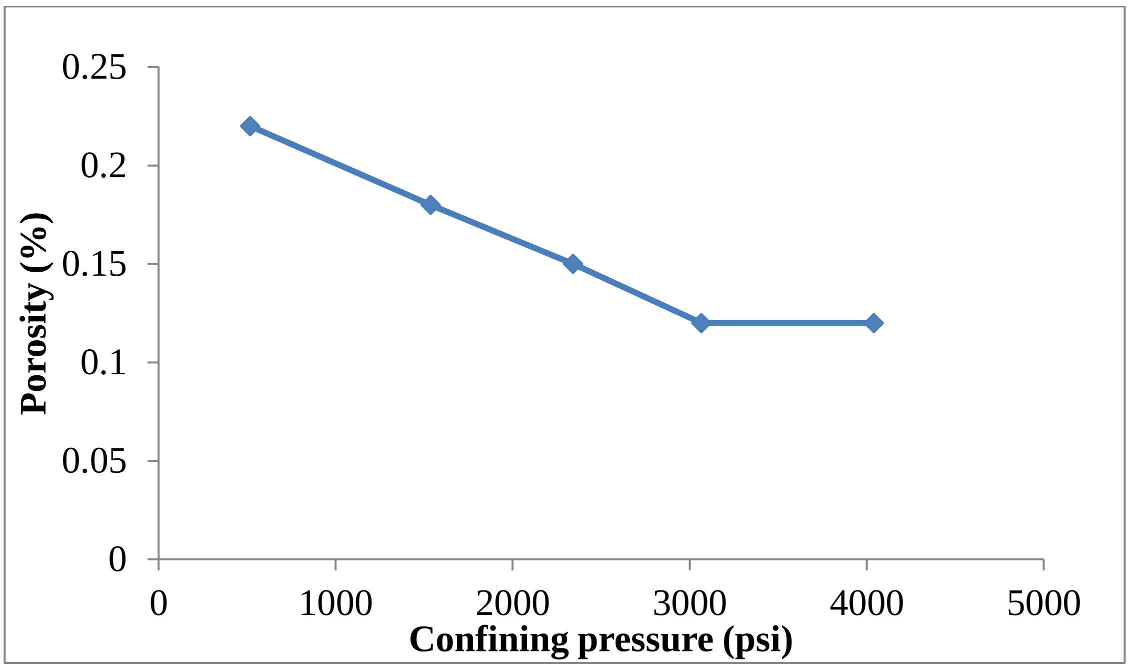

Figure 238: Variation of porosity with confining pressure for sample GEO-N2-4361-V3.

Sample GEO-N2-4180-H1:

Figure 239: Pictures of sample GEO-N2-4180-H1 before testing

Variation of Porosity and permeability with changing confining pressure

The porosity –permeability relationship with changes in confining pressure was measured using a AP-608 Automated Permeameter-Porosimeter. The porosity of the sample as a function of confining pressure (300 psi to 2800 psi) was measured and found to vary from 19.51%-18.41% and is shown below:

Table 46: Porosity vs confining pressure for GEO-N2-4180-H1

Confining pressure (psi)	Connected Porosity (%)
308	19.51
800	18.98
1832	18.62
2800	18.41

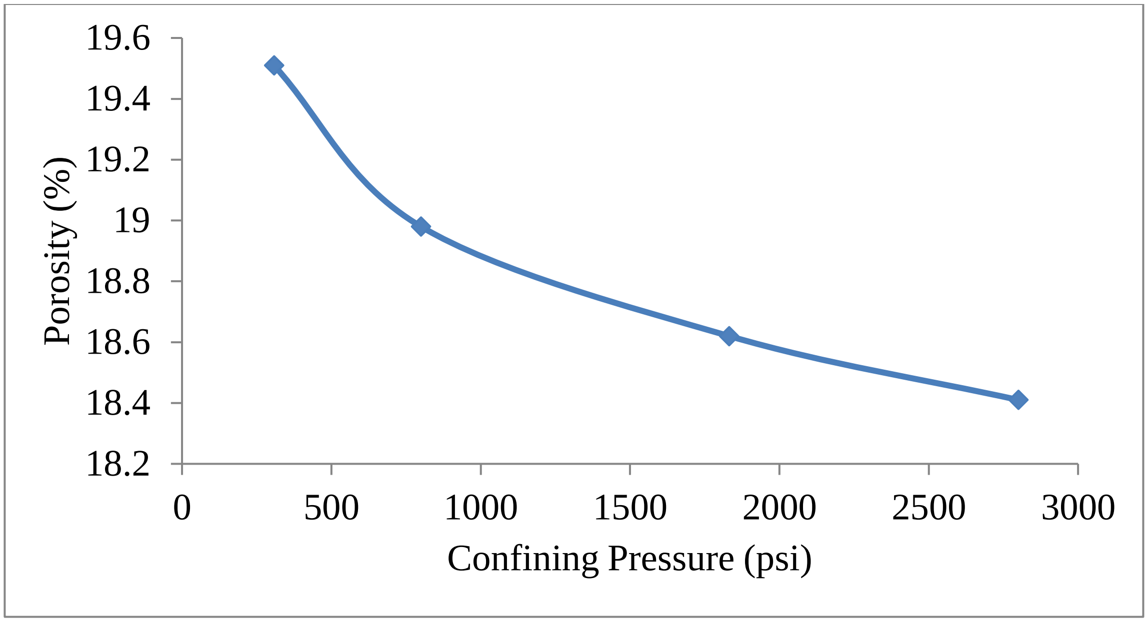

Figure 240: Porosity vs Confining pressure for sample GEO-N2-4180-H1.

The permeability of the sample as a function of confining pressure (300 psi to 2800 psi) varies from 0.45 mD-0.11 mD and is shown below in tabular format. Note that these are Klinkenberg slip corrected values.

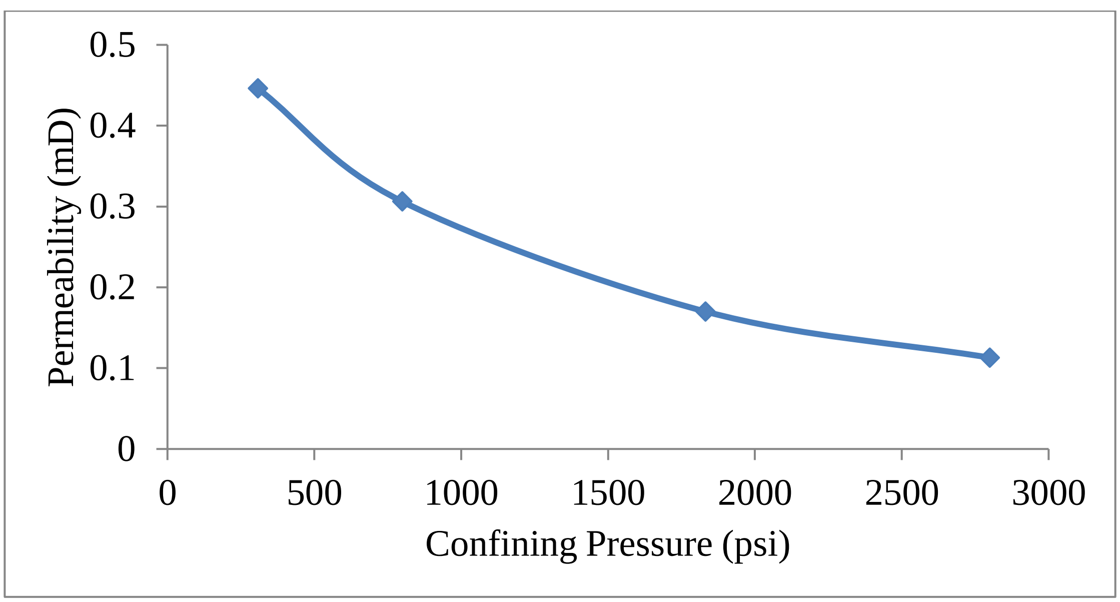

Figure 241: Permeability vs Confining pressure for GEO-N2-4180-H1

Table 47: Permeability vs confining pressure for GEO-N2-4180-H1

Confining pressure (psi)	Permeability (mD)
308	0.446
800	0.306
1832	0.170
2800	0.113

The porosity-permeability variation plot for the sample is shown below:

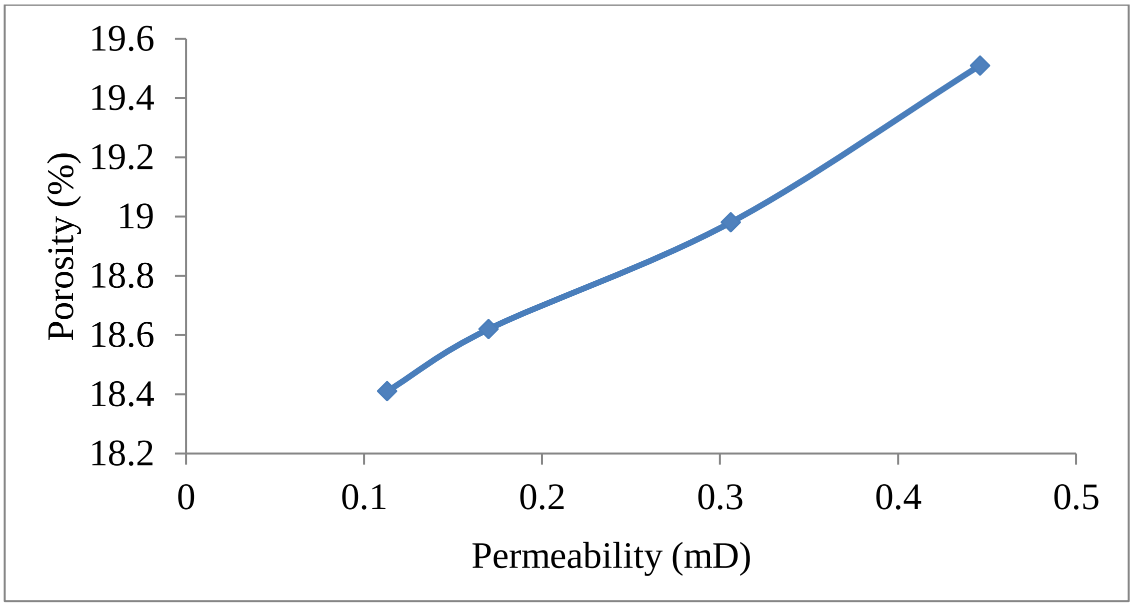

Figure 242: Porosity vs permeability for GEO-N2-4180-H1

Compressional and Shear velocity testing results

Dynamic velocity tests were carried within the triaxial cell just before the test. These were measured at confining pressures of 0 to 3100 psi - these are reported below.

In the case of sample GEO-N2-4180-H1, a huge difference of 45.1% was observed between the compressional velocities measured between 1 psi or 3000 psi, while the difference for shear velocities was higher at 56% over the same confining pressure range. This shows the non-consolidated nature of these rocks (further validated by the low Young's modulus of the sample). Average V_p/V_s ratio of 1.55 was observed for this sample. Tests were carried out with axially placed compressional and shear crystals, both of frequency 500 Hz, placed within the top and bottom platens. Results are tabulated below.

Table 48: Compressional and shear velocities for sample GEO-N2-4180-H1

Confining Pressure (psi)	P-wave velocity (m/s)	S-wave velocity (m/s)	Dynamic Elastic Modulus (GPa)	Dynamic Poisson's ratio
60	1648	912	4.71	0.28
500	2443	1660	13.05	0.07
1000	2592	1754	14.66	0.08
3000	3011	2073	19.94	0.05

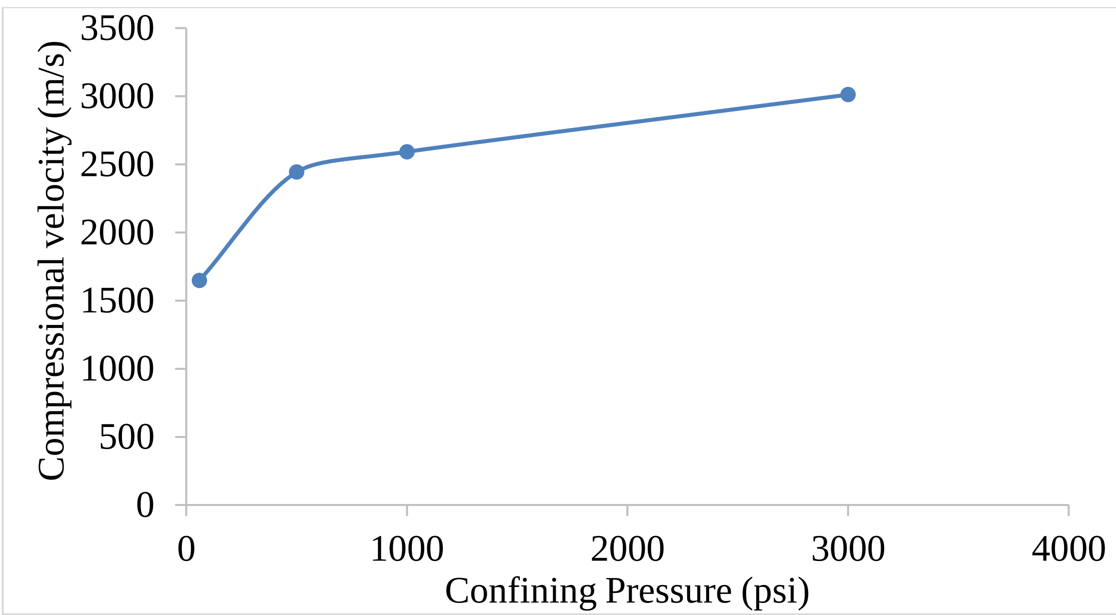

Figure 243: Figure showing variation of compressional velocity for sample GEO-N2-4180-H1 with change in confining pressure. Results show about 45% variation in velocities as confining pressure changes from 60 to 3500 psi. This is indicative of a weakly consolidated rock. Note that the porosity of this sample was high at ~20%

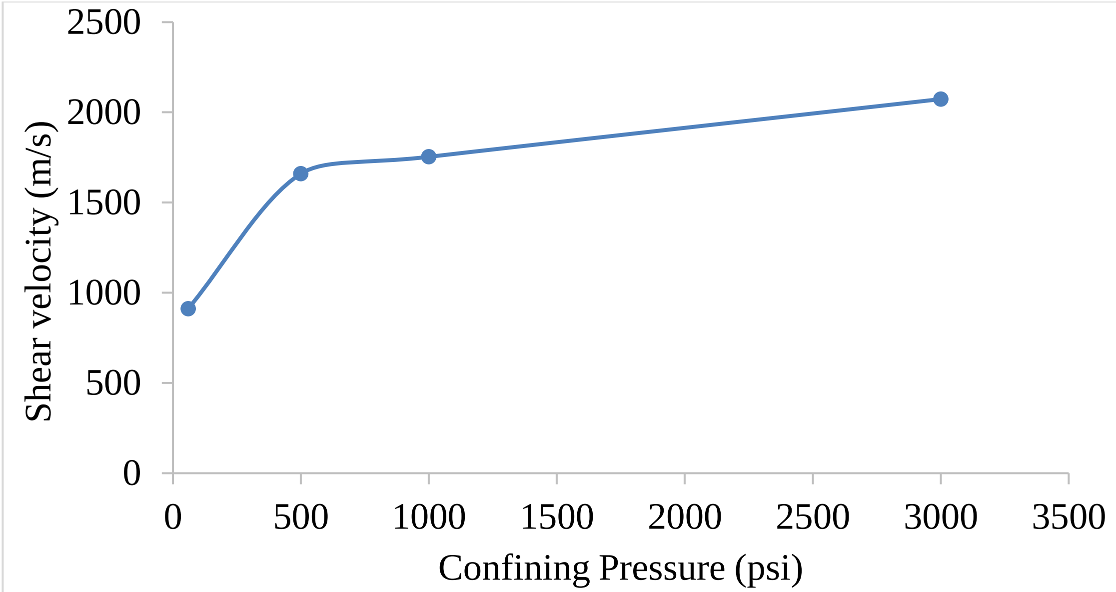

Figure 244: Figure showing variation of shear velocity for sample GEO-N2-4180-H1 with change in confining pressure. Results show about 56% variation in velocities as confining pressure changes from 60 to 3000 psi.

Figure 245: Above two figures show compressional (top) and shear waves for sample GEO-N2-4180-H1. Corrections were applied to these waves to remove effect of platen travel time.

APPENDIX 2: MOMENT TENSOR INFORMATION

The seismic moment tensor, M, is a 3x3 tensor, representing the orientation and magnitude of nine possible force-couples (Graham et al., 2010):

$$\mathrm{M} = \begin{pmatrix} m_{11} & m_{21} & m_{31} \\ m_{12} & m_{22} & m_{32} \\ m_{13} & m_{23} & m_{33} \end{pmatrix}$$

The diagonal elements represent normal force-couples, which exert no torque, whilst the remaining elements represent shear force-couples (Aki and Richards, 2002).

The SiGMA method by Ohtsu, 1991; Shgieshi, 2001 and Dahm et. al., 1999 describes how to calulate the Amplitude of the P-wave created due to the AE source as follows:

$$A(x) = \frac{C_s Ref(t,r)}{4\pi\rho R v_p^3}(r1, r2, r3)\begin{pmatrix} m_{11} & m_{21} & m_{31} \\ m_{12} & m_{22} & m_{32} \\ m_{13} & m_{23} & m_{33} \end{pmatrix}\begin{pmatrix} r_1 \\ r_2 \\ r_3 \end{pmatrix}$$

Where, A is displacement produced by an AE source at point y and recoded at a position, x which is at a distance R away, in a direction r = (r1,r2,r3). Ref (t,r) is the reflection coefficient at the observationm surface. ρ is the density of the medium, Vp is the P-wave velocity and Cs is the calibration coefficient. Therefore a minimum of six sensors are needed to solve for the unique moment tensor elements.

Knopoff and Randall, 1970 decsribe how after the moment tensor has been claculated, decomposition can be carried out by uisng its eigenvalues and then the shear, tenisle and mixed components can be calculated (also refer Graham et al, 2008).

The moment tensor analysis provided here for Sample GEO-N2-4243-I1 of the GEO N2 full core samples has been done using the low frequency and far field approximation of the Point-Source Model of the elasto-dynamic field by Rice (1979). This model is appropriate if the following conditions are met (from author):

1. Source distance R is much larger (10 times or more) than source region radius L.
2. Wavelengths must be larger than L, which means that low pass region w<Cp/L of signal spectra may be used in analysis.
3. The source distance is much larger than Cp/w.
4. Material is isotropic and homogeneous (at least in frequency band where analysis is applied).
5. Source function is considered as a step-like function ignoring any crack lips motion details.

The algorithm of the SiGMA3D MT analysis is well documented in several publications by its originator Dr. Masayasu Ohtsu, Professor at Kumamoto University, Japan. This method is used here to do the full moment tensor inversion.

APPENDIX 3 – BRAZILIAN TEST RESULTS FOR GEO-N2 SAMPLES

Indirect tension tests often referred to as Brazilian tests were performed on several plugs. The indirect tensile strength of the specimens was calculated as follows:

$$\sigma_t = \frac{2P}{\pi D t}$$

Where, σ_t is the Brazilian tensile strength (MPa); P is the load at failure (N); D is the diameter of the specimen (mm); t is the thickness of the specimen (mm) (ISRM 1978). A test result for the sample GEO-N2-4382-I1 is shown below.

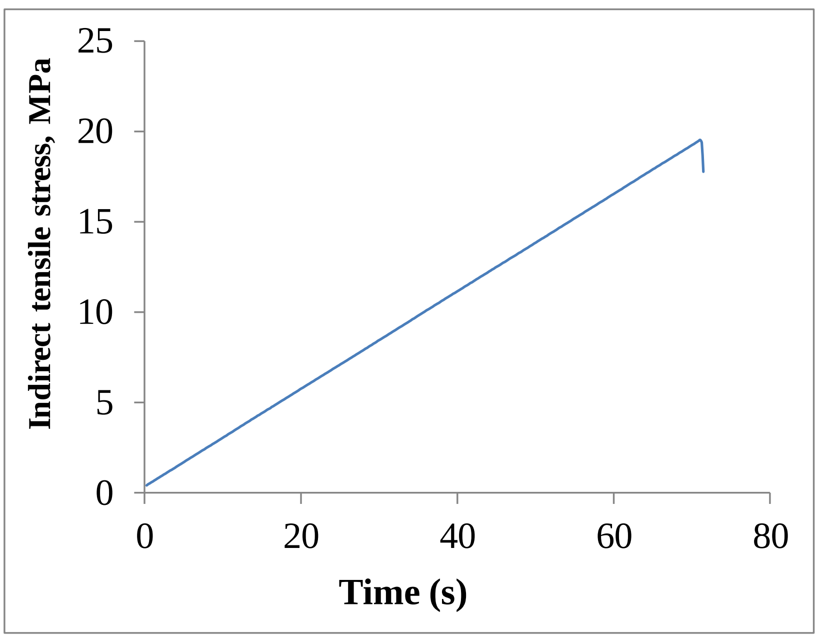

Figure 246: Axial force vs time plot for sample GEO-N2-4382-I1-S1 Brazilian test.

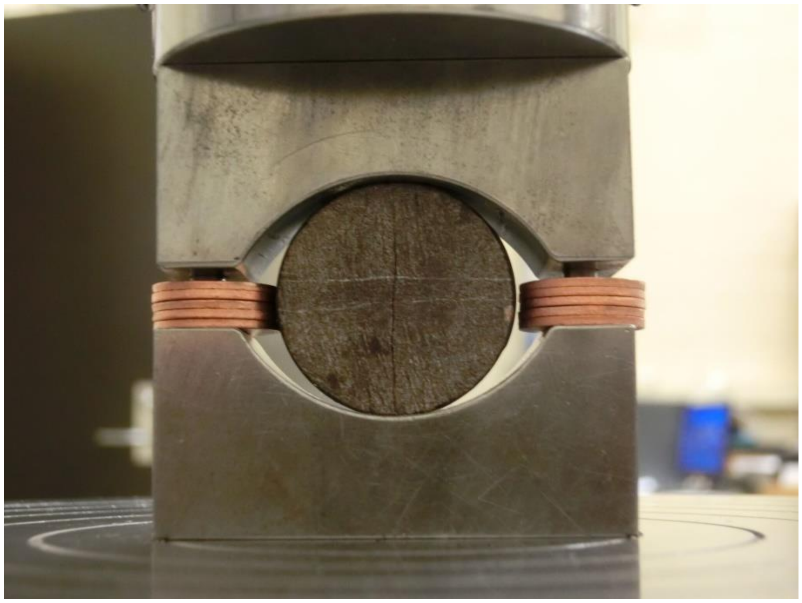

Figure 247: Brazilian strength test picture for Sample GEO-N2-4243-I1-S1 showing the set up and fracture passing through the vertical axis after failure.

Table 49: Brazilian test results for GEO-N2 samples

Sample name	Indirect Tensile Strength (MPa)
Sample GEO-N2-4382-I1-S1	19.2
Sample GEO-N2-4382-I1-S2	13.2
Sample GEO-N2-4243-I1-S1	20.9
Sample GEO-N2-4243-I1-S2	27.2